

The Pennsylvania State University

The Graduate School

Department of Energy and Mineral Engineering

**MEASUREMENT AND MODELING THE COEFFICIENT OF RESTITUTION OF CHAR
PARTICLES UNDER SIMULATED ENTRAINED FLOW GASIFIER CONDITIONS**

A Dissertation in

Energy and Mineral Engineering

by

LaTosha M. Gibson

Submitted in Partial Fulfillment
of the Requirements
for the Degree of

Doctor of Philosophy

May 2014

The dissertation of LaTosha Gibson was reviewed and approved* by the following:

Dr. Sarma Pisupati
Associate Professor of Energy and Mineral Engineering
Dissertation Advisor
Chair of Committee

Dr. Yaw Yeboah
Dean of the College of Engineering of Florida State University and
Florida Agricultural and Mechanical University

Dr. Derek Elsworth
Professor of Energy and Geo-Environmental Engineering

Dr. Robert Santoro
George L. Guillet Professor Emeritus of Mechanical Engineering

Dr. Lawrence Shadle
Team Leader of Reactor and Process Development Team, Energy Process Innovation
Division, NETL, US Department of Energy
Special Member

Dr. Luis F. Ayala H.
Associate Professor of Petroleum and Natural Gas Engineering and Associate
Department Head for Graduate Education

*Signatures are on file in the Graduate School

ABSTRACT

Inefficiencies in plant operations due to carbon loss in flyash, necessitate control of ash deposition and the handling of the slag disposal. Excessive char/ash deposition in convective coolers causes reduction in the heat transfer, both in the radiative (slagging) section and in the low-temperature convective (fouling) heating section. This can lead to unplanned shutdowns and result in an increased cost of electricity generation. CFD models for entrained flow gasification have used the average bulk coal composition to simulate slagging and ash deposition with a narrow particle size distribution (PSD). However, the variations in mineral (inorganic) and macerals (organic) components in coal have led to particles with a variation in their inorganic and organic composition after grinding as governed by their Particle Size Distribution (PSD) and mineral liberation kinetics. As a result, each particle in a PSD of coal exhibits differences in its conversion, particle trajectory within the gasifier, fragmentation, swelling, and slagging probability depending on the gasifier conditions (such as the temperature, coal to oxygen ratio, and swirling capacity of the coal injector).

Given the heterogeneous behavior of char particles within a gasifier, the main objective of this work was to determine boundary conditions of char particle adhering and/or rebounding from the refractory wall or a layer of previously adhered particles. In the past, viscosity models based on the influence of ash composition have been used as the method to characterize sticking. It is well documented that carbon contributes to the non-wettability of particles. Therefore, it has been hypothesized that viscosity models would not be adequate to accurately predict the adhesion behavior of char. Certain particle wall impact models have incorporated surface tension which can account the contributions of the carbon content to the adhesive properties of a char particle. These particle wall impact models also predict the coefficient of restitution (COR) which is the ratio of the rebound velocity to the impacting velocity (which is a necessary boundary condition for Discrete Phase Models). However, particle-wall impact models do not use actual geometries of char particles and motion of char particles due to gasifier operating conditions. This work attempts to include the surface geometry and rotation of the particles.

To meet the objectives of this work, the general methodology used for this work involved (1) determining the likelihood of particle becoming entrapped, (2) assessing the limitations of

particle-wall impact models for the COR through cold flow experiments in order to adapt them to the non-ideal conditions (surface and particle geometry) within a gasifier, (3) determining how to account for the influence of the carbon and the ash composition in the determination of the sticking probability of size fractions and specific gravities within a PSD and within the scope of particle wall impact models, and (4) using a methodology that quantifies the sticking probability (albeit a criterion or parameter) to predict the partitioning of a PSD into slag and flyash based on the proximate analysis.

In this study, through sensitivity analysis the scenario for particle becoming entrapped within a slag layer was ruled out. Cold flow educator experiments were performed to measure the COR. Results showed a variation in the coefficient of restitution as a function of rebound angle due rotation of particles from the educator prior to impact. The particles were then simply dropped in “drop” experiments (without educator) to determine the influence of sphericity on particle rotation and therefore, the coefficient of restitution. The results showed that in addition to surface irregularities, the particle shape and orientation of the particle prior to impacting the target surface contributed to this variation of the coefficient of restitution as a function of rebounding angle. Oblique particle impact measurements and images suggested the possibility of particles simultaneously rolling and sliding due to non-sphericity.

Calculations also showed that the COR due to viscoelasticity is most sensitive. Therefore, the critical velocity was derived from a viscoelastic particle wall impact model based upon the yield strength and a variable termed the plastic loss factor. However, by setting the plastic loss factor equal to the COR, trivial solutions were obtained in the derivation of critical velocities where the COR had to equal zero in order for the particle to stick. Therefore, the damping ratio was set to a value of 1 to indicate critical damping while the COR was set to zero to independently solve for the plastic loss factor. By solving for the plastic loss factor, critical velocities were determined for particles in each specific gravity and size fraction used in this study. An alternative “rules based method” based upon the contact angle and the temperature of critical velocity was also used to determine a sticking probability. With the exception of some of the larger size fractions, there was a better agreement between the sticking probabilities based on the critical velocities and the sticking probabilities calculated using the “rules-based-criteria”

than the “rules-based-criteria” and the conventional model (in which only the temperature of critical velocity was used). Capture efficiencies of these particles were calculated using sticking probabilities and impact efficiencies. The range of values of the capture efficiencies determined through the rules-based-criteria were similar to the range of values reported in previous experimental work concerning ash and char deposition.

Conventional viscosity models only predicted a significant variation in the adhesion between particles of different specific gravities not particle sizes. By using the “rules-based-criteria”, the influence of the particle size fractions was also discerned in addition to that of the specific gravities within the PSD. With the influence of unburnt carbon accounted for, the particles from “lighter” specific gravity fractions (SG1 and SG2) among the largest size fractions contributed the most to the flyash whereas, the “heavier” specific gravity fractions (with the exception of SG4, SF1) contributed the most to the slag. Therefore, by reducing the largest size fractions and increasing the smallest size fractions, syngas increased incrementally, flyash decreased incrementally, and slag increased marginally.

This work has identified the importance of characterizing particle orientation due to rotational motion in all three Cartesian coordinates prior to impact in addition to characterizing simultaneous sliding and rotation in oblique impact for non-spherical particles. A sticking probability based on the critical velocity was developed to provide consistency between CFD models and an industrial friendly model to predict partitioning of slag and flyash. Based on the results of this model developed in this work, flyash was shown to be reduced by reducing the average particle size. In summary, the connection between the physics of char particles impacting the wall of a gasifier and their ash as well as carbon composition has been comprehensively investigated in this study.

TABLE OF CONTENTS

LIST OF FIGURES	ix
LIST OF TABLES	xiv
NOMENCLATURE	xvii
ACKNOWLEDGEMENTS	xxiii
CHAPTER 1 INTRODUCTION	1
1.1 Description of the Integrated Gasification Combined Cycle	1
1.1.1 Description of the Gasification Block	1
1.2 Conventional Methods for Characterizing Sticking	4
CHAPTER 2 BACKGROUND	11
2.1 Population Models	11
2.1.1 Grinding	11
2.1.2 Particle Size Distribution	13
2.1.3 Circulating Fluidized Bed Sulfur Capture	13
2.2 Mineral Transformation and Mechanisms for Conversion	15
2.3 Modes of Particle Deposition	17
2.4 Surface Tension	18
2.5 The Role of Sintering in Ash Adhesion	20
2.6 Contribution of Molecular Structure to Particle Stiffness	23
2.6.1 Crosslinking Density Pertaining to Organic Polymers and Coal Matrix	24
2.6.2 Crosslinking Density Pertaining to the Structure of Glass Oxides	27
2.7 Viscoelastic, Elastic, and Plastic Properties of materials	28
2.7.1 Linear Elastic Model	28
2.7.2 Linear Viscoelastic Model	29
2.7.3 Voigt (Kelvin) Model	31
2.8 Particle Wall Impact Models	32
2.8.1 Elastic Adhesive Model	33
2.8.2 Viscoelastoplastic (VEP) Model	36
2.8.3 Liquid Droplet Impact (LDI) Model	39
2.9 The Role of Mechanical Vibrations in Particle Wall Collisions	40
2.10 Particle Oblique Impact	43
2.10.1 Tangential and Normal Coefficient of Restitutions	43
2.10.2 Impulse Ratio and Particle Rotational Motion	44
2.10.3 Sliding versus Rotation and Micro-slip	45
CHAPTER 3 PROBLEM DEFINITION, HYPOTHESIS, AND OBJECTIVE	47
3.1 Problem Definition	47
3.2 Hypothesis	50
3.3 Objective	50

CHAPTER 4 APPROACH AND METHODOLOGY	52
CHAPTER 5 EXPERIMENTAL METHODS	56
5.1 Nanoindentation Experimental Measurements	56
5.1.1 Apparatus	56
5.1.2 Approach and Application.....	57
5.1.3 Results	58
5.2 Particle Wall Collision Experiments.....	61
5.2.1 Selection of Substrates	61
5.2.2 Model Equations used to Calculate Coefficient of Restitution	62
5.2.3 Apparatus and Particle Description.....	64
5.2.4 Post-Processing High Speed Video Images	66
CHAPTER 6 RESULTS AND DISCUSSION.....	69
6.1 Particle Impact Experiments	69
6.1.1 Particle Wall Impact Experiments with High Density Polyethylene Particles.....	69
6.1.1.1 Flat Metal Case.....	69
6.1.1.2 Case for Hard Viscosity Substrate, Soft Viscosity Substrate, and Adhered Particles	69
6.1.2 Critical Velocity	70
6.1.3 Drop Experiments	75
6.1.4 Variance in Impact Angle.....	76
6.1.5 Analysis of Variance (ANOVA)	84
6.2 Model Development.....	86
6.2.1 Particle Entrapment Model Development	86
6.2.1.1 Force Balance	86
6.2.1.2 Cases.....	87
6.2.2 Sensitivity Analysis.....	90
6.3 Conventional Methods of Sticking	92
6.3.1 Mineral Transformation and Liquid Fraction.....	92
6.3.2 Sticking Probability due to Viscosity and Liquid Slag Fraction	93
6.3.3 Sticking Probability Method based on Temperature of Critical Viscosity and Contact Angle.....	99
6.4 Coefficient of Restitution and Critical Velocity	99
6.4.1 Total Coefficient of Restitution.....	99
6.5 Partitioning Between Slag, Flyash, and Syngas.....	109
6.5.1 Approach	109
6.5.2 Sticking Efficiency, Impact Efficiency, and Capture Efficiency	109
6.5.3 Partitioning of Ash versus Slag	111
6.5.3.1 Temperature Dependence	111
6.5.3.2 Impact Efficiency and Carbon Conversion	112
6.5.3.3 Capture Efficiency	112
6.5.3.4 Particle Size Distribution.....	113
CHAPTER 7 CONCLUSIONS	124
CHAPTER 8 FUTURE WORK.....	127

8.1 High Temperature Measurements	127
8.2 Hot Flow Particle Wall Collision Experiment	127
8.3 Determining Coefficient of Restitution, Plastic Loss Factor, and Damping Ratio	128
REFERENCES	131
APPENDIX A CHARACTERIZATION OF PARTICLE SIZE DISTRIBUTION OF BAILEY COAL.....	136
APPENDIX B CALCULATION OF CRITICAL VELOCITIES	140

LIST OF FIGURES

Figure 1-1: Diagram of Integration Gasification Combined Cycle with Entrained flow gasifier	2
Figure 1-2: Entrained flow gasifier, Radiant Syngas Cooler, and Convective Syngas Cooler	3
Figure 1-3: Slag, flyash, brine, and process water flow diagram.....	4
Figure 2-1a-b: Particle size distribution due to abrasion, cleavage, and fracture	11
Figure 2-2: Breakage distribution as a function of shatter and cleavage	12
Figure 2-3: Size classification of particles to the bottom ash and Flyash streams	14
Figure 2-4: Partition curve for a particle size distribution	14
Figure 2-5: Partitioning of coal particles into syngas, flyash, and slag	18
Figure 2-6: Schematic of contact angle and interfacial surface tension between solid particle and liquid	19
Figure 2-7: Plot of contact angle versus time between select carbon containing particles with set slag composition	20
Figure 2-8: Schematic illustration of liquid phase transport in a silicate system.....	21
Figure 2-9: Zone of close pores formation, pore shrinkage, and diffusion of melts.....	22
Figure 2-10a-b: Plot showing the modulus of elasticity and degree of crosslinking versus temperature.....	23
Figure 2-11: Macromolecular and molecular model of low rank bituminous coal.....	26
Figure 2-11: Schematic of the four basic mechanical rheological models	28
Figure 2-12 a-b: The stress and strain curve as a function of time for the linear elastic model	28
Figure 2-14a-b: Stress and strain as a function of time for the Maxwell model	30
Figure 2-16: Forces of microsphere impact with surface.....	33
Figure 2-17: Schematic of microspherical particle impacting a planar surface.....	34
Figure 2-18a-b: Schematic of the viscoelastoplastic model and stress-strain curve	36
Figure 2-19: Modes of impacting droplet behavior	39
Figure 2-20: Basic schematic of un-damped system Motion.....	41

Figure 2-22: Basic Schematic of damped motion	41
Figure 2-23: Schematic of oblique impact	43
Figure 3-1: The three modes of behavior of particle impacting a slag layer	47
Figure 4-1: Density and size separated sample preparation flow diagram where SGO represents the whole coal and PSO represents the sample before separation	52
Figure 5-1a-b: Schematic of the nanoindentation system showing various parts	56
Figure 5-2: Plot of load versus displacement for multiple loading	57
Figure 5-4: Slope for determining reduced modulus of elasticity.....	58
Figure 5-3: A load displacement measurement for HDPE.....	58
Figure 5-6: Distribution of modulus of elasticity values	58
Figure 5-7: Slope for the determination of reduced modulus of elasticity for one data set of low viscosity silicone	59
Figure 5-8: Slope for the determination of reduce modulus of one set of data for high viscosity silicone	60
Figure 5-9: Schematic of a microspherical particle on a planar surface	62
Figure 5-10: Schematic of rolling object without slipping	63
Figure 5-11: Distribution of HDPE particle velocities in eductor experiment for steel metal plate using $1.13 \text{ m}^3/\text{h}$ air flow	66
Figure 5-12 Apparatus for particle wall impact experiments.....	67
5.12a: Vibrating particle feeder, funnel, and eductor.....	67
5.12c: Overall schematic of particle wall impact apparatus	67
5.12b: Steel plate connect to remote controlled rotational mount.....	67
Figure 5-13: Determination of the degree of equancy	68
Figure 6-1d: Normal coefficient of restitution versus rebound angle, metal plate, $1.13 \text{ m}^3/\text{hr}$ air flow for normal impact.....	71
Figure 6-1b: Normal coefficient of restitution versus rebound angle, metal plate, $0.28 \text{ m}^3/\text{hr}$ air flow for normal impact.....	71
Figure 6-2: Normal coefficient of restitution versus rebound angle for HDPE particles impacting adhered particles using $1.13 \text{ m}^3/\text{hr}$ air flow for normal impact.....	72

Figure 6-3: Normal coefficient of restitution versus rebound angle for HDPE particles impacting hard silicone using	72
Figure 6-4: Normal coefficient of restitution versus rebound angle for HDPE particles impacting soft silicone using 1.13 m ³ /hr air flow for normal impact.....	73
Figure 6-5: Average calculated rotational velocity versus degree of equancy of metal plate impact	78
Figure 6-6: Average rotational velocity versus normal coefficient of restitution of particle impact upon metal plate	79
Figure 6-7: Normal coefficient of restitution versus degree of equancy.....	80
Figure 6-8: Polystyrene pellet rebounding normal to steel	81
Figure 6-9: Polyethylene prior to impacting steel plate	81
Figure 6-10: Polyethylene rebounding from steel plate	81
Figure 6-11: Coke particle rebounding from steel plate	81
Figure 6-12a-c: Sequence of coke particle impacting and rebounding from steel plate	82
Figure 6-13a-d: Sequential images showing trajectories of HDPE particles impacting soft silicone adhesive at 70° from the horizontal using 1.13 m ³ /hr air flow	83
Figure 6-14: Slag displacement for a Newtonian fluid	87
Figure 6-15: Slag displacement for a Bingham fluid	87
Figure 6-16: Displacement and velocity of SG4 PS1 fraction penetrating SG 4 slag	89
with a velocity of 2 m/s.....	89
Figure 6-17: Displacement and velocity of SG4 PS1 fraction penetrating SG 4 slag	89
with a velocity of 8 m/s.....	89
Figure 6-18a-f: Displacement and velocity versus time for conditions in Table 6.4	91
Figure 6-19: Mineral transformation versus temperature for BSG1 and PS1	95
Figure 6-20: Mineral transformation versus temperature for BSG2 and PS1	95
Figure 6-21: Mineral transformation versus temperature for BSG3 and PS1	96
Figure 6-22: Mineral transformation versus temperature for BSG4 and PS1	96
Figure 6-23: Sticking probability versus temperature for each BSG	97

Figure 6-24: Liquid fraction of minerals versus temperature for each BSG.....	97
Figure 6-25: Probability of sticking for each size fraction for BSG1	98
Figure 6-26: Probability of sticking for each size fraction for BSG2	98
Figure 6-28: Probability of sticking for each size fraction for BSG4	98
Figure 6-27: Probability of sticking for each size fraction for BSG3	98
Figure 6-29a-c: Coefficient(s) of restitution as a function of surface tension to viscosity ratio	102
Figure 6-30: Coefficient of restitution versus the damping ratio for various plastic loss factors	103
Figure 6-31: The sticking efficiencies predicted for each SG and SF based on the plastic loss factor for each SG and SF	107
Figure 6-32: The sticking efficiencies predicted for each SG and SF with the plastic loss factor normalized.....	108
Figure 6-33: The flow diagram for determining the partitioning between slag, flyash, and syngas	110
Figure 6-34: Rosin Rammler distribution based on average particle sizes	115
Figure 6-35: Percentage of ash for each BSG and SF in the particle size distribution	115
Figure 6-36: Percentage of slag for each BSG and SF in the particle size distribution	116
Figure 6-37: Percentage of ash for each BSG and SF in the particle size distribution for 1434 K to 1541K.....	116
Figure 6-38: Percentage of slag for each BSG and SF in the particle size distribution for 1434 K to 1541K.....	117
Figure 6-39: Carbon conversion for each BSG and SF in the particle size distribution	117
Figure 6-40: Impact efficiency for each BSG and SF in the particle size distribution	118
Figure 6-41: Capture efficiency for each BSG and SF in the particle size distribution.....	118
Figure 6-42: Percentage of slag, unconverted char and ash, and converted char and syngas for different particle size distributions	121
Figure 6-43: Capture efficiency versus carbon conversion for SG1	122
Figure 6-44: Capture efficiency versus carbon conversion for SG2.....	122
Figure 6-46: Capture efficiency versus carbon conversion for SG4.....	123
Figure 6-45: Capture Efficiency versus carbon conversion for SG3	123

Figure 8-1: High temperature drop tube furnace with viewport	130
--	-----

LIST OF TABLES

Table 1-1 Coefficients for the high temperature and low temperature range of the Senior model.....	8
Table 2-1 Contributions of molecular structural groups to the cohesive energy of a particle.....	25
Table 2-2 Variation in coal rank with coal solubility.....	25
Table 2-3 Corresponding damping response and displacement profile for damping ratio values..	42
Table 4-1 Weight% (as received basis) of each specific gravity for the PSD of Bailey coal.....	53
Table 4-2 Particle size distribution of different density fractions (all sizes in μm), wt% (as received basis).....	54
Table 4-3 Proximate analysis of particle size distribution according to specific gravity.....	54
Table 4-4 Ash Analysis of particle size distribution according to specific gravity.....	54
Table 5-1 Average values for modulus of elasticity of "soft" low viscosity silicone adhesive.....	59
Table 5-2 Average value for modulus of elasticity of "hard" high viscosity silicone adhesive.....	60
Table 5-3 Properties of particles used in drop and eductor experiments.....	64
Table 5-4 Properties of surfaces used in eductor experiments.....	65

Table 6-1 Summary of average coefficient of restitution for eductor experiments for normal impact using HDPE Particles.....	74
Table 6-2 Summary of average coefficient of restitution for eductor experiments for substrate 70° from horizontal for HDPE particle.....	74
Table 6-3 Slag density and viscosity calculated based on the slag composition for each specific gravity.....	88
Table 6-4 The particle properties for Figure 18a-f penetrating a slag layer with viscosity of 5.48 Pa*s and density of 520 kg/m ³	90
Table 6-5 Partitioning fraction from size and density analysis of coal, wt% dry coal	114
Table 6-6 Percentage of increase of particle sizes in attaining each particle size distribution...	114
Table 6-7 Fixed carbon from proximate analysis.....	119
Table 6-8 Ash composition from proximate analysis.....	120
Table 6-9 Volatile Matter from Proximate Analysis.....	120
Table A-1 Particle size analysis for particle size distribution of Bailey coal.....	139
Table A-2 Mineral analysis for particle size distribution of Bailey coal.....	140
Table A-3 Ash composition for particle size distribution of Bailey coal.....	141
Table B-1 Calculated critical velocities for SG1 PS1.....	143
Table B-2 Calculated critical velocities for SG1 PS4.....	144
Table B-3 Calculated critical velocities for SG1 PS4.....	145

Table B-4 Calculated critical velocities for SG2 PS1.....	146
Table B-5 Calculated critical velocities for SG2 PS4.....	147
Table B-6 Calculated critical velocities for SG2 PS7.....	148
Table B-7 Calculated critical velocities for SG3 PS1.....	149
Table B-8 Calculated critical velocities for SG3 PS4.....	150
Table B-9 Calculated critical velocities for SG3 PS7.....	151
Table B-10 Calculated critical velocities for SG4 PS1.....	152
Table B-11 Calculated critical velocities for SG4 PS4.....	153
Table B-12 Calculated critical velocities for SG4 PS7.....	154

NOMENCLATURE

Symbol	Definition	Units
α	Contact radius Function of mill condition to determine ball mill size for grinding	m
A	Empirical constant for viscosity model Area Ash matrix	$\left(\frac{Poise}{K}\right)$ Chapter 1 m^2
A_H, A_L	High temperature and low Temperature empirical constants of Senior model	$\left(\frac{Poise}{K}\right)$
c	Damping coefficient	Dimensionles s
C	Fixed carbon matrix	
C_f	Drag coefficient	(kg/s)
e	Coefficient of Restitution	Dimensionles s
E	Energy Modulus of elasticity	$(Joules)$ GPa
F	Force Fraction of ash	N

G	Gibbs energy	<i>Joules</i>
H	Enthalpy	<i>Joules</i>
h_e	Elastic indentation depth	<i>m</i>
I	Impact matrix Moment of ratio	$kg * m^2$
k	Spring stiffness	<i>N/m</i>
K, K_y	Stiffness, Linear stiffness	<i>(1/GPa)</i>
k_d	Partition function	
K_i	Kinetic energy	<i>Joules</i>
$K_{i,a}$	Attrition coefficient of particles of species coarse enough to report to bottom ash	
L	Length	<i>meters</i>
m	Mass of particle	<i>gram</i>
M	Mass fraction Mass of displaced slag	$\frac{gram}{gram}$ <i>gram</i>

Mw	Molar weight	$\frac{gram}{mole}$
P	Impulse Load Pressure	$kg * \frac{m}{s}$ N Pa
r	Radius	<i>meters</i>
R	Gas constant	$J/mol \cdot K$
S	Specific rate of breakage Strength Syngas matrix	(1/s) GPa
S_i	Surface energy	<i>Joules</i>
ST	Sticking efficiency	
t	Time	s
T, T_s	Temperature, Shift temperature	K
U	Displacement of incompressible liquid Internal energy	m <i>Joules</i>
V	Velocity Volume Volatile matrix	m/s m^3
W	Mass fraction present after grind time	

w_A	Surface energy	J/m^2
x	Upper size of particle size in interval i	
X	Chemical potential Displacement Partition function matrix	J/mol m
X_m	Particle size for which the selection function is the maximum for given ball diameter	m
Z	Displacement	m

Greek Symbols

α	Expansion coefficient Function of material for ball mill Shape factor	$1/K$ Dimensionless Dimensionless
\bar{a}	Proportional constant used to determine ball diameter	
γ	Plastic loss factor	
δ	Solubility parameter	$(J^{1/2}/cm^{3/2})$
η	Viscosity	$Pa \cdot s$
ε	Strain	m/m
	Pore shrinkage rate	$1/s$
$\dot{\varepsilon}$	Strain Rate for viscoelastic properties	$1/s$

$\dot{\epsilon}_f$	Thermal strain rate	1/s
ζ	Damping ratio	
λ	Empirical function of material for ball mill	
μ	Impulse ratio	
$\bar{\mu}$	Proportional constant for determining ball mill diameter	
ρ	Density	g/m^3
τ	Shear stress	GPa
ν	Poisson ratio	m/m
σ	Stress	GPa
	Surface tension	N/m
Φ	Crosslinking density	m^3/mol
ψ_A	Dimensionless adhesive parameter	
ψ_H	Dimensionless Hertzian parameter	
ω	Angular velocity	1/s
	Natural frequency	1/s

Symbol	Definition	Symbol	Definition
A	Adhesive component	AD	Damping adhesive component
ba	Bottom ash	c	Compressive, compression
ca	Composite ash flow	f	Final
fa	Flyash	H	Hertzian

HD	Hertzian damping component	i	Initial Integral in defining different size interval impacting
I_C	Instantaneous center of zero velocity	k_d	Bottom ash in absence of attrition
lv	Liquid vapor	m	Maximum length Maximum force
n	Natural Normal	o	Initial
pl	Plastic	sl	Solid liquid interface
sv	Solid vapor interface	t	Tangential direction
tr	Reference Temperature	vap	Vaporization
x	Cartesian coordinate	y	Yield Cartesian coordinate

ACKNOWLEDGEMENTS

I would like to thank my adviser, Dr. Sarma Pisupati, for his guidance and patience during the completion of my research. With such excellent guidance, I have gained a new appreciation for energy conversion processes and its potential to meet the energy needs with minimal influence to the environment. I would also like to acknowledge my mentor, Dr. Lawrence Shadle, who has navigated me through the intricate process of conducting research and attaining the necessary resources. I would also like to thank Mr. Nari Soundarrajan, who at times has been a research partner in my graduate research group for the Carbon Particulate Partitioning Project. I would also like to thank Dr. Peter Rozelle, who I admire and respect, and has been an influential mentor and provided much needed career guidance.

I very much appreciate the graciousness of Mrs. Phyllis Mosesman, Mrs. Cyndi Freeman, and Dr. Catherine Lyons, who made sure that I had access to the support available through Penn State University to finish my matriculation requirements. I also like to thank the Alfred Sloan Fellowship for helping with the travel between Penn State University and my internship location.

Most of all, I would like to thank my parents who have provided me with the strong foundation to pursue all of my interests.

CHAPTER 1 INTRODUCTION

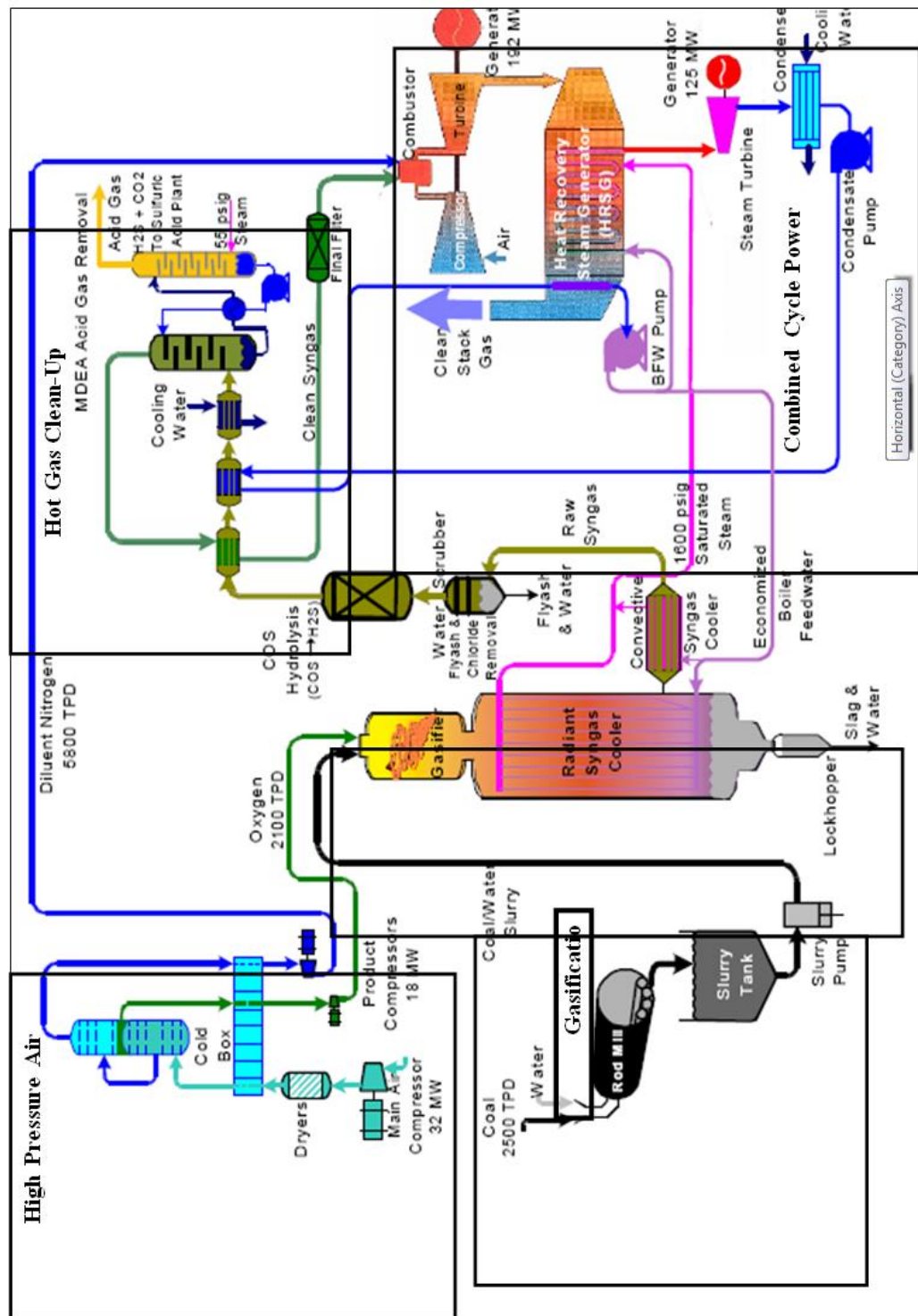
1.1 Description of the Integrated Gasification Combined Cycle

To meet energy demand economically, power plants try to attain the maximum carbon conversion possible based on their plant design. As a plant configuration, the Integrated Gasification Combined Cycle (IGCC) plant has proven to be more efficient than the pulverized coal combustion plant [1]. The IGCC contains the gasifier, air separation unit, gas clean-up block, and the combined cycle power generation block (Figure 1-1). In the IGCC, oxygen is separated from air in the air separation unit (1). This oxygen and coal is then fed into the gasifier (2). Synthesis gas “syngas”, which is composed mainly of hydrogen and carbon monoxide is produced during the gasification process. The syngas is then cleaned from the sulfur components in the hot gas clean-up block (3). Thereafter, the gas is directed to the combustor of the gas turbine where it is burned as a fuel (4). The volume increases in the combustor under a constant pressure that drives the turbine and powers the generator. The heat recovery steam generator recovers the heat from the gas turbine exhaust gases through heat exchangers and powers the steam turbine (5). Some waste heat escapes through the stack gases. The gasifier of interest is the entrained flow gasifier due to its high capacity, which is made possible by the relatively low residence time of the coal particles within the gasifier [2]. In the entrained flow gasifiers, fine coal concurrently reacts with steam and an oxidant. This gasifier uses oxygen as the oxidant and operates at high temperatures, well above the critical temperature for the solidification of the slag. These conditions are set to ensure high carbon conversion [3].

1.1.1 Description of the Gasification Block

The operation of the gasification block begins with the preparation of the coal slurry (Figure 1-1) [4]. Coal is fed into the rod mill by a weigh feeder along with the process water containing recycle fines. Additives that reduce the viscosity of the slurry and/or adjust the pH may also be fed into the mills. The slurry passes through openings in the trommel screen and falls into an agitated mill discharge tank. A centrifugal pump delivers the slurry to a finer screen at the top of a large tank. The screen removes any metal or coal particles that are large enough to be troublesome to the main slurry feed pump that delivers slurry to the gasifier. The coal slurry from the slurry feed pump and the oxygen from the air separation plant is fed into the gasifier through a series of valves. The oxygen and slurry are then combined in the process feed injector.

Figure 1-1: Diagram of Integration Gasification Combined Cycle with Entrained flow gasifier



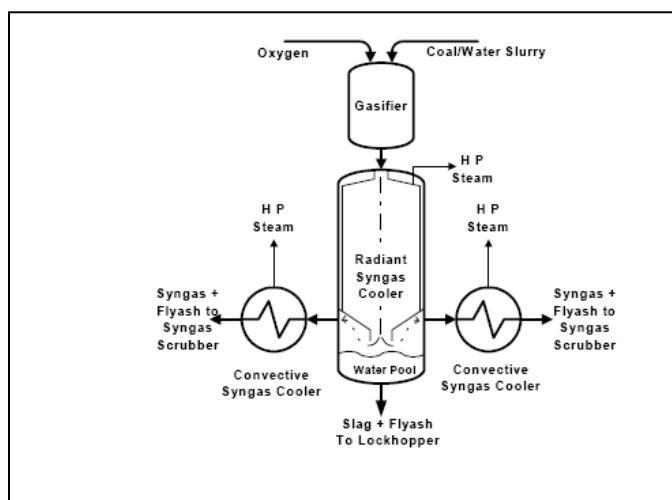
From Tampa Electric Company [4]

The coal slurry and the oxygen react in the gasifier to produce three products: Product gas, slag, and flyash.

Product gas: Product gas consists primarily of hydrogen, carbon monoxide, water vapor, carbon dioxide, hydrogen sulfide, carbonyl sulfide, methane, and nitrogen.

Slag: Slag is composed of the mineral matter that melts at the gasifier's elevated temperature and flows down the gasifier's refractory lined wall. This mineral matter ultimately solidifies into an inert glassy frit (granules of glass) with very little residual carbon content.

Figure 1-2: Entrained flow gasifier, Radiant Syngas Cooler, and Convective Syngas Cooler

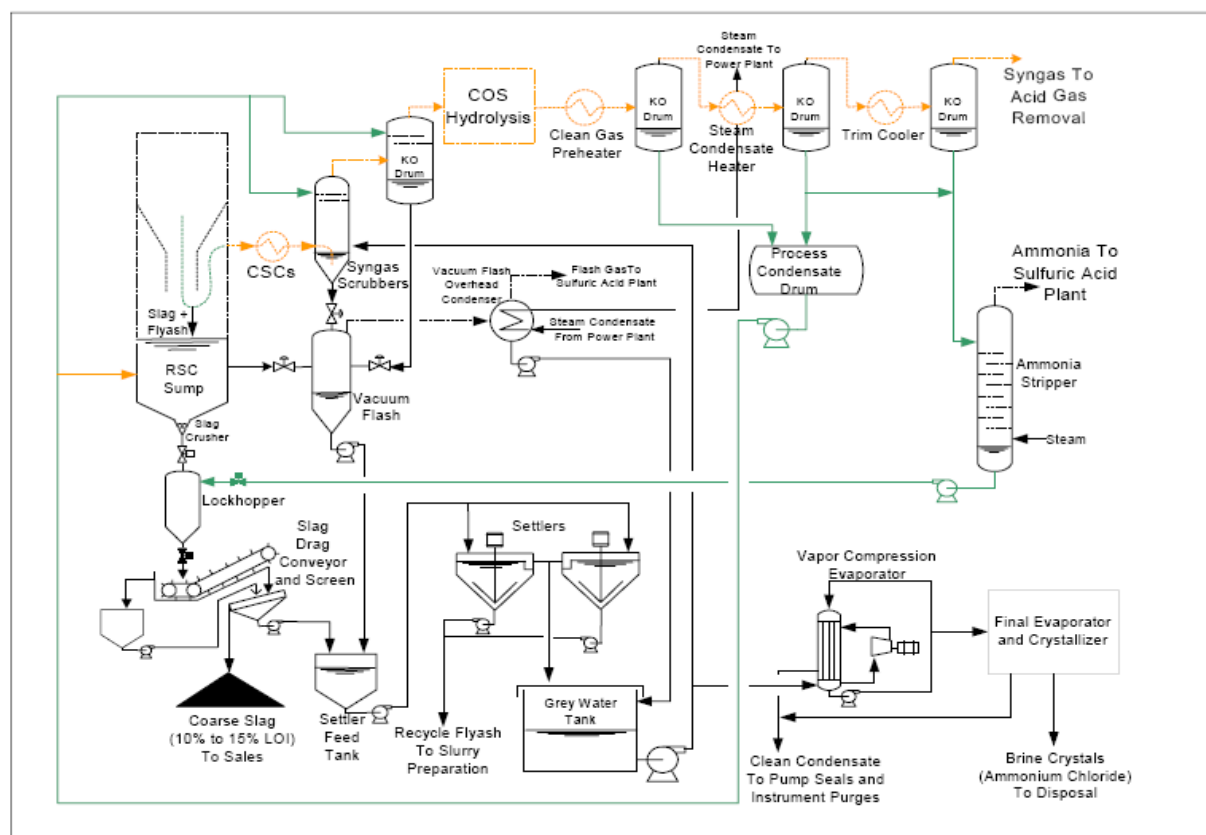


From Tampa Electric Company [4]

The gasifier exit stream is either immediately quenched in water (cooling it to less than 756K) or diverted through a Radiant Syngas Cooler (RSC). In the RSC, the syngas passes over the surface of a water pool located at the bottom of the unit before exiting. This water pool is called the RSC Sump and consists of particulate- and chloride-free process condensate. The RSC Sump collects virtually all of the slag and a portion of the flyash. The flyash that is not captured follows the syngas stream. The slag and the flyash which are captured by the RSC Sump descends through the water and passes through a slag crusher en-route to a lock hopper (Figure 1-3). The lock hopper discharges three to four times per hour to a drag flight conveyor, which deposits the slag and the flyash onto a washed slag screen. The coarse material from the top of

the screen is collected and sold to the cement industry. The water and fine solids that pass through the screen are pumped to the settler feed tank.

Figure 1-3: Slag, flyash, brine, and process water flow diagram



From Tampa Electric Company [4]

The flyash that is not captured travels with the syngas through the Convective Syngas Coolers (CSC) to the syngas scrubbers, where it is removed by intimate contact with water. Additional particulates and chlorides are removed from the syngas through the polishing of trays at the top of the scrubber. The syngas later leaves saturated with a portion of water vapor.

1.2 Conventional Methods for Characterizing Sticking

Conventional methods for characterizing ash adhesion have included slag indices, determination of the ash fusion temperature, temperature of critical viscosity, as well as the

viscosity itself. All these four parameters are based on the ash composition. Those ratios include iron to calcium ratio, silica to alumina ratio, silica ratio, and base to acid ratio. In comparing the performance of the slagging indices, there are two deposition indices used to describe the slagging propensity: capture efficiency and energy based growth rate (GRE) [5]. Capture efficiency is the ratio of the mass of particles deposited to the mass of the flyash particles flowing across the projected area of the probe during a test period. GRE is calculated as the mass of a deposit divided by the product of the flow heating value and the mass of the coal burned in the test [5]. As an example, the base to acid ratio correlates well with GRE for coal with low slagging tendencies, but should not be applied to subbituminous coal with a high CaO content. Likewise, other indices are limited to the coals from which they have been derived.

For the ash fusion temperature, ash fusibility is characterized by visually observing a small cone (pyramid) of ash in an oven where the temperature is increased under reducing atmosphere. There are four characteristic temperatures that are determined in the experiment. The Initial Deformation Temperature (IDT) is the temperature at which the specimen apex starts to round (deform). After the IDT, the Softening Temperature (ST) takes precedence and is the temperature at which the height of the specimen is equal to its width. After the ST, comes the Hemispherical Temperature (HT), which is the temperature at which the height becomes equal to half of the width. Lastly, the Fluid Temperature (FT) is the temperature at which the fused mass spreads out in a nearly flat layer with a maximum height of 1.5 mm [6, 7]. Although the ash fusion temperature AFT is one of the most common parameter used by furnace and boiler operators to predict the melting behavior of coal, it falls short as a predictive tool due to poor repeatability and reproducibility. Apart from the AFT, the temperature of critical viscosity, T_{CV} , is used in the characterization of the sticking probability of particles. T_{CV} is the temperature at which the viscosity changes from that of a Newtonian fluid to that of a Bingham Plastic. Above the T_{CV} , the viscosity is independent of the shear rate. However, determining the relationship between T_{CV} and the ash composition has been more complex than predicting the fluidity of the slag due to crystal formation [7]. To determine the sticking propensity of a particle, T_{CV} has been used in viscosity models to determine the critical viscosity.

In terms of viscosity, silicate melts can be described as a polymer network composed of SiO_4^{4-} anions which can accommodate different cations. These cations fall into three categories depending on their interaction within the network [8]:

Glass formers	$\text{Si}^{4+}, \text{Ti}^{4+}, \text{P}^{5+}$	Form basic anionic polymer units
Modifiers	$\text{Ca}^{2+}, \text{Mg}^{2+}, \text{Fe}^{2+}, \text{K}^+, \text{Na}^+$	Disrupt the polymer chains by bonding with oxygen and effectively terminating chains
Amphoterics	$\text{Al}^{3+}, \text{Fe}^{3+}, \text{B}^{3+}$	Act either as a glass former or modifier

Modifier ions disrupt the glass structure and thus tend to lower the viscosity of the slag. Amphoteric ions can act as glass formers when they combine with modifier ions, which balance their charge, thus forming stable metal oxygen anion groups that can fit into the silicate network. However, if insufficient number of modifier ions disrupts the glass structure, it tends to lower the viscosity.

One of the most common viscosity models used has been the Urbain model. This model relates the viscosity of the Weymann relation, where a statistical vacancy distribution and a probability function for the jump from one vacancy site is described as

$$\eta = ATe^{(1000B/T)}. \quad (1.1)$$

Here A and B are two empirical constants with units in Poise/K and K, respectively. Urbain had linked the parameters A and B through Equation 1.2

$$\ln A = 0.2693B + 11.6725, \quad (1.2)$$

where the parameter B is a function of the silica mole fraction, N, and the quantity β , which is in turn a function of the mole fractions of CaO and Al_2O_3 ,

$$\beta = \frac{\text{CaO}}{\text{CaO} + \text{Al}_2\text{O}_3} \text{ and } N = \text{SiO}_2, \quad (1.3)$$

$$B = B_0 + B_1N + B_2N^2 + B_3N^3. \quad (1.4)$$

Here

$$B_0 = 13.8 + 39.9355\beta - 44.049\beta^2, \quad (1.5)$$

$$B_1 = 30.481 - 117.1505\beta + 129.9978\beta^2, \quad (1.6)$$

$$B_2 = -40.9429 + 234.0486\beta - 300.04\beta^2, \quad (1.7)$$

$$B_3 = 60.7619 - 1531.9276\beta - 211.1616\beta^2. \quad (1.8)$$

Kalmanovitch modified the Urbain model with a modification of β and Equation 1.9 in order to expand the Urbain model to accommodate magnesium, potassium, and titanium], as:

$$\ln A = 0.2812B + 11.8279, \quad (1.9)$$

$$\beta = \frac{CaO+MgO+Na_2O+K_2O+FeO+TiO_2}{Al_2O_3+CaO+MgO+Na_2O+K_2O+FeO+TiO_2}. \quad (1.10)$$

The Browning model calculates the viscosity through the temperature shift, which is set to an initial value of zero:

$$\log\left(\frac{\eta}{T-T_S}\right) = \frac{14788}{T-T_S} - 10.931. \quad (1.11)$$

The temperature shift is related to the molar ratio A. The expression for the molar ratio A discerns the network formers in the numerator from the modifiers in the denominator

$$T_S = 306.63 \ln(A) - 574.31, \quad (1.12)$$

$$A = \frac{3.19Si^{4+}+0.855Al^{3+}+1.6K^+}{0.93Ca^{2+}+1.50Fe^{n+}+1.21Mg^{2+}+0.69Na^++1.35Mn^{n+}+1.47Ti^{4+}+1.91S^{2-}}, \quad (1.13)$$

where each quantity is based on each mole fraction:

$$Si^{4+} + Al^{3+} + Ca^{2+} + Fe^{n+} + Mg^{2+} + Na^+ + K^+ + Mn^{n+} + Ti^{4+} + S^{2-} = 1. \quad (1.14)$$

While the Browning model is inclusive of the role of network formers versus modifiers, the Senior model uses the ratio of non-bridging oxygen to tetrahedral oxygens:

$$NBO/T = \frac{CaO+MgO+FeO+Na_2O+K_2O-Al_2O_3-FeO_3}{\frac{SiO_2+TiO_2}{2}+Al_2O_3+Fe_2O_3}. \quad (1.15)$$

The viscosity has the same dependence on temperature as suggested by the Urbain and the modified Urbain model. However, the parameter A is calculated in terms of NBO/T while the parameter B is calculated in terms of coefficients determined through a multiple regression analysis. Moreover, the parameters A and B are divided into two sets of equations for high temperatures and low temperatures. For high temperatures, parameter A is described by the following:

$$A_H = -2.81629 - 0.46341B - 0.35342 NBO/T. \quad (1.16)$$

For low temperatures at various NBO/T ratios, parameter A becomes the following:

$$A_L = -0.982 - 0.902473B \quad \text{for } \text{NBO}/T \geq 1.3, \quad (1.17)$$

$$A_L = 2.478718 - 0.902473B - 2.662091 \text{NBO}/T \quad \text{for } 0.2 \leq \text{NBO}/T < 1.3, \quad (1.18)$$

$$A_L = 9.223 - 0.902473B \cdot \text{NBO}/T \quad \text{for } 0.0 \leq \text{NBO}/T < 0.2, \quad (1.19)$$

$$A_L = 9.223 - 0.902473B \quad \text{for } \text{NBO}/T < 0.0. \quad (1.20)$$

Parameter B is determined from a set of coefficients, the silica molar fraction N ($N = \text{SiO}_2$), and the quantity β :

$$B = b_0 + b_1\beta + b_2\beta^2 + b_3N + b_4N\beta + b_5N\beta^2 + b_6N^2 + b_7N^2\beta + b_8N^2\beta^2 + b_9N^3 + b_{10}N^3\beta + b_{11}N^3\beta^2, \quad (1.21)$$

$$\text{where } \beta = \frac{\text{CaO}}{\text{CaO} + \text{Al}_2\text{O}_3}.$$

The following table lists the coefficients to determine parameter B for low and high temperatures:

Table 1-1: Coefficients for the high temperature and low temperature range of the Senior model

Coefficient	High Temperature (K)	Low Temperature (K)
b_0	-224.98	-7563.46
b_1	636.67	24431.69
b_2	-418.70	-17685.4
b_3	823.89	32644.26
b_4	-2398.32	-103681.0
b_5	1650.56	74541.33
b_6	-957.94	-46484.8
b_7	3366.61	146008.4
b_8	-2551.71	-104306.0
b_9	387.32	21904.63
b_{10}	-1722.24	-68194.8
b_{11}	1432.08	48429.31

Of the various viscosity models, the BCURA S^2 for British Coal Ash Slags makes use of the silica ratio S :

$$S = \frac{100 \times SiO_2}{SiO_2 +_{equiv} Fe_2O_3 + CaO + MgO}, \quad (1.22)$$

$$SiO_2 + Al_2O_3 +_{equiv} Fe_2O_3 + CaO + MgO = 100, \quad (1.23)$$

$$_{equiv} Fe_2O_3 = Fe_2O_3 + 1.11FeO + 1.43Fe. \quad (1.24)$$

The viscosity is determined by Equation 1.25:

$$\log \eta = 4.468 \left(\frac{S}{100} \right)^2 + 1.265 \left(\frac{10^4}{T} \right) - 7.44. \quad (1.25)$$

Each of the viscosity models has its limitations. For instance, in the modified Urbain model, the prediction of the coal slag viscosity was poor for slags outside of the SiO_2 - Al_2O_3 - CaO - MgO phase system. Meanwhile, the BCURA S^2 model had a tendency to under predict viscosities greater than 100 Pa·s. In fact, this model's accuracy hinged on slags having the silica and iron oxide content less than 55% and 5%, respectively [9]. On the other hand, the Senior model was limited to viscosities in the range of 10^4 - 10^9 Pa·s.

Although the limitations of viscosity models has been thoroughly investigated, the grinding conditions and the composition of the bulk coal governs the initial particle size distribution. Being that the grinding mills govern the particle size distribution, any wear of abrasion of mills from grinding can skew the particle size distribution [10]. Minerals such as quartz and pyrite in the form of excluded minerals have been identified as mineral components responsible for wear and abrasion due to their hardness to steel[10]. However, the same minerals responsible for the reduction of the ball mill performance overtime are the simultaneous occurrence of mineral transformation and particle deposition. Therefore, the inorganic and organic composition can be can be tied to the physics of such behavior through the physical and adhesive properties of char particles. However, the applicability of particle wall impact models are limited to a specific range of deformation whereas this range of deformation is dependent upon those physical properties for which adhesion (or rebound) is most sensitive. The conditional use of these models necessitate the need to garner literature on previous work in characterizing the structure of coal as well as its adhesive properties. This information has non

only been instrument in identifying the range of deformation, but in collecting key information of how viscosity models fall short. With the reduction of ash as a key objective, a more suitable alternative to viscosity models could be used to find the optimal operating conditions of the grinding circuit to coordinate with conditions of the gasifier. Therefore, the next section not only provides a brief overview of how ball milling conditions relates to the PSD, but how a partition function has served as a powerful tool in the improvement of sulfur capture performance. Although the algorithm and end objective of this work differs from the work on sulfur capture performance cited in this work, the concept behind a partitioning tool for optimization is the same.

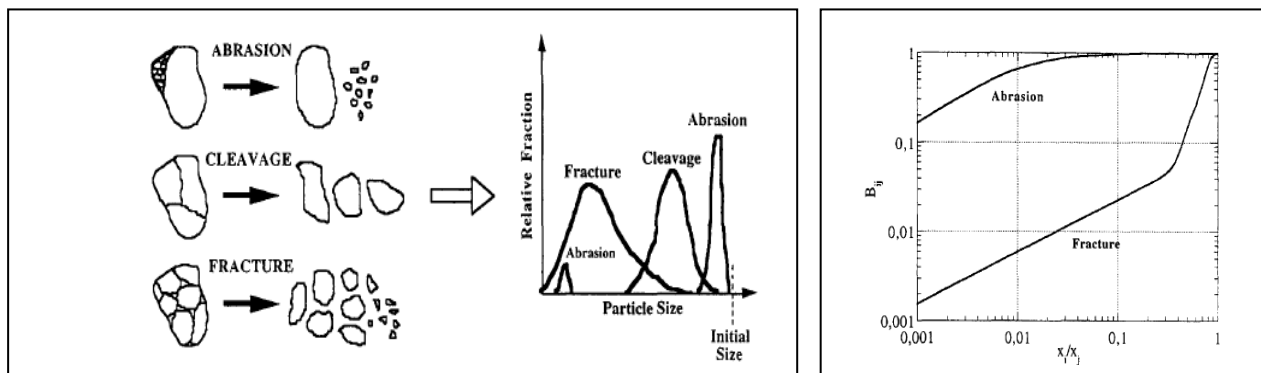
CHAPTER 2 BACKGROUND

2.1 Population Models

2.1.1 Grinding

The fragmentation mechanism involved in the rod milling process includes abrasion, cleavage, and fracture. Abrasion results from the application of local, low-intensity surface stresses, while fracture results from a rapid application of intense stresses that leads to fragments. On the other hand, cleavage is the slow application of relatively intense stresses.

Figure 2-1a-b: Particle size distribution due to abrasion, cleavage, and fracture [11]



It has been demonstrated that large balls promote impact breakage (fracture), while small balls promote breakage by abrasion through ball milling [12]. The population balance model is based on the breakage distribution function which takes into consideration both fragmentation and cleavage. In the population balance, the size reduction consists of two basic components: the fracture *event* (represented by the breakage distribution function) and the fracture *process* (represented by the rate or selection function). The breakage distribution function can be defined as the average size distribution resulting from the fracture of a single particle.

Figure 2-2: Breakage distribution as a function of shatter and cleavage [12]

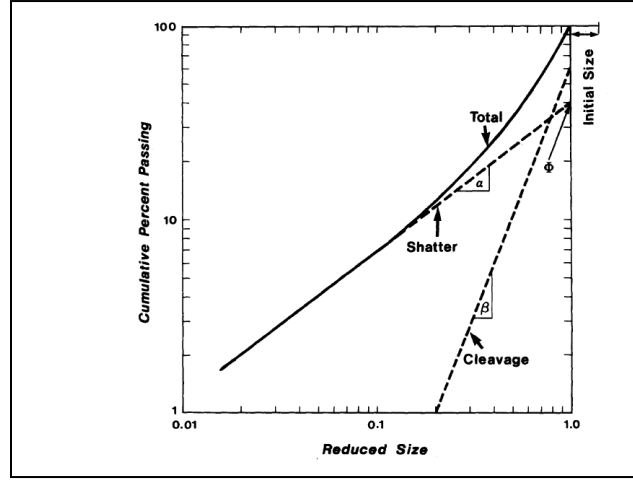


Figure 2-2 shows the particle size distribution (PSD) as a result of the breakage distribution function. In this figure, ϕ is the intercept on the right hand ordinate of the plot, α and β are the slopes of the lower and the higher section of the cumulative distribution respectively, d_i is the particle size, and d_1 is the initial particle size. For the particle size range below the maximum size, the relationship between the specific rate of breakage and the particle size is the selection function

$$-S_j = A \left(\frac{x_j}{x_0} \right)^\alpha, \quad (2.1)$$

where A is a parameter that depends on mill specifications, α is a characteristic parameter that changes according to the material, x_j is the particle top size interval j , and x_0 is the standard particle size [13]. In a batch grinding process, the mass balance for the size interval, i , is due to the disappearance of the material by breakage into smaller size and the appearance of material by breakage from the larger sizes

$$\frac{dw_i(t)}{dt} = -S_i W_i(t) + \sum_{j=1}^{i-1} B_{ij} S_j w_j(t), \quad n \geq i \geq j \geq 1, \quad (2.2)$$

where $w_i(t)$ is the mass of material in size interval i . B_{ij} is the breakage distribution in which the breakage of material occurs from x_j into x_i . Equation 2.2 can be solved using the Reid solution to obtain the product size distribution as a function of the grinding time:

$$w_i(t) = \sum_{j=1}^i a_{ij} e^{-S_j t} . \quad (2.3)$$

For the ball mill, the empirical model used is

$$S_i = a_i x_i^\alpha \frac{1}{1 + \left(\frac{x_i}{\mu}\right)^\Lambda} . \quad (2.4)$$

Here x_i is the upper size of the particle size interval i under consideration, α_i and μ are parameters that are mainly a function of the mill conditions, and α and Λ are parameters that are a function of the material. The ball size affects the magnitude of the parameters α_i and μ through the Equations 2.5a-c:

$$\alpha = \bar{\alpha} / d^\varepsilon, \quad (2.5a)$$

$$\mu = \bar{\mu} \cdot d^\eta, \quad (2.5b)$$

$$x_m = \mu \left(\frac{\alpha}{\Lambda - \alpha} \right)^{1/\Lambda}. \quad (2.5c)$$

2.1.2 Particle Size Distribution

The variation in the ash content across the coal particles can be described by the specific gravity distribution. Development of an ash content distribution is used to account for non-uniformity in its distribution. The attrition behavior is expected to vary with ash content, which is a function of the particle specific gravity [14]. The amount of ash will influence the probability of a particle to fragment. A particle with lower ash content will lose a majority of its mass through combustion. As the combustible mass of a particle is lost through the reaction, the remaining mass is weakened enough such that the particle can fragment, a condition known as percolation.

2.1.3 Circulating Fluidized Bed Sulfur Capture

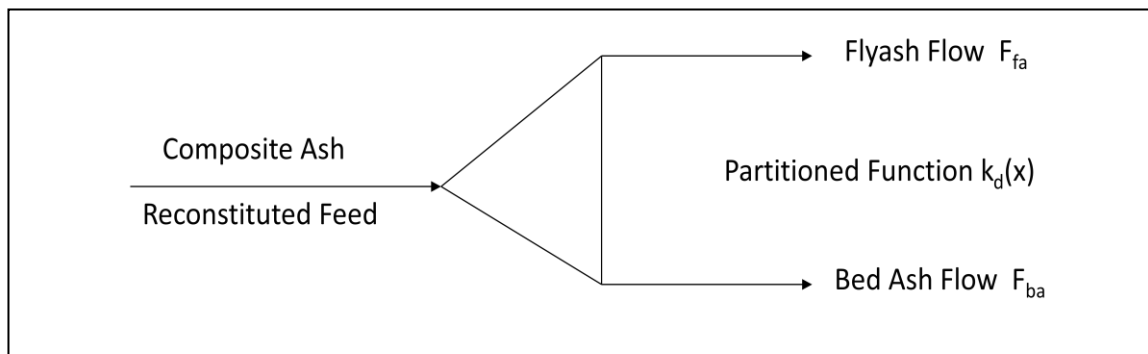
The population model has been utilized in predicting the sorbent performance in a CFB boiler. For the power plants equipped with such boilers, calcium based sorbents (limestones or dolostones) would be commonly added for emissions control. In terms of the applicability in predicting the sorbent performance, there are a wide variety of sorbent properties that may

influence sulfur capture performance [15]. Among them, the grain size is a characteristic of limestone that is described by a petrographic analysis [15] :

1. Sorbents classified as micrites have a grain size of $4\ \mu\text{m}$
2. Sorbents that are sparry have a grain size in the range of $30\ \mu\text{m}$

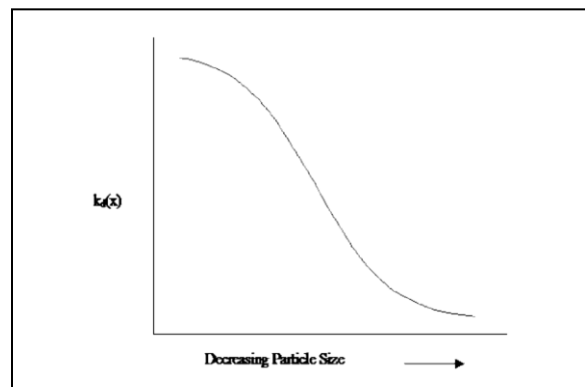
Given the variation of the sorbent grain size and the partition of ash into bottom ash and flyash, there is a need to partition the sorbent. The goal of the population model is to develop the fuel attrition indices that can assist in predicting bottom ash flow rates from a CFB boiler through a partition function, $k_d(x)$. This partition function is defined as the fractional yield to the bottom ash stream of interval x .

Figure 2-3: Size classification of particles to the bottom ash and Flyash streams [16]



The relationship between the reconstituted feed stream, or composite ash flow, and the bottom ash flow can be represented by the following function [17],

Figure 2-4: Partition curve for a particle size distribution [16]



$$F_{ba} = \sum_{x=1}^{nx} k_d(x) M_{ca,x} F_{ca}. \quad (2.6)$$

Here M_{ca} is the mass fraction in the reconstituted composite ash flow, and F_{ca} is the relationship among the bottom ash, flyash, and composite ash flow, and is defined as [17]

$$F_{ba} + F_{fa} = F_{ca}. \quad (2.7)$$

With regards to the partitioning of composite ash as a result of the chemical and physical processes that occur through the circulating fluidized bed boiler, particle attrition directly impacts the particle size distribution of the composite ash stream. The attrition behavior is described by means of a system attrition coefficient, which denotes the cumulative particle shrinkage over the total residence time of a particle class in the system:

$$K_{i,a} - 1 = \left(\frac{M_{i,ba}}{M_{i,k_d}} \right). \quad (2.8)$$

2.2 Mineral Transformation and Mechanisms for Conversion

Although CFD models based on bulk coal it is the PSD influences the carbon conversion and the hydrodynamic behavior of the particles within the gasifier. However, the coal conversion processes not only alter the PSD, but can also influence the time-temperature profile. Particle size altering mechanisms include swelling, shrinkage, and fragmentation (not included in the CFD model). Upon entering the gasifier, the coal particles (and included minerals) go through the process of heating, moisture release, pyrolysis, and char gasification. Although heating and moisture vaporization occur simultaneously in entrained flow gasification, in the Fluent simulation, the heating of the coal particles occurs until the vaporization temperature is reached [18]. Upon reaching a certain temperature in accordance with the CFD model, moisture is released prior to pyrolysis. Three chemical reactions are assumed to occur simultaneously within a coal particle undergoing pyrolysis [18]. These reactions are devolatilization, cracking, and mineral transformation [19]. The products of pyrolysis are categorized as char, tar, and gas. Char is the material that remains in the form of solids, while tar is the distillable liquid that has a molecular weight larger than C_6 [19]. Meanwhile, swelling behavior occurs during pyrolysis and is characterized by an increase in the size as well as the porosity of the char particle. The concept of volatile matter transport via gas bubbles is used as a mechanism to model the secondary

reactions during the pyrolysis of coal, and therefore, swelling [20]. The physics of the multi-bubble mechanism can be summarized as follows:

- 1) Volatile matter is carried by the bubbles.
- 2) Volatile matter is released through bubble movements rather than by a direct diffusion to the surface of the particles.
- 3) Particle swelling is caused by the growth of bubbles due to the generation of volatile matter.
- 4) Rupture of the bubbles at the surface of the particles is then determined by a force balance for which the viscous force is a major component [20].

Although the bubbles are deemed as the mode of transport, the change in the internal structure of a char during pyrolysis determines the mass transport of the volatile matter.

After pyrolysis, char gasification ensues where the heterogeneous char-gas reactions occur in the forms of volumetric and surface reactions [19]. In the volumetric reaction mode that takes place when particle temperature and kinetic rates are low, the gas can diffuse into the entire volume of the particles through the pores on the inside. In the surface reaction mode that takes place when the particle temperature and kinetic rates are high, the reacting gas does not penetrate into the inner part of the particle since the reactants are consumed at its external surface [19]. Based on these two reaction modes, there are three regimes that arise due to the interaction between the species mass transport and reaction kinetics: kinetically controlled (regime I), combined diffusion-kinetically controlled (regime II), and diffusion controlled (regime III) [21]. Shrinkage occurs when the char particle decreases in density. The cause of shrinking in the diffusion phase of char gasification is due to the breakage of joints within the structural network. However, shrinkage has also been observed in the kinetic regime for carbon conversion. Such shrinkage has been linked to the restructuring of joints within the structural network of the organic matter [22]. Fragmentation can also occur within the carbonaceous structure of the char particle to influence the resulting size fractions of the char particles that form from the parent particle. Fragments can be formed by three mechanisms: breakage of particles due to the internal force, high internal pressure during devolatilization, and the attrition and percolation of particles, wherein the latter arises due to the loss of connectivity among the phases within the particle. Percolation is considered to be the primary mode of fragmentation, both during the diffusion

phase of char gasification [23] as well as within the carbon matrix of the char particle containing the included minerals. The loss of the connection within the joints between the carbonaceous structure of char reduces the thermal resistance of the char particle, which in turn makes the particle susceptible to fragmentation due to the temperature gradient between the char particle and the gaseous medium.

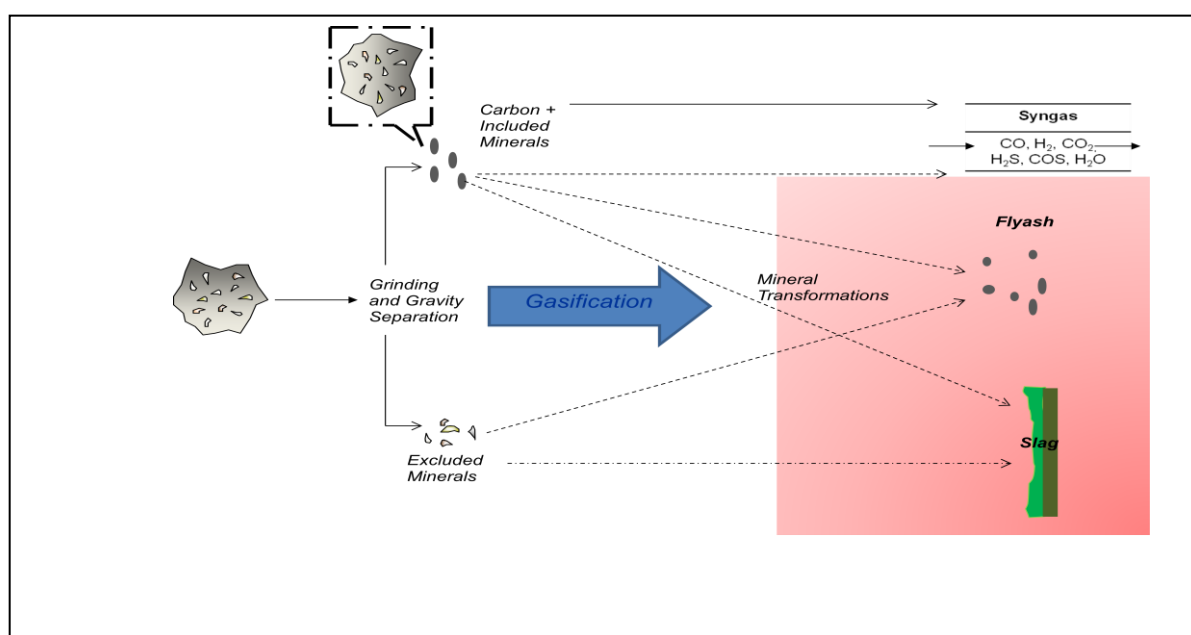
For excluded minerals, fragmentation due to an internal force is the predominant behavior that adjusts the original size fraction of the particle [24]. Fragmentation occurs commonly when pyrite is present in the excluded form; however, it depends on the structure geometry and threshold porosity. The fragmentation due to the internal force is thought to occur during the kinetic regime of char gasification. During this mode of fragmentation, the internal temperature gradient generated during heating causes thermal stresses within the char. These stresses can ultimately lead to the mechanical failure of the coal particle when the tensile stresses within the particle exceeds the tensile failure while the stresses on the outer region are compressive [25]. Dacombe et al. showed that a number of particles due to fragmentation increased exponentially as a function of both the particle size and the mechanical strength for bituminous coals [26]. However, Baxter found that the extent of fragmentation is strongly dependent on the size and the coal rank [26]. For instance, the bituminous coal fragments more than the lignite coal [23]. The time-temperature profile of the char particle is determined by the local gas phase conditions that the particle experiences, and is governed by the equations of particle motion and enthalpy, which are related to both the convective and radiative heat transfer, in addition to devolatilization and heterogeneous reactions. The size, temperature, velocity, and composition of the particle determines its fate and the resulting trajectory after striking the gasifier wall. These properties can be obtained from a CFD simulation.

2.3 Modes of Particle Deposition

The mode of transport of a particle to the gasifier wall will depend on the particle size and composition that results from mineral transformation and mechanisms for conversion in addition to initial properties of the PSD. The modes of deposition include condensation, heterogeneous reactions, thermophoresis, and inertial impact. Condensation and heterogeneous reactions are likely to be the transport mechanism of salt or organic bound cations of low rank coal. However, the two most common modes of transport of a particle to a gasifier wall are

thermophoresis and inertial impact. Thermophoresis occurs when there is particle transport due to the temperature gradient resulting from the exposure of cool surfaces to high temperature [27]. It has been reported to influence particles less than 10 μm , but has been most significant for particles in the size range of 0.2 - 5.0 μm [27]. Inertial impact is the result of the drag and the gravitational forces acting on a particle that are likely to occur for larger sized particles and is the focus of this work. The following schematic shows the mechanism of ash formation and deposition.

Figure 2-5: Partitioning of coal particles into syngas, flyash, and slag

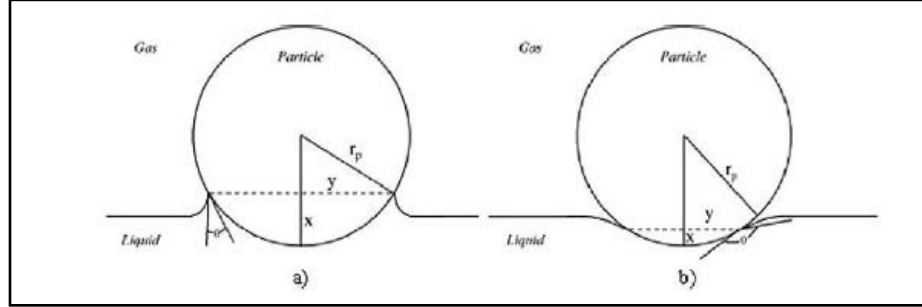


2.4 Characterizing the Adhesive Properties of Ash Particles through the Interfacial

2.4 Surface Tension

The adhesive properties of a particle and liquid droplets have been described through the interfacial surface tension, which is described through the Young's equation where it is expressed as a product of the surface tension of the liquid vapor interface and the contact angle between a solid and a liquid interface. The following diagram shows the contact angle between a solid particle and a liquid interface.

Figure 2-6: Schematic of contact angle and interfacial surface tension between solid particle and liquid [28]



$$\sigma_{sv} - \sigma_{sl} = \sigma_{lv} \cos \theta. \quad (2.9)$$

Here σ is the surface tension and the subscripts sv, sl, and lv represent the solid vapor interface, solid liquid interface, and liquid vapor interface, respectively. When the contact angle is below 90° , the particle is considered to undergo wetting, while at contact angles above 90° , the particle is considered to be non-wetting. Because surface tension is the work per unit area required to produce a new surface, it can be expressed in terms of Gibbs free energy (ΔG) per unit area as

$$\delta W' = -\sigma dA, \quad (2.10)$$

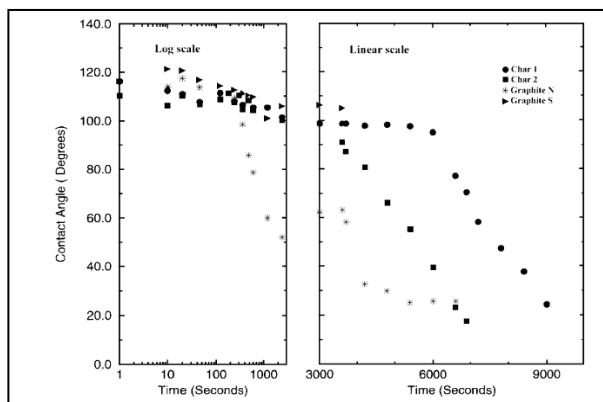
$$dG = \sigma dA, \quad (2.11)$$

$$\sigma = \left(\frac{\partial G}{\partial A} \right)_{T,P}. \quad (2.12)$$

Therefore, spontaneously occurring processes are characterized by negative values of the change in ΔG . Surfaces that initially possess higher ΔG have the most to gain in terms of decreasing ΔG of their surface by adsorption. With regard to carbon, slags have been reported to demonstrate non-wetting behavior of graphite and other carbon forms [29, 30]. It is only through the reduction reactions that contribute to the mass transfer across the interface that the contact angle is reduced [31]. Through this process, ΔG acts as the driving force for wetting. Wetting at the slag and carbon (or char) interface is due to the reduction of silica and formation of SiC [32, 33]. For slags rich in iron oxide, the deposition of reduced iron at the interface restricts further reduction of silica. However, if no reaction or transport phenomenon occurs, then the balance of

the interfacial energies through the Young's equation governs the wettability. Figure 2-7 shows the measurements of the change in contact angle versus time for char and graphite particles.

Figure 2-7: Plot of contact angle versus time between select carbon containing particles with set slag composition [31]



Based on this change of contact angle versus time, the time scale for the reduction reactions involving FeO and SiO_2 are orders of magnitude larger than the time scales of particles impacting the refractory within the gasifier. Therefore, the contact angle of the char particles impacting the wall is governed by the Young's equation. Although not used in conventional “viscosity” models, the role of surface tension has been used to characterize the process of sintering.

2.5 The Role of Sintering in Ash Adhesion

Although sintering has been associated with agglomeration in fluidized bed, the mechanism has been used to describe deposit growth. According to Hupa, there are three descriptions regarding sintering [34]:

1. Solid-state sintering is where the mass transfer can take place by means of surface diffusion, lattice diffusion, boundary diffusion, or by the interactions between the solid material and the surrounding gas, such as sublimation and recondensation.

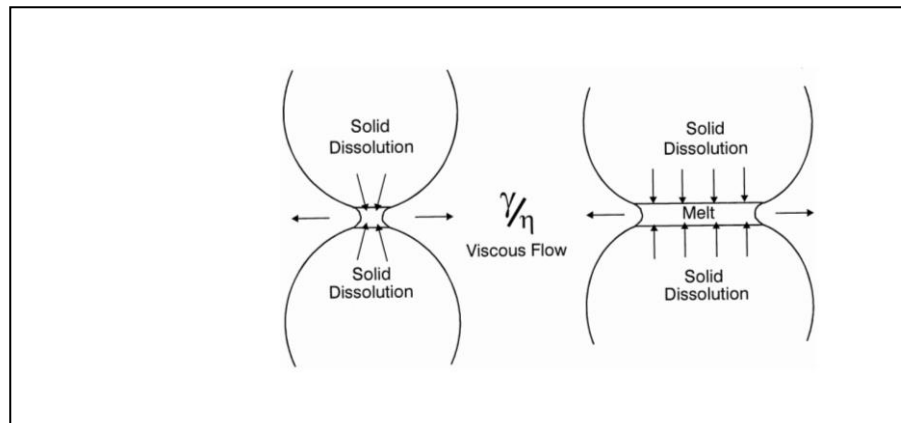
2. Sintering by viscous flow (vitrification) is where sintering is due to the flow of a viscous, non-crystalline material. This type of sintering occurs in silicate systems.
3. Sintering in the presence of a liquid phase is where the solid phase shows a degree of solubility in the liquid at the sintering temperature.

The earliest models describing sintering were developed by Frenkel [35], who assumed that the mass transfer takes place under the influence of a surface tension gradient. The driving force responsible for this mass flux is due to the capillary forces resulting from the surface tension of the melt. Mineral transport also occurs through the liquid phase in inertially impacted coal ash particles as a result of the capillary forces that are governed by the surface tension of the liquid and the simultaneous action of the grain boundary tensions [35]. Factors such as ash particle shape, PSD, furnace temperature, and atmosphere can influence the course of the sintering process. Frenkel's equation is represented as

$$x^2 = \frac{3r\sigma t}{2\eta} . \quad (2.13)$$

The sintering model by Frenkel indicates that the formation of particle-to-particle bonding should lead to an increased density of the sintered ash samples [36].

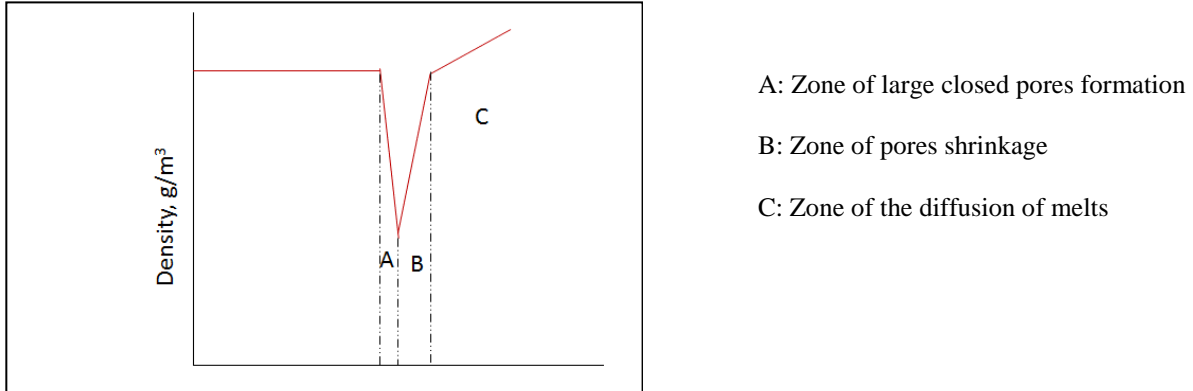
Figure 2-8: Schematic illustration of liquid phase transport in a silicate system [37]



The increase in the density can be explained by densification, which is a pore-filling process characterized by liquid phase flow and pore shrinkage. The three steps in the sintering of pulverized coal ashes undergoing densification are [38]:

1. Formation of closed pores at temperatures below the minimum density
2. Shrinkage of pores at temperatures above the minimum density
3. Diffusion and/or reactive diffusion of melts.

Figure 2-9: Zone of close pores formation, pore shrinkage, and diffusion of melts



This viscous sintering of coal ashes containing large closed pores that proceed at temperatures above the minimum density may arise from inward-acting stresses caused by the surface and grain-boundary tensions. Nowak et al. assumed that the compressive stress of spherical pores with radius r (cm) are given by the equation [38]

$$S_C = \frac{-2\sigma}{r}. \quad (2.14)$$

By treating the deposited material as a viscoelastic solid, the densification strain is related to the pore shrinkage rate, $\dot{\epsilon}$, by

$$\dot{\epsilon} = \dot{\epsilon}_f + S_C(1 - 2\nu)/3\eta, \quad (2.15)$$

$$\dot{\epsilon} = \dot{\epsilon}_f - \frac{2}{3}(\sigma/\eta)(1 - 2\nu)/3r. \quad (2.16)$$

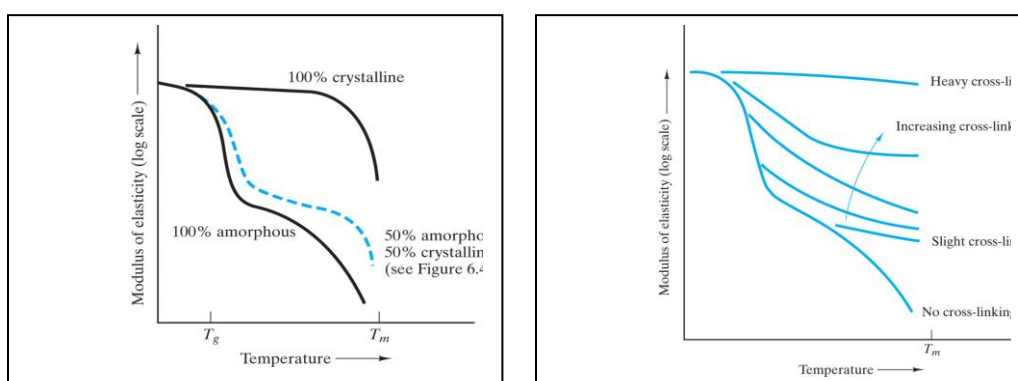
Here $\dot{\epsilon}_f$ is the thermal strain rate, ν is the poisson ratio, and η is the viscosity. Therefore, there is a direct correlation between the compressive strength and the ratio of the surface tension to the viscosity. The compressive strength of sintered coal ashes depends on temperature, time, and the surrounding atmosphere [38]. This mechanical strength can be affected by the severity and distribution of cracks and microcracks, pores, and flaws when the ash particles are below the

critical viscosity temperature [35]. However, when the particle is above the critical viscosity temperature, then the mechanical properties resemble the properties of a Newtonian liquid. In the elastic-plastic model with adhesion, the temperature dependence of the deposition rates is primarily through the effects of temperature on the yield stress and the surface energy. However, the presence of char has been reported to increase the sintering temperature [39]. Moreover, char can also serve as a non-melting component and prevent the deposits from undergoing any sintering.

2.6 Contribution of Molecular Structure to Particle Stiffness

Although adhesive properties are of interest, cohesive properties have given way to Hertzian forces to counteract adhesion. Therefore, the structural properties of coals must be revisited. Coals are described as macromolecular structures that consist of hydroaromatic units connected by crosslinks such as methylene, oxygen, and sulfur. Such crosslinking through poor alignment produces extensive porosity in coal. Because coals consist of crosslinked macromolecules, they are not soluble and will swell upon contact with a solvent having comparable solubility. Because coals deform with a viscosity approaching that of Bakelite when subjected to stress, they are considered to be viscoelastic [40].

Figure 2-10a-b: Plot showing the modulus of elasticity and degree of crosslinking versus temperature [41]



In the context of the modulus of elasticity, there is a direct correlation between the degree of crosslinking and the particle stiffness. The glass transition temperature (T_g) indicates the

transition of a particle from a rigid (or crystalline) state to a more elastic state whereas the melting temperature indicates the transition from a Bingham fluid to a more Newtonian liquid. Although the inorganic and organic portions of coal differ in molecular structure, both the constituents can be characterized in terms of the crosslinking density as a function of temperature.

2.6.1 Crosslinking Density Pertaining to Organic Polymers and Coal Matrix

Because the degree of solubility is related to crosslinking, the former has been related to cohesive energy through the solubility parameter, as shown in Equation 2.17:

$$\text{Solubility parameter } \delta = \left(\frac{E_{coh}}{V} \right)^{1/2} \left(\frac{J^{1/2}}{cm^{3/2}} \right). \quad (2.17)$$

Since polymers cannot be evaporated, indirect methods have been used to determine the cohesive energy:

$$E_{coh} = \Delta U_{vap} = H_{vap} - P\Delta V = \Delta H_{vap} - RT. \quad (2.18)$$

Because the solubility parameter is an additive function, the contribution of the dispersion forces (E_d), polar forces (E_p), and hydrogen bonding (E_h) to the cohesive energy (E_{coh}) can be determined based on the contributions of each of these parameters to the solubility parameter, δ as

$$E_{coh} = E_d + E_p + E_h, \quad (2.19)$$

$$\delta^2 = \delta_d^2 + \delta_p^2 + \delta_h^2. \quad (2.20)$$

The following table shows the contributions due to E_d , E_p , and E_h :

Table 2-1: Contributions of molecular structural groups to the cohesive energy of a particle

Structural Group	$E_d \text{ J}^{1/2} \text{ cm}^{3/2} \text{ mol}$	E_p	E_h
$-\text{CH}_3$	420	0	0
$-\text{CH}_2-$ 	280	0	0
$\text{CH}-$	140	0	0
$-\text{C}-$ 	0	0	0
$=\text{CH}_2$	400	0	0
$=\text{CH}_2$	200	0	0
$=\text{C} \begin{array}{l} \diagup \\ \diagdown \end{array}$	70	0	0
$-\text{OH}$	210	500	200

For a complex macromolecular system such as the coal matrix, it has been assumed that similar contribution increments as those for liquids and amorphous polymers could be used [40]. However, the solubility of coal (up to 90% carbon) ceases due to crosslinking. Therefore, the aromaticity of coal needs to be determined.

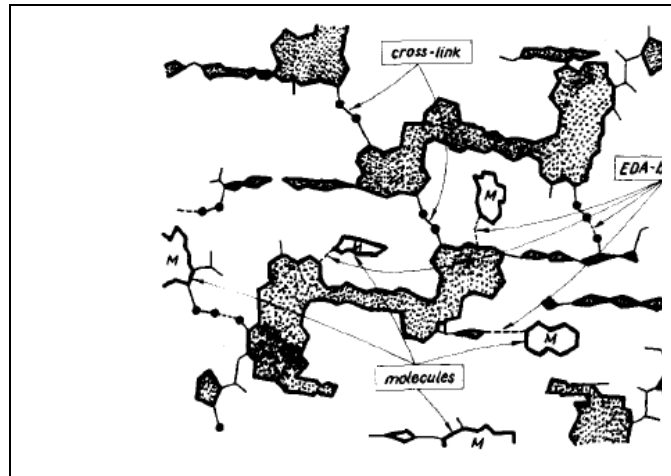
Table 2-2: Variation in coal rank with coal solubility

Coal Rank	Estimated Aromaticity	Calculated Solubility δ for Coal
75.5	0.70	27.5
81.5	0.80	25.0
85.0	0.83	23.9
87.0	0.84	23.2
89.0	0.85	22.1

Due to the influence of aromaticity, coal has been characterized using the elasticity theory. According to this theory (as it relates to the structure of coal),

1. The first order structure is an arrangement of vibrated material bodies connected by “springs” (chemical bonds). In coal, a matrix of aromatic cluster (averaged by “spring” bonds) is connected via aliphatic and carbonyl side attachments to other aromatic clusters. Moreover, hydrogen bonds and other secondary forces provide additional crosslinking.
2. The second order structure is considered to be the mean molecular weight of a macromolecular aromatic structural unit fragment between two adjacent crosslinking bonds or entanglements.

Figure 2-11: Macromolecular and molecular model of low rank bituminous coal [42]



Due to the variation of the coal rank and aromaticity on the solubility parameter of coal, the crosslinking density (Φ) is determined based on the ratio of the density to the molecular weight of the polymer chain section

$$\Phi = \rho / M_C ,$$

where ρ is the density and M_C is the molecular weight of the chain. (2.21)

The relation between the Young's modulus of elasticity, E_0 , and the crosslinking density, Φ , of coal can be represented by:

$$E_0 = 3\Phi RT. \quad (2.22)$$

2.6.2 Crosslinking Density Pertaining to the Structure of Glass Oxides [43]

According to Ray et al [41], unlike polymers, where carbon dominates the bonding structure, glass oxides comprise an assembly of oxygen atoms bonded through covalent bonds. As a result, glass oxides melt without decomposition through bond switching transfer that occurs at high temperature. As previously stated, crosslinking in organic polymers refers to the fraction of monomer units that are crosslinked. However, crosslinking in glass oxides exists through charge carrying oxygen atoms, oxygens linked to only one network, and hydroxyl groups. In other words, it is combination of ionic charges and weak hydroxyl groups that contributes to the crosslinking density, unlike the aliphatic bridges in the coal carbon matrix. Oxygen atoms that are not bridging or bonded to other atoms contribute to the packing density, which in turn depends on the coordination number and the cation size. Because the coordination number for cations increase with an increase in the ionic radius, entities with a larger radius can form more links with other atoms, and hence the reduction on the packing density due to a lower density of oxygen atoms is counteracted. However, the segmental forces are strong for smaller cations and thus increase the oxygen density [41]. Therefore, both the packing density and the crosslinking density in glass oxides have a combined influence on the resulting Young modulus of elasticity.

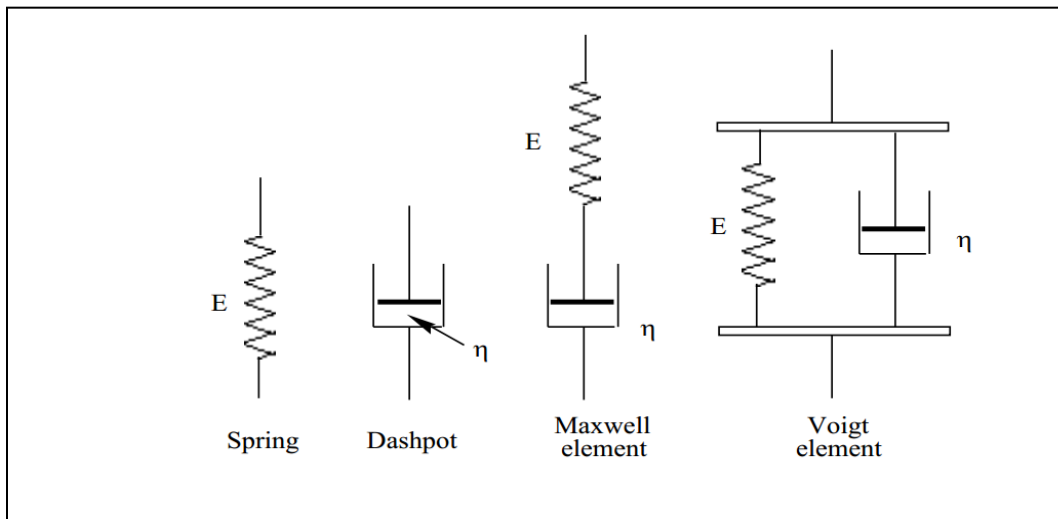
The amount of energy lost due to dissipation upon impact is considered to be hysteresis, wherein a portion of the input is unrecoverable due to its degradation to heat. Energy input into an isothermal sample would be in the form of work [44]: $w = \int \sigma d\epsilon$, where σ is the stress applied in (N/m²) and ϵ is the strain resulting from that stress in (m/m).

In cases of viscoelastic behavior, the elastically stored energy is recoverable whereas the viscously dissipated energy is not. Therefore, the unrecoverable portion of the energy in coal is a reflection of significant frictional resistance to network chain motions in response to the applied stress [44]. Moreover, the T_{CV} of ash (1300-1500K) is twice as high as measured T_g values for the overall coal (inorganic/organic) (573-473K) [7, 45, 46]. Therefore, the stiffness is predominantly governed by the ash composition.

2.7 Viscoelastic, Elastic, and Plastic Properties of materials

In terms of stiffness and the range of deformation, solid materials can be classified as elastic, elastoplastic, or viscoelastic. A material that undergoes an elastic deformation with non-time dependent plastic deformation is called elasto-plastic [47]. A material that deforms elastically but exhibits time-dependent plastic deformation is viscoplastic. There are four basic mechanical models (linear elastic, linear viscous, Maxwell, and Voigt) that exist to describe the range of deformation as it relates to the amount of strain as a result of applied stress.

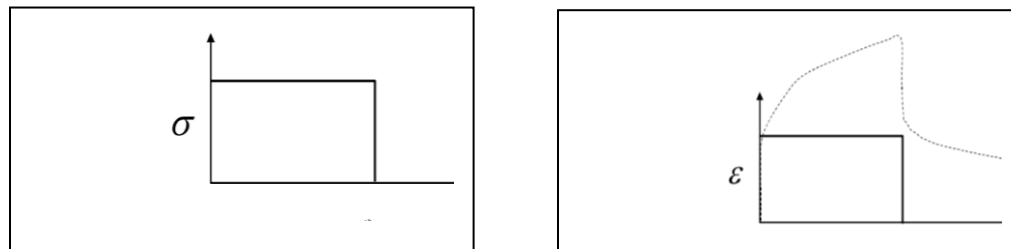
Figure 2-11: Schematic of the four basic mechanical rheological models [48]



2.7.1 Linear Elastic Model

In the linear elastic model, the stress is directly proportional to the strain based on the modulus of elasticity through the Hooke's Law. Because there are no time-dependent properties, the strain remains constant throughout the duration of applied stress

Figure 2-12 a-b: The stress and strain curve as a function of time for the linear elastic model [49]



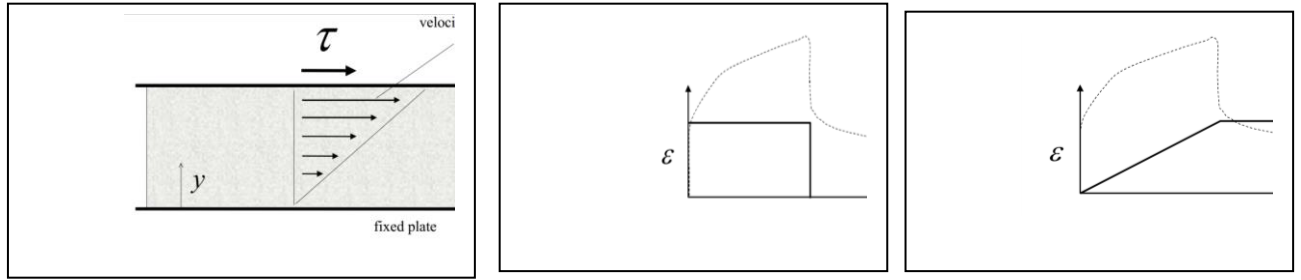
$$\varepsilon = \frac{1}{E} \sigma , \quad (2.23)$$

where ε is the strain, E is the modulus of elasticity, and σ is the normal stress.

2.7.2 Linear Viscoelastic Model

In the linear viscous model, the ideal incompressible fluid (Newtonian) is considered.

Figure 2-13a-c: The velocity profile, and stress and strain as a function of time for the linear viscoelastic model [49]



If a condition is assumed wherein a fixed plate exists under a body of (Newtonian) fluid at rest, shear stress can be applied by a movable upper plate. This shear stress causes a shear strain that can be correlated to the displacement of the fluid. Therefore, the velocity gradient is related to the shear stress through viscosity as

$$\frac{dV}{dy} = \frac{1}{\eta} \tau , \quad (2.24)$$

where V is the velocity, η is the viscosity, and τ is the shear stress.

If U_x is the displacement of the fluid, and V is the rate of this displacement, then the relationship between these two parameters can be represented as:

$V = \frac{d(U_x)}{dt}$, Thus the rate of strain is derived to be:

$$\frac{dV}{dy} = \frac{d}{dy} \left(\frac{dU_x}{dt} \right) = \frac{d}{dt} \left(\frac{dU_x}{dy} \right) = \frac{d\gamma}{dt} . \quad (2.25)$$

Therefore, the relation between the strain rate and the shear stress becomes the following:

$$\frac{d\gamma}{dt} = \frac{1}{\mu} \tau = \frac{d\gamma}{dt} \rightarrow \dot{\gamma} = \frac{1}{\eta} \tau . \quad (2.26)$$

By presuming that the dashpot represents a piston moving through the fluid, the strain rate becomes proportional to the applied stress under constant viscosity conditions:

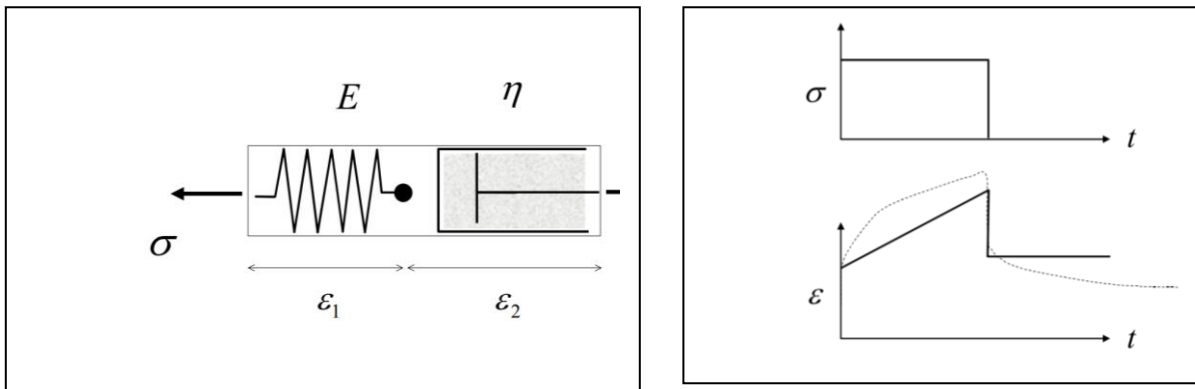
$$\dot{\epsilon} = \frac{1}{\eta} \sigma . \quad (2.27)$$

Upon integration, with an initial load and zero initial strain, the strain for a viscous element becomes

$$\epsilon = \frac{\sigma_0}{\eta} t . \quad (2.28)$$

For materials with elastic and time-dependent viscous properties, the Maxwell model represents these properties in series.

Figure 2-14a-b: Stress and strain as a function of time for the Maxwell model [49]



Based upon Figure 2-14a, strain one (ϵ_1) can be defined according to the linear elastic model while strain two (ϵ_2) can be defined according to the linear viscous model. Because the strain elements are represented in a series, they become additive properties for the total strain:

$$\begin{aligned}
 \text{Spring, } \varepsilon_1 &= \frac{1}{E} \sigma \\
 \text{Dashpot, } \dot{\varepsilon}_2 &= \frac{1}{\eta} \dot{\sigma} \rightarrow \varepsilon = \varepsilon_1 + \varepsilon_2 .
 \end{aligned}
 \tag{2.29}$$

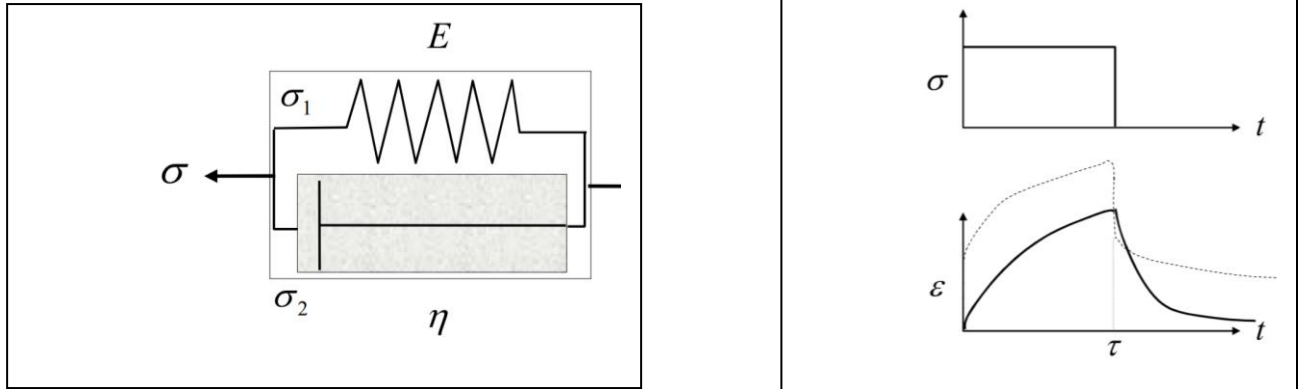
In terms of the strain rate, the constitutive equation becomes

$$\dot{\varepsilon} = \frac{1}{E} \dot{\sigma} + \frac{1}{\eta} \sigma .
 \tag{2.30}$$

2.7.3 Voigt (Kelvin) Model

In the Voigt model, the elements for strains are represented in parallel, unlike the Maxwell model. Moreover, an absence of bending is assumed [49]. Thus, the strain experienced by the spring is theoretically equal to the strain experienced by the dashpot.

Figure 2-15a-b: Schematic showing stress and strain as a function of time for the Voigt (Kelvin) model [49]



Therefore, the constitutive relation between the applied stress and the resulting strain becomes the following:

$$\begin{aligned}
 \text{Spring, } \varepsilon &= \frac{1}{E} \sigma_1 \\
 \text{Dashpot, } \dot{\varepsilon} &= \frac{1}{\eta} \dot{\sigma}_2 \rightarrow \sigma = \sigma_1 + \sigma_2 .
 \end{aligned}
 \tag{2.31}$$

By substituting σ_1 and σ_2 , the following relationship is obtained:

$$\sigma = E\varepsilon + \eta\dot{\varepsilon} .
 \tag{2.32}$$

With the initial condition of $\varepsilon(0) = 0$, the strain rate becomes

$$\varepsilon(t) = \frac{\sigma_0}{E} \left(1 - e^{-(E/\eta)t}\right). \quad (2.33)$$

Compared to the previous models discussed, the standard linear model is considered to be most realistic, since the two springs are in series and one spring is in parallel to the dashpot. However, the viscoelastic model proposed by Yigit follows the Maxwell model in the manner in which the applied stress relates to the resulting strain [50]. Nevertheless, the plasticity of elastoplastic and viscoplastic materials should be taken into consideration when interpreting nanoindentation measurements for the modulus of elasticity [47]. However, understanding the rheological properties of materials are key to selecting appropriate wall impact models

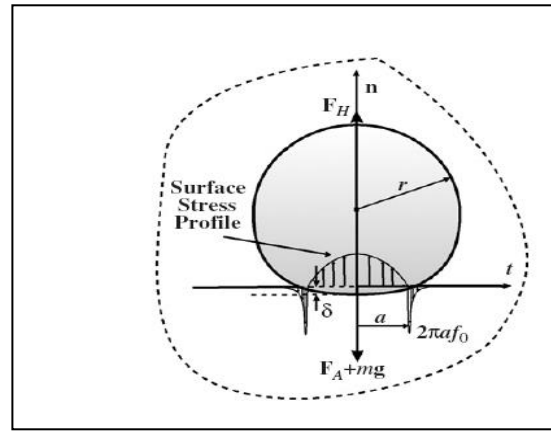
2.8 Particle Wall Impact Models

One of the earliest theories involving particle wall impact is the Hertz theory in which a frictionless punch impacts a half-space in the absence of an adhesion force [51]. The Johnson-Kendall-Roberts (JKR) theory improved upon the Hertz theory by including the adhesion forces in the vicinity of the contact area and balancing the elastic energy with the mechanical and surface energy of impact [52]. An alternative theory by Derjaguin, Muller, and Toporov, called the DMT Theory, was developed for a rigid sphere and a plane in which adhesion forces act in the annular region around the contact zone [53]. Tabor developed a dimensionless parameter representing the ratio between the gap outside the contact zone and the equilibrium distance between the atoms to indicate the applicability of the JKR-Hertz model as compared to the DMT model [54]. The Hertz maximum contact area and the Hertzian indentation depth was employed in the Brach and Dunn model for elastic impact [55, 56]. Models for inelastic impact also assume a Hertzian profile for variations in the contact radius [57]. Wall et al., Dunn et al., and Dahneke have reported experimental data for normal impact, while Li et al., Gorham et al., and Cross have reported data for oblique impact [56, 58-62]. Finite element simulations for normal and oblique impact models have been performed by other research groups [63, 64]. However, of all the experiments reported, only a few have sought to study the influence of initial particle spin or the behavior of non-spherical particles [62, 65]. The three models examined in this work are the elastic adhesive (EA) model (for elastic impact), the viscoelastoplastic model (for viscoplastic impact), and the liquid impact model (for viscous impact).

2.8.1 Elastic Adhesive Model

Brach and Dunn have proposed an EA model in which elastic and adhesive forces are considered.

Figure 2-16: Forces of microsphere impact with surface



In Figure 2-16, F_H is the Hertzian compressive force due to the stiffness between the particle and the surface, and F_A is the adhesive force due to particle and surface interfacial surface energy. The adhesive force is the force that acts along the perimeter of the contact area of the particle and the surface and is equal to $2\pi\alpha f_0$, where f_0 is the circumferential surface tension of the adhesion force per unit length and α is the equilibrium contact radius. The following equations represent the force balance where F_n denotes forces acting in the normal direction and F_t denotes the forces acting in the tangential direction:

$$F_n = F_H + F_{HD} + F_A + F_{AD} = m\ddot{n} , \quad (2.34)$$

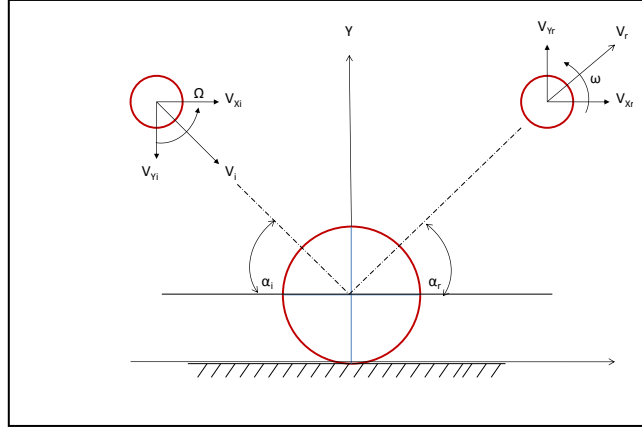
$$F_t = m\ddot{t} . \quad (2.35)$$

Based on the force balance of the EA model, the damping adhesive force, F_{AD} , and the damping Hertzian Force, F_{HD} , act to counteract the adhesive and the Hertzian forces. Because the

coefficient of restitution is defined as the ratio of the rebound velocity to the impacting velocity, this coefficient has been derived through the following energy balance based on the EA model:

$$\frac{mV_i^2}{2} + \frac{I\Omega^2}{2} = \frac{mV_r^2}{2} + \frac{I\omega^2}{2} + W_A + W_{diss} . \quad (2.36)$$

Figure 2-17: Schematic of microspherical particle impacting a planar surface



In Figure 2-17, \mathbf{V} represents the velocity while the subscripts r, i, x, and y denote the rebound phase, impacting phase, x direction, and y direction, respectively. The variables Ω , ω , and α represents the rotational velocity prior to impact, the rotational velocity after impact, and the angle of the impacting and rebounding phases, respectively. In equation 2.36, W_A is the work of adhesion while W_{diss} is the work of dissipative forces. Based on this energy balance, the normal coefficient of restitution (COR_n), denoted by e_n , can be expressed as

$$e_n^2 = 1 - \frac{W_A + W_{diss}}{mV_i^2/2} . \quad (2.37)$$

The work of adhesion is a function of the maximum contact radius, as per the Hertzian theory, and the adhesion force. Moreover, the adhesion force is a function of the radius of the contact area, a , the circumferential tension of the adhesion force per length, f_0 , and the surface roughness damping coefficient, C_R . In addition, f_0 is a function of the Hertzian stiffness and the combined surface energy. These relationships are shown in the following equations:

$$W_A = -\frac{2a_m^2 F_A}{3r} , \quad (2.38)$$

$$F_A = 2\pi a f_0 C_R , \quad (2.39)$$

$$f_0 = \left(\frac{9KrW_A^2}{2\pi} \right) . \quad (2.40)$$

The Hertzian stiffness is a function of the stiffness of the particle and the surface of impact, and the latter two parameters are a function of the modulus of elasticity of the particle and the surface, respectively:

$$K = \frac{4}{3\pi(K_1 + K_2)}, \quad (2.41)$$

$$k_i = \frac{1 - \nu_i^2}{3\pi E_i}. \quad (2.42)$$

The maximum contact radius, a_m , is a function of the mass, normal velocity, and Hertzian stiffness according to the Hertzian theory:

$$a_m = [5r^2 m v_n^2 / (4K)]^{1/5}. \quad (2.43)$$

By combining Equation 2.38 and Equation 2.43 for the maximum Hertzian contact radius, the adhesive parameter, ψ_A , can be obtained to represent the adhesive contribution to the overall coefficient of restitution as

$$\psi_A = \frac{W_A}{m v_n^2 / 2}. \quad (2.44)$$

For the dissipative Hertzian force, a Hertzian parameter is introduced, which is a function of the Hertzian stiffness, normal velocity, and the maximum Hertzian contact radius through the damping component of the Hertzian force:

$$e_H = \frac{\delta F_{HD}}{m v_n^2 / 2} = 2 \frac{a_m^5}{m r^2} K (2/3)^{5/2} \left(\frac{c_H}{v_n} \right) = \psi_H c_H. \quad (2.45)$$

COR_n is expressed as a function of the adhesive COR and the Hertzian COR. Therefore, COR_n becomes a function of the adhesive parameter, Hertzian parameter, adhesive damping coefficient, and the Hertzian damping coefficient

$$e_n = \sqrt{1 - (e_A + e_H)} = \sqrt{1 - \psi_A(1 + c_A v_n) - \psi_H c_H}. \quad (2.46)$$

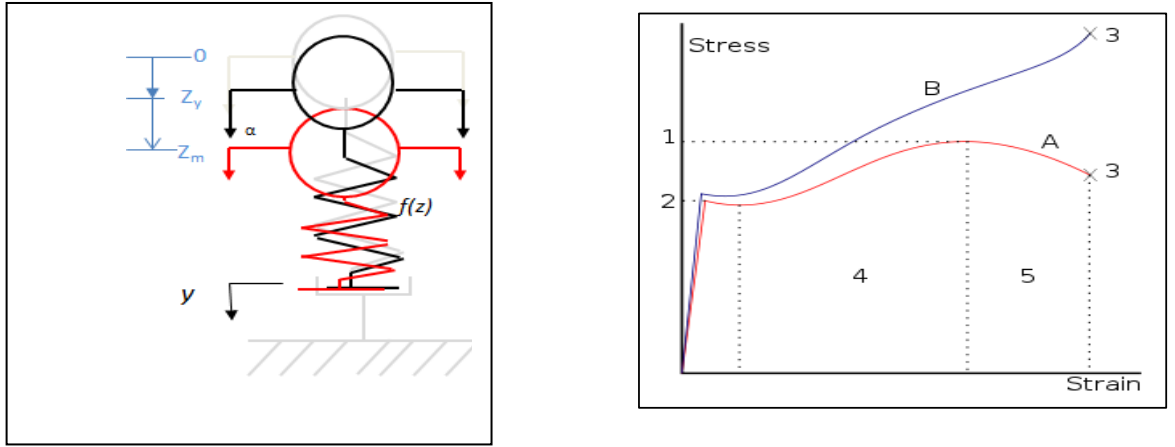
The tangential velocity has been determined through the impulse ratio:

$$\mu = \frac{V_{t-v_t}}{V_n - v_n}. \quad (2.47)$$

According to Kim et al., a critical angle exists such that a particle impacting below this angle will slide while a particle impacting above this angle will roll [55]. However, this dependence of the impulse ratio on the critical angle assumes that the particle is spherical and that particle rotation does not occur prior to impact.

2.8.2 Viscoelastoplastic (VEP) Model

Figure 2-18a-b: Schematic of the viscoelastoplastic model and stress-strain curve



In the VEP model, the damping forces are considered to be negligible since the plastic effects can be significantly small at low velocities. Instead of using the model by Biryukov and Kandotsev as proposed by Kim et al., the VEP model by Yigit et al. has been chosen to model the plastic effects in order to incorporate the viscoelastic behavior [50]. In terms of elastoplastic behavior, there are three phases that exist through the approach and the rebounding phases of a particle impacting a surface:

Phase I: Hertzian elastic loading phase

$$F = K_h z^{3/2} \quad \text{for } 0 \leq z \leq z_y . \quad (2.48)$$

In this phase, the force present is the Hertzian compressive force outlined in the EA model. The parameter z is the deformation of the particle and the parameter z_y is the threshold amount of deformation when the particle begins to yield due to plastic deformation. Plastic

deformation occurs when the particle deformation rate is higher and no longer proportional to the applied force as illustrated at point 4 of the stress strain curve shown in Figure 2-18b [66].

Phase II: Elastic-plastic phase loading

$$F = K_y(z - z_y) + K_h z_y^{3/2} \quad \text{for } z_y \leq z \leq z_m. \quad (2.49)$$

In this phase, the particle has been deformed past the yield strength and deforms at a maximum length denoted as z_m . This scenario is shown using Equation 2.49, where K_y is the linear contact stiffness of the elastic plastic loading phase and is a function of the Hertzian compressive stiffness and plastic deformation, z_y .

Phase III: Hertzian elastic unloading phase loading

$$F = K_h(z^{3/2} - z_m^{3/2} + z_y^{3/2}) + K_y(z_m - z_y). \quad (2.50)$$

In this phase, the force is unloaded for both the elastic-plastic and the Hertzian elastic loading phase. In the VEP Model, the elastic-plastic loading and the Hertzian loading phases are combined into one loading phase. By reducing the three phases for particle impact into two, the end result is a linearization of the particle impact process for viscoelastic behavior. Based on this linearization, the plastic loss factor (γ), which is based on the linear and Hertzian contact stiffness, can be equated as the coefficient of restitution for plastic impact. Thus,

$$e_{pl} = \gamma^2 = 1 - \left(1 - \frac{K_y}{K_h \sqrt{z_m}}\right). \quad (2.51)$$

For large velocities, the equation for the viscoelastic model can be derived through the binomial theory

$$\gamma^2 = \left(\frac{2}{3}\right) \left(\frac{K_y}{K_h}\right) \left(\frac{K_y}{mv_0^2}\right)^{1/4}, \quad (2.52)$$

where K_h is the Hertzian contact stiffness given by

$$K_h = \frac{4}{3} \sqrt{R} E^*. \quad (2.53)$$

Here, R is the radius and E^* is the effective contact modulus.

The effective contact modulus is given by

$$\frac{1}{E^*} = \frac{1-v_1^2}{E_1} + \frac{1-v_2^2}{E_2}. \quad (2.54)$$

Other variables in the equation include mass, m , and the initial velocity, v_o . K_y is the linear contact stiffness of the elastic plastic loading phase as described by Yigit et al. for the nonlinear viscoelastoplastic impact model, and is a function of z_y , the deformation where yielding or damage occurs. This relationship is shown below:

$$K_y = 1.5K_h\sqrt{z_y}. \quad (2.55)$$

The deformation where yielding or damage occurs, z_y , is given as a function of the yield strength S_y :

$$z_y = \frac{0.68S_y^2\pi^2R}{E^{*2}}. \quad (2.56)$$

The parameter γ can be equated with the coefficient of restitution when damping is absent; in fact, it is assumed to be absent in order to determine the coefficient of restitution. Because the coefficient of restitution of the model as described by Yigit et al. is based upon the point of impact, the normal as well as the tangential component has to be calculated based on the impact angle. For large velocities, the coefficient of restitution for the viscoelastoplastic model has been derived through binomial theory. This is represented as

$$\gamma^2 = \left(\frac{2}{3}\right) \left(\frac{K_y}{K_h}\right) \left(\frac{K_y}{mv_o^2}\right)^{1/4}. \quad (2.57)$$

The viscoelastic model by Yigit et al. does not consider the influence of adhesion. Kim et al. proposed Equation 2.58 with the plastic coefficient of restitution derived from the Biryukov and Kandotsev model:

$$e_n = \sqrt{e_{pl}^2 + e_A^2 - 1}, \quad \text{where, } e_A = \sqrt{1 - 2W_A/mv^2} \text{ without damping forces.} \quad (2.58)$$

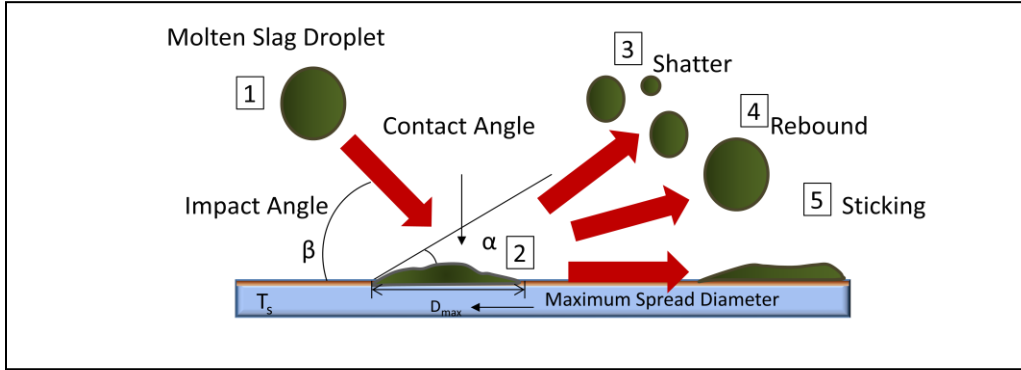
However, Losurdo proposed taking the product of the three coefficients for the adhesive coefficient (e_A), the viscoelastic coefficient of restitution (e_{vep}), and the coefficient of restitution due to wave dissipation (e_w), assumed to be 0.95, as given by Equation 2.59:

$$e_n = e_A \times e_{vep} \times e_w. \quad (2.59)$$

2.8.3 Liquid Droplet Impact (LDI) Model

The LDI model has been used to characterize the impact of slag hitting the refractory wall. There are three different modes of behavior for a liquid particle impacting the wall: shattering, rebounding, and sticking.

Figure 2-19: Modes of impacting droplet behavior



For the LDI model proposed by Ni et al., the energy balance of the particle impacting the surface is shown by [67]:

$$E_{k1} + E_{s1} = E_{k2} + E_{s2} + W + \Delta E_k \quad (2.60)$$

where, E_{k1} is the initial kinetic energy, E_{s1} is the initial surface energy ($E_{s1} = A\sigma = \pi D_0^2 \sigma$), E_{k2} is the kinetic energy at state 2, E_{s2} is the surface energy at state 2, W is the work in deforming the droplet against viscosity, and ΔE_k is the change in kinetic energy. At state 2, the droplet is at its maximum extension and the kinetic energy is zero ($E_{k2} = 0$)

$$E_{s2} = \frac{\pi}{4} D_{max}^2 \sigma (1 - \cos \theta) . \quad (2.61)$$

Here, θ is the contact angle, σ is the surface tension, and D_{max} is the maximum diameter. The work in deforming the droplet and the change in kinetic energy is approximated in Equation 2.62 and Equation 2.63, respectively:

$$W = \frac{\pi}{3} \rho u_0^2 D_0 D_{max}^2 \frac{1}{\sqrt{Re}} , \quad (2.62)$$

$$\Delta E_k = \left(\frac{\pi}{4} \bar{d}^2 \bar{s} \right) \left(\frac{1}{2} \rho V_0^2 \right) . \quad (2.63)$$

Here, V_0 is the initial velocity, ρ is the density, D_0 is the initial diameter, \bar{d} is the average diameter, and \bar{s} is the dimensionless solid layer thickness ($\bar{s} = s/D_0$). By substituting Equation 2.61- Equation 2.63 into Equation 2.60, the maximum spread factor can be determined as

$$\varepsilon_{max} = \sqrt{\frac{We+12}{3(1-\cos\alpha)+\frac{4We}{\sqrt{Re}}}}, \quad \text{with } We = \frac{\rho D^2 V_0}{\sigma} \text{ and } Re = \frac{\rho D V_0}{\mu}, \quad (2.64)$$

where, μ is the viscosity.

According to Equation 2.64, the maximum spread factor is dependent upon the Weber number, We , and the Reynolds number, Re . The spread factor is then determined based on an empirical relation called the excessive rebound energy, E_{re} , as follows:

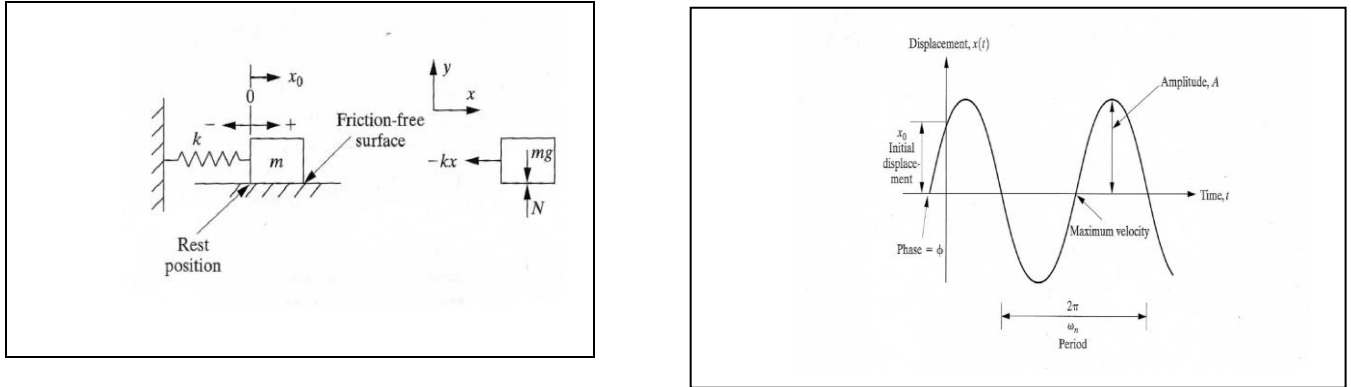
$$E_{re} = 0.25(\varepsilon_{max})^2(1-\cos\alpha) - 0.12(\varepsilon_{max})^{2.3}(1-\cos\alpha)^{0.63} + (2/3)(\varepsilon_{max}) - 1. \quad (2.65)$$

If the value of E_{re} is negative, then the coefficient of restitution is zero. Otherwise, the excessive rebound energy is equated with the coefficient of restitution. However, this model does not account for the break-up of liquid drops upon impact. Therefore, the droplet is assumed to retain the total volume for positive E_{re} .

2.9 The Role of Mechanical Vibrations in Particle Wall Collisions

The E_A model characterizes the role of damping through the damping coefficients while VEP ties the influence of the damping ratio to the plastic loss factor. However, the probability of the particle to penetrate must be accounted for through calculation of the displacement through slag. Therefore, the energy dissipation as it is described through Mechanical Vibrations is visited. Vibration is the study of repetitive motion of objects relative to a stationary frame of reference or nominal position (usually equilibrium) [68]. In a vibratory system, there are three elements: inertial elements, stiffness elements, and dissipation elements. For the stiffness element, Equation 2.66 represents the force balance for un-damped motion,

Figure 2-20: Basic schematic of un-damped system Motion [65]



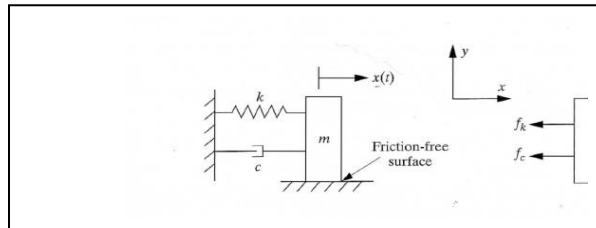
$$m\ddot{x}(t) = -kx(t) \rightarrow m\ddot{x}(t) + kx(t) = 0. \quad (2.66)$$

Here m is the mass, k is the stiffness in N/m, $x(t)$ is the displacement, $\dot{x}(t)$ is the velocity, and $\ddot{x}(t)$ is the acceleration. By dividing Equation 2.66 by m , Newton's law of motion can be expressed in terms of the natural frequency ω_n :

$$\ddot{x}(t) + \frac{k}{m}x(t) = 0 \rightarrow \ddot{x}(t) + \omega_n^2 x(t) = 0, \quad \text{where } \omega_n = \sqrt{k/m} \quad (2.67)$$

For damped motion, the dissipation element is introduced, and the force balance is shown in Equation 2.68 and Equation 2.69 as

Figure 2-22: Basic Schematic of damped motion [63]



$$m\ddot{x}(t) = -f_k - f_c, \quad (2.68)$$

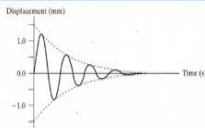
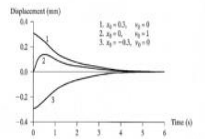
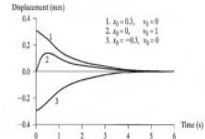
$$m\ddot{x}(t) + c\dot{x}(t) + kx(t) = 0, \quad (2.69)$$

$$\ddot{x}(t) + \zeta\omega_n\dot{x}(t) + \omega_n^2 x(t) = 0, \quad (2.70)$$

$$\text{where } \zeta = \frac{c}{c_{Cr}}, \omega_d = \omega_n\sqrt{\zeta^2 - 1}, \text{ and } c_{Cr} = 2\sqrt{km}.$$

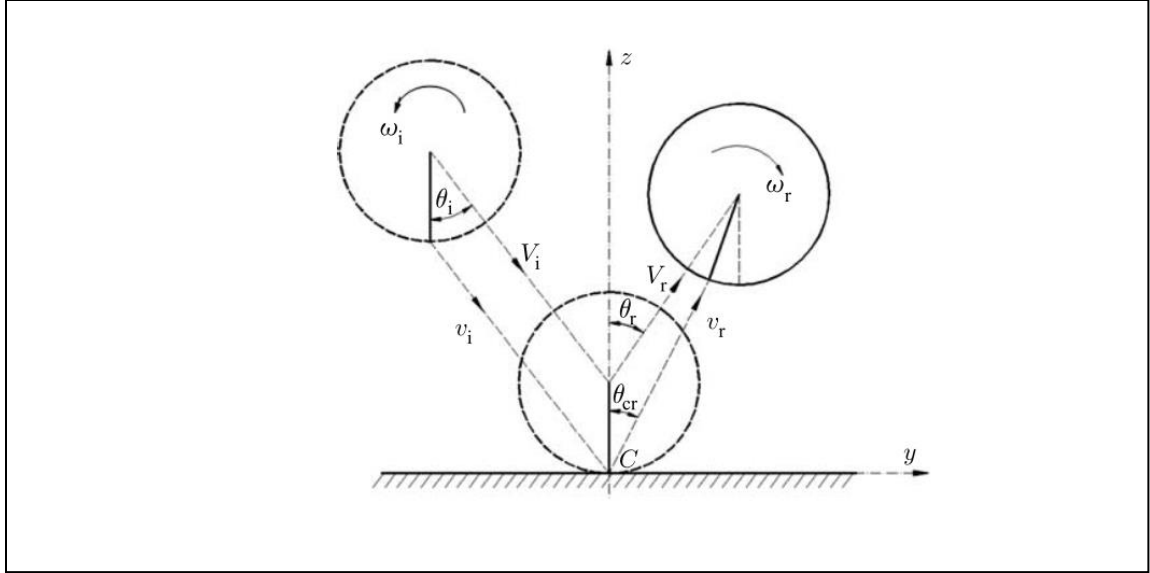
Here, ζ is the damping ratio, c_{cr} is the critical damping coefficient, and ω_d is the damping frequency. Based on the value of the damping ratio, there are three kinds of damped motion: under-damped, over-damped, and critically-damped. Because the damping ratio governs the damping response to the force balance, it also governs the solution for the displacement.

Table 2-3: Corresponding damping response and displacement profile for damping ratio values [63]

Damping Ratio	Damping Response	Displacement Profile
$0 < \zeta < 1$	Under-Damped	
$\zeta > 1$	Over-Damped	
$\zeta = 1$	Critically Damped	

2.10 Particle Oblique Impact

Figure 2-23: Schematic of oblique impact [61]



2.10.1 Tangential and Normal Coefficient of Restitutions

For oblique impact, the coefficient of restitution has two components: the normal coefficient of restitution, e_n , and the tangential coefficient of restitution, e_t . The normal coefficient is defined as the ratio of the normal rebounding velocity to the initial rebounding velocity, while the tangential coefficient of restitution is the ratio of the tangential rebounding velocity to the initial tangential velocity, as shown below:

$$e_n = -\frac{V_{nr}}{V_{ni}} , \quad (2.71)$$

$$e_t = \frac{V_{tr}}{V_{ti}} . \quad (2.72)$$

The relationship between the total coefficient of restitution, e , e_n , and e_t is shown in Equation 2.73:

$$e = \frac{V_r}{V_i} = \sqrt{\frac{V_{nr}^2}{V_{ni}^2 \cos^2 \theta_i} + \frac{V_{tr}^2}{V_{ti}^2 \sin^2 \theta_i}} = \sqrt{e_n^2 \cos^2 \theta_i + e_t^2 \sin^2 \theta_i} . \quad (2.73)$$

2.10.2 Impulse Ratio and Particle Rotational Motion

Impulse ratio (μ) is defined as the ratio of the tangential impulse (P_t) to the normal impulse (P_n):

$$\mu = \frac{P_t}{P_n} = \frac{\int F_t dt}{\int F_n dt} = \frac{m[V_{tr} - V_{ti}]}{m[V_{nr} - V_{ni}]} = \frac{V_{tr} - V_{ti}}{V_{nr} - V_{ni}}. \quad (2.74)$$

Equation 2.75 can be obtained by combining Equations 2.71, Equation 2.72, and Equation 2.74 to relate e_n and e_t to μ :

$$e_t = 1 - \frac{\mu(1+e_n)}{\tan \theta_i}. \quad (2.75)$$

The tangent of the impact angle is calculated from the ratio of the tangent impact velocity to the normal impact velocity.

$$\tan \theta_i = \frac{V_{ti}}{V_{ni}}. \quad (2.76)$$

The rotational impulse is

$$P_\omega = I(\omega_r - \omega_i). \quad (2.78)$$

According to the conservation of angular motion about point C in Figure 2-23, it can be stated that

$$P_\omega = RP_t. \quad (2.79)$$

By implementing the expressions for tangential and rotational impulses in Equation 2.79 the relation between the angular motion and the tangential coefficient of restitution can be obtained:

$$I(\omega_r - \omega_i) = mR(V_{tr} - V_{ti}), \quad (2.80)$$

$$\omega_r = \omega_i + \frac{mR(V_{tr} - V_{ti})}{I}, \quad (2.81)$$

$$\omega_r = \omega_i - \frac{mRV_{ti}(1-e_t)}{I}. \quad (2.82)$$

Hence, the relationship among angular velocity, the normal coefficient of restitution, and the impulse ratio can be obtained:

$$(1 - e_t)V_{ti} = \mu(1 + e_n)V_{ni} , \quad (2.83)$$

$$\omega_r = \omega_i - \frac{mR\mu(1-e_n)V_{ni}}{I} . \quad (2.84)$$

Thus, Equations 2.80 and 2.84 show that e_n , impulse ratio, and e_t are interdependent variables that, in unison, affect the angular velocities. In the EA model, e_n is calculated first based on the adhesive and Hertzian force balance while e_t is calculated based on the e_n and the impulse ratio. In this case the criteria of the impulse ratio which is based on the critical angle is used. However, for the VEP model, the total coefficient of restitution, e is calculated since the deformation of yield is based on the point of incidence. However, once e is calculated, the tangential and normal components can be calculated based on Equations 2.71-2.73.

2.10.3 Sliding versus Rotation and Micro-slip

To address the transition between sliding and rolling, the ratio of the friction and impulse has been specified as a parameter to indicate the critical angle at which this transition occurs. In Equation 2.85 the ratio of the friction and impulse ratio equals one at the critical angle.

$$f/\mu = 1 \quad \theta_{critical} . \quad (2.85)$$

Based on the literature review, no criteria has been developed for the possibility of simultaneous sliding and rotation due to particle irregular shape and previous rotation. If CFD gasifier models are to be improved in modeling char particle behavior, the shortfall in this criteria must be resolved. Moreover, the scant data for the modulus of elasticity (and yield strength) and inclusiveness of adhesive and viscoelastic properties introduce uncertainty. The lack of a sensitivity analysis for the proposed equations of Kim and Losurdo to incorporate the effects of adhesion as well as viscoelasticity have introduced uncertainty of how much influence of a COR due to adhesion, wave dissipation, or viscoelasticity would have on the overall COR. However, previous work has made certain that coal should be classified as a viscoelastic solid under high

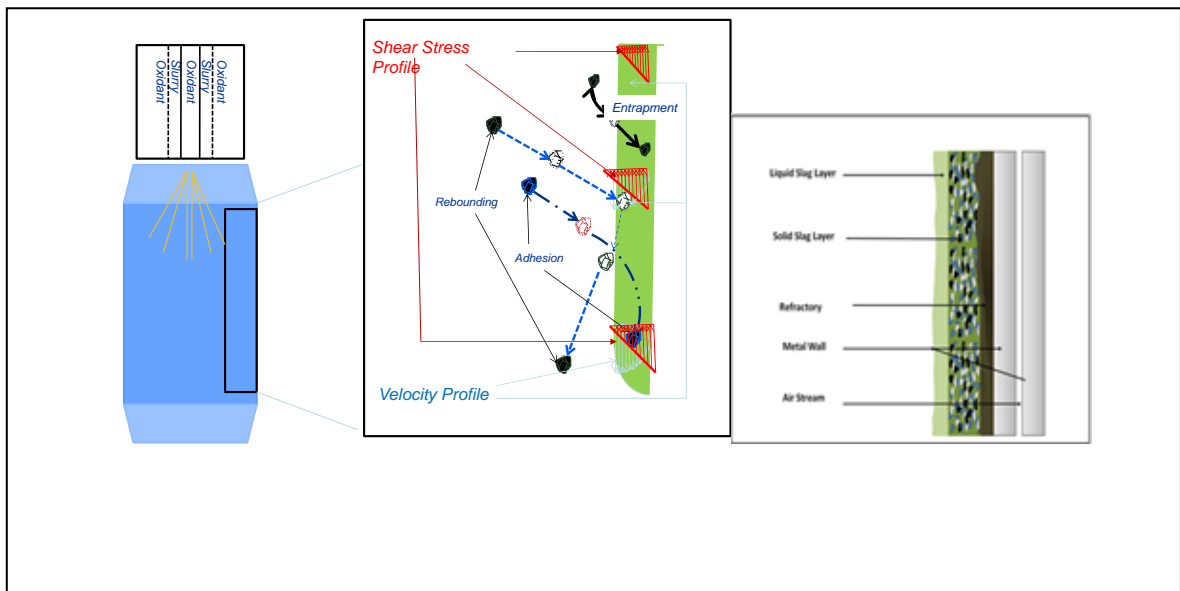
temperature and that it is the T_{CV} (1300-1500 K) that governs the stiffness of coal more so than T_g (573-743K) [7, 45, 46]. Therefore, the stiffness is governed predominantly by the ash deposition. Likewise, the adhesive properties is governed predominantly by carbon by evidence of contact angle experiments. The scope of the work not only includes the behavior of particle impacting refractory, but particles impacting a slag layer or other adhered particles. However, the issues laid out in terms of the non-ideal geometry of the particles and interdependence between viscoelasticity and adhesion to determine a sticking probability consistent with the physics of predicting the COR underscores the reference point for which the problem definition is based upon.

CHAPTER 3 PROBLEM DEFINITION, HYPOTHESIS, AND OBJECTIVES

3.1 Problem Definition

Because of the inefficiencies in plant operations due to flyash, there is a need to control ash deposition and the handling of slag disposal. Excessive char deposition in convective coolers can lead to unplanned shutdowns, while the char captured in slag can render the slag useless for the cement industry. Ash deposition also leads to a reduction in heat transfer, both in the radiative (slagging) section and in the low temperature convective (fouling) heating section, resulting in an increased cost of electricity generation [69]. Therefore, the objective of the Coal Particulate Partitioning Project was to characterize the behavior of coal based upon their specific gravities and size fractions in order to determine the particles within the population that were responsible for contributions to flyash. Nevertheless, by employing the discrete phase model, a computational tool that represents the gas phase as a continuum and the particles as a discrete phase, the trajectories of particles can be determined through a Lagrangian characterization. For those particles that are predicted to impact the wall, the COR must be defined.

Figure 3-1: The three modes of behavior of particle impacting a slag layer



COR, which is the ratio of the rebounding velocity to the impacting velocity, is not only dependent on the properties of the particles, but also on the properties of the surface of impact. Particles with a COR of zero are predicted to stick, while those with a COR greater than zero are predicted to rebound. Although experimental and analytical work has been performed to characterize ash and char deposition, such efforts have fallen short in addressing the probable variation in behavior that can occur when char impacts the refractory wall, in part due to variability in the carbon and particle temperature. Figure 3-1 illustrates the three modes of behavior of a char particle, which are adhesion, rebound, and entrapment. The three scenarios of particle impact include: (1) particle impacting the refractory wall, (2) particle impacting a slag layer on the wall, and (3) particle impacting adhered particles onto the wall. Taken together, the behavior for impact and the three scenarios listed above outline the scope of the problem.

Of the different empirical models, such as slagging indices and ash sticking temperatures, the viscosity models have been widely used to determine the threshold for particle sticking. Among the viscosity models, the modified Urbain model, which is empirically based on the acid to base ratio, has been widely used. Such models based on the acid to base ratio have been correlated with the ratio of network forming cations to network disrupting cations, the latter being those that discontinue the network chain of oxides due to a lack of available vacancies. Typically, the temperature of critical viscosity (i.e., the temperature where slag transforms from a glassy Newtonian phase to a crystalline non-Newtonian phase) is determined. This temperature is then used within the viscosity models to determine the critical viscosity. The probability of the particle sticking is then based on the ratio of the predicted particle viscosity at a certain temperature to the critical viscosity. Therefore, the closer the value of the particle viscosity to the critical viscosity, the lower the likelihood of the particle sticking and vice versa. However, the main pitfall of relying on the viscosity models to predict particle sticking is the fact that they only take the effect of ash composition into consideration. Char particles that have a significant amount of residual carbon may not have the appropriate ash composition to influence sticking or enough minerals located in the peripheral areas of the carbon matrix as suggested by Li et al. [70]. Furthermore, the viscosity models are still approximate at best when applied to different coals, and cannot be used for particle tracking purposes to predict the magnitude and direction of the particles that are predicted to rebound from the surface. In addition, they do not indicate the

influence of the impacting char particles that have adhered to the refractory walls and subsequently cooled.

Previous efforts in developing the modeling tools to characterize ash deposition include the efforts of Rushdi et al. and the Energy and Environmental Research Center (EERC) [69, 71]. For the mechanistic tool described by Rushdi et al., a subroutine was implemented to predict the particle shift temperature to determine the particle viscosity. Meanwhile, the slagging and the prediction tools to assess slagging and fouling by EERC depended on the inputs regarding the sticking efficiency and the ash impaction rate, which had to be empirically determined. Both of these efforts were largely based on the characterization of ash behavior as compared to char; however, they did not address the physics behind the tendency of a particle to adhere or rebound. One such model to predict the adhesion of char particles has been proposed by Shmizu et al., which assumes that the gasifier temperature is higher than the melting point of the ash [72]. This model also assumes that the char will be captured by the slag surface and will rebound from where char has adhered. The probability for the char capture rate is based on the ratio of the surface area covered by the unreacted char to the total surface area. However, the basis for this probability contradicts the experimental work of other authors who have shown the resistance to wettability by slag and carbon [30, 31, 73, 74] and presented empirical evidence that the probability of adhesion only increases as a function of carbon conversion [75]. Wang et al. [76] have utilized a model developed by Lee et al. [73] to predict the adhesion of char particles in order to determine the slag layer thickness on the wall of a combustor. However, the model of Lee et al. [77] was based on the empirical results of Tabkoff and Malak to determine the COR, which was measured at room temperature [78]. However, at high temperatures, the char particles have been described to exhibit viscoelastic behavior, as shown through swelling studies [45]. Without a particle-wall impact model that can correlate the carbon and ash composition to the viscoelastic particles to predict the probability of rebound (or adhesion), most models fall short of being a reliable parameter that can be used in a partition methodology in the efforts to reduce the amount of flyash.

3.2 Hypothesis

Whether a particle becomes entrapped or not will depend on the interplay between the inertial force of the particle and the viscous force of the particle impacting the slag layer. If the particle fails to penetrate the slag through a significant displacement within the slag, then the particle impacting the refractory wall, slag layer, and other adhered particles can be reduced to two modes of behavior - adhesion and rebound. If the behavior of char particles impacting the wall is indeed reduced to these two modes of behavior, a rules-based sticking probability function incorporating the influence of carbon and viscosity will predict a lower sticking efficiency for particles with significant amount of carbon than conventional viscosity models. A sticking probability function, based on a critical velocity as predicted by the viscoelastic model with the influence of carbon on the interfacial surface tension, will predict sticking efficiencies closer to that of a rules-based function based on the contact angle and the temperature of critical velocities than the viscosity models. The differences among critical velocity, temperature of critical viscosity, and critical contact angle are due to the differences in the particle velocities as compared to the critical velocities. With respect to the resulting coefficient of particles impacting the wall, the variation in the sphericity of particles (as characterized by the degree of equancy) together with the variability in the surface geometry will lead to variations in the normal COR. In the case that a sticking probability function that considers the influence of carbon on the adhesion properties of the particle is used, it can be shown that the partition of flyash, and slag can be altered by changing the particle size distribution.

3.3 Objectives

Specific objectives of this work entail the following:

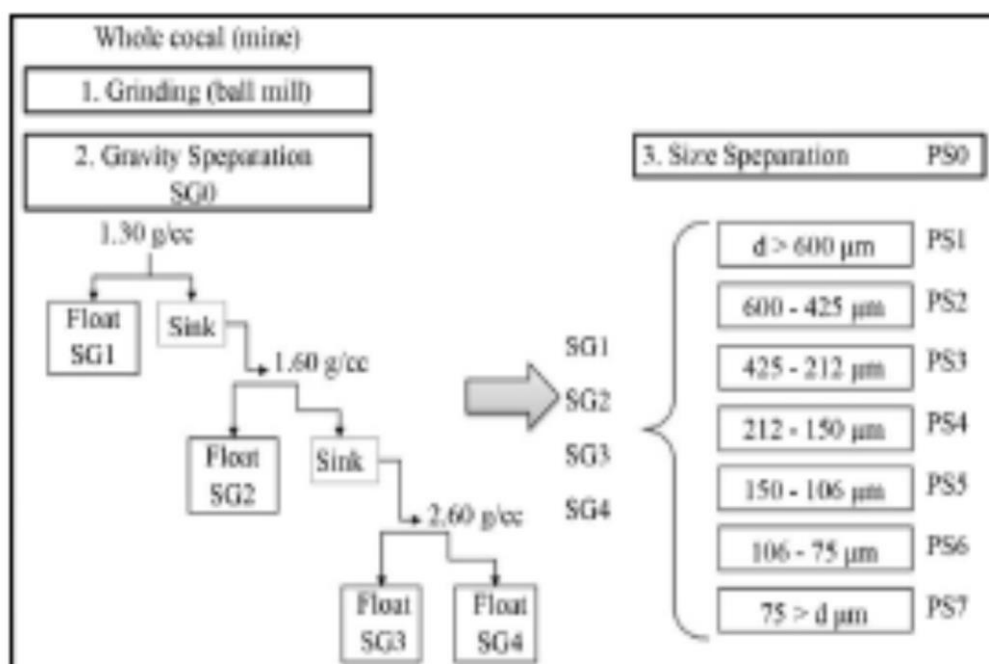
1. Determine the influence of sphericity, particle rotation, and uneven surface geometry on the coefficient of restitution and how such results compares to the predictions of current particle wall impact models based on the assumptions of a spherical shape and irrotational motion.

2. Show that the carbon content has an influence on the adhesion of char particles by using a sticking probability that uses the temperature of critical velocity and the contact angle as a “rules-based-criteria” to determine adhesion.
3. Determine a sticking probability based on critical velocities derived from a viscoelastic particle wall impact model. This sticking probability is to be compared to the sticking probability determined from the “rules-base-criteria” and the conventional “viscosity” model.
4. Show that the amount of flyash can be reduced by decreasing the average particle size in a particle size distribution (PSD) utilizing a population model based on an algorithm using the proximate analysis, impact efficiencies, and sticking probability.

CHAPTER 4 APPROACH AND METHODOLOGY

To achieve the objectives of incorporating the influence of carbon and assessing the limitations of the particle-wall impact models, the first major task was the characterization of the organic and inorganic composition of the particles in the population as shown in Tables 4.3-4.4. The coal of interest was obtained from the Bailey Mine in Wind Ridge, Pennsylvania and had ash composition and proximate analysis that resembled that of the Pittsburgh 8 Coal. The bulk coal sample, acquired from the Pittsburgh No. 8 seam of the Bailey Mine in Clatsville PA, (BSG0PS0) was separated by float-sink experiments into four gravity fractions BSG1 (floating at 1.3 g/cc), BSG2 (1.3 to 1.6 g/cc), BSG3 (1.6 to 2.6 g/cc) and BSG4 (sinking at 2.6 g/cc) (see Figure 4-1) [79]. The separated density cuts were sieved into seven size fractions. The density cut distribution is provided in Table 4-1 and the size distribution of each individual density cut is shown in Table 4-2. The size distributions vary from PS1 ($> 600 \mu\text{m}$) to PS7 ($< 75 \mu\text{m}$) [80].

Figure 4-1: Density and size separated sample preparation flow diagram where SGO represents the whole coal and PSO represents the sample before separation [80]



Based on the existing empirical models, the ash composition was used to determine the temperature of critical viscosity, yield stress, as well as viscosity.

Thereafter, cold flow particle wall impact experiments were performed to investigate the influence of non-ideal properties such as non-sphericity, surface roughness, and surface irregularities.. These experiments were designed to mimic the particle trajectories in an entrained flow gasifier resulting from a spray injector so as to assess the assumptions of previously validated particle-wall collision models that minimized particle rotation and adhered to a perfect spherical geometry. Although the particles in the cold flow particle-wall impact experiments have not been confirmed to be viscoelastic, their results have provided insights on how the particle orientation and shape contributes to the rebound angle. Given that this orientation is possibly a result of angular velocities in each direction of the Cartesian coordinate system, the particle rotation should not be ignored.

Once the influence of non-ideal conditions that have not been considered in existing particle-wall impact models have been addressed, the emphasis was placed on the possible characterization methods after determining the likelihood of particles impinging the slag. The inputs to these models are the results from a computational fluid dynamic (CFD) model that considered parameters such as carbon content, particle temperature, and particle velocities. For the sticking probability models, the temperature of critical viscosity as predicted by the Seggiani regression model was used as a representative model for the conventional viscosity approach of predicting sticking [7]. To incorporate the influence of carbon, a rules-based method using the contact angle as a parameter to determine adhesion, in addition to the temperature of critical viscosity, was used as a benchmark to gauge the predictions of a critical velocity method. Moreover, this method was validated by previous experimental work on particle wall sticking experiments based on char particle and ash deposition.

Table 4-1: Weight% (as received basis) of each specific gravity sample for the PSD of Bailey coal

Gravity Fraction	BSG1PS0	BSG2PS0	BSG3PS0	BSG4PS0
Weight %	47.84	47.57	3.46	1.12

Table 4-2: Particle size distribution of different density fractions (all sizes in μm), wt% (as received basis)

	PS1 d > 600μ	PS2 425 - 600μ	PS3 212 - 425μ	PS4 150-212μ	PS5 106-150μ	PS6 75-106μ	PS7 d < 75μ
BSG1	5.31	10.85	31.15	13.36	11.57	10.79	16.97
BSG2	3.91	9.53	21.66	9.15	7.38	6.9	41.39
BSG3	16.15	11.50	23.38	10.71	9.12	8.79	20.40
BSG4	8.69	5.93	17.50	8.31	8.65	13.49	37.43

Table 4-3: Proximate analysis of particle size distribution according to specific gravity

	BSG1	BSG2	BSG3	BSG4
Carbon	86.3	77.7	32.2	6.8
Hydrogen	6.1	5.7	2.2	0.3
Oxygen	2.6	0.8	0.6	0.4
Nitrogen	1.6	1.4	0.4	0.2
Sulfur	1.0	2.04	9.4	32.1
Ash	2.3	12.4	55.2	60.2

Table 4-4: Ash analysis of particle size distribution according to specific gravity

Ash	BSG1	BSG2	BSG3	BSG4
SiO₂	51.7	52.90	51.72	16.93
Al₂O₃	27.89	25.42	21.06	6.05
Fe₂O₃	11.72	16.50	20.44	71.86
CaO	3.84	1.04	3.18	4.19
MgO	0.99	0.72	0.72	0.21
Na₂O	0.42	0.39	0.31	0.10
K₂O	1.64	1.86	1.63	0.38
SO₃	0.00	0.00	0.00	0.00
Other	2.33	1.18	0.95	0.28

The critical velocity was derived from a viscoelastic model where the sintering data on the ratio of surface tension to viscosity that had been correlated to the compressive strength was used to indicate the yield stress of the char particles. The influence of carbon was incorporated in the interfacial surface tension using the Young's equation, and then the surface tension to viscosity ratio was calculated in order to determine the yield stress as a function of ash composition and carbon content. For the Yigit linear viscoelastoplastic model, the plastic loss factor was equated to the coefficient of restitution (COR) [50], and the COR was used in Equation 2.57 to account for the effects of viscoelastoplasticity. However, since setting this plastic loss factor to zero to calculate the critical velocity leads to a trivial solution, it was solved independently with the COR set to zero and the damping ratio set to one to indicate critically damping motion. Based on these methods, the sticking probability was determined for each specific gravity and size fraction. In using the temperature of critical viscosity method, particle temperatures were compared with the predicted temperature of critical viscosity for that particular size fraction and specific gravity. Particles at temperatures above this temperature were considered to be sticking, while those equal or below this temperature were considered to rebound. For the method employing the combination of contact angle and temperature of the critical viscosity, a contact angle as a function of carbon was used to predict the wettability of the impacting char particles. If the contact angle was equal or greater than 90° , the particles were considered to rebound; however, if the contact angle was less than 90° , the particles were considered to adhere. With respect to the critical approach velocity, particles that exceeded the critical velocity were predicted to adhere, while those below it were predicted to rebound.

Upon verification of the rules-based method that employed the temperature of the critical viscosity and the critical contact angle as the two parameters to indicate sticking, the use of a sticking probability method with CFD particle impact data and conversion was demonstrated and used to determine the partitioning between the flyash, syngas, and the slag. The effect of the variability in particle temperatures, resulting from different gasifiers conditions, on the sticking probability was addressed. Changes in the particle distribution were assessed in order to quantitate the increase or decrease in the amount of slag, flyash, and predicted syngas.

CHAPTER 5 EXPERIMENTAL METHODS

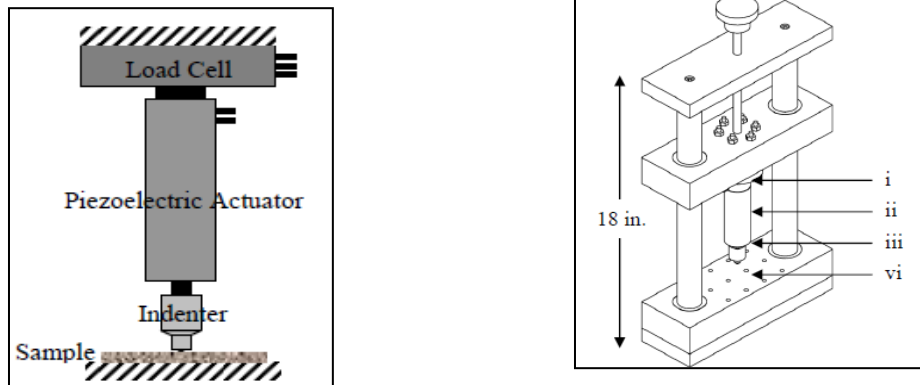
5.1 Nanoindentation Experimental Measurements

The modulus of elasticity was measured using a multiple loading nanoindentation system [81]. The particles that were measured using this technique were used in cold flow particle-wall collision with slag impact (PWCS Project) experiments to determine the coefficient of restitution based on the stiffness, adhesive properties, and sphericity of the selected materials.

5.1.1 Apparatus

The apparatus for the multiple loading nanoindentation system consists of (i) load cell, (ii) piezoelectric actuator, (iii) indenter, and (iv) sample stage, as outlined in Figure 5-1(a,b).

Figure 5-1a-b: Schematic of the nanoindentation system showing various parts [81]

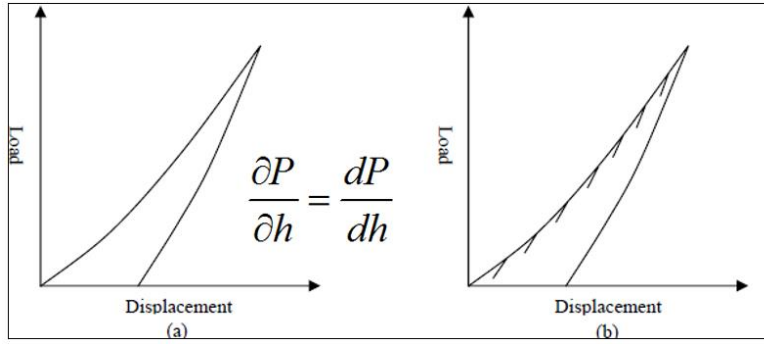


All the components of the nanoindentation system established the boundary conditions for ideal contact mechanics in order to reduce the deflection referred as system compliance. Because of the variability in the sphericity of the particles in the experiment, an average of 53 measurements of high density polyethylene (HDPE) particles with acceptable R-squared values based on least squares data fit were considered. The average was taken for four flat multiple loading nanoindentation measurements for the “high viscosity” and the “low viscosity” silicone adhesive that was used as a substrate in the experiments.

5.1.2 Approach and Application

To determine the Young's modulus of elasticity for the HDPE particles, the displacement versus change in load data was correlated to the load data using the relation,

Figure 5-2: Plot of load versus displacement for multiple loading [76]



$$\frac{\partial h_e}{\partial P} = \frac{\partial h}{\partial P} = (6RE_R^2)^{-1/3} P^{-1/3} = CP^{-1/3}. \quad (5.1)$$

Here h_e is the elastic indentation depth, h is the indentation depth, E_R is the effective modulus of elasticity, and P is the applied load. The value of h is based on the Hertzian displacement, such that $(h = \frac{a^2}{R})$, where a is the contact radius and R is the particle radius. Based on the particle radius, the effective modulus of elasticity can be determined from the slope, C . Once the effective modulus is calculated, the particle's modulus of elasticity is determined based on its the relationship with the effective modulus of elasticity and the modulus of elasticity of the flat indenter:

$$\frac{1}{E_R} = \frac{1-\nu^2}{E} - \frac{1-\nu_i^2}{E_i} \quad (5.2)$$

For the silicon adhesive, the displacement versus the change in load data was correlated to the inverse of the load to determine the slope, provided that the diameter of the flat indenter was known:

$$\frac{\partial h_e}{\partial P} = \frac{\partial h}{\partial P} = (6RE_R^2)^{-1/3} P^{-1/3} = CP^{-1/3}. \quad (5.3)$$

As mentioned earlier, the reduced modulus was determined based on the slope and was subsequently used to calculate the modulus of elasticity for the silicon adhesives using Equation 5.3.

5.1.3 Results

Based on the nanoindentation measurements for the HDPE particles, the average modulus of elasticity was found to be 1.116 ± 0.6 GPa. It is interesting to note that this value was only 1.06% different from an industry reported value of 1.172 GPa [82]

Figure 5-3: A load displacement measurement for HDPE

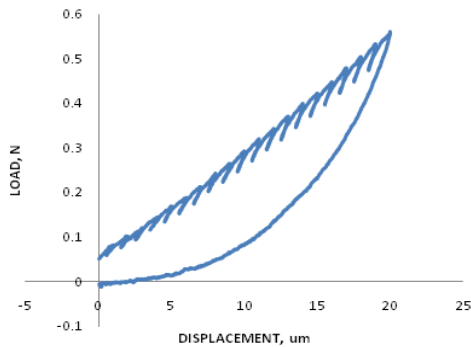
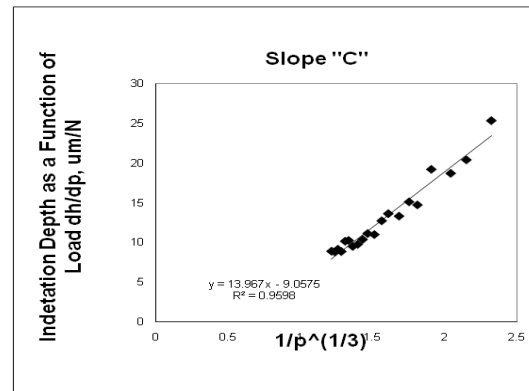


Figure 5-4: Slope for determining reduced modulus of elasticity



The average R-squared value for all of the data sets used to calculate the modulus of elasticity was 0.91.

Figure 5-6: Distribution of modulus of elasticity values

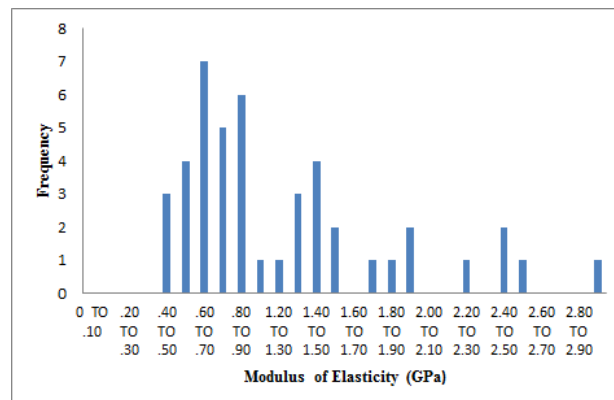


Table 5-1: Average values for modulus of elasticity of “soft” low viscosity silicone adhesive

Soft (Low Viscosity) Silicone		
No.	Modulus of Elasticity (GPa)	R-Value
1	0.919	0.99
2	1.075	0.96
3	0.867	0.92
4	0.766	0.95
Average Measurement		0.907
Average Deviation		0.129
		0.96
		0.027

Figure 5-7: Slope for the determination of reduced modulus of elasticity for one data set of low viscosity silicone

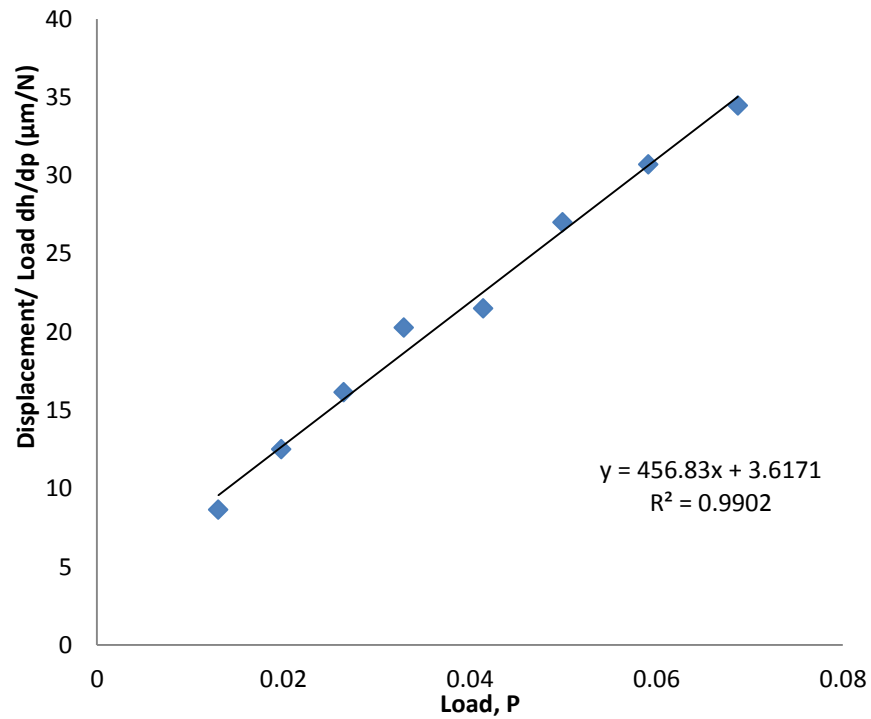
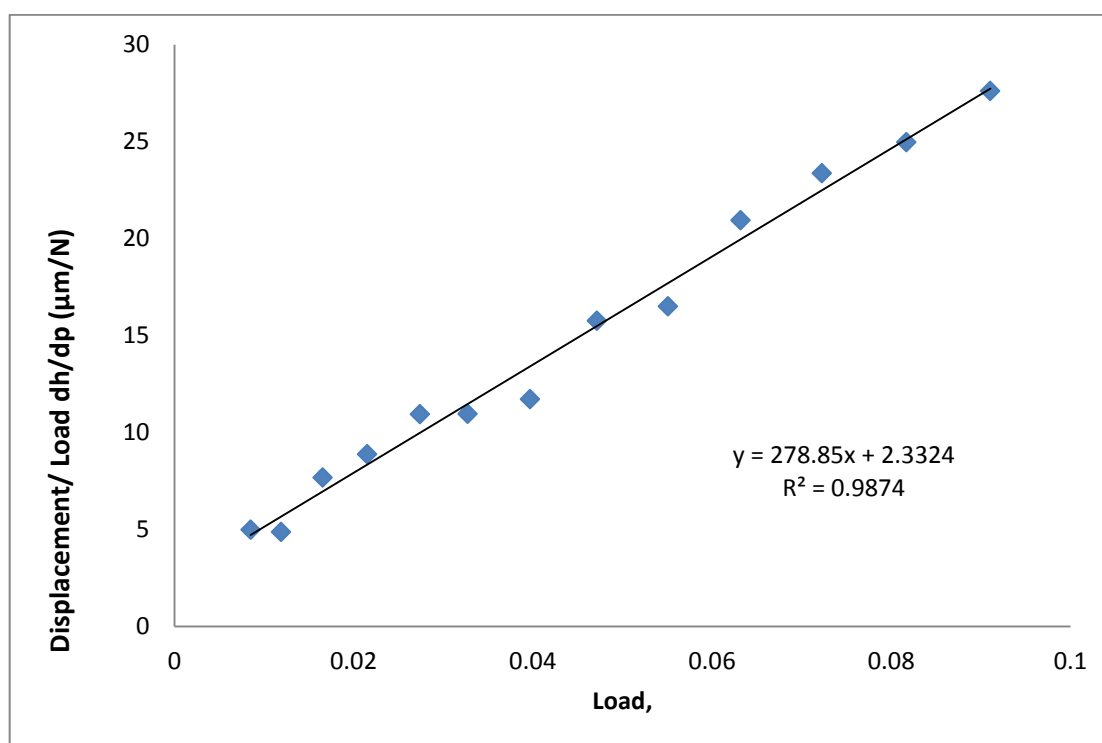


Table 5-2: Average values for modulus of elasticity of “hard” high viscosity silicone adhesive

Hard (High Viscosity) Silicone		
No.	Modulus of Elasticity (GPa)	R-Value
1	1.469	0.99
2	1.898	0.95
3	1.403	0.97
4	1.087	0.98
Average Measurement		1.464
Average Deviation		0.334
		0.97
		0.178

Figure 5-8: Slope for the determination of reduce modulus of one set of data for high viscosity silicone



5.2 Particle Wall Collision Experiments

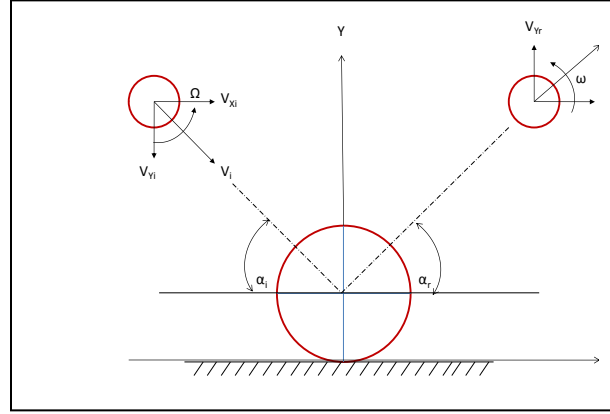
5.2.1 Selection of Substrates

Adapting the current particle wall impact models to the behavior of char particles hitting a refractory or slag layer within a gasifier is not trivial. For instance, the sphericity of the char particles can range from 0.47 (mixed porous type char) to 0.82 (Crassi-sphere type char) and can vary according to the particle size distribution of the original coal [83]. This variability in shape can lead to a variation in particle-to-particle collisions and thus the rotational motion. Moreover, turbulence in zones such as the jet and the reflux region is likely to contribute to particle rotation in addition to the particle-to particle collisions upstream in the gasifier [84]. The stiffness of the refractory wall, and that of the particle, also influences the magnitude of the rebound. Within an entrained flow gasifier, there are three scenarios for a particle impacting the surface of the gasifier: particle slag interaction, particle hitting adhered particles, and particles hitting the refractory. Although various models have been developed for liquid impact [67] and particle rebounding from a wetted surface [85], only a few experiments have been performed to investigate particle impacting adhered particles. To simulate the physical conditions of the three scenarios within a gasifier, four surfaces have been selected: (1) a flat metal plate, (2) a low viscosity silicone adhesive, (3) a high viscosity silicone adhesive, and (4) adhered particles on a flat metal plate. In this scenario, the metal plate represents the refractory, the low viscosity silicone represents the low viscosity slag, the high viscosity silicone represents the high viscosity slag, and the adhered HDPE particles represent the adhered char particles. The velocity range and an angle of 70° from the horizontal plane was pre-selected based on a CFD simulation for a down flow entrained flow gasifier [86].

5.2.2 Model Equations used to Calculate Coefficient of Restitution

Figure 5-9 illustrates the case for a particle impacting and then rebounding off of a flat surface.

Figure 5-9: Schematic of a microspherical particle on a planar surface



Based on the diagram, the variable V represents the velocity while the subscripts r , i , x , and y denote the rebound phase, impacting phase, x direction, and y direction, respectively. The coefficient of restitution (COR) in the x and y direction, and the overall COR are expressed as:

$$e_x = \left| \frac{V_{xr}}{V_{xi}} \right|, \quad (5.4a)$$

$$e_y = \left| \frac{V_{yr}}{V_{yi}} \right|, \quad (5.4b)$$

$$e = \left| \frac{V_r}{V_i} \right|. \quad (5.4c)$$

The following equation represents the COR in terms of the impact angle:

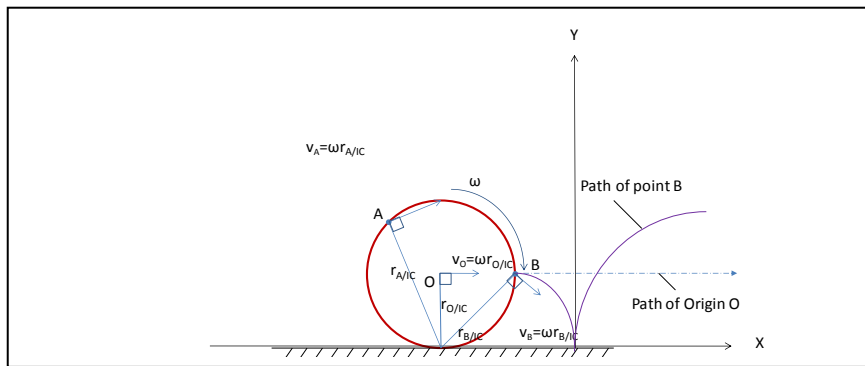
$$e = \sqrt{\frac{V_{yr}^2}{V_{yi}^2 \cos^2 \alpha_i} + \frac{V_{xr}^2}{V_{xi}^2 \sin^2 \alpha_i}} = \sqrt{e_y^2 \cos^2 \alpha_i + e_x^2 \sin^2 \alpha_i}. \quad (5.5)$$

The relation between the normal and the tangential impact is expressed by the impulse ratio, which is the ratio of the tangential impulse to the normal impulse:

$$f = \frac{V_{xr} - V_{xi}}{V_{yr} - V_{yi}}. \quad (5.5)$$

Although rotational kinematics has not been experimentally measured, the total kinetic energy loss includes the rotational as well as the translational components of motion. When a particle is moving normal to the plane during the impact phase, any translational motion during the rebound phase can be thought of as the result of rolling, provided that the no-slip condition applies. In the case of particle motion along the plane of the impacted surface, a point is termed as the *instantaneous center of zero velocity (IC)* when the point lies on the *instantaneous axis of zero velocity*, $r_{O/IC}$, as illustrated in Figure 5-10.

Figure 5-10: Schematic of rolling object without slipping



At the point of *IC*, the particle velocity is zero and the velocity at the origin is equal to the product of the rotational velocity and the radial distance from the origin to the point of *IC*, as shown below [87]:

$$V_O = V_{IC} + \omega r_{O/IC} = \omega r_{O/IC}; V_{IC} = 0. \quad (5.6)$$

Equation 5.6 provides a reasonable estimation of the rotation of particles after impact, provided that the horizontal component of the velocity is known in addition to the radial distance of the particle origin from the planar surface. Gorham and Kharaz suggested a formula to determine the rotation of the spheres upon impacting a surface based on the radius of gyration [61]. However, their equation is based on a spherical geometry, while the equation listed above can be used for any generic shape.

5.2.3 Apparatus and Particle Description

The apparatus for the air-injected experiments consisted of an eductor, vibrating feeder, and a remote controlled mount inside a plexiglass container as shown in Figures 5-12a-c. The eductor was constructed in order to accelerate the particles to different velocities prior to impacting them on the surfaces. The vibrating feeder, Sympatec Vibri, was selected to continuously feed a relatively uniform stream of particles while varying the particle concentration. The particles were fed by adjusting the gap and the feed rate of the vibrating feeder. Thereafter, the particles entered a funnel and were entrained into the eductor. Air was injected into the eductor, thereby creating suction and pulling the particles through the funnel. Once inside the tube, the particles were then entrained through the tube until they impacted the plate or the substrate upon ejection. A remote controlled mount was used to precisely control the angle of impact in the field of view of the camera. For drop experiments, the eductor was replaced with a 107 cm long plexiglass tube with a 10 cm inner diameter to remove the influence of injected air. The eductor, with and without a nozzle, was calibrated using Laser Doppler Velocimetry (LDV) and Fiber Optic System (FOS) with nozzle only to establish a range of particle velocities. The nozzle was used to ensure that the particles were ejected straight upon exiting the tube.

The experiments with the eductor were carried out using the HDPE particles. To investigate the influence of sphericity on particle wall impact using drop experiments, Coke was used as a non-spherical particle while polystyrene pellets along with HDPE were used as spherical particles. Table 5-3 lists the properties of all three types of particles used in the experiment.

Table 5-3: Properties of particles used in the drop and eductor experiments

Particle Type	Density (g/cc)	Modulus of Elasticity (GPa)	Average Size Fraction ± Std Deviation (µm)	Equancy
High Density Polyethylene	0.863	1.12	809±153	0.8
Coke	1.67	14.00	816±159	0.6
Polystyrene	1.028	2.00	5933	1

To simulate the conditions of a slag layer and adhered particles within a gasifier, the four surfaces listed in Table 5.4 were used. The steel metal plate was used as a control surface for a set of experiments using the eductor.

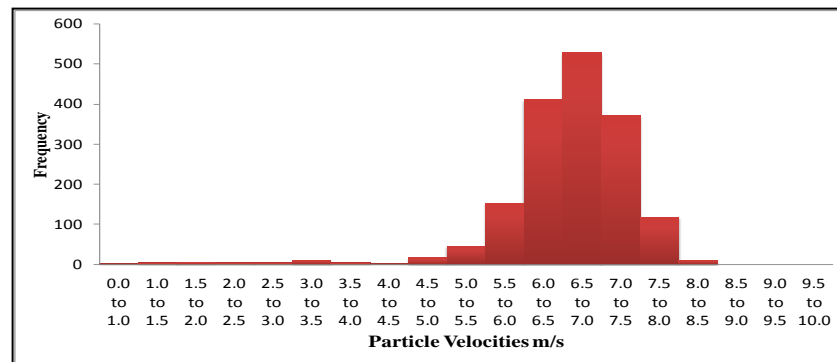
Table 5-4: Properties of surfaces used in eductor experiment

Substrate	Modulus of Elasticity (GPa)
Stainless Steel	190
High Density Polyethylene	1.12
SS-6664B “Soft” Silicone	0.90
SS-380 “Hard” Silicone	1.46

Although there was variability in the signal of the LDV data representing the distribution of particle velocities for Coke and HDPE, the average velocity for the first peak in the binomial distribution coincided with the average velocity data calculated from the FOS data. Because the LDV data exhibited a binomial velocity distribution with the nozzle as compared to a more even distribution without it, the nozzle was not used for the experiments involving the eductor. Based on the FOS measurements, the average particle velocities for Coke and polyethylene particles increased as a function of the volumetric gas flow rate in the range of 2 to 8 m/s. The particle feed rate was adjusted to attain a sufficient number of particle collisions (1000 particles or more) within a three-minute time frame for each experimental run.

For experiments involving the educator, the images of the particles impacting the substrate were taken with a Phantom v7.1 high-speed camera manufactured by Visions Research located at Wayne, NJ. The sampling rate, 3000 frames per second (fps), was used to attain the images of the polyethylene particles at higher velocities ($\sim 6 - 8$ m/s), and the air flow rate was $1.13 \text{ m}^3/\text{hr}$, as shown in Figure 5-11. For lower velocities, the frame rate and the airflow rate were set to 2000 fps and $0.283 \text{ m}^3/\text{hr}$ for the HDPE particles, respectively. Images for the drop experiments were taken at 1000 fps for the Coke and polyethylene particles, and at 500 fps for the polystyrene pellets. The field of view for the actual images was $1.85 \times 1.85 \text{ cm}^2$ with a resolution of 512 pixels for Coke and HDPE particles, and $5.84 \times 5.84 \text{ cm}^2$ for the polystyrene particles. During the eductor experiments, the HDPE particles impacted the substrate both normal to the plane and with the substrate held at 70° from the horizontal position.

Figure 5-11: Distribution of HDPE particle velocities in eductor experiment for steel metal plate using 1.13 m³/h air flow

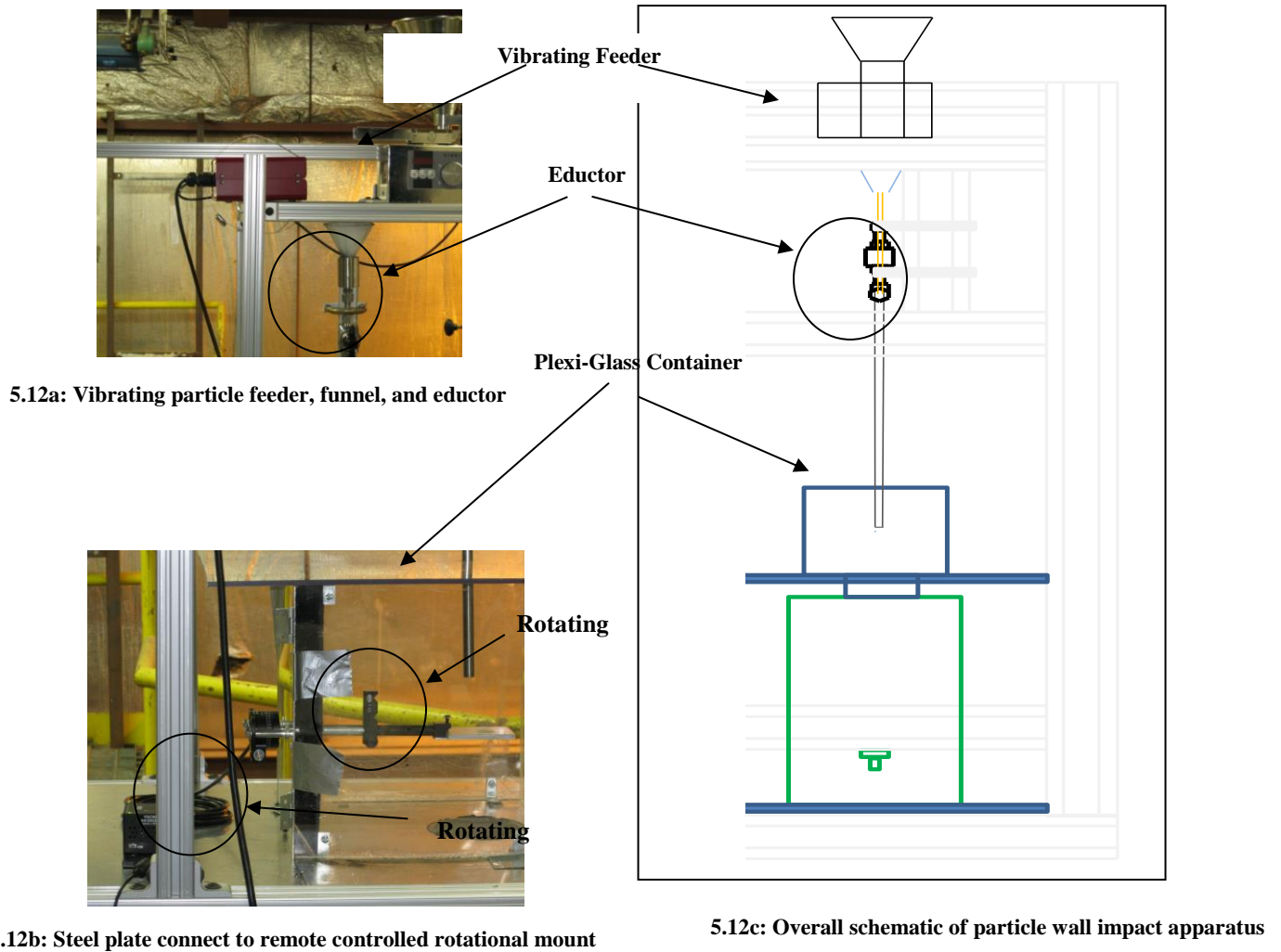


5.2.4 Post-Processing High Speed Video Images

The recorded high speed images were post processed using Image J [88]. Image processing and segmentation (partitioning digital images into multiple segments such as pixels) provided the location of the particle centroids as they collided with the substrate. Subsequently, the particle tracking algorithm developed by National Energy Technology Laboratory [89, 90] was utilized to track the particles before and after collision with the substrate. This state of the art algorithm can track particles from dilute to dense particulate flows and provides a means to measure the detailed statistics of the particle-substrate collisions.

To measure COR, the particle tracks before and after collision needed to be related. In order to accomplish this task, a separate predictive matching algorithm was developed where a search area was defined to locate the particles after their collision with the substrate. The search area was created based on the nature of the substrate and particle, collision angle, and particle velocity. Consequently, the particle trajectory after the collision was related to that before it. Also, since the particle velocity was measured just before and after it collided with the wall, the effects of gas flow, particle interactions, and gravity were negligible. The accuracy of the large statistics pertaining to the particle collision data was manually confirmed by calculating the particle velocities based on their positions in the frame.

Figure 5-12 Apparatus for particle wall impact experiments

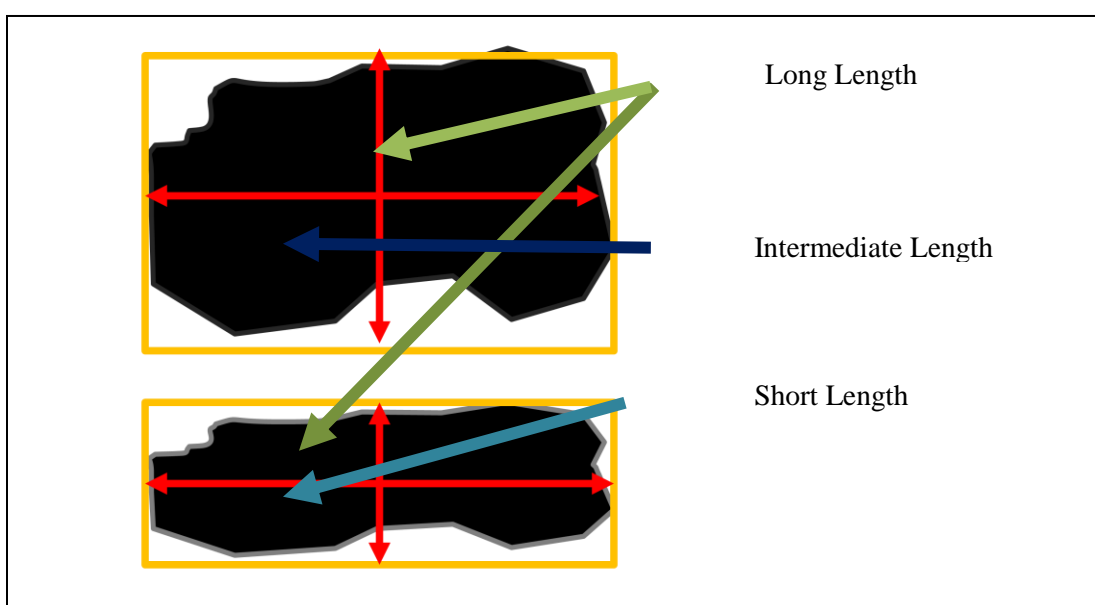


5.2.5 Data Analysis

Each recorded frame was converted to a tiff image file. Particle tracks were applied to the selected particles through a sequence of tiff images using MTrack J, which is a plug-in in the Image J software. This plug-in identifies the x and y position of the particle based on the x and y centroid. Having identified the x and y centroid for each tracked particle, the velocity in the x and y direction for both, the impacting and the rebound phase was calculated based on the frame rate and the particle position. In addition, the COR was calculated based on Equations 5.4a-c. To analyze the influence of the sphericity on the rotational behavior and thus the COR, particles tracks that had the least deviation from the impact angle of 90° were selected for each particle

type for the drop experiments. For these particles, the average deviation was 0.022, 0.063, and 0.13 degrees for HDPE, polystyrene pellets, and Coke, respectively. As a standard method of characterizing the shape of the particle, the degree of equancy, as described by Clayton et al. [91] was used due to the variability of formulas for calculating sphericity and their limitations to certain particle shapes. To determine the degree of equancy, three lengths, termed the short length (S), intermediate length (I), and long length (L), were manually measured based on the scale of the tiff images for two planar faces of each particle.

Figure 5-13: Determination of the degree of equancy



Once the dimensions of the short and long lengths were deciphered from the intermediate length, the ratio of the short length to the long length was calculated to determine the degree of equancy. The radial distance from the origin was measured using the point tool in Image J in terms of the scale of pixels per cm, and was found to be 1.91/512 (cm/pixel) for the Coke and HDPE particles, and 5.84/512 (cm/pixel) for the polystyrene pellets. This value for the radial distance, along with the horizontal velocity based on the particle position as a function of the interval time, was used in equation 5.6 to calculate the planar rotational velocity in the x and y plane. The individual rotational value of each particle was averaged for the total number of particles.

CHAPTER 6 RESULTS AND DISCUSSION

6.1 Particle Impact Experiments

6.1.1 Particle Wall Impact Experiments with High Density Polyethylene Particles

6.1.1.1 Flat Metal Case

Using the particle tracking technique [89], it was observed that the distribution of the impacting angle was rather narrow (Figures 6-1a,c). In contrast, the rebound angle varied over a wide range. Based on the results of the first set of experiments, it was found that the rebound angle varied from less than -40° to more than 40° (normalized) for the metal plate involving the eductor (Figures 6-1b,d). This variation in the rebound angle significantly influenced the measured COR, and may be attributed to the rotation that occurred in two dimensions, or the orientation of the non-spherical particles upon impact, i.e. the particle rebound angle was dependent on the orientation of the particle that contacted the substrate. For the flat metal plate, the particles that were spherical, or close to being spherical and near the center of the jet, demonstrated a tendency to rebound normal to the plate. The COR decreased significantly as the rebound angle varied more than 15° from the perpendicular for the eductor experiment using the steel metal for both cases using 0.28 or $1.13\text{m}^3/\text{hr}$ air flow rate. Again, as shown in Figure 6-1d, the highest COR was at the peak at 0° (normalized). Although the average COR value decreased from 0.68 to 0.64 as the air flow rate increased, the velocity seems to have had a relatively small influence on the overall profile [92].

6.1.1.2 Case for Hard Viscosity Substrate, Soft Viscosity Substrate, and Adhered Particles

In contrast to the flat metal case, the COR was nearly constant in cases where the particles impacted the rough surface with adhered HDPE particles, with the exception of a few outliers, as shown in Figure 6-2. The parabolic profile for the cases involving the adhered particles was flatter than the parabolic profile of the metal plate shown in Figure 6-1a. For the rough plate with adhered particles, the incoming particles hit other adhered particles at different orientations, and only when particles collided in the crevice between two particles, or normal to a particle, did the particles rebound at 90° .

The spread of data for both the silicone-coated substrates was not as well defined as the cases involving the flat steel plate and the adhered particles. The surfaces for both silicone adhesives were slightly concave at the center. Particles hitting at the center of the “soft” silicone substrate were likely to rebound at 90° , while those hitting at the edges rebounded between 45° and 70° due to the concavity of the substrate. This variation appears to have occurred due to the particles rolling along the edges of the silicone. In case of the “hard” silicone substrate, the particles hitting at the center as well as the edges rebounded at an angle other than 90° due to some surface deflection. As a result, a spread of data was obtained as shown in Figures 6-3 and 6.4. In Figure 6-3, the domain for the normalized rebound angle extends from -80° to 40° , while the COR range extends from 0.2 to 0.6. In addition, it was observed that most of the data was clustered between COR values of 0.3 and 0.5. However, as shown in Figure 6-4 for the “soft” silicone substrate, particle impact was less defined with a wide range of COR values between 0.1 to 1, and a domain of 80° to -80° (normalized) for the rebound angle. Overall, the wide variation in rebound angles not only suggested particle rotation but also prompted the decision to perform the drop experiments.

6.1.2 Critical Velocity

Particles adhered to the soft silicone substrate using an air flow rate $0.28 \text{ m}^3/\text{hr}$, and the COR value of 0 was assigned in this case. Moreover, the particles were not observed to rebound until a layer of particles had built-up on the substrate. Such behavior is consistent with the previously reported work of Huan Li et al., who showed that the softer and thicker a film, the lower the COR, and the larger the impact velocity necessary for a particle to rebound from the surface [93]. It is generally believed that particles must exceed a critical velocity in order to rebound from a given surface. The stiffness of the soft silicone adhesive used here was much lower than that of the Tedlar rubber used by Brach and Dunn [59, 65], and is not believed to be totally elastic. Although efforts were made to measure the interfacial surface tension in this study, the particles were too heavy to be attached to the probe used in the adhesive force measurement device.

Figure 6-1a: Distribution of impacting angles for flat metal plate, 0.28 m³/hr air flow

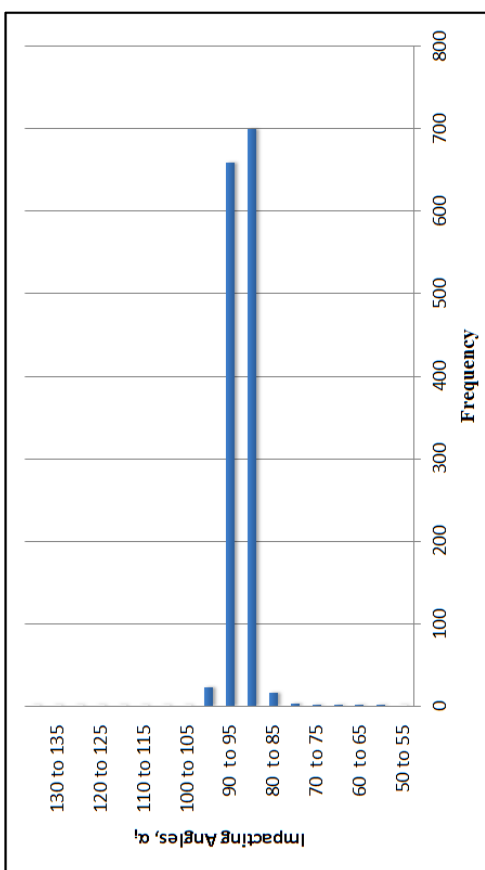


Figure 6-1c Distribution of impacting angles for flat metal plate, 1.13m³/hr air flow

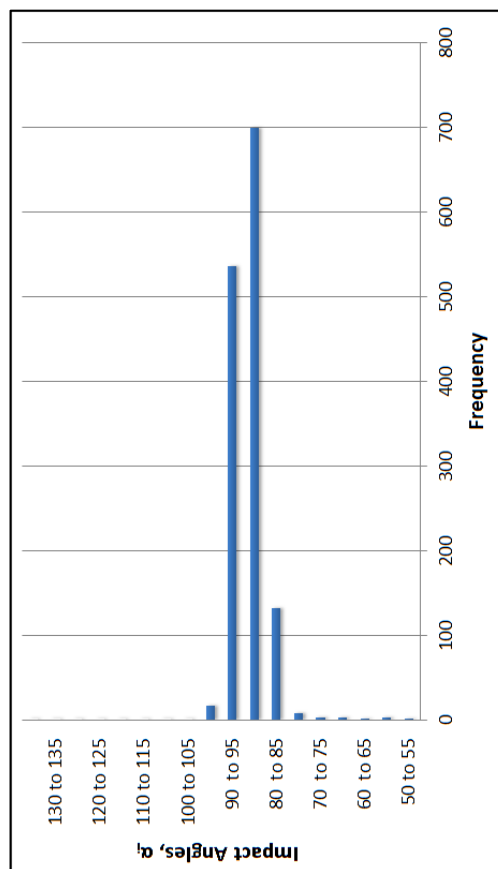


Figure 6-1b: Normal coefficient of restitution versus rebound angle, metal plate, 0.28 m³/hr air flow for normal impact

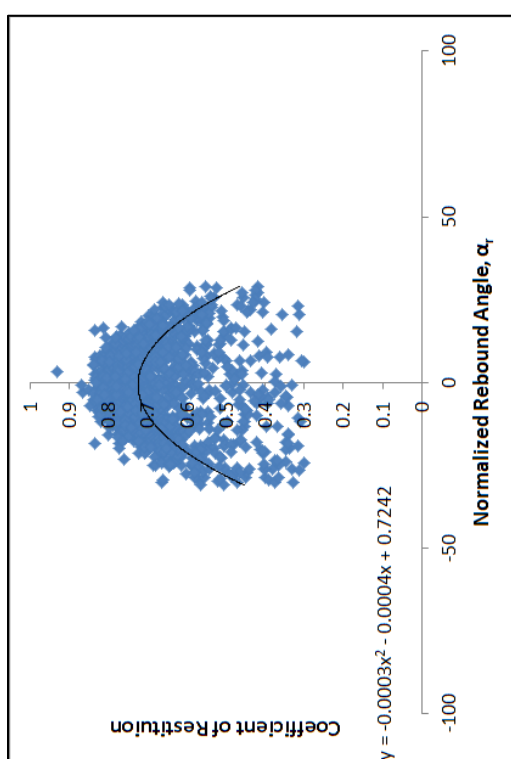


Figure 6-1d: Normal coefficient of restitution versus rebound angle, metal plate, 1.13 m³/hr air flow for normal impact

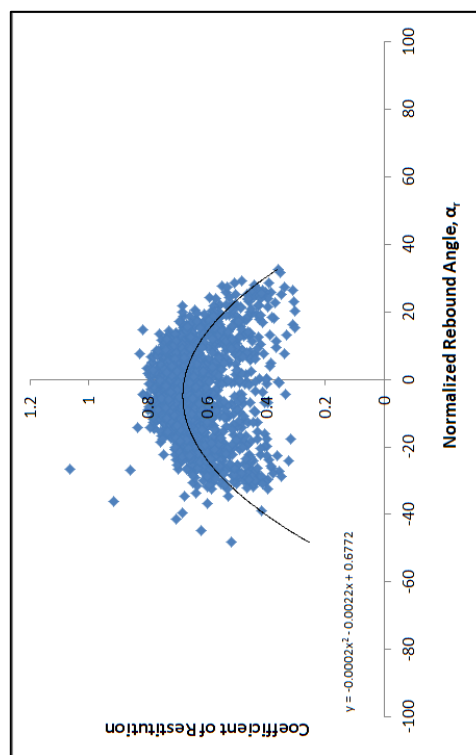


Figure 6-2: Normal coefficient of restitution versus rebound angle for HDPE particles impacting adhered particles using 1.13m³/hr air flow for normal impact

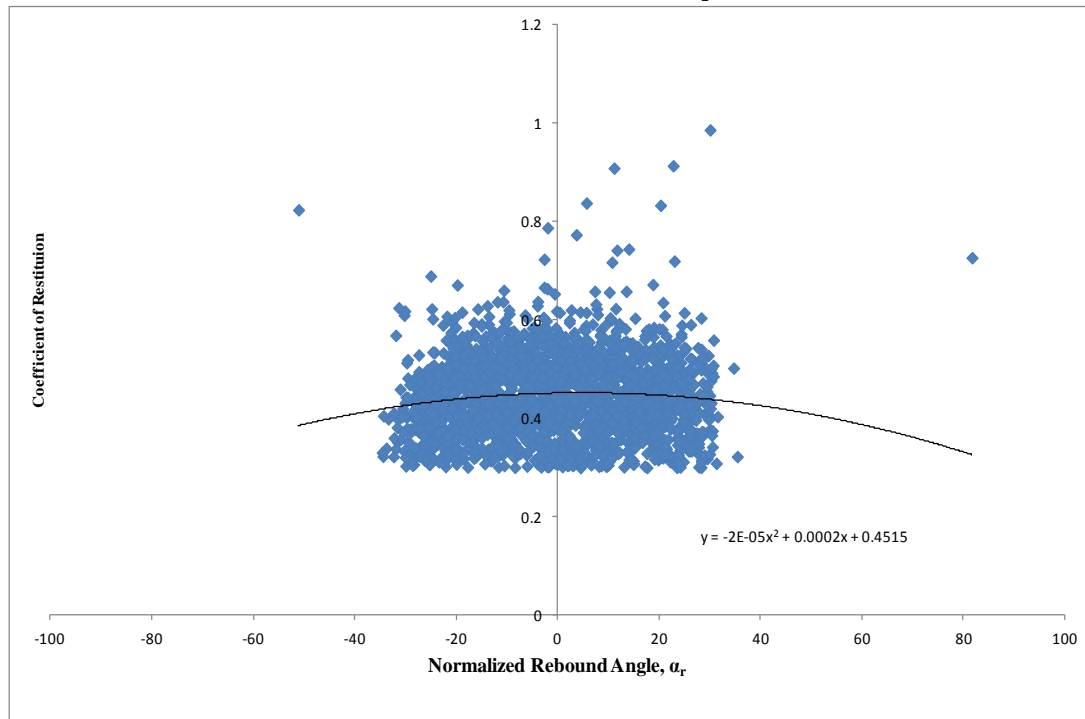


Figure 6-3: Normal coefficient of restitution versus rebound angle for HDPE particles impacting hard silicone using 1.13 m³/hr air flow for normal impact of HDPE particles

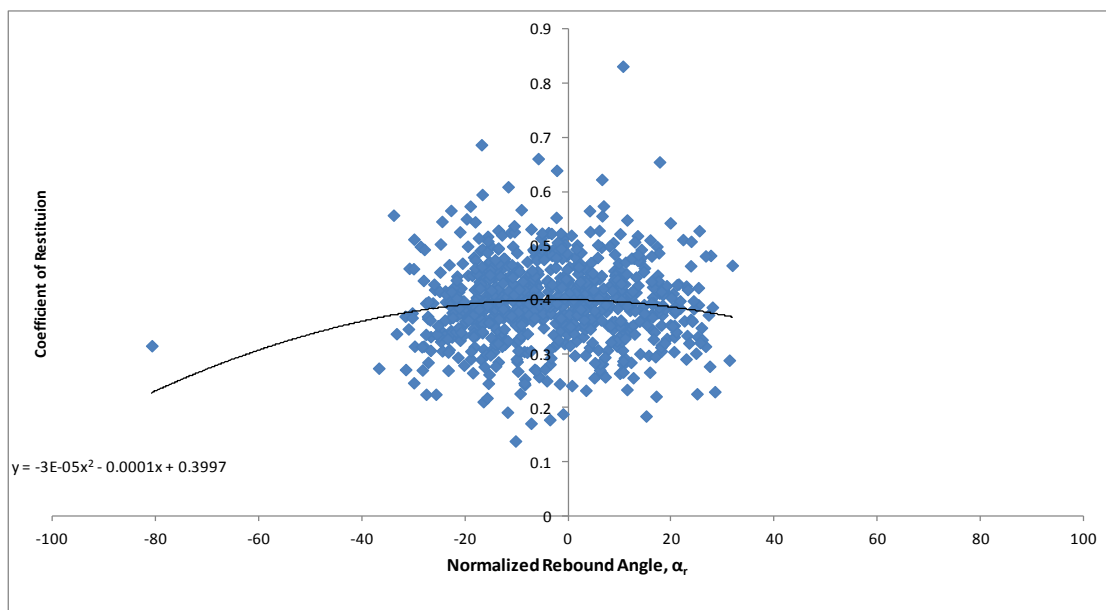


Figure 6-4: Normal coefficient of restitution versus rebound angle for HDPE particles impacting soft silicone using 1.13 m³/hr air flow for normal impact

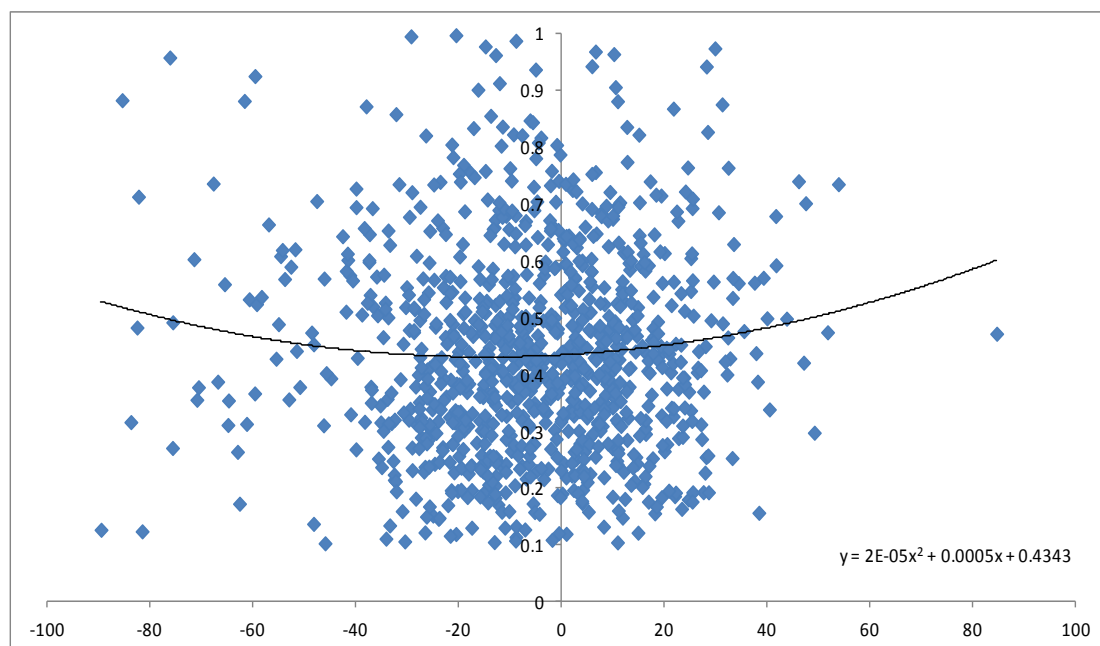


Table 6-1: Summary of average coefficient of restitution for eductor experiments for normal impact using HDPE particles

Case Substrate	Normal Impacting Velocity(m/s) Average/Deviation	Normal Coefficient of Restitution Average/Deviation	Skewness of Restitution Coefficient	Total Particle Count
Steel Plate				
(0.283m ³ /hr)	3.24±0.29	0.68±0.11	-1.14	1407
(1.13m ³ /hr)	6.57±0.85	0.64±0.10	-0.89	1689
Adhered HDPE				
(0.283m ³ /hr)	3.48±0.39	0.44±0.12	0.04	739
(1.13m ³ /hr)	7.62±0.72	0.45±0.08	0.73	2024
“Hard” Silicone				
(0.283m ³ /hr)	3.27±0.75	0.54±0.13	-0.55	114
(1.13m ³ /hr)	7.39±0.96	0.39±0.08	0.34	766
“Soft” Silicone				
(0.283m ³ /hr)	3.43±0.34	0	NA	NA
(1.13m ³ /hr)	7.24±1.18	0.40±0.11	0.33	985

Table 6-2: Summary of average coefficient for eductor experiments for substrate at 70° from horizontal for HDPE particles

Case Substrate	Normal Impact Velocity (m/s) Average/Deviation	Normal Coefficient of Restitution Average/Deviation	Tangential Impact Velocity (m/s) Average/ Deviation	Tangential Coefficient of Restitution Average/ Deviation	Total Particle Count
Steel					
(0.283m ³ /hr)	1.05±0.15	0.66±0.17	2.65 ±0.32	0.86±0.078	614
(1.13m ³ /hr)	2.29±0.33	0.69±0.16	6.97 ±0.34	0.85±0.049	1346
“Hard” Silicone					
(0.283m ³ /hr)	1.14±0.16	0.41±0.25	3.45 ±0.42	0.76±0.13	571
(1.13m ³ /hr)	2.50±0.41	0.69±0.16	7.58 ±0.60	0.72±0.09	139
“Soft” Silicone					
(0.283m ³ /hr)	1.29±0.16	0.64±0.23	3.54 ±0.65	0.72±0.19	304
(1.13m ³ /hr)	2.61±0.33	0.57±0.25	7.16 ±0.40	0.67±0.14	505

The critical velocities derived through previously published works are based on the elastic behavior [94, 95]. However, the nature of interaction between the HDPE particles and the soft substrate is believed to be viscoelastic, as are the collisions of the char particles with the refractory at high temperatures [44]. Although the damping coefficients C_A and C_H have been redefined as adhesive and repulsive, respectively [96], no investigation has been pursued to quantify these coefficients outside of fitting existing particle impact data to the dynamic model. In other words, there has not been an attempt to quantify the damping coefficients in terms of the measurable properties of the particles and the surfaces. For elastoplastic impact, yield velocity has been used as the limiting velocity for which rebounding does not occur. However, to determine the yield velocity, the variable for the yield strength is based on the properties of the particle and not the surface. In cases where the surface is softer than the particle, such as in the case of soft silicone, the sensitivities of various properties of the particle and the surface must be examined in order to assess the accuracy of the existing equations for the critical velocity. However, such an effort would require various adhesives to exhibit the same behavior of no rebound, and is beyond the scope of this work.

6.1.3 Drop Experiments

For the drop experiments, there was a strong correlation between the geometry of the particle and the rotational velocity, based on the analysis of the relationship between the particle rotational velocity and the degree of equancy as shown in Figure 6-5. The value of the COR, e decreased by nearly one-third with a decrease in the degree of equancy and an increase in the measured rotational rate, as shown in Figures 6-6 and 6-7. The value of e_n is linearly dependent on the degree of equancy as defined by Clayton et al. [91]. This dependency is not only supported by the plot showing the correlation between the degree of equancy and the average rotational velocities, but also by the images shown in Figures 6-8 to 6-11 and Figures 6-12a to 6-12c. As evidenced by the tracks, the more the irregularity in the shape of the particle, the higher the deviation of the rebounding angle from the impacting angle normal to the plane. However, the correlation between the standard error of rotational velocities and the average calculated rotational velocity was even more suggestive (error bars in Figure 6-5), since this uncertainty indicated that decreasing equancy resulted in increasing the variance in the rotational velocity, in

addition to increasing the average rotational velocity. The degree of equancy and the particle orientation relative to the surface have a strong influence on the rotational velocity after rebound. However, rotational velocity as a second factor was considered. Rotational velocity prior to rebound also influences the rotational velocity after rebound through the moment coefficient. The HDPE and Coke particles had wide particle size distributions (Table 6.1), and the size differences would exacerbate, through Equation 5.6 the effect of equancy and particle orientation on the variability of rotational velocities after rebound.

6.1.4 Variance in Impact Angle

The results showed that the coefficient of restitution did not change significantly for different velocities (Table 6.1 and 6.2). During oblique impact, the particles were observed to be moving (either rolling or sliding) across the substrate. However, such sliding motion was not observed upon normal impact. This combination of sliding and rolling is demonstrated in the video images for the case where the plate was positioned at 70° to the horizontal (Figure 6-13). The propensity of the particles to slide was probably due to the relatively low coefficient of friction on the surface. It was difficult to observe the particles near the wall because the images became blurry in that region. The HDPE particles were thought to be mostly sliding across the different substrates. There may have been some rolling involved; however, the shape of these particles made it difficult to visualize. The Coke particles were the easiest to observe in a rolling motion because of the rough geometry of these particles. In addition, sliding Coke particles were also observed. The sliding behavior contradicts the notion of a critical angle requirement as specified by Kim and Dunn [55], which is based on the analysis of spherical particles. However, their analysis on the existence of a threshold that delineates between particle rolling and sliding does not consider the contribution of gross slip which was investigated by Maw et al. [97]. The behavior of simultaneously sliding and rolling as described by Maw et al. appears to be more applicable to this study using non-spherical particles [97]. The geometry, and therefore, the degree of equancy and the orientation of the particles upon impact are thought to have interfered with the propensity for particles to roll along the surface at steep impact angles.

Overall, the steel plate demonstrated the highest coefficient of restitution followed by the hard silicone adhesive surface, probably due to the differences in the Young's modulus of

elasticity. However, at the lower air velocity, the soft silicone adhesive surface showed slightly higher coefficient of restitution than the hard silicone adhesive surface. Again, this behavior is believed to be due to the particle sliding across the surface of the soft silicone adhesive as compared to the hard silicone adhesive [92].

Figure 6-5: Average calculated rotational velocity versus degree of equancy of metal plate impact

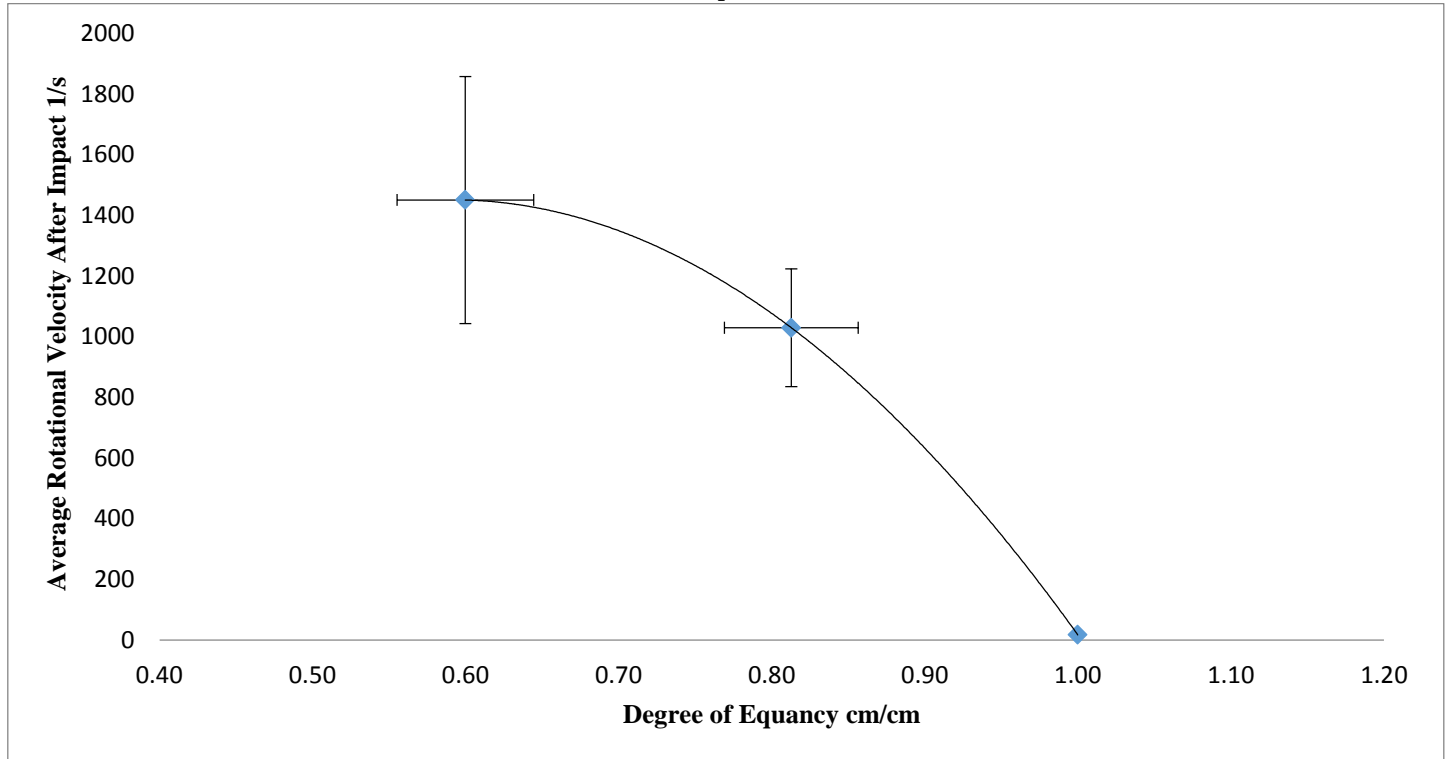


Figure 6-6: Average rotational velocity versus normal coefficient of restitution of particle impact upon metal plate

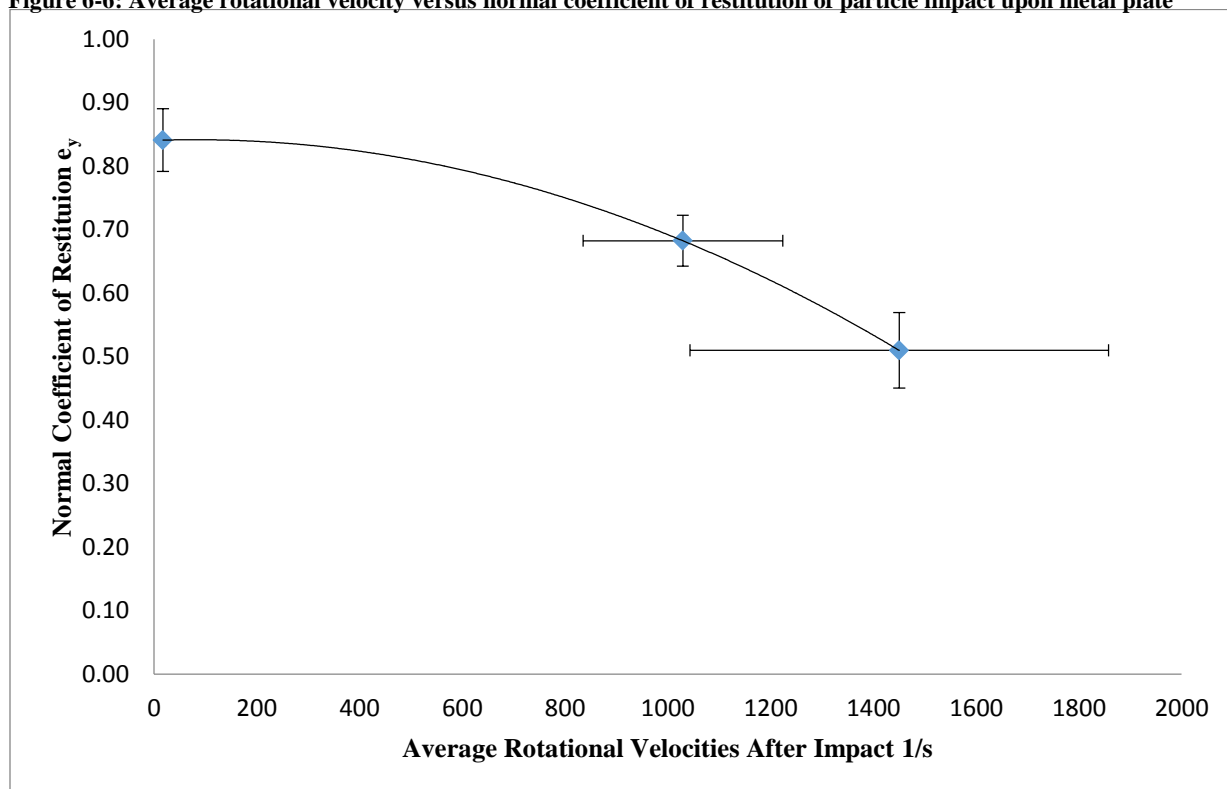


Figure 6-7: Normal coefficient of restitution versus degree of equancy

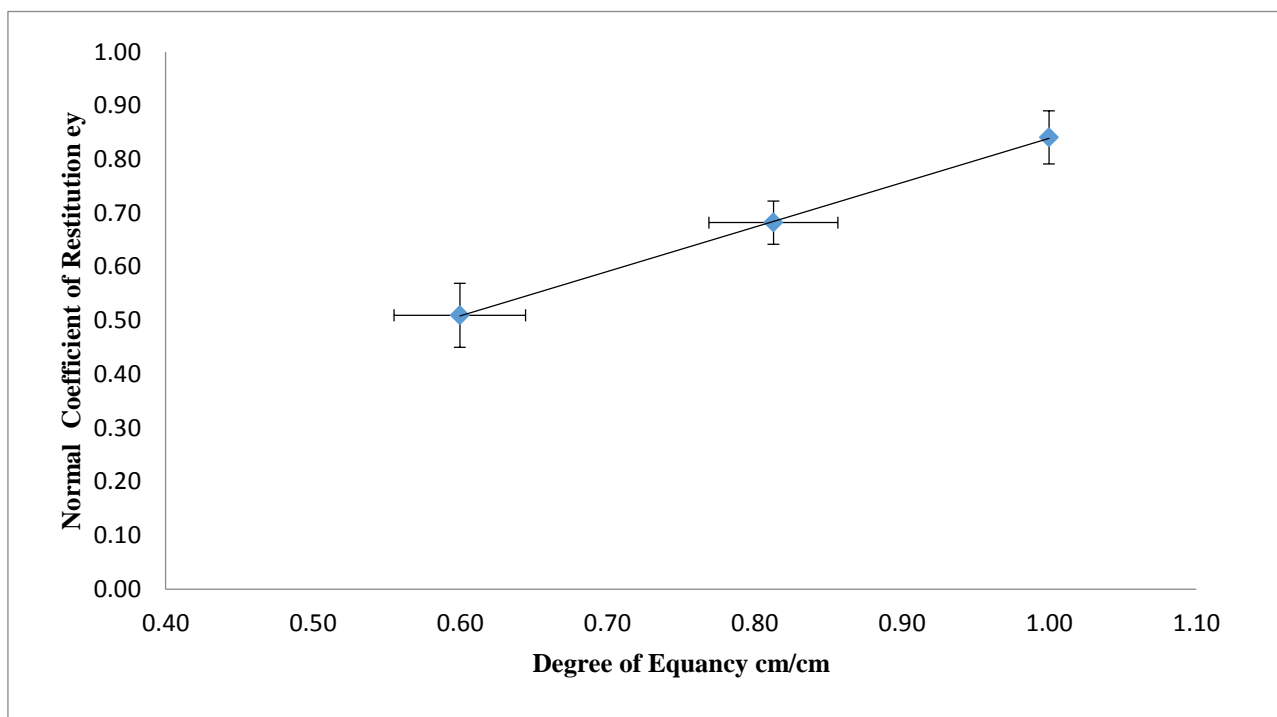


Figure 6-8: Polystyrene pellet rebounding normal to steel plate

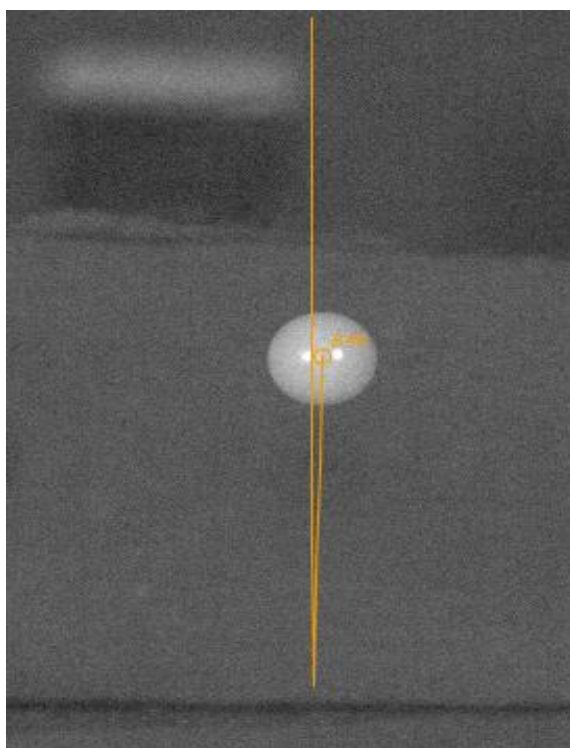


Figure 6-9: Polyethylene prior to impacting steel plate

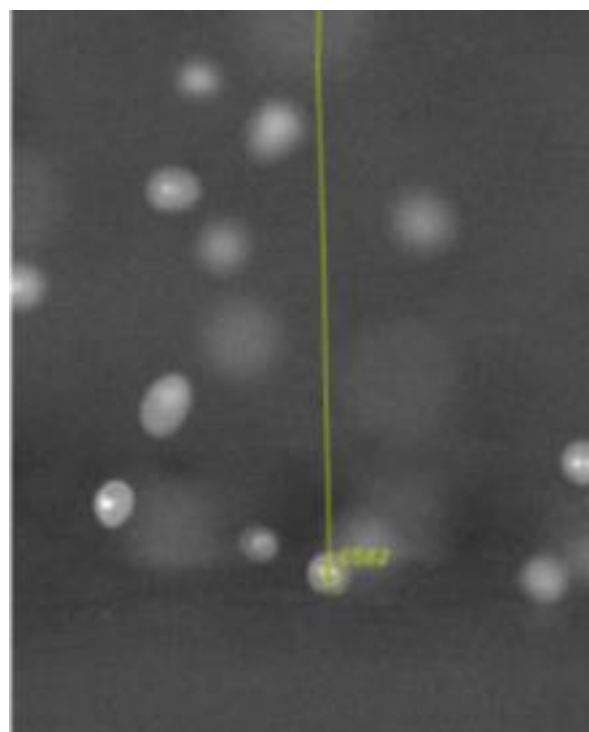


Figure 6-10: Polyethylene rebounding from steel plate

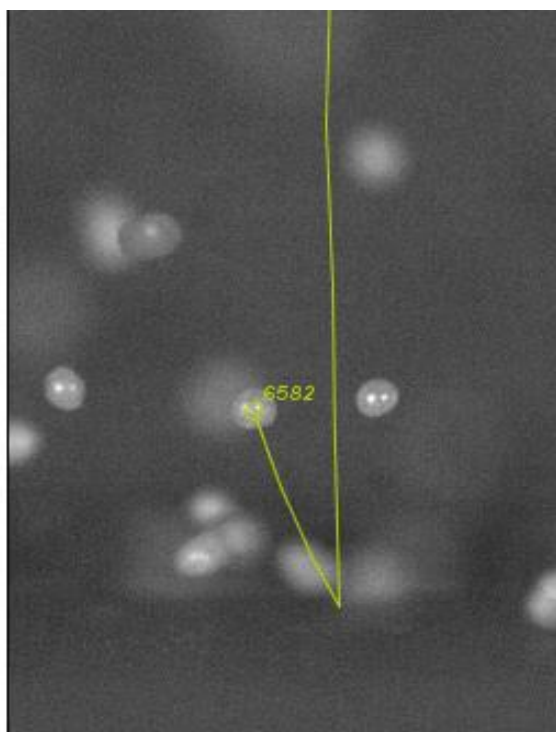


Figure 6-11: Coke particle rebounding from steel plate

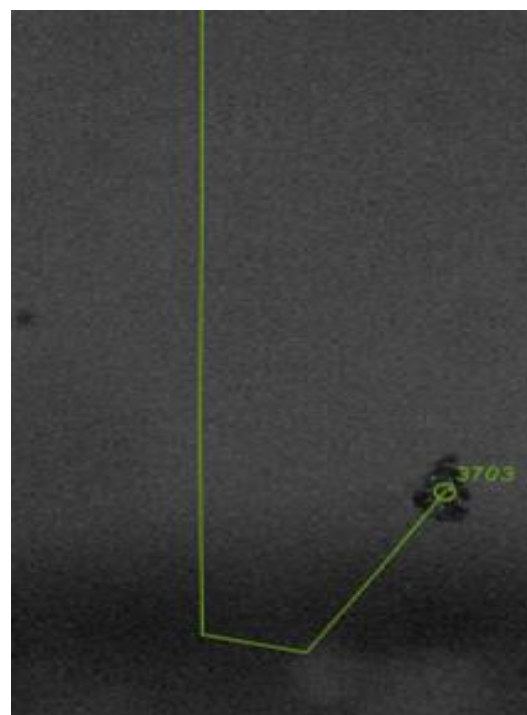


Figure 6-12a-c: Sequence of coke particle impacting and rebounding from steel plate

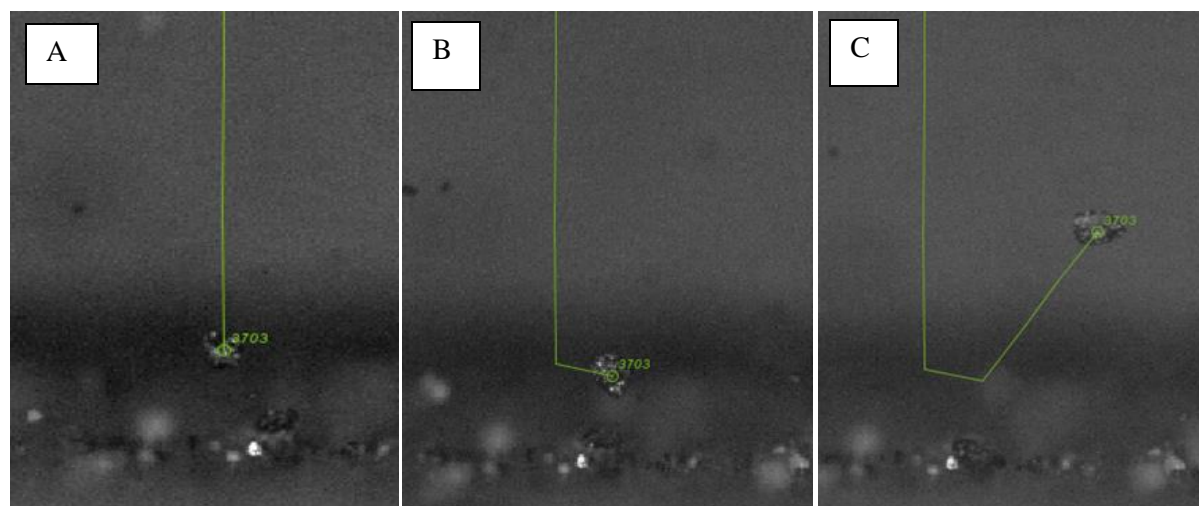
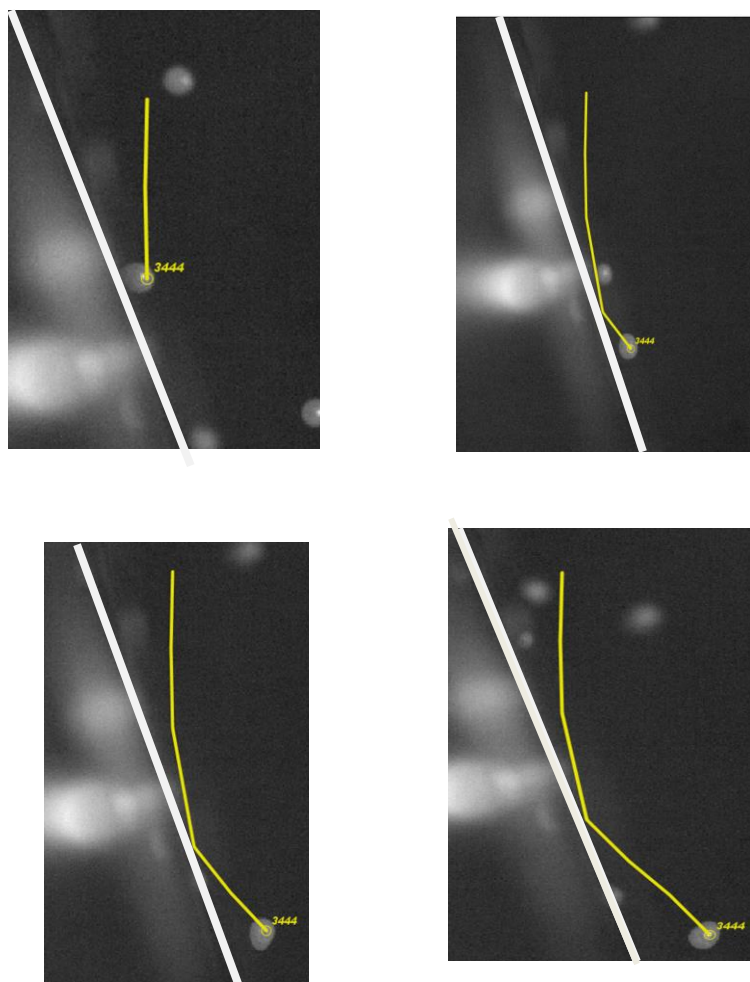


Fig 6-12: Coke Particle (A) prior to normal impact onto steel plate (B) rebounding and rotating, and (C) following an off-normal trajectory.

Figure 6-13a-d: Sequential images showing trajectories of HDPE particles impacting soft silicone adhesive at 70° from the horizontal using 1.13 m³/hr air flow



6.1.5 Analysis of Variance (ANOVA)

ANOVA was performed to assess the relative influence of the independent variables on the COR, e . To assess the dependent parameter, e_n , the independent parameters included the effects of the particle modulus of elasticity, surface modulus of elasticity, normal velocity, the degree of equancy (\emptyset), and the angle of impact. The independent parameters were transformed, thereby making them dimensionless to allow simplification of the resulting expression. The Young's modulus of the particle was added to the Young's modulus of the substrate, and the sum was then divided by the Young's modulus of elasticity of steel to formulate the dimensionless elasticity E' :

$$E' = \frac{E_p + E_s}{E_{\text{steel}}} . \quad (6.1)$$

Similarly, the velocity was made dimensionless by dividing it by the terminal velocity. The data pertaining to the average COR obtained using HDPE particles for normal impact as well as the impact when the substrate was positioned at 70° from the horizontal (as reported in Tables 6-1 and 6-2) was analyzed using ANOVA. It should be noted that mean values were used to represent the several hundred individual measurements since the distributions of each of these parameters could be approximated to be normally distributed. The number of test points included in this analysis was 10, each representing a population of impacts for a given particle, surface, velocity, and equancy. F-test was conducted on each variable after formulating a general linear model using only the main factors, V_n/V_t (the ratio of normal velocity to terminal velocity), E' (Young's modulus of elasticity), and \emptyset . The statistical analysis tested the null hypothesis whether the value of e_n was the same at high and low levels of each of these main factors, or not. Based on the F-values, the null hypothesis could be rejected with 95% confidence for E' and \emptyset . The analysis showed that E' and \emptyset had probabilities of only 0.0004 and 0.0005, respectively, given that the e_n was the same at different levels. Thus, E' and \emptyset were identified as being statistically significant at the 95% confidence level. On the other hand, the impact velocity was not statistically significant with a probability of 0.1755, given that the e_n were the same at high and low levels of V_n/V_T . Statistically, the null hypothesis could not be rejected in this case; however, theoretical studies indicate that the higher impact velocity reduces e_n when the spherical particles have a viscoelastic impact on the surface. Moreover, the magnitude of the

impact velocity was relatively small over the range of velocities relevant to the char gasifier wall impacts, but the trend is still consistent with the theory. It is believed that the variations in the impact angle, particle shape, and surface roughness were sufficient to mask such effect, but that the trend is still valid. Thus, this parameter $[V_n/V_T]$ was included in development of a heuristic expression for e_n . The linear regression equation in Equation 6.2 was attained:

$$e_n = 0.202E' + 0.899\phi - 0.034 V_n/V_T - 0.229 \quad \text{for } 1 \text{ m/s} < V_n < 8 \text{ m/s} . \quad (6.2)$$

The analyses showed that the Equation 6.2 has a R^2 value of 0.94, indicating that 94% of the variance in the data can be explained by Eq. 6.2. As a result of including the velocity parameter, the variance in the model increased by 2%, from 92 to 94 %. It must be noted that there was some extent of confounding in the test design such that the only truly smooth surface was the steel plate, while the HDPE surface was inherently rough and the silicone substrates were imperfectly smooth. In addition, the shape factor was confounded with differences in the diameter and the density of the particles - the largest particle was also the most spherical one. The relatively large coefficient for the shape parameter highlights the importance of this parameter in determining the COR. This expression was developed to be used in CFD models for a boundary condition when naturally occurring, non-spherical particles collide with the wall.

In CFD models, many of the collisions are not normal to the wall. In addition, the particle transfers a portion of the momentum in the tangential direction, a phenomenon that has been measured in terms of the tangential restitution coefficient, e_t . Therefore, ANOVA was also performed on the e_t parameter, where E' was the only significant independent variable tested. The data analyzed included six test points taken from Table 6.2 using an impact angle of 70° from the perpendicular. The null hypothesis that the value of e_t was unaffected by different levels of E' could be rejected. A probability of only 0.0077 was calculated, which indicates that e_t at different levels of E' would lie within the standard F-distribution. In other words, the elasticity parameter was statistically significant at the 95% confidence limit on the dependent parameter, e_t . The analysis also showed that the root mean square error was 0.032. Moreover, the velocity was not found to be statistically significant. Since the different particle equequancy values were not tested at non-normal angles of impact, we could not test its effect on e_t . As a result of the variance of the E' , the following regression equation in Equation 6.3 was attained:

$$e_t = 0.139E' + 0.716 \quad \text{for } 0.9 \text{ m/s} < V_n < 8.5 \text{ m/s} . \quad (6.3)$$

In this regression model, a R^2 value of 0.86 was obtained, indicating that 86% of the variance was explained by this single parameter. This expression also indicates that for small values of E' , the tangential velocity was reduced by over 67% of the original velocity. Such a reduction in the tangential velocity could be attributed to the losses in energy due to particle rotation or sliding. An increase in elasticity resulted in preserving more of the tangential component of the impact velocity. Since the shape affects the rotational velocity for rebounding particles, it is expected that this parameter will also have a similar influence on the tangential component of coefficient of restitution as well.

There was essentially no sensitivity of the normal COR with respect to the Young's modulus of the particle. On the other hand, the normal COR exhibited a slight sensitivity to the surface modulus of elasticity. Similarly, the tangential COR was more sensitive to the surface modulus of elasticity than to the particle modulus of elasticity as shown in Equation 6.3. In addition, the effect of velocity on the normal COR was less than that of the surface modulus of elasticity, but it was higher than that of the particle modulus of elasticity. Hence, the velocity was not a significant variable. On the other hand, the degree of equancy had the greatest influence on the magnitude of the normal COR. These results indicate that, overall, the sensitivity analysis is in agreement with the statistical significance of each variable.

6.2 Model Development

6.2.1 Particle Entrapment Model Development

6.2.1.1 Force Balance

Whether the particle penetrates the slag layer and becomes entrapped depends on the inertial forces of the particle relative to the viscous forces of the slag layer. The resistance of this viscous force to the inertial force results in displacement within the slag layer. For a particle penetrating a Newtonian liquid slag layer as in Figure 6-14, the force balance is shown in Equation 6.4-6.5. According to the scenario laid out in Figure 6-14, $f(t)$ is the external time dependent applied force and $f_1(t)$ is the time dependent force exerted by the fluid on the mass due to motion on the mass. These relationships can be expressed as,

Figure 6-14: Slag displacement for a Newtonian fluid

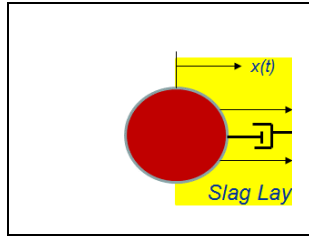
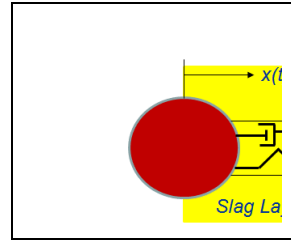


Figure 6-15: Slag displacement for a Bingham fluid



$$m \frac{d^2x}{dt^2} = f(t) + f_1(t), \text{ where } f_1(t) = -K_0 M \frac{d^2x}{dt^2} - C_f \frac{dx}{dt}, \quad (6.4)$$

$$(m + K_0 M) \frac{d^2x}{dt^2} - C_f \frac{dx}{dt} = f(t), \quad (6.5)$$

where K_0 is the “added mass” coefficient that is a function of the shape of a rigid particle for the displaced slag, M is the mass of the displaced slag, and C_f is the drag coefficient. In case of Bingham fluid, where the slag is non-Newtonian, a stiffness element is included to represent the stiffness of the slag layer. In this case, the force balance is represented as

$$(m + K_0 M) \frac{d^2x}{dt^2} - C_f \frac{dx}{dt} + kx = f(t), \text{ with stiffness } k = \frac{AE}{L}. \quad (6.6)$$

6.2.1.2 Cases

To determine the probability of a particle penetrating a slag layer, the SG4PS1 fraction was selected as the model particle due to its density and size in the particle size distribution. The slag composition was then determined by using FACTSAGE by Thermfact/CRCT in Motreal, Canada and GTT Technologies in Aachen, German, which predicted the slag and transformed phases of the minerals based on the Gibbs minimization principle in Equation 6.7:

$$G = \sum_{Ideal\ Gas} (g_i^\circ + RT \ln P_i) + \sum_{\substack{Pure \\ Condensed \\ Phases}} n_i g_i^\circ + \sum_{\substack{Solution_1 \\ Solution_2}} n_i (g_i^\circ + RT \ln X_i + RT \ln \gamma_i) + \dots \quad (6.7)$$

The density of the slag (ρ_{slag}) was determined by dividing the molar weight (Mw_{slag}) of the slag by the molar volume (V_{P,T_r}) of the slag:

$$\rho_{slag} = \frac{Mw_{slag}}{V_{P,T_r}}, \quad (6.8)$$

where V_{P,T_r} was determined through an empirical formula derived by Ghiorso [98]:

$$V_{P,T_r} = V_{0,T_r} e^{\alpha(T-1673)}, \quad (6.9)$$

$$V_{0,T_r} = \sum n_i \bar{v}_{i,T_r}. \quad (6.10)$$

Here, V_{0,T_r} is the total initial molar volume at the reference temperature, n_i is the number of each slag oxide component, and \bar{v}_{i,T_r} is the molar volume of each slag oxide component.

The viscosity was calculated using the Urbain model at 1700 K. The two particle velocities chosen were 2 m/s and 8 m/s. Table 6-3 shows the viscosity calculated based on the slag composition predicted for each SG4 of SF 1.

Table 6-3: The Slag density and viscosity calculated based on the slag composition for each specific gravity

Slag Mixture	Slag Density (kg/m ³)	Viscosity (Pa*s)
SG 1, SF4	2640	137.73
SG 2, SF4	2110	114.04
SG 3, SF4	2270	45.07
SG 4, SF4	2680	0.54

Based on these results, there was no displacement for the SG4 SF 1, which is the largest and heaviest particle in the population for even the slag composition with the lowest viscosity, which is SG 4 (listed in Table 6-3).

Figure 6-16: Displacement and velocity of SG4 PS1 fraction penetrating SG 4 slag with a velocity of 2 m/s

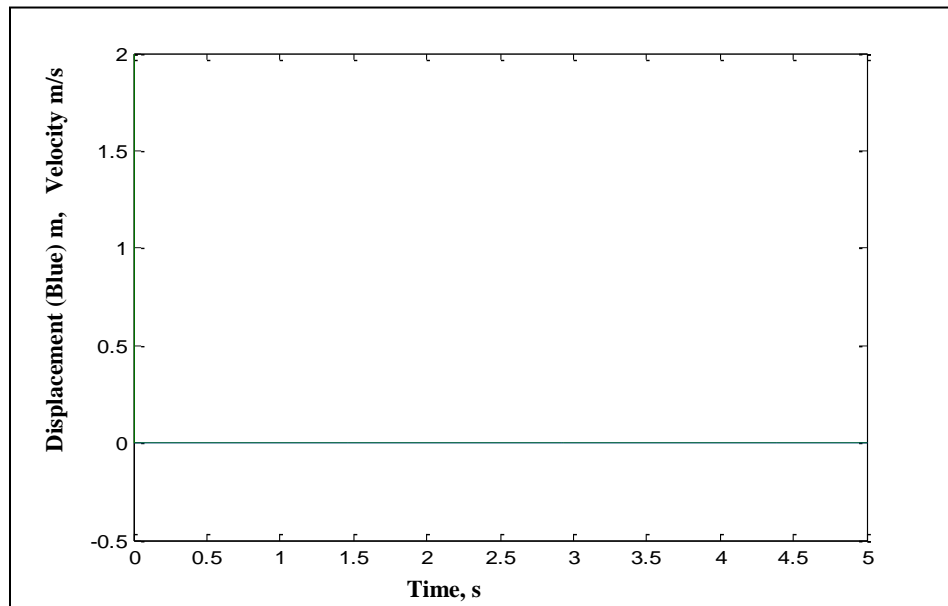
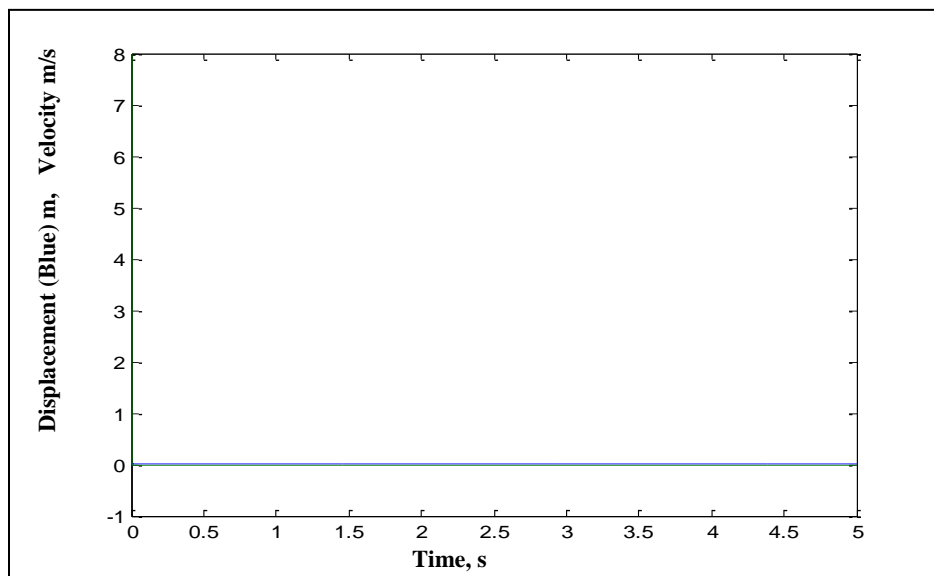


Figure 6-17: Displacement and velocity of SG4 PS1 fraction penetrating SG 4 slag with a velocity of 8 m/s



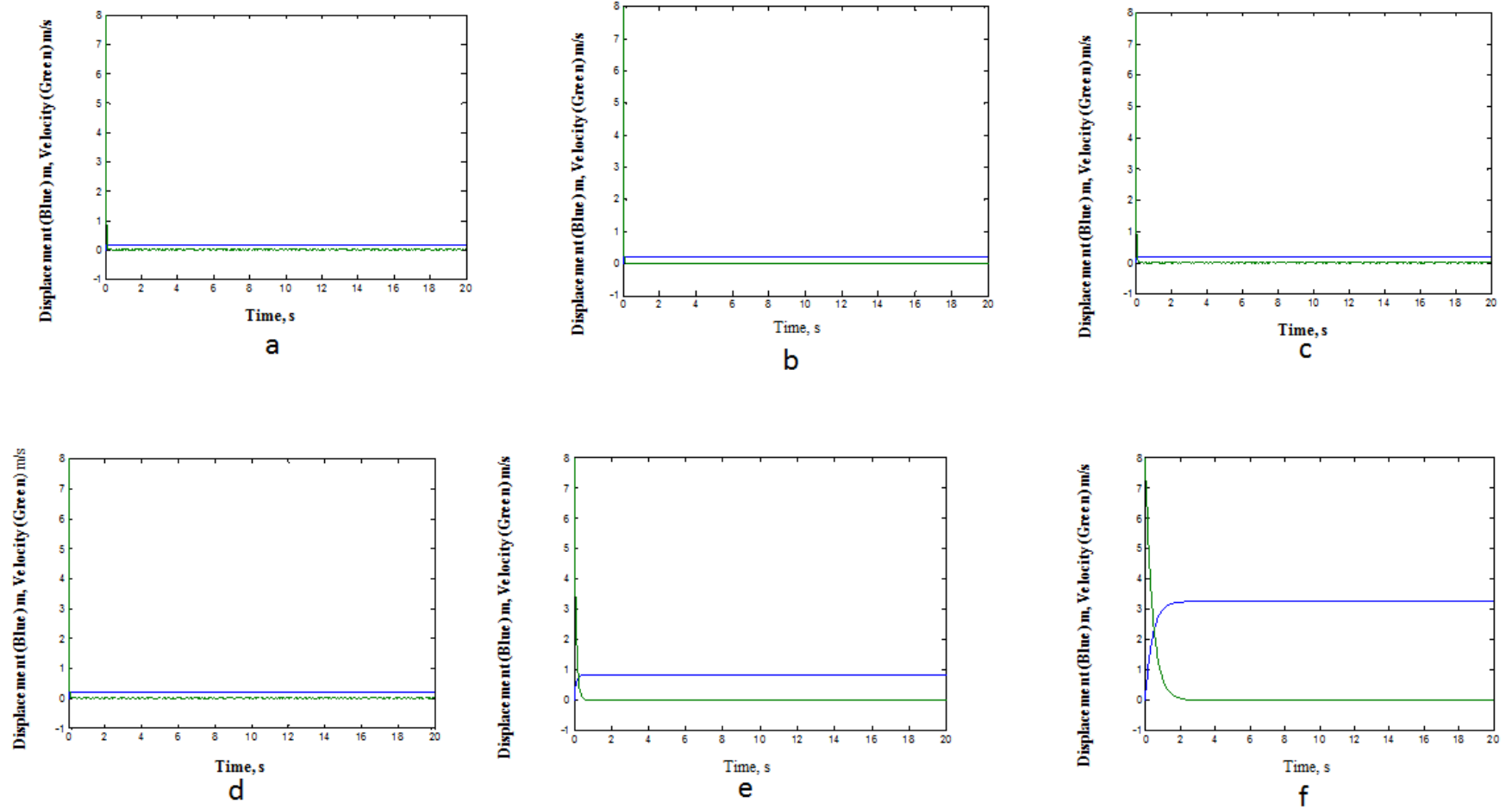
6.2.2 Sensitivity Analysis

Due to the lack of displacement of the SG4 SF1 particle in the slag, a sensitivity analysis was performed using low viscosity butane (5.84 Pa*s) with different metals having a radius of 8 mm and a density of 520 kg/m³ as shown in Table 6-4 (Figure 6-18a-c). Using molybdenum as the material of choice, the radius was increased to determine the influence of the size on the displacement. Based on the displacement results of the SG4 particle against each slag representing the composition of each of the average SG composition and the sensitivity analysis, the defining parameter of whether a particle penetrates the slag layer is the ratio of the drag coefficient to the sum of the mass and added mass ($C_f/(m + K_0M)$). When the drag coefficient is increased, the viscous forces are higher. Therefore, the motion into the slag layer becomes more damped. On the other hand, when the mass of the particle increases the motion becomes less damped. Because SG4 in the particle form has the highest specific gravity, while the SG4 slag has the lowest viscosity, it has been concluded that none of the particles in the population had enough inertia to penetrate the slag layer. Therefore, the particles either adhere to the surface or rebound from it.

Table 6-4: The particle properties for Figure 18a-f penetrating a slag layer with viscosity of 5.48 Pa*s and density of 520 kg/m³

No.	Metal	Metal * Density (kg/m ³)	Particle Mass (kg)	Particle Diameter (mm)
a	Titanium	4500	9.65E-3	8
b	Steel	8000	1.72E-2	8
c	Molybdenum	10188	2.18E-2	8
d	Molybdenum	10188	2.18E-2	8
e	Molybdenum	10188	2.18E-2	16
f	Molybdenum	10188	2.18E-2	32

Figure 6-18a-f: Displacement and velocity versus time for conditions in Table 6.4



6.3 Conventional Methods of Sticking

6.3.1 Mineral Transformation and Liquid Fraction

To draw a correlation between the deposits on the gasifier walls and original minerals in the parent coal, mineral transformation must be addressed. For the Bailey coal, which is a Pittsburgh 8 coal, the four dominant minerals are illite, quartz, kaolinite, and pyrite. The most dominant minerals due to transformation seem to be the leucite (KAlSi_2O_6) and mullite ($\text{Al}_6\text{Si}_2\text{O}_{13}$), which transformed from illite and kaolinite, respectively, according to Factsage predictions (Figure 6-19 to 6-22). A previous study has described illite transforming to semi-metallite at ~ 550 K, while the second reaction of the semi-metallite to metallite occurred at ~ 900 K [99]. However, it has been reported that dehydroxylation occurs between 873 - 973 K [100]. At higher temperatures, metallite dissolves in a glassy phase, while mullite begins to form and persist at 1700 K [99]. However, illite has been reported to melt at lower temperatures due to the presence of iron impurities. For kaolinite, the decomposition occurs at 600 K due to the release of water leading to the formation of metakaolinite, which converts to mullite at higher temperatures (1800 K) [99]. Regarding leucite formation, previous predictions based on oxyfuel combustion of bituminous coals suggested the probability of such formation due to decreasing char particle temperature [101]. FactSage predictions suggest its stable formation up to 1600 K in two specific gravities while leucite has been reported to melt at approximately 1318 K [101]. Cordierite ($\text{Mg}_2\text{Al}_4\text{Si}_5\text{O}_{18}$) and anorthite ($\text{CaAl}_2\text{Si}_2\text{O}_8$) are formed as minor phases up to 1400 K. Previous FactSage modeling for the crystallization of coal ash slags has predicted the stability of cordierite from 1423 to 1573 K [102]. This difference in the temperature range is probably due to the amount of calcium in the coal ash slag when Yuan's method is applied to the particles employed in this work [102].

Of particular interest is the difference in the iron phases between SG 1 and SG 4 shown in Figure 6-19 and Figure 6-22. Iron carbide forms in SG 1 while magnetite (Fe_3O_4), pyrrhotite (FeS), and hercynite (FeAl_2O_4) forms in SG 4. This difference may be attributed to the variability in the amount of carbon in SG1 as compared to SG4, which has predominantly pyrite. Previous work on the transformation of extraneous pyrite has shown that pyrite decomposes to pyrrhotite, which leads to a Fe-S-O melt upon oxidation [103]. The mixture then gets oxidized to magnetite, and then finally, hematite [104]. However, pyrrhotite in the char matrix does not

begin to oxidize until it is exposed by a receding surface and can mix with silicates [103]. Among the boiler deposits, hematite was found to be the dominant iron oxide, although both hematite and magnetite were reported as the products of pyrite that have traveled through the drop-tube reactors [105]. The formation of hercynite has been reported as a result of the reaction between FeO and SiO₂ at 1273 K under CO₂/CO conditions [106]. Therefore, the formation of pyrrhotite, magnetite, and hercynite from pyrite as predicted by FactSage is consistent with previous studies. Although condensation may influence the probability of certain mineral transformation within the char particles for minor species, FactSage predictions suggest that different phases of the same mineral can develop between different specific gravities due to the magnitude of the presence of other minerals. This difference in mineral transformation cannot be accounted for in bulk composition. Combined with modeling fragmentation, coalescence, and condensation, incorporating mineral transformation can lead to more precise predictions of the slag composition based on the original particle size distribution.

6.3.2 Sticking Probability due to Viscosity and Liquid Slag Fraction

To determine the probability of sticking due to viscosity, the reference viscosity of 5 log₁₀ Pa*s based on the ash characterization study of Van Dyk was used [107]. Because the reference viscosity is used to indicate sticking, the probability of sticking is in the range of 0.6 at ~1250 K, to 1.0 at ~1700 K. Slag of any specific gravity approached the sticking probability of 1.0 in a descending order of the specific gravity shown in Figure 6-23. This is likely due to the fact that the amount of iron increased with an increase in the specific gravity of the particle population. The reduction in viscosity and the increase in sticking probability coincides with the fact that iron acts as an amphoteric material as compared to silicon oxide, which act as a glass former. At the same time, the liquid fraction of the slag of any specific gravity increases as a function of temperature. Figure 6-24 shows the slag fraction of the minerals and the slag. In each case, there is convergence above 1500 K. The liquid fraction in the case of SG1 decreases and then increases due to the formation of iron carbide. Meanwhile, the liquid fraction in SG4 shows the sharpest increase of slag fraction due to the pyrite. Overall, the relative content of liquid fraction and solid material is consistent with the probabilities of sticking that have been predicted based on the reference viscosity. However, the reference viscosity itself is based on bulk ash and

not on the critical viscosity of each particle size and density cut. With respect to the size fraction, there is little discernible difference in the sticking probabilities as shown in Figures 6-25 to 6-28.

Figure 6-19: Mineral transformation versus temperature for BSG1 and PS1

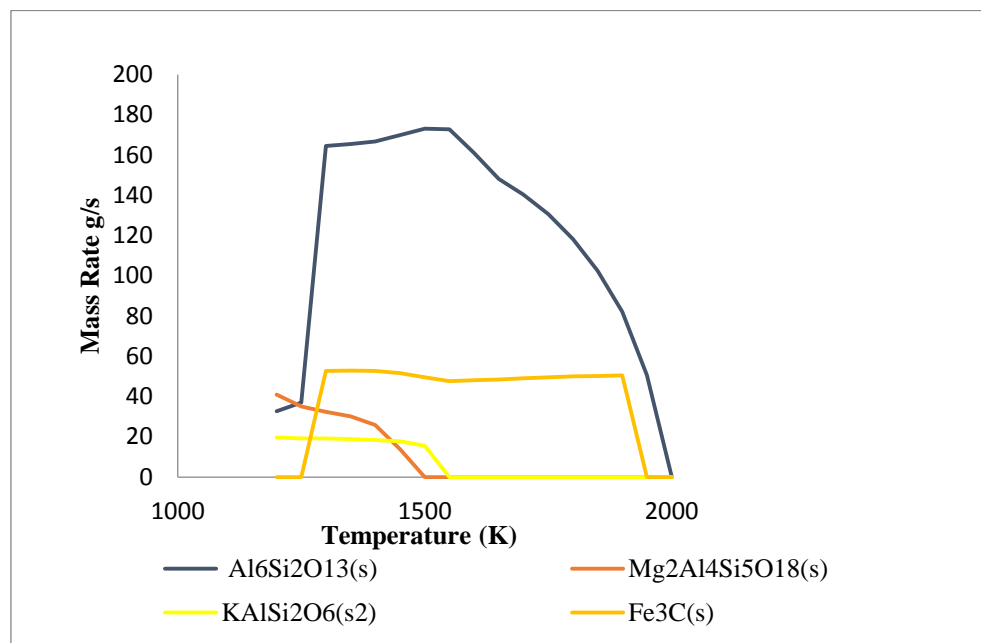


Figure 6-20: Mineral transformation versus temperature for BSG2 and PS1

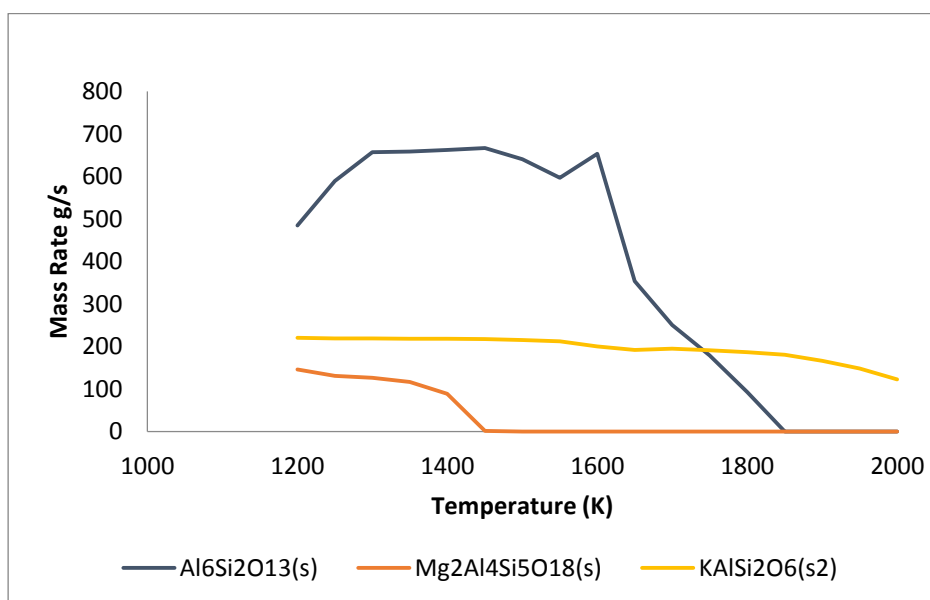


Figure 6-21: Mineral transformation versus temperature for BSG3 and PS1

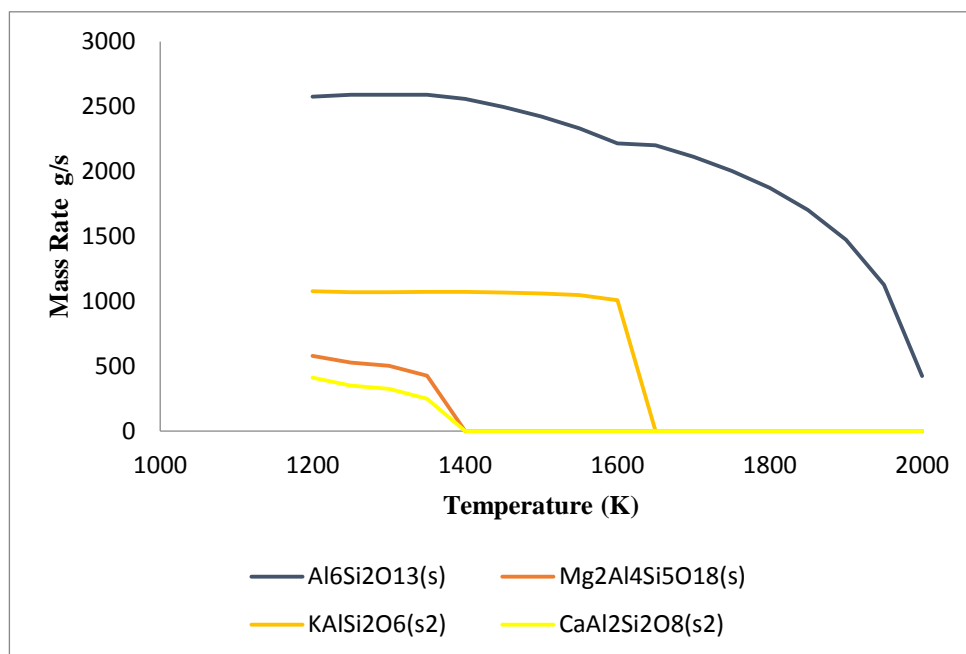


Figure 6-22: Mineral transformation versus temperature for BSG4 and PS1

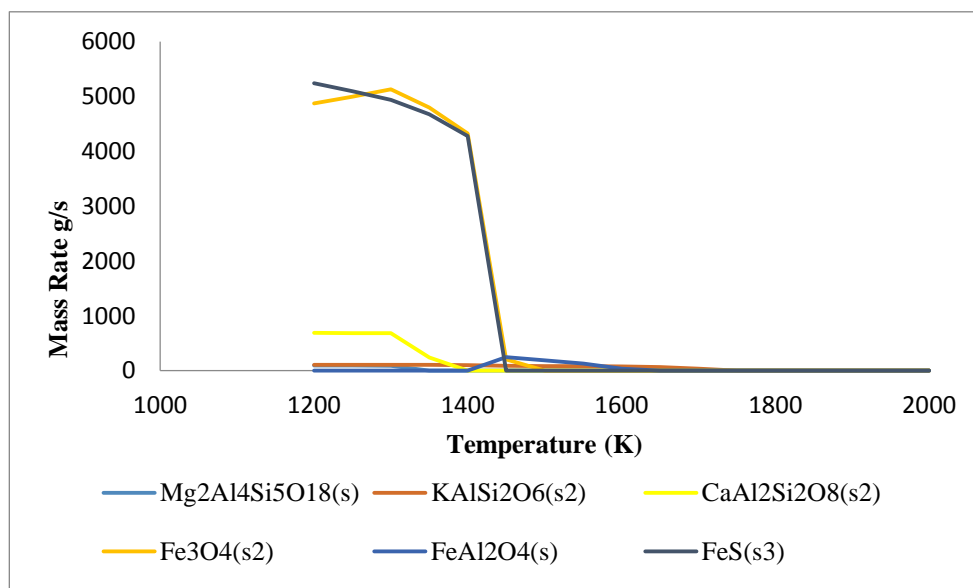


Figure 6-23: Sticking probability versus temperature for each BSG

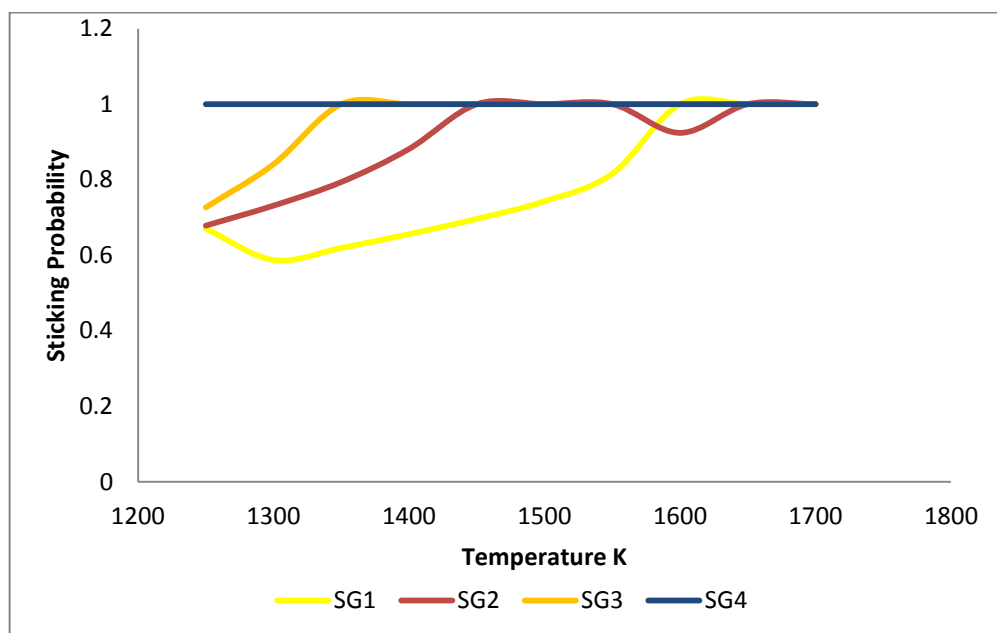


Figure 6-24: Liquid fraction of minerals versus temperature for each BSG

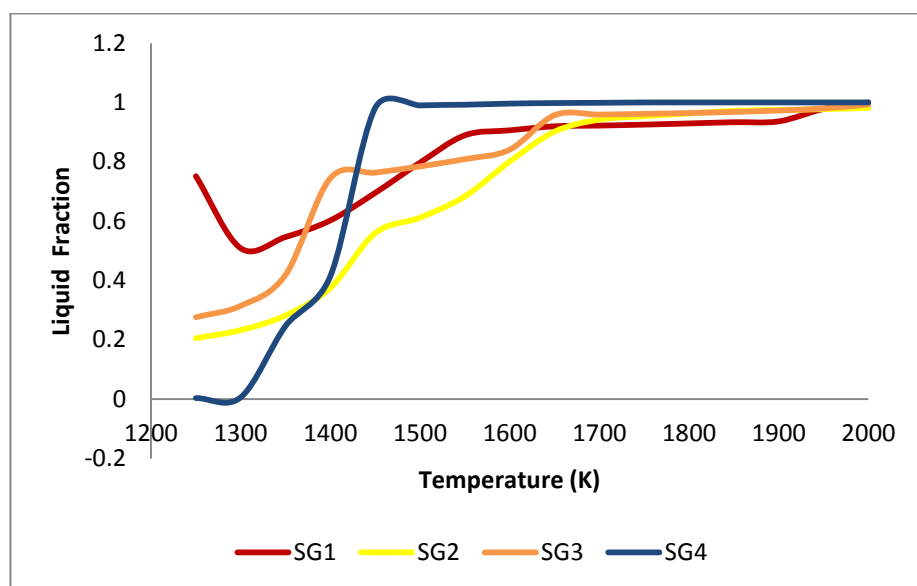


Figure 6-25: Probability of sticking for each size fraction for BSG1

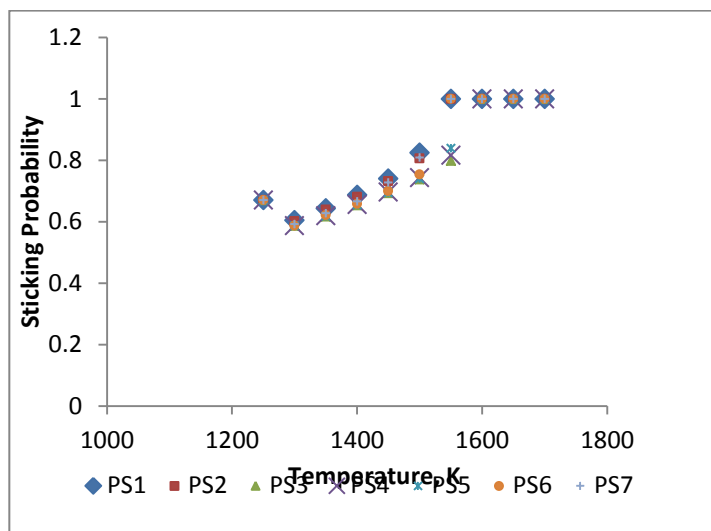


Figure 6-26: Probability of sticking for each size fraction for BSG2

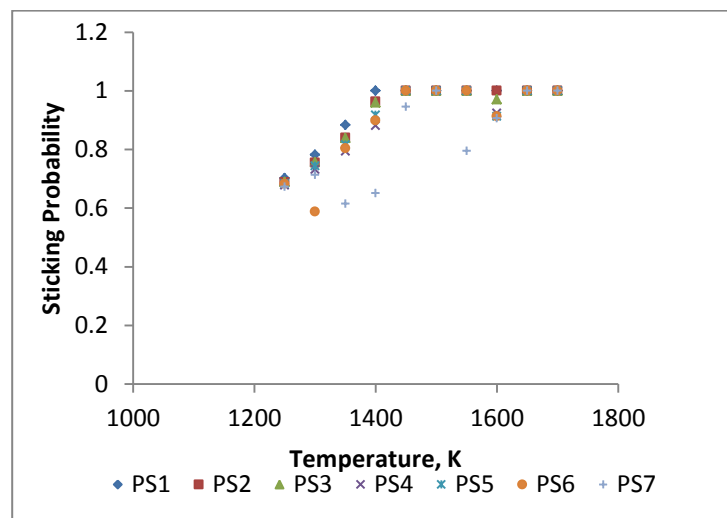


Figure 6-27: Probability of sticking for each size fraction for BSG3

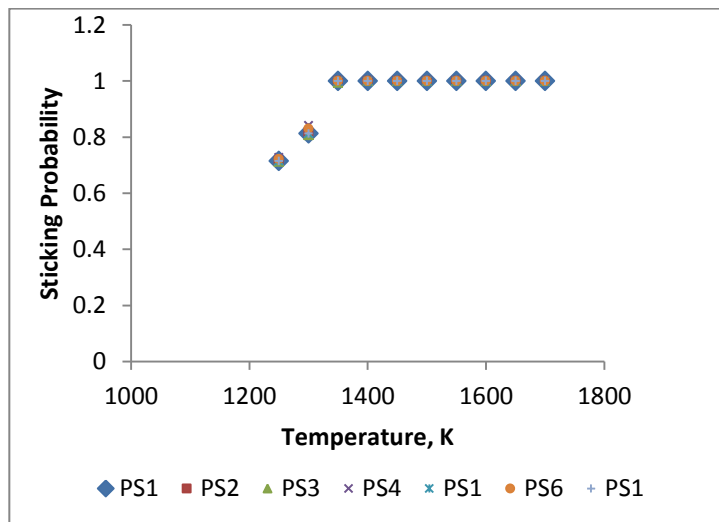
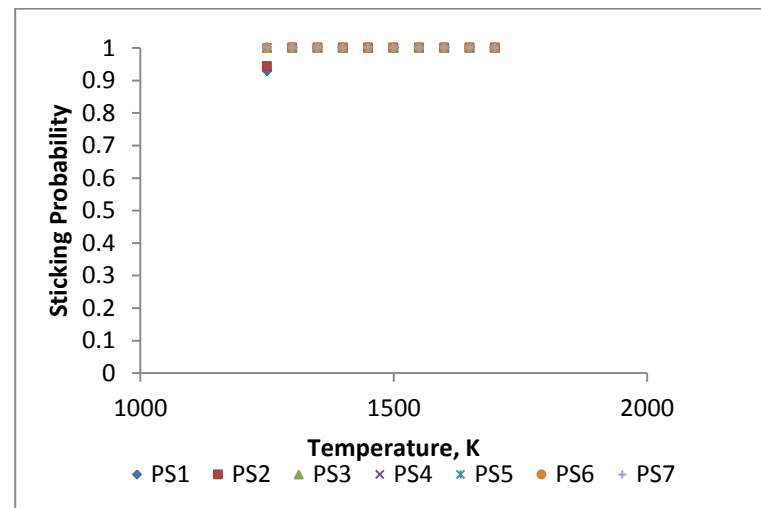


Figure 6-28: Probability of sticking for each size fraction for BSG4



6.3.3 Sticking Probability Method based on Temperature of Critical Viscosity and Contact Angle

The contact angle has been calculated as a function of carbon based on the initial empirical contact angle measurements between slag and char particles:

$$\theta_c = 1.11 \times C\% + 16.5 \quad . \quad (6.11)$$

The contact angle was calculated based on the carbon content predicted in the particle within the downflow gasifier. If the contact angle was less than 90° , the particle was predicted to stick, while if the contact angle was 90° or greater, the particle was predicted to rebound. However, in order to attain a prediction for adhesion, the particle temperature had to be greater than the temperature of critical viscosity, and the particle had to have a contact angle of less than 90° . The calculated temperature of critical viscosity was based on the partial least squares regression model of Seggiani et al. [7]. In this model, the temperature of critical viscosity (dependent variable) is expressed as a function of the oxide components of the ash and their corresponding coefficients. Of the 433 coal samples, 80% were used to develop the model while the remaining 20% were used to validate it [7]. Overall, the partial least squares regression model reduced the number of significant variables from 49 to 17 when compared to the multiple linear regression model from which it was derived. For the CFD results, if the particle temperature was lower than the temperature of the critical viscosity, or if the contact angle was 90° or higher, the particle was predicted to rebound. Once adhesion and rebounding was predicted for a group of particles according to the particle size and the density cut, the sticking probability was determined by the ratio of the particles sticking to the wall to the total number of particles impacting the wall [108].

6.4 Coefficient of Restitution and Critical Velocity

6.4.1 Total Coefficient of Restitution

The two previous methods to obtain a sticking probability relied on adhesive properties based on the ash composition and the amount of carbon. However, in CFD models such as the discrete phase model, the coefficient of restitution (COR) is a necessary boundary condition to determine the particle trajectory after impacting the wall. The value of the COR ranges from zero

to one; a value of zero indicates particle sticking, while a value of one is considered perfectly elastic. Therefore, in this approach, the critical velocity was derived from a linear viscoelastoplastic model proposed by Yigit et al. [50] since (1) previous research has described coal as viscoelastic under high temperature, and (2) this model has previously been used to predict the COR. However, in order to use this model, the properties of the modulus of elasticity and the yield strength should be known (the model is most sensitive to the property of the yield strength). Although char particles have been described as viscoelastoplastic, very little information has been published on their compressive stress [35, 36, 38]. However, Nowak et al. have reported the measurements of compressive stress versus the ratio of the surface tension to viscosity as it relates to the Frenkel equation describing sintering [35]. Based on the linear-fit of the data showing the compressive strength versus viscosity (σ/η) ratio, Equation 6.11 was used to determine the yield strength:

$$S_y = 55.032e^{-0.067(\sigma/\eta)}. \quad (6.12)$$

In this equation, the interfacial surface tension was calculated from the Young's equation and the empirical equation for contact angle in Equation 6.11. For the slag surface tension, σ_{lv} , each component was calculated as a function of the temperature based on the temperature dependence as described by Hanao et al. [109]. The mole fractions were determined by calculating the number of moles based only the total amount of weight in grams. The surface tension was then determined through the additive formula [67]:

$$\sigma_{lv} = X_{SiO_2}\sigma_{SiO_2} + X_{CaO}\sigma_{CaO} + X_{Al_2O_3}\sigma_{Al_2O_3} + X_{MgO}\sigma_{MgO} + X_{Na_2O}\sigma_{Na_2O} + X_{K_2O}\sigma_{K_2O}. \quad (6.13)$$

Because the data obtained was limited for char particles under high temperature, Equation 6.14, derived from the viscoelastic response of molten steel suggested by Massoudi, was used [110]:

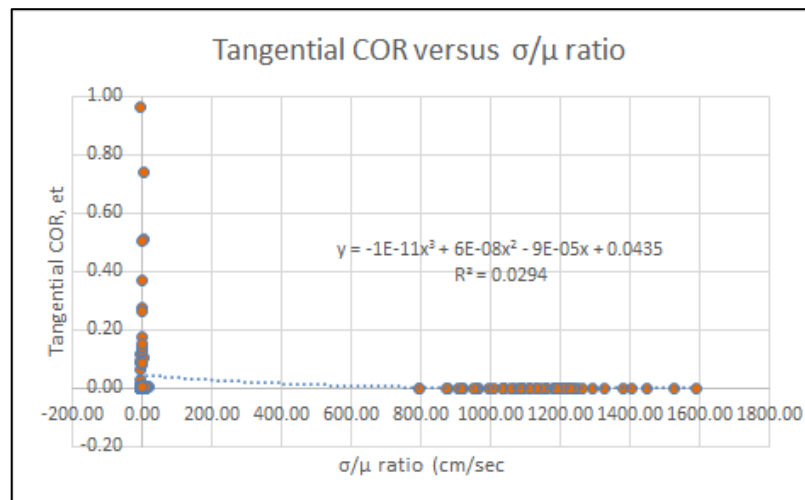
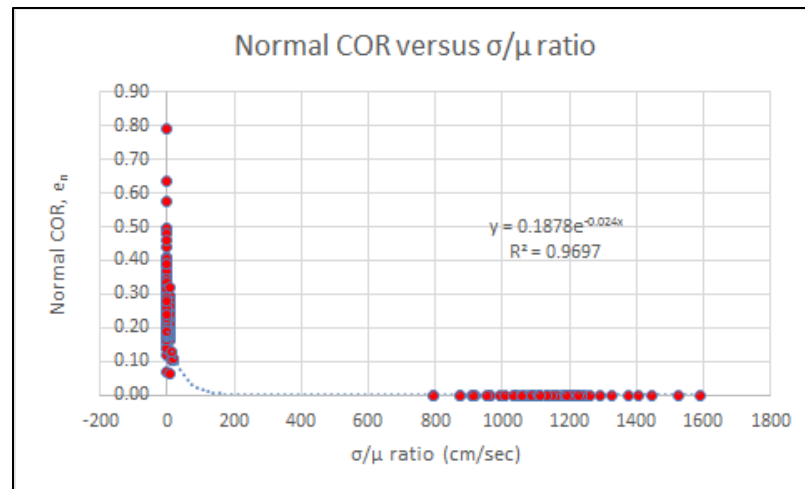
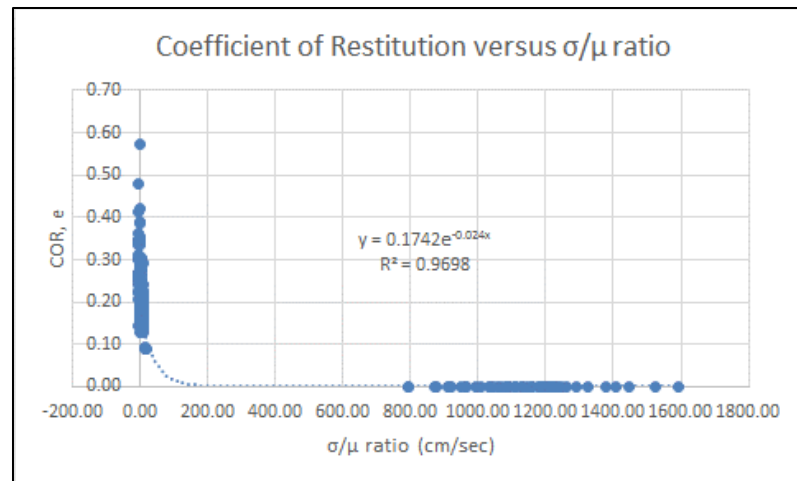
$$E[GP a] = 968 - 2.33(T - 273) + 1.90 \times 10^{-3}(T - 273)^2 - 5.87 \times 10^{-3}(T - 273)^3. \quad (6.14)$$

With the modulus of elasticity and yield strength known, Equations 2.52-2.56 were used to determine the COR. The plastic loss factor, γ , can be equated with the COR when damping is absent. Therefore, in order to determine the COR, an absence of damping was assumed. Because the COR in the model described by Yigit et al. was based on the point of impact [47], the normal as well as the tangential component has to be calculated based on the impact angle. Equations

2.52 - 2.56 developed for oblique impact were used to solve for the normal COR, tangential COR, tangential rebound velocity, and the normal rebound velocity simultaneously [64].

Based on these results, the COR demonstrated an exponential relationship with the ratio of the surface tension to viscosity. Because the yield strength is inversely proportional to the surface tension to viscosity ratio, the COR decreases as this ratio increases, as shown in Figure 6-29a. While the surface tension decreases only slightly as a function of temperature, the viscosity decreases significantly near the temperature of critical viscosity. Therefore, the yield stress is likely to decrease with an increase in the surface tension to viscosity ratio due, in part, to the decrease in the viscosity as a function of the temperature, and hence, the decrease in COR. However, for the larger size fractions in SG 1 and SG 2 cases, the relatively large contact angle provided a negative interfacial surface tension versus viscosity. This negative value increased the yield stress markedly, thereby providing the highest overall COR values. As for the size fractions in SG4, with exception of SF1, the low viscosities resulted in the highest ratios of the surface tension to viscosity; for these fractions, the COR became zero. However, because Microsoft Excel does not provide an exponential trend-line for zero values, these values were replaced with low numbers, such as 1E-13. Since the normal velocity dominated the magnitude of the resultant velocity, the value of the total COR was mostly dominated by the normal COR whereas the tangential COR had a magnitude of 1E-4.

Figure 6-29a-c: Coefficient(s) of restitution as a function of surface tension to viscosity ratio



Having determined the COR values, the critical velocity was derived thereafter, based on Equation 2.57. However, because setting the plastic loss factor to zero ($\gamma = 0$) leads to a trivial solution, the plastic loss factor had to be solved independently. As previously stated, the plastic loss factor can only be equal to COR when damping is absent. However, to determine the plastic loss factor, the assumption of the absence of damping must be negated. The amount of damping is described through the damping ratio ζ which, in the case of viscoelastoplastic impact, has in turn been defined as a function of the mass m , the natural frequency ω_0 , and the damping coefficient c as

$$\zeta = \frac{m\omega_0}{2c}. \quad (6.15)$$

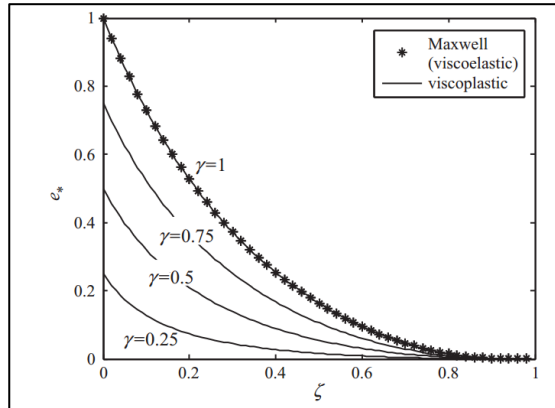
In the case of the Yigit model, ω_0 and ζ are defined as

$$\omega_0 = \sqrt{\frac{K_y}{m}}, \quad (6.16)$$

$$\zeta = \sqrt{\frac{mK_y}{2c}}. \quad (6.17)$$

To determine the plastic loss factor, COR was set to zero, while the damping ratio was assumed to be one based on its maximum limit. As shown in Figure 6-30 of COR for viscoelastoplastic compliance model with plastic deformation and rate-dependent energy losses, COR approaches zero as the damping ratio approaches one [111]:

Figure 6-30: Coefficient of restitution versus the damping ratio for various plastic loss factors [98]



Given that the damping ratio approaches one, and that the plastic loss factor is in the range of zero to one, the latter case was applied to develop a relation between γ , ζ , and COR [111]. A second case, as described by Ismail et al., is applied where the COR is set to zero, ζ is set to one, and the terminal time t_f and γ are solved simultaneously with the compression time known through the Equations 6.18 - 6.20:

$$e_* = -\frac{\gamma^2}{2\zeta\sqrt{1-(\gamma^2/\zeta^2)}}e^{-\zeta\omega_0 t_c} \left[e^{-(\zeta/\gamma^2)\left(1+\sqrt{1-(\gamma^2/\zeta^2)}\right)\omega_0(t_f-t_c)} - e^{-(\zeta/\gamma^2)\left(1-\sqrt{1-(\gamma^2/\zeta^2)}\right)\omega_0(t_f-t_c)} \right], \quad (6.18)$$

$$\omega_0 t_f = -\frac{\gamma^2}{2\zeta\sqrt{1-(\gamma^2/\zeta^2)}} \ln \left[\frac{\left(1-\sqrt{1-(\gamma^2/\zeta^2)}\right)}{\left(1+\sqrt{1-(\gamma^2/\zeta^2)}\right)} e^{-(2\zeta/\gamma^2)\sqrt{1-(\gamma^2/\zeta^2)}\omega_0 t_c} \right]. \quad (6.19)$$

With ζ set to one, and ω_0 determined by Equation 6.16, the compression time can be found using Equation 6.20thi:

$$\omega_0 t_c = \frac{1}{\sqrt{1-\zeta^2}} \left[\pi - \tan^{-1} \left(\frac{\sqrt{1-\zeta^2}}{\zeta} \right) \right]. \quad (6.20)$$

Since γ is not equal to zero, the critical velocity (V_{cr}) can be derived from the viscoelastoplastic model:

$$V_{cr} = \frac{K_y}{[(3/2)\gamma^2(K_h/K_y)]^4 m}. \quad (6.21)$$

With the plastic loss factor, and thus critical velocity, derived for each size fraction, the sticking probability was determined. In the case of viscoelastic particles, those that exceeded the critical velocity were considered to be sticking, while those impacting at velocities lower than the critical velocity were considered to have rebounding. The sticking probability was then compared to predictions based on the T_{CV} (temperature of the critical viscosity), as well as the T_{CV} and θ_{CR} (critical angle) methodology. The normalized results, where one value of the plastic loss factor was used for all size fractions in a specific gravity, were also compared to the previous methods for predicting sticking probability.

The sticking probability based on the critical velocity was closer to the predictions based on T_{CV} and θ_{CR} , as compared to the predictions based just on T_{CV} . However, there were gaps in the sticking probability calculations for the larger size fractions for SG3 and SG1. The sticking probability based on T_{CV} and θ_{CR} alone does consider the influence of the particle inertial force with the wall. Moreover, there is some uncertainty with the values of the modulus of the elasticity and the yield stress, possibly due to the methodology used to calculate the critical velocity. To determine the yield stress, the surface tension and viscosity measurements were performed well above T_{CV} [35]. Ash was then melted into pellets and sintered at 1373K prior to the measurement of compressive strength as described by Nowak et al. [35] Therefore, the yield strength values for each of the specific gravities and size fractions may not be equal to the actual yield stress at the particle temperature reported from the CFD models. Because the temperature under which the compressive measurements were undertaken is likely to be lower than the particle temperature reported from the CFD gasifier model, the actual yield stress values are probably lower. This discrepancy appears to be the likely cause of the disagreement between the sticking probabilities of the larger size fractions of SG3. Nevertheless, there is some agreement between the probability of the critical velocity and the probability of the contact angle and T_{CV} , in addition to the validation from Whitty's experimental results showing the influence of carbon [70]. Despite this agreement, the magnitudes of the critical velocities were likely to be over-predicted due to the negative surface tension to viscosity ratio relation with the contact angle. Again, because the relation between the yield stress and the surface tension to viscosity ratio was a negative exponential function, any negative value of this ratio tends to increase the yield strength markedly. Because of the relatively low average velocities of the lower specific gravities due, in part, to their trajectories, the lower critical velocities could have attained a closer sticking probability based on the current critical velocities predicted (see Appendix). Moreover, the critical velocity itself cannot be described solely as a function of the ratio of the surface tension to viscosity (despite the defined exponential relation to the coefficient of restitution), since the damping ratio cannot be excluded. Because mass and damping ratio is incorporated in the model, the size fraction and the density, both of which are used to calculate mass, also influence the magnitude of the critical velocity. Therefore, to provide consistency between the predictions of the sticking probability due to the critical velocities of the particles in a population, it is suggested to determine the plastic loss factor and the damping ratio empirically using the COR

as described by Ismail et al. This approach allows the sticking probability to be validated both empirically and computationally. In other words, if the damping ratio were less than the critical damping ratio, then the particle would be predicted to rebound. If the damping ratio approaches one, then the particle would be predicted to stick, provided that the $COR = 0$ at the critical damping ratio. For the CFD models, the equation of COR as a function of the damping ratio and the plastic loss factor could be used (Equation 6.18), while for the normal and tangential components, the simultaneous Equations 2.71 - 2.73 could be used. Given that the calculation of the plastic loss factor (for this case), solved independently in order to determine the critical velocity, hinges on the assumption that the damping ratio equals or approaches one, the parameter for the damping ratio could possibly be used to predict sticking where the empirical value is the damping coefficient c in Equation 6.17 for the damping ratio.

Figure 6-31: The sticking efficiencies predicted for each SG and SF based on the plastic loss factor for each SG and SF

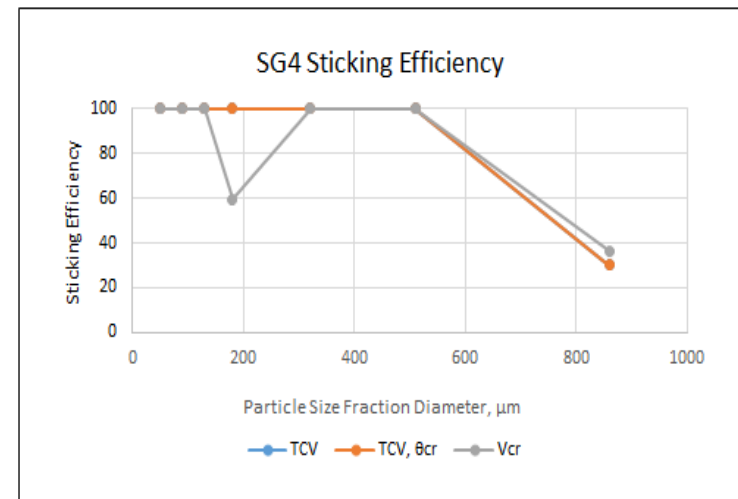
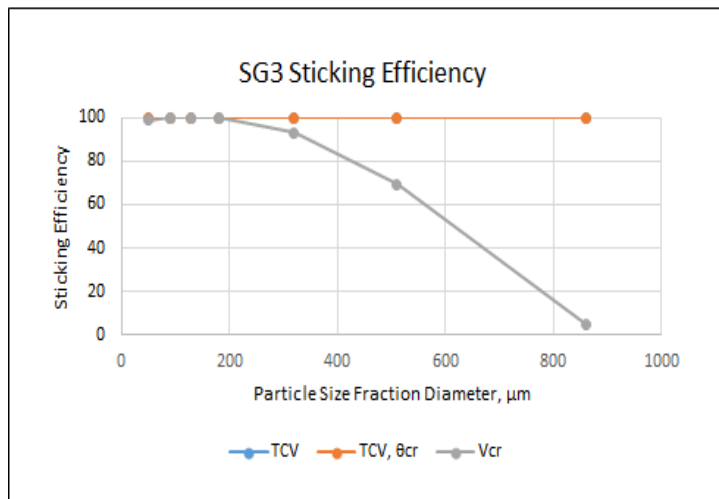
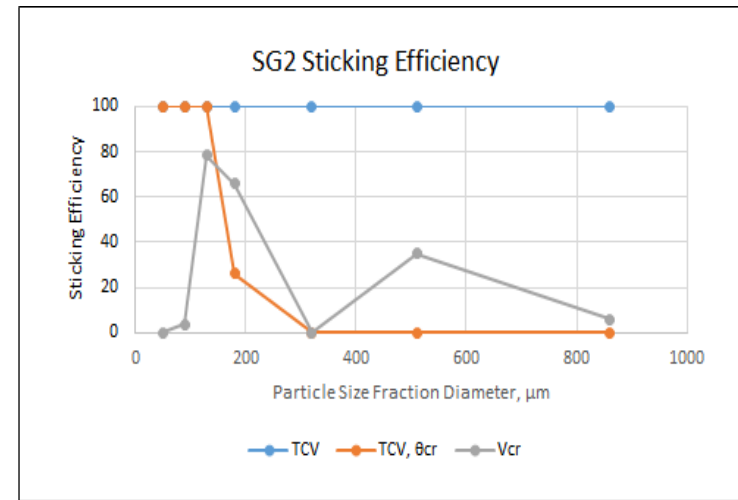
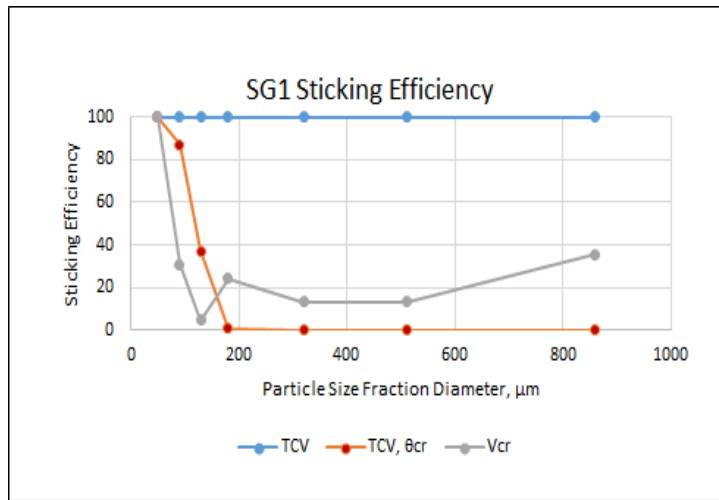
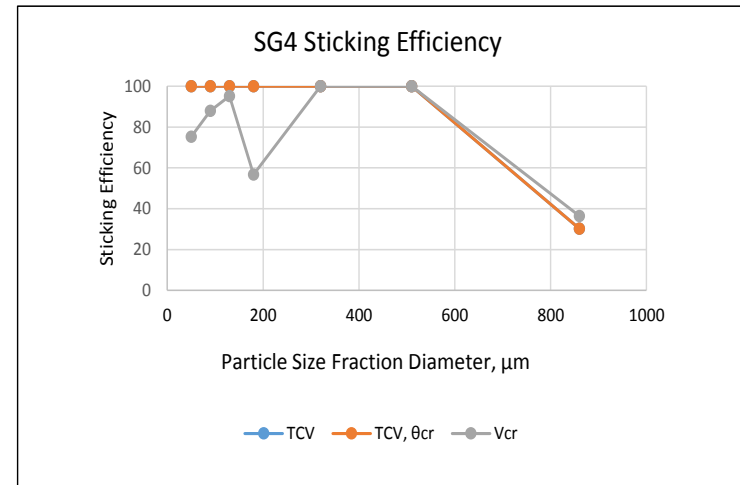
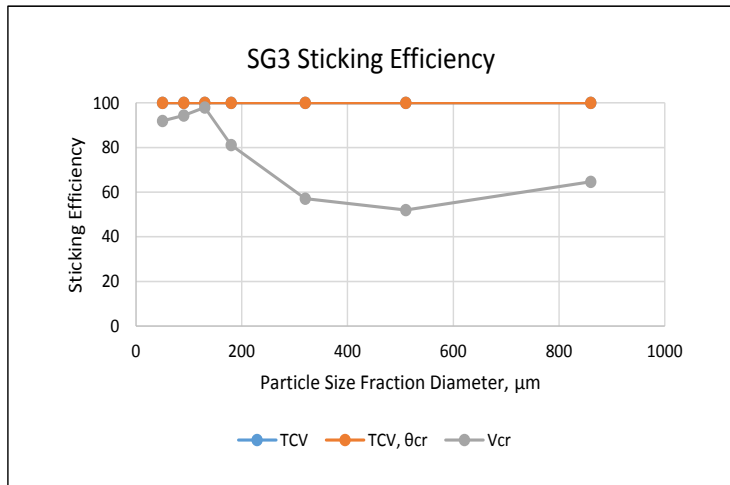
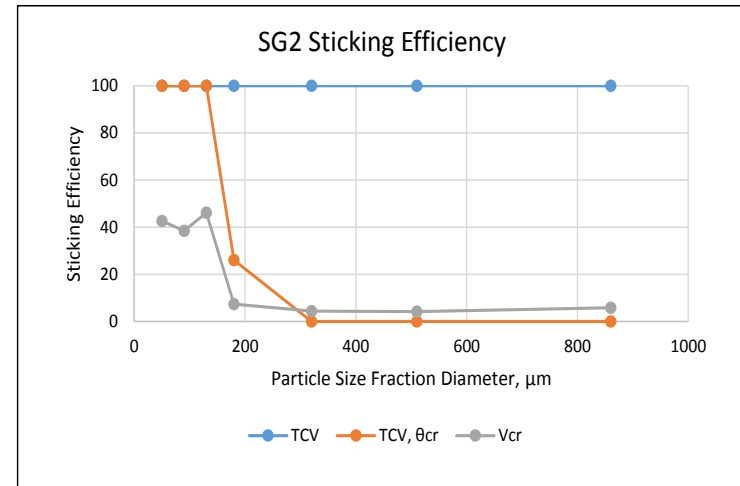
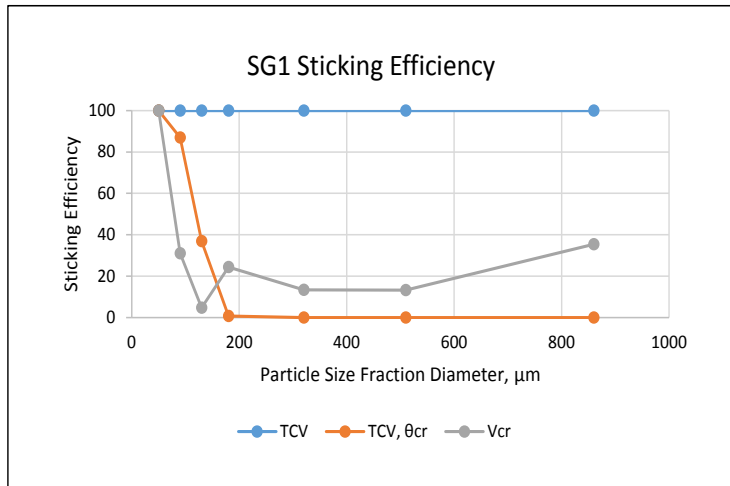


Figure 6-32: The sticking efficiencies predicted for each SG and SF with the plastic loss factor normalized



6.5 Partitioning Between Slag, Flyash, and Syngas

6.5.1 Approach

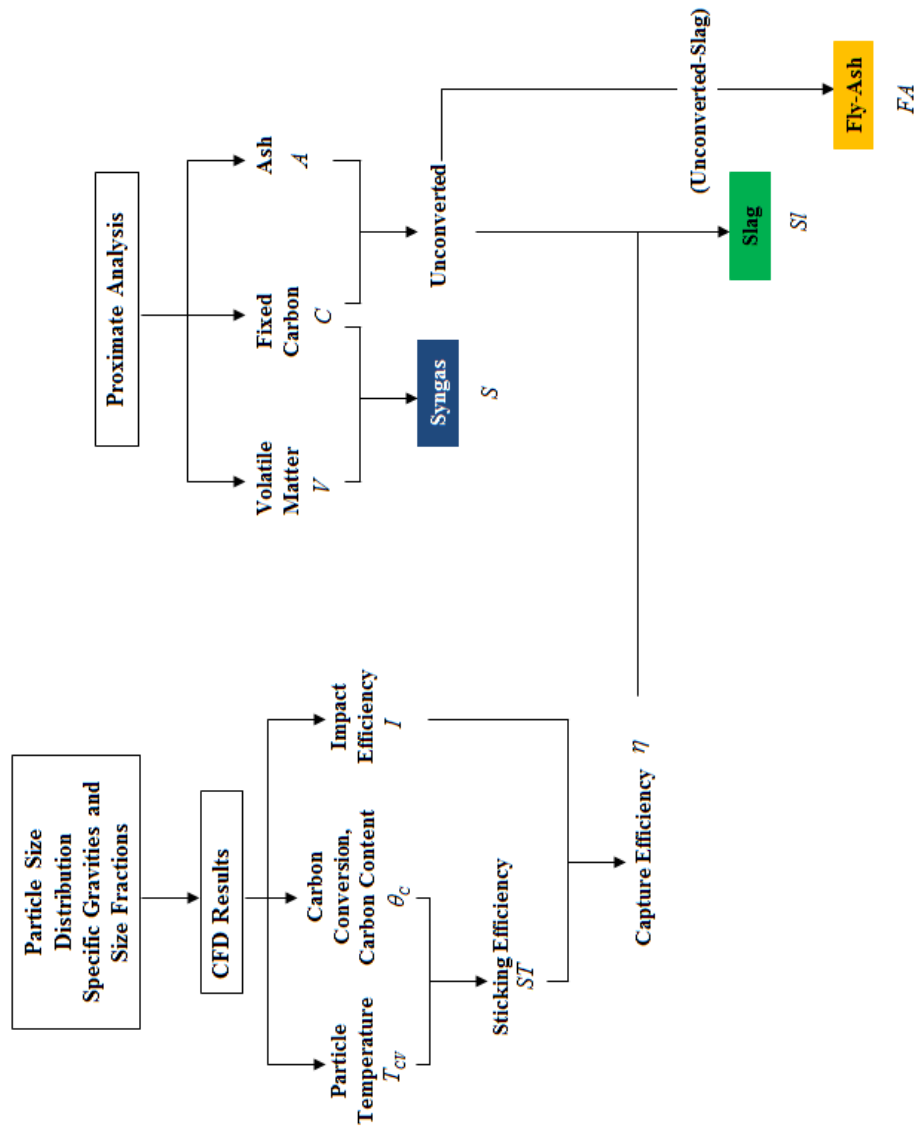
Figure 6-33 shows a logic flow diagram that leads to the partitioning of the pulverized coal particles with size and density distributions into syngas, slag, and flyash in a gasifier [86]. The coal particles comprising all of the four specific gravities and seven particle size cuts were used as inputs for the CFD simulations for the entrained flow gasifier. The output of the CFD model included particle temperature, residual carbon content, and the impact statistics. The sticking efficiency was calculated using the method involving the temperature of critical viscosity and the contact angle. Both the sticking efficiency and the impact statistics as determined from the CFD model were used to determine the capture efficiency. In addition, proximate analysis was used in the model to predict the percentages of volatile matter, fixed carbon, and ash. Syngas was derived from the volatile matter that evolved during particle heating, and from the carbon that was converted via oxidation and gasification and subsequently released into the gas phase [18, 86]. The unconverted matter that impacts the gasifier walls may stick or rebound depending on the contact angle and material properties. With this rationale, the influence of the average particle size for a particular size distribution on the amount of flyash and slag relative to the amount of syngas has been quantified [108].

6.5.2 Sticking Efficiency, Impact Efficiency, and Capture Efficiency

To determine the impact efficiency (I), the ratio of the particles striking the wall (p_w) to the particles ejected into the gasifier (p_I) was calculated:

$$I = p_w / p_I . \quad (6.22)$$

Figure 6-33: The flow diagram for determining the partitioning between slag, flyash, and syngas



The collection efficiency (η) was then determined based on the impact efficiency and probability of sticking (ST):

$$\eta = I \times ST \quad . \quad (6.23)$$

For validation, the carbon conversion (W) has been calculated to compare the calculated capture efficiencies with existing empirical measurements. To determine the carbon conversion, the ash percentage in the resulting char particle was calculated based on the amount of carbon. Then, the carbon conversion was calculated based on the relation

$$W = \frac{10^4(A_1 - A_0)}{A_1(100 - A_0)} \quad . \quad (6.24)$$

Here, A_1 is the ash remaining in the char particle and A_0 is the ash in the original feed.

6.5.3 Partitioning of Ash versus Slag

The temperature range of the particles was found to be between 1813 - 1869 K. Based on this temperature range, the larger particle sizes for SG 1 and SG 2 were predicted to rebound as shown in Figure 6-35. On the other hand, the smaller size fractions for SG 1 and SG 2, in addition to particle sizes for SG 3 and SG 4, were predicted to adhere, as shown in Figure 6-36. Due to the temperature of the critical viscosity, particle size fraction one of SG 4 was predicted to rebound. Due to the greater amount of carbon in SG 1 and SG 2, the contact angle was predicted to be greater than 90°. Therefore, a relatively high proportion of the larger size fractions were predicted to contribute to the flyash. Regarding the overall ash/slag partition, if fragmentation was likely to occur in case of excluded pyrite, there would possibly be a higher contribution to the slag, since the particle temperatures of the smaller size fractions of SG 4 were greater than the temperature of critical viscosity as compared to the largest size fraction. However, fragmentation is less likely to occur in the case of illite and kaolinite. Therefore, there is a high probability that the larger size fractions with significant carbon contribute to the amount of flyash.

6.5.3.1 Temperature Dependence

To address the temperature sensitivity, another prediction in terms of the partitioning of ash and slag was based on the particle temperature distribution in the range of 1434 - 1541 K. As

a result of the temperature decrease, there was a higher contribution to ash, particularly in the case of particle size fraction five and six for SG 1 as shown in Figure 6-37. This is due to the fact that some of the particle temperatures approached the temperature of the critical viscosity for that particular specific gravity and size fraction. Although not as significant, there was also more contribution to ash in SG 2 for the size fractions in the mid-range. In the case of SG 3 and SG 4, there was no discernible change in the partition of the size fractions between the ash and slag contributions, with the exception of particle size one and two of SG 3. For SG 3 and SG 4, the particle temperatures were predominantly higher than the temperature of critical viscosity, with the exception of particle size one for SG 4.

6.5.3.2 Impact Efficiency and Carbon Conversion

The carbon conversion for particles impacting the wall is shown in Figure 6-39. The conversion for the smaller size fractions approached 100% in all cases. The conversion for the size fractions one through four for SG 1 ranged between 61 to 75%. However, the conversion for the size fractions one through four for SG 2 was lower - in the range of 48 to 70% for the size fractions one through four.

Based on the carbon conversion percentages, the conversion process increased with a decrease in the particle size and an increase in the specific gravity due to the reduction of carbon in the particle population. The impact efficiency seemed to decrease with an increase in the particle size fraction across all the specific gravities, as shown in Figure 6-40. Although this reduction in the impact efficiency could be partially due to particle trajectories, the complete or the near-complete conversion resulting in the contribution to syngas could also be possibly responsible. In terms of the specific gravities, there is not much discernible difference between the specific gravities of the same particle size class.

6.5.3.3 Capture Efficiency

For SG 1 and SG 2, the capture efficiencies shown in Figure 6-43 and 6-44 were consistent with the work of Li et al., in which the capture efficiency dramatically increased after 88% conversion [70] These figures show that the capture efficiency only reaches a value of 40 to

50%, provided that conversion approaches 100%. In these plots, the points with the lower carbon conversion correspond to the larger size fractions, while the points with the higher carbon conversion correspond to the smaller size fractions. For the specific gravity parameter, the collection efficiency ranges between 50 to 60%. It was also found that the capture efficiency, in this case, slightly decreases with carbon conversion, which may have been due to the fact that the larger size fractions in SG 3 and SG 4 had higher impact efficiency than the smaller size fractions. For SG 4, the first point shows 20% collection efficiency beyond the 88% conversion, which was attributed to the temperature of critical velocity that reduced the sticking probability. Overall, the capture efficiencies for SG 3 and SG 4 in Figure 6-45 and 6-46 are consistent with the particle temperatures approaching 1400 K, as described in a study by Harbs et al. [112]. In their report, capture efficiencies between 60 to 70 % were reasonable values for particles having high ash content and low carbon content. Overall, the capture efficiencies show the influence of the size fractions, whereas the sticking probabilities, based on the viscosity, show a negligible difference. In the context of these results, it can be said that the specific gravities dictate the range of the capture efficiency, while the size fractions determine the individual capture efficiencies.

6.5.3.4 Particle Size Distribution

To determine the influence of the particle size distribution, this parameter was adjusted such that, the largest particle sizes (size fraction one through three) were reduced by a certain set percentage, while the smallest size fractions were increased by this same value. Table 6 shows the percentage adjustments used to attain each particular particle size distribution. Each subsequent decrease in the average size of the particle size distribution increased the percentage of particles below 100 μm as shown in Figure 6-34.

Table 6-5: Partitioning fraction from size and density analysis of coal, wt.% dry coal

	PS1	PS2	PS3	PS4	PS5	PS6	PS7
BSG1	2.54	5.19	14.90	6.39	5.54	5.16	8.12
BSG2	1.86	4.53	10.30	4.35	3.51	3.33	19.69
BSG3	0.56	0.40	0.81	0.37	0.32	0.30	0.71
BSG4	0.10	0.07	0.20	0.09	0.10	0.15	0.42

Table 6-6: Percentage of increase of particle sizes in attaining each particle size distribution

Avg. SF	SF 1	SF2	SF 3	SF 4	SF 5	SF 6	SF 7
204	-25%	-25%	-25%	No Change	+25%	+25%	+20%
154	-50%	-50%	-50%	No Change	+50%	+50%	+40%
114	-75%	-75%	-75%	No Change	+75%	+75%	+60%

The percentage increase in the size fraction seven for each particle size distribution was adjusted in order to maintain the net specific gravities and size fractions in the original particle size distribution. Once the new particle size distributions were developed, calculations were performed in order to predict the amount of slag, flyash, as well as the converted char and syngas. The matrix for the capture efficiency was derived from the matrix for the sticking probability and the impact matrix. The capture efficiencies, in addition to the carbon conversion for each of the specific gravities and size fractions, were used to estimate the syngas percentage by using the relation

$$S_{ij} = \sum_l \sum_m X_{il} C_{lm} W_{mj} + \sum_l X_{il} V_{lj} . \quad (6.25)$$

Figure 6-34: Rosin Rammler distribution based on average particle sizes

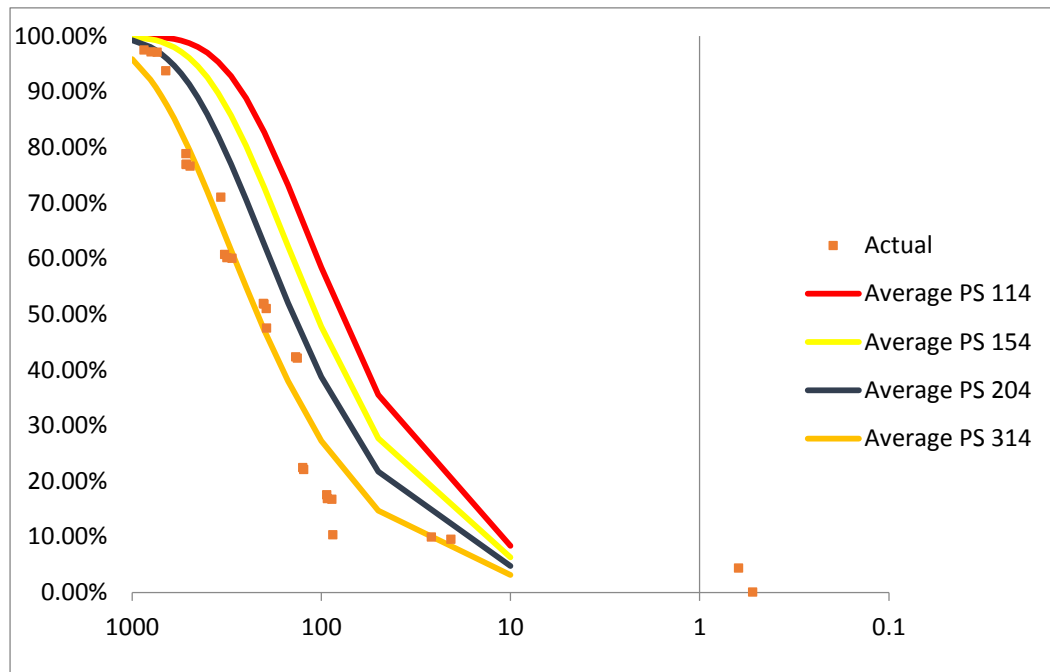


Figure 6-35: Percentage of ash for each BSG and SF in the particle size distribution

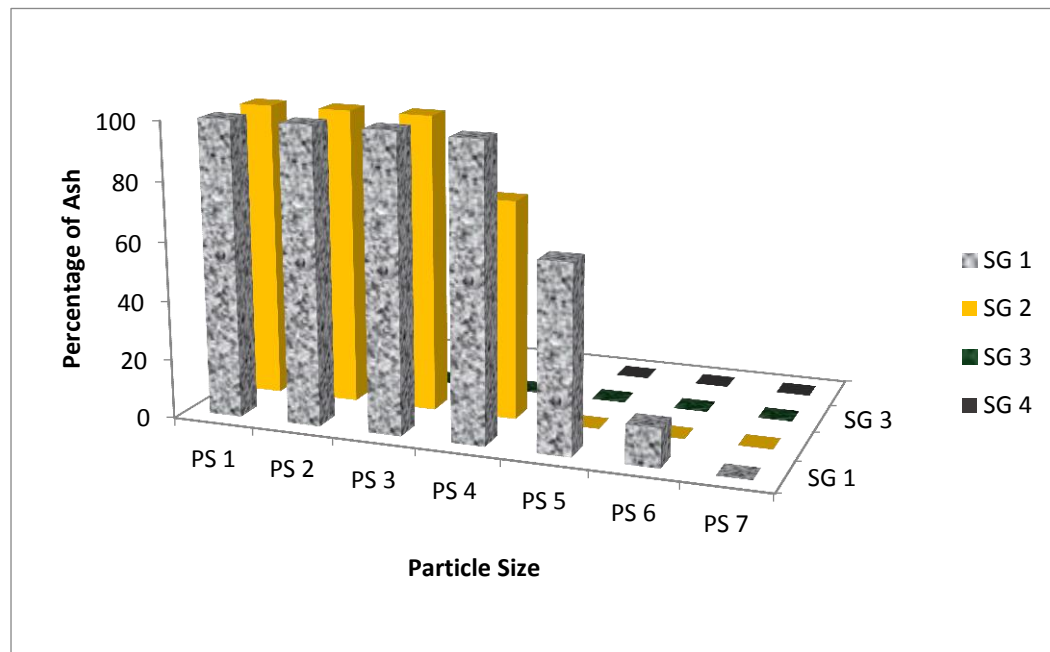


Figure 6-36: Percentage of slag for each BSG and SF in the particle size distribution

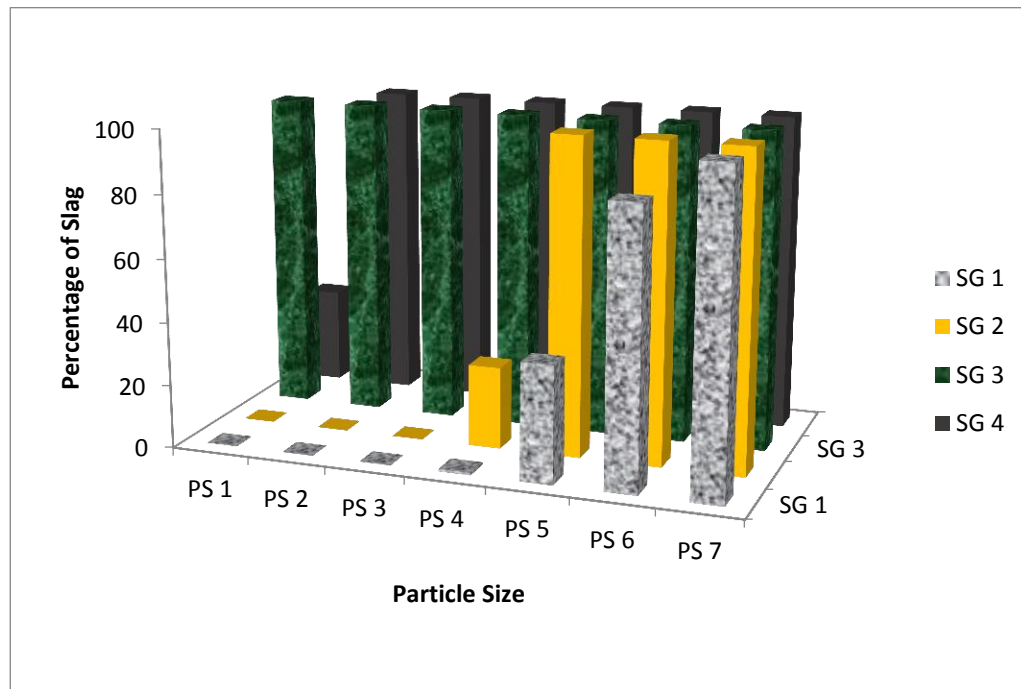


Figure 6-37: Percentage of ash for each BSG and SF in the particle size distribution for 1434 K to 1541K

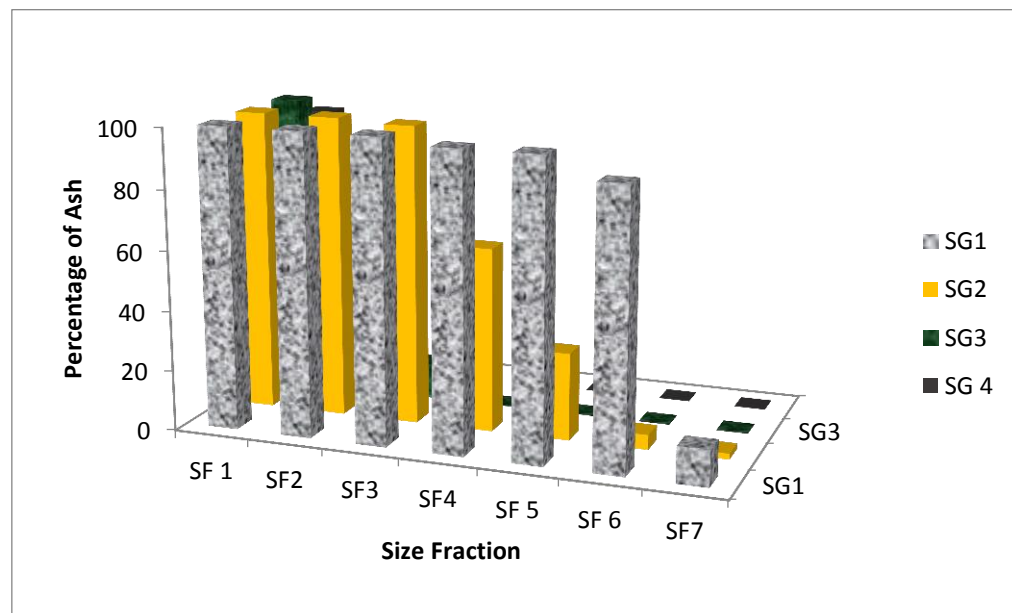


Figure 6-38: Percentage of slag for each BSG and SF in the particle size distribution for 1434 K to 1541K

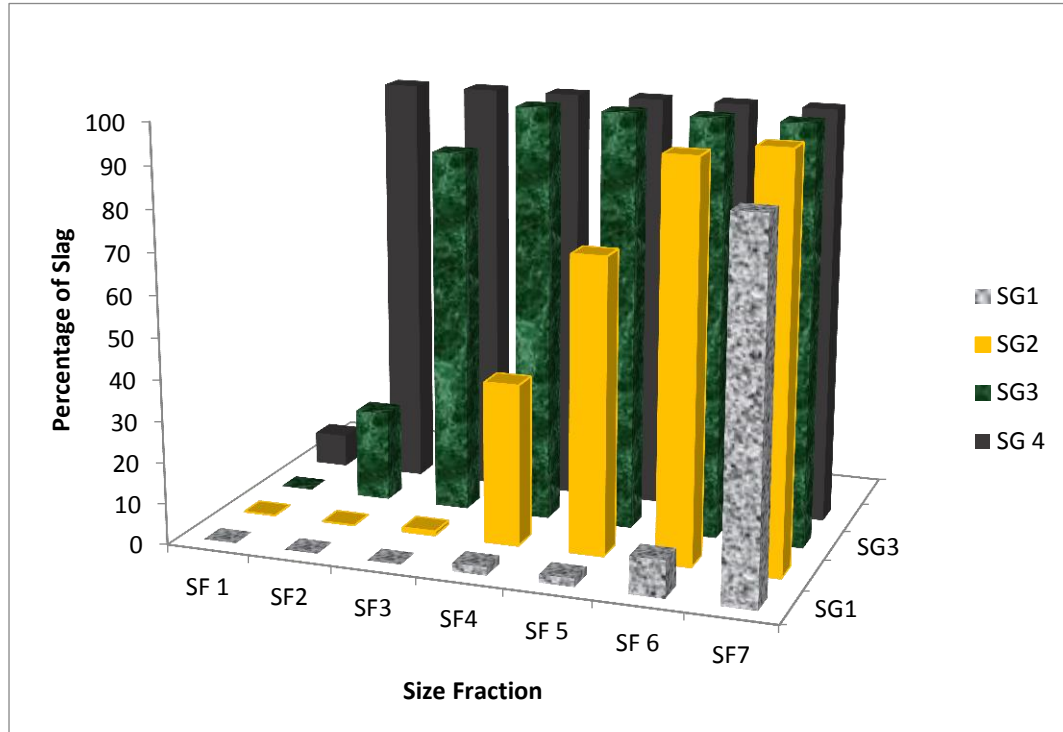


Figure 6-39: Carbon conversion for each BSG and SF in the particle size distribution

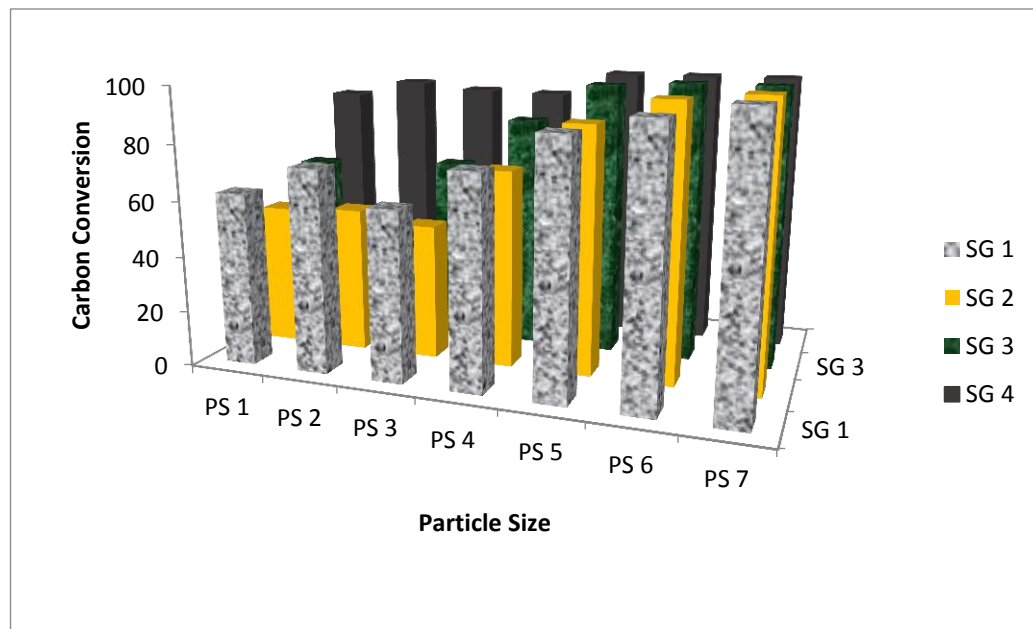


Figure 6-40: Impact efficiency for each BSG and SF in the particle size distribution

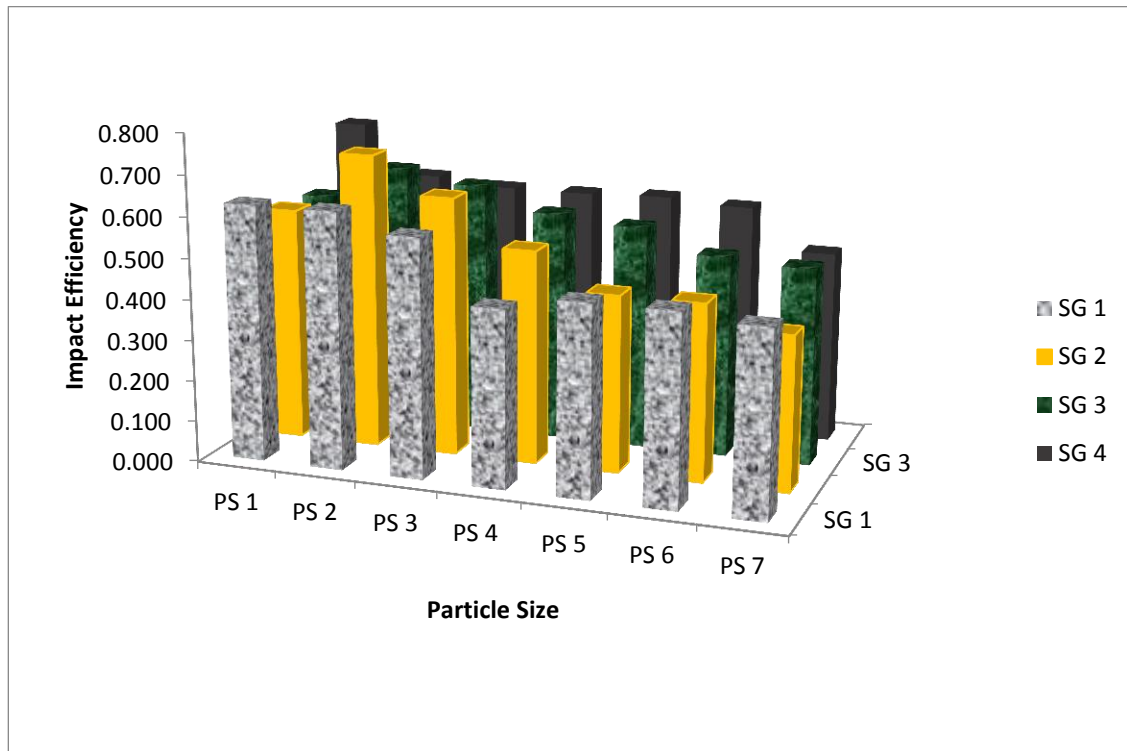
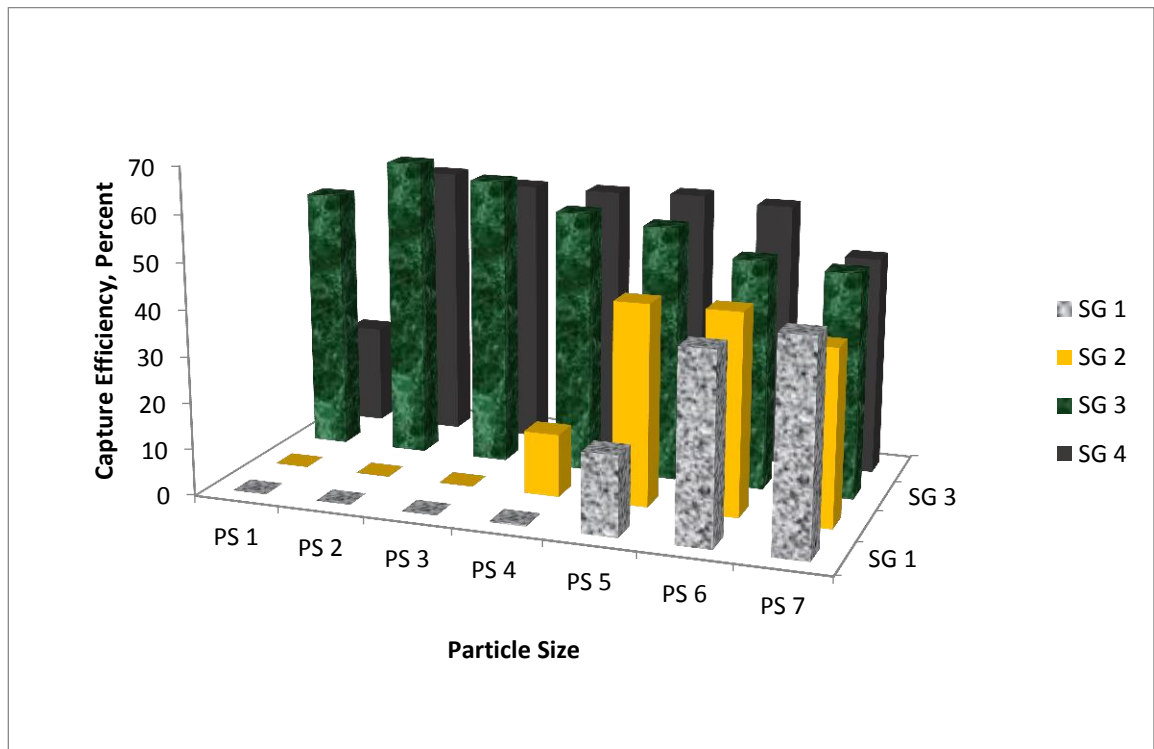


Figure 6-41: Capture efficiency for each BSG and SF in the particle size distribution



Here S_{ij} is the matrix for the syngas percentage, X_{il} (Table 6-5) is the partition fraction for the particle size distribution, W_{mj} is the carbon conversion matrix, V_{lj} (Table 6-9) is the volatile matter matrix, and C_{lm} is the fixed carbon matrix (Table 6-7). The unconverted matter is determined from the syngas percentage matrix, the partition fraction for the particle size distribution, the carbon matrix, and the ash matrix, A_{lj} (Table 6-8):

$$U_{ij} = \sum_l \sum_m X_{il} C_{lm} (1 - W_{mj}) + \sum_l X_{il} A_{lj} . \quad (6.26)$$

To determine the slag percentage, the capture efficiency was determined based on the sticking probability and the impact efficiency of the particles:

$$\eta_{ij} = \sum_l S T_{il} I_{lj} . \quad (6.27)$$

Thereafter, the slag percentage was calculated by considering the product of the capture efficiency matrix and the unconverted matter matrix:

$$Sl_{ij} = \sum_l \eta_{il} U_{lj} . \quad (6.28)$$

As a result of the adjustments to the particle size distribution, there is very slight change in the amount of syngas - from 80 to 86% as shown in Figure 6-42. At the same time, the ash decreased from 17 to 10%, while the slag only increased slightly from 3.1 to 3.86%. Therefore, a decrease in particle size not only increases the syngas production, but also decreases the amount of flyash, which is contributed by the larger size fractions.

Table 6-7: Fixed carbon from proximate analysis

	PS1	PS2	PS3	PS4	PS5	PS6	PS7
BSG1	55.86	56.77	56.91	55.34	57.31	57.66	58.33
BSG2	50.84	51.78	52.20	52.07	51.78	53.05	56.60
BSG3	27.58	29.13	28.42	27.80	24.73	22.28	21.01
BSG4	13.41	11.67	17.26	12.51	14.46	16.64	14.82

Table 6-8: Ash composition from proximate analysis

	PS1	PS2	PS3	PS4	PS5	PS6	PS7
BSG1	3.52	3.18	2.80	2.34	2.42	2.10	2.54
BSG2	13.80	12.75	12.00	12.35	12.03	11.59	9.08
BSG3	52.00	50.09	49.56	50.19	53.03	55.02	58.11
BSG4	66.66	65.39	64.51	64.39	63.06	65.00	67.44

Table 6-9: Volatile matter from proximate analysis

	PS1	PS2	PS3	PS4	PS5	PS6	PS7
BSG1	40.62	40.05	40.29	42.32	40.26	40.24	39.13
BSG2	35.36	35.47	35.81	35.58	36.18	35.36	34.32
BSG3	20.42	20.79	22.02	22.02	22.23	22.70	20.88
BSG4	19.93	22.94	18.24	23.10	22.48	18.37	17.74

Figure 6-42: Percentage of slag, unconverted char and ash, and converted char and syngas for different particle size distributions

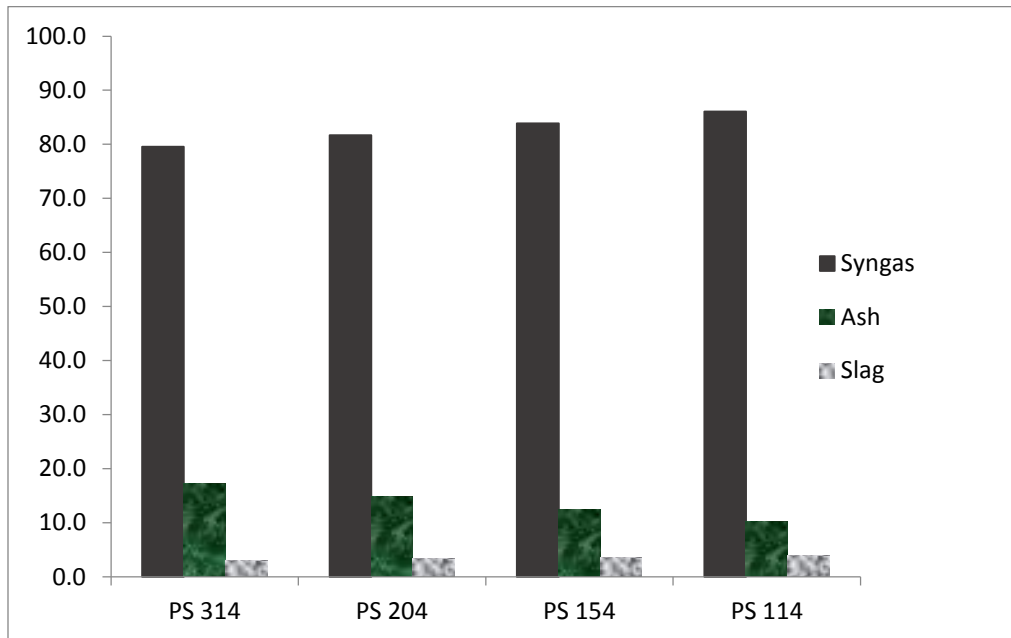


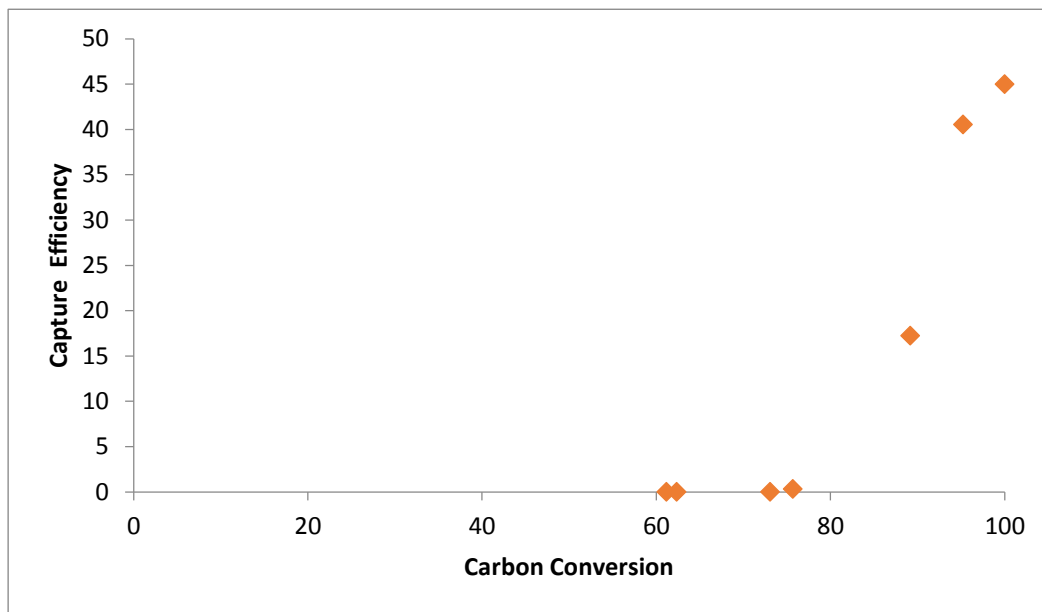
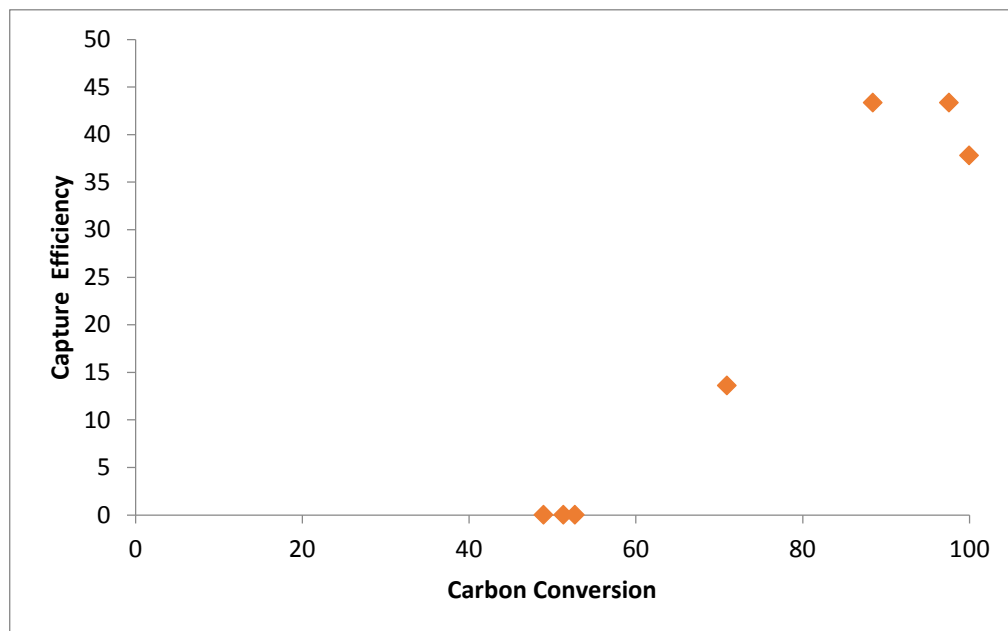
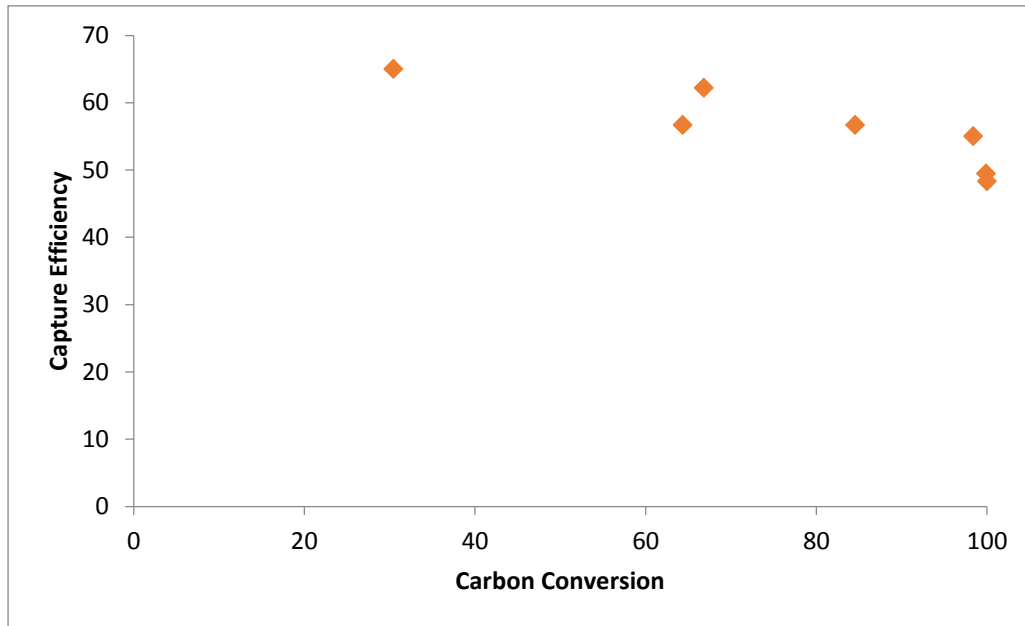
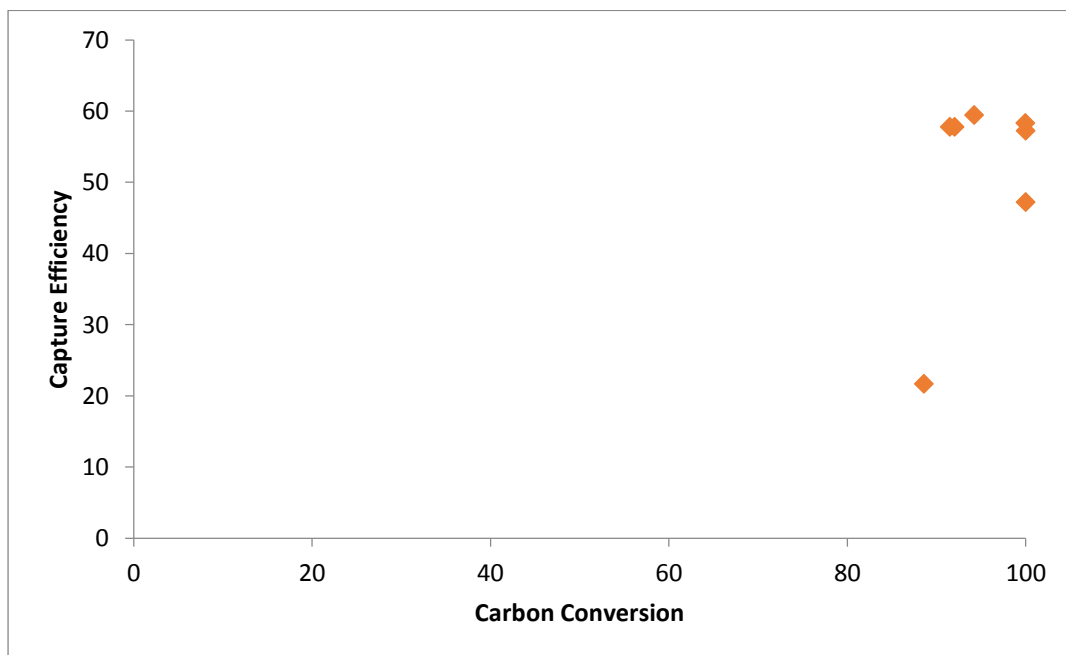
Figure 6-43: Capture efficiency versus carbon conversion for SG1**Figure 6-44: Capture efficiency versus carbon conversion for SG2**

Figure 6-45: Capture Efficiency versus carbon conversion for SG3**Figure 6-46: Capture efficiency versus carbon conversion for SG4**

CHAPTER 7 CONCLUSIONS

The main objective of this work was to incorporate the influence of both the inorganic and organic composition of the char particles on the physical properties utilized in the particle-wall collision models to determine whether the particles will rebound or adhere to the wall. By taking this approach, the desired end result was to create a consistent sticking probability method governed by the physics of the process as opposed to just the intrinsic properties. Specifically, this consistency was to entail critical velocities calculated outside of CFD models by utilizing output data that would accurately reflect the coefficient of restitution values to be predicted for the appropriate particle wall collision model to be used in a CFD model for an entrained flow gasifier. Once the sticking probability method was developed, this method was used to partition the flyash from the slag. Meanwhile the cold flow experiments involving non-spherical particles and non-smooth surfaces tested the assumptions of non-rotating particles involving perfectly shaped spheres in existing particle wall collision models.

1. In this work, the particle becoming entrapped within a slag layer has shown to be unlikely. The focus of this work has been to identify the conditions under which the particles can rebound or adhere. To that extent,
 - a. Based on the experimental portion of this work, non-ideal conditions influencing the rebounding behavior of the particles due to sphericity and surface incongruity were observed in terms of the resulting rebounding angle. Based on these results, it was found that the coefficient of the restitution could only attain its maximum value when the rebounding angle approached the impact angle (90°) for normal impact. The variation in the rebounding angle was deemed to be due the variability in the particle sphericity and its orientation to the surface prior to the impact. This behavior inspired an investigation to correlate the particle sphericity to the coefficient of restitution through “drop” experiments.
 - b. Based on these “drop” experiments, the results demonstrated that there is a strong correlation amongst the degree of equancy of the particles, the resulting average rotational velocities, and the measured coefficient of restitution. This particle rotation was observed to have led to a partitioning of the translational and the rotational energies, which resulted in a significant decrease in the COR, e . In addition to

rotation, the particular area of the surface (whether a soft or hard viscous adhesive, metal plate, or surface covered in HDPE particles) where the particle hits, also led to a decreased e , while the non-spherical geometry of the HDPE particles, combined with the coefficient of friction of the silicone adhesive, led to sliding. Based on these observations, it was determined that the rotation of particles cannot be neglected if the goal is to improve the simulation of the particle behavior in a gasifier. Therefore, the equancy or the sphericity did have a significant influence on the e in the context of this analysis.

2. This study also showed that the sticking probability, based on the critical velocity, was closer to the predictions based on the temperature of the critical viscosity and critical angle than the prediction based on the temperature of the critical viscosity alone. However, significant gaps in the sticking probability calculations of the larger size fractions for SG3 and SG1 suggested the likelihood of over-predicting the critical velocities for those size fractions, as well as for the other specific gravities due to the uncertainty in the values of the Young modulus of elasticity and the yield stress, as predicted by previous empirical data. However, the sticking probability based on the temperature of the critical viscosity and the critical contact angle alone did not take into consideration the influence of the particle inertial forces with the wall. Therefore, the sticking probabilities computed in this work have been in the similar range of values reported in previous work on ash and char deposition.
3. For the partitioning of the particles in a size distribution into flyash, and slag, the bulk coal sample was separated by float-sink experiments into four specific gravity fractions. These were further separated into seven size fractions.
 - a. In the context of size fraction, there was little discernible difference in the sticking probabilities as predicted by the viscosity models. The contact angle, as a function of carbon, has been calculated based on the initial empirical contact angle measurements between the slag and the char particle. This function, in addition to the temperature of critical viscosity, was used to indicate the occurrence of sticking or rebounding. In the original particle size distribution, the larger size

fractions contributed to the flyash. Moreover, a decrease in the particle temperature distribution increased the amount of flyash through the contribution of the mid-size particles due to the temperature of the critical viscosity.

- b. In terms of the capture efficiency, the specific gravity dictated the range of the capture efficiencies, while the size fraction influenced the capture efficiency within that range. Higher capture efficiencies were attained for the smaller size fractions due to carbon conversion. Moreover, the heavier specific gravities demonstrated higher capture efficiencies than the lighter specific gravities. Overall, reducing the higher size fractions by an increase in the smaller size fractions reduced the contribution to flyash while increasing the contribution to slag.

The particle wall impact experiments have shown that the moment of inertia in all the three Cartesian coordinates should be characterized in order to describe the particle orientation prior to and after the impact – even for two-dimensional models. This step would lead to a greater accuracy in characterizing the particle behavior within an entrained flow gasifier. Despite the uncertainty in the particle's physical properties used in predicting the critical velocity, the efforts to derive the critical velocity has identified the capability of another parameter, the damping ratio, to characterize rebound and adhesion that is independent of the particle velocities. This property could possibly be empirically characterized as a function of the interfacial surface tension, viscosity, and mass of the particles. By including the interfacial surface tension as a property within such a model to characterize adhesion, the influence of carbon as well as ash composition is captured. The mass of the particle prior to the impact influences the density and the particle size. Provided that a sticking probability methodology could be developed, this work has demonstrated the process to use such a methodology to utilize the adhesion probability as part of an algorithm to partition a particle size distribution into slag, ash, and syngas based on the proximate analysis. Although the impact data for particles are required, either through experimental measurements or through CFD simulation (compared to carbon conversion, which can be determined numerically), the algorithm used in this work serves as a practical method to assess the performance of a gasifier with the objective of achieving high conversion with minimal ash deposition.

CHAPTER 8 FUTURE WORK

8.1 High Temperature Measurements

Due to the uncertainty in the values of the modulus of elasticity and the yield stress, a continuation of this work should involve the measurements of these properties under high temperature conditions. Given that both of these properties are needed for the Yigit linear viscoelastoplastic model [50], the uniaxial compression and the fatigue loading experiments are of interest, since the modulus of elasticity and the yield stress can be obtained from the resulting stress-strain curve. According to Chen et al., the stress-strain curves of the heated granite could be divided into three stages: (1) compaction stage, where the micro-cracks close when subjected to external loads, (2) elastic stage, where the stress-strain curve is almost linear and the stress reaches the maximum value at the end of the stage, and (3) softening stage, where the stress-strain curve declines steeply and the rock specimen fractures rapidly [113]. The modulus of elasticity can be obtained by the linear section of the stress-strain curve before the peak stress [113]. The yield strength can be equated with the peak stress on the yield stress curve. In order to attain the modulus of elasticity as a function of temperature, a stress-strain curve has to be obtained at each temperature. Prior to performing these measurements, the samples should be heated to the desired temperature at a heating rate of 2°C/s and held under constant conditions for two hours. Moreover, since the specimens are usually in the shape of pillars or blocks; therefore, multiple coals would have to be used in order to attain a regression function in terms of the carbon and ash composition.

8.2 Hot Flow Particle Wall Collision Experiment

While the uncertainty in the properties of the particle stiffness would have to be resolved for the model, validation is still necessary for both, the critical velocity sticking criteria and the criteria using the temperature of the critical viscosity and the contact angle. The major components of the hot flow version of the experiment would be the furnace, laser, camera, particle feeding mechanism, inlet gas configuration, and exhaust handling mechanism. The furnace for this experiment should be an electric drop tube furnace, and it should be comprised

of ceramic walls and at least six sapphire viewing ports to capture the images of the particle positions at different time intervals. The particle feeder will be an injection mechanism that can withstand the temperature of the hot furnace. The inlet gas mechanism will consist of four lines for the entry of the gases that include steam H_2 , CO, and CO_2 . These gases would travel through the pre-heater before entering the furnace and are expected to form a laminar flow upon entry. Once the gases exit the chamber, they would be directed to a catalytic converter as the first stage of the exhaust handling mechanism. The catalytic converter, with the aid of the air supply mechanism, would convert CO to CO_2 , and H_2 gas to water. The resulting gases from the catalytic converter will be directed to a heat exchanger where heat will be transferred between the exhaust gas and the process water. The cooled gas would then be vented to the atmosphere. The particles will be injected in parallel to the gas flow and the sheet of the laser, and a high-speed camera will be positioned perpendicular to the laser sheet to capture the images of the particle's position at set intervals of time. N_2 gas will be used to clear the furnace of other gases prior to and after the use of the furnace. Because the experiment would be performed at 1773 K and atmospheric pressure, instruments such as a thermocouple and a pressure gauge would be required. The laser must be aligned in parallel orientation to the initial and the rebound velocity of the particles in order to capture their images. Because the size fraction of the particles is 100 to 750 μm , a class IV laser would be required to supply enough light to capture the images. The diameter for the coal feed would be set at $1/8^{th}$ of an inch, and the diameter for the secondary flow will be set at one-half of an inch. The mass flow rate from the secondary air flow would be used to control the impact velocity of the coal or char particles entering the drop tube furnace.

8.3 Determining Coefficient of Restitution, Plastic Loss Factor, and Damping Ratio

Because of the high temperatures within the gasifier (1500 °C), there are no load cells or force sensors that can be used under such conditions. However, the shape factor as suggested by Ismail et al. [111] can be calculated based on the Hertzian stiffness and maximum compression. The equation for the shape factor, based on the maximum force and the time of the maximum force, can be equated to the Hertzian stiffness and the maximum compression function

$$\alpha = \frac{F_m t_m}{m v_0} = \frac{1.47 K_h u_m^{5/2}}{m v_0^2} . \quad (8.1)$$

Here K_h is defined by Equation 2.53. Equation 8.2 shows the expression for the maximum compression:

$$u_m = \left(\frac{m v_0^2}{4 K_h} \right)^{2/5} . \quad (8.2)$$

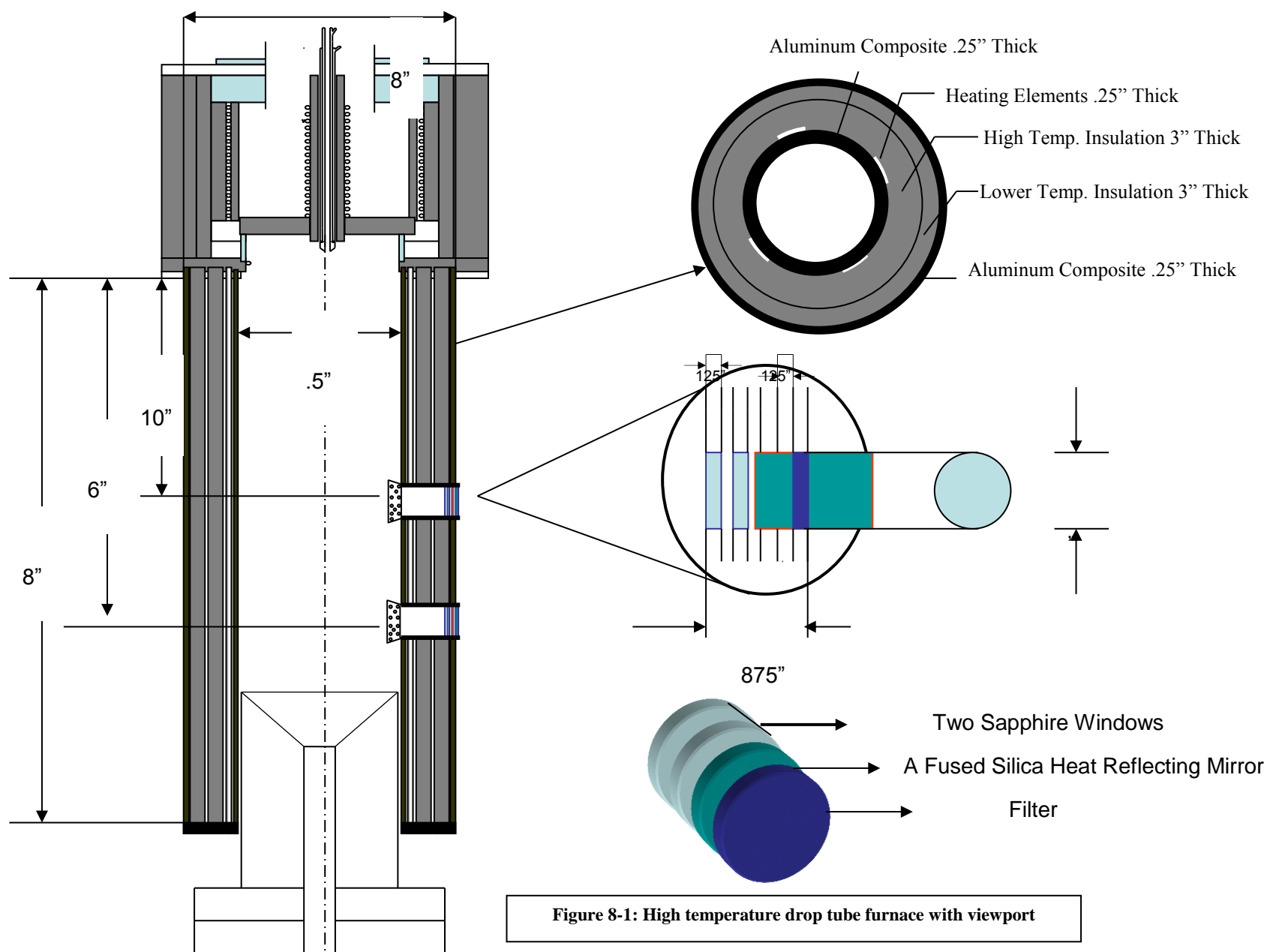
Once the shape factor is determined, the damping ratio can be calculated using

$$\alpha = \frac{1}{\sqrt{1-\zeta^2}} \tan^{-1} \left(\frac{\sqrt{1-\zeta^2}}{\zeta} \right) e^{-\left(\zeta / \sqrt{1-\zeta^2} \right) \tan^{-1} \left(\sqrt{1-\zeta^2} / \zeta \right)} . \quad (8.3)$$

Using Equation 8.4 for the natural frequency and Equation 8.5 for the time of compression with a known damping ratio, Equation 6.18 (for the coefficient of restitution as a function of the damping ratio and the plastic loss factor) can be used to determine the plastic loss factor and to validate the model. The damping ratio could then be used as a methodology to determine sticking based on whether the damping ratio is < 0.8 for rebound or ≥ 0.8 for sticking:

$$\omega_0 = \sqrt{\frac{K_y}{m}} , \quad (8.4)$$

$$\omega_0 t_c = \frac{1}{\sqrt{1-\zeta^2}} \left[\pi - \tan^{-1} \left(\frac{\sqrt{1-\zeta^2}}{\zeta} \right) \right] . \quad (8.5)$$



REFERENCES

1. Collot, A.G., *Matching gasification technologies to coal properties*. International Journal of Coal Geology, 2006. **65**(3-4): p. 191-212.
2. Choi, Y.C., et al., *Numerical analysis of the flow field inside an entrained-flow gasifier*. Korean Journal of Chemical Engineering, 2001. **18**(3): p. 376-381.
3. Kristiansen, A., *Understanding Coal Gasification*. IEA Coal Research. 1996, London: IEA Coal Research.
4. McDaniel, J., *Tampa Electric Polk Power Station Integrated Combined Cycle Project Final Report*. 2002, Tampa Electric Company: Tampa. p. 1-15-1-71.
5. Barroso, J., et al., *Study of coal ash deposition in an entrained flow reactor: Influence of coal type, blend composition and operating conditions*. Fuel Processing Technology, 2006. **87**(8): p. 737-752.
6. Wall, T.F., et al., *Coal ash fusion temperatures - New characterization techniques, and implications for slagging and fouling*. Progress in Energy and Combustion Science, 1998. **24**(4): p. 345-353.
7. Seggiani, M. and G. Pannocchia, *Prediction of coal ash thermal properties using partial least-squares regression*. Industrial & Engineering Chemistry Research, 2003. **42**(20): p. 4919-4926.
8. Senior, C.L. and S. Srinivasachar, *Viscosity of ash particles in combustion systems for prediction of particle sticking*. Energy & Fuels, 1995. **9**(2): p. 277-283.
9. Aquino, T.F.d., et al. *Evaluation of Viscosity Models for Slagging Entrained Gasifiers Using Bituminous Coals*. in *2011 International Pittsburgh Coal Conference*. 2011. Pittsburgh, PA.
10. Wells, J.J., et al., *The relationship between excluded mineral matter and the abrasion index of a coal*. Fuel, 2004. **83**(3): p. 359-364.
11. Varinot, C., et al., *Identification of the fragmentation mechanisms in wet-phase fine grinding in a stirred bead mill*. Chemical Engineering Science, 1997. **52**(20): p. 3605-3612.
12. Kelly, E.G. and D.J. Spottiswood, *THE BREAKAGE FUNCTION - WHAT IS IT REALLY*. Minerals Engineering, 1990. **3**(5): p. 405-414.
13. Lee, H., M.S. Klima, and P. Saylor, *Evaluation of a laboratory rod mill when grinding bituminous coal*. Fuel, 2011. **92**(1): p. 116-121.
14. Dunnrankin, D. and A.R. Kerstein, *Numerical-simulation of particle-size distribution evolution during pulverized coal combustion*. Combustion and Flame, 1987. **69**(2): p. 193-209.
15. Rozelle, P.L., S.V. Pisupati, and A.W. Scaroni, *Prediction of sorbent performance in a circulating fluidized bed boiler based on petrographic properties*. Journal of Engineering for Gas Turbines and Power-Transactions of the Asme, 2007. **129**(2): p. 565-571.
16. Rozelle, P.L., S.V. Pisupati, and A.W. Scaroni, *Effect of fuel properties on the bottom ash generation rate by a laboratory fluidized bed combustor*. Journal of Energy Resources Technology-Transactions of the Asme, 2007. **129**(2): p. 144-151.
17. Soundarajan, N., P.L. Rozelle, and S.V. Pisupati, *Development and use of a method for prediction of the ash split in a CFBC boiler to improve the energy efficiency*. Fuel. **102**: p. 9-15.
18. Shi, S.P., et al., *Modelling coal gasification with CFD and discrete phase method*. Journal of the Energy Institute, 2006. **79**(4): p. 217-221.
19. Wen, C.Y., H. Chen, and M. Onozaki, *User's manual for computer simulation and design of the moving-bed coal gasifier. Final report*, in *Other Information: Portions are illegible in microfiche products. Original copy available until stock is exhausted*. 1982. p. Medium: ED; Size: Pages: 99.
20. Yu, J.L., J.A. Lucas, and T.F. Wall, *Formation of the structure of chars during devolatilization of pulverized coal and its thermoproperties: A review*. Progress in Energy and Combustion Science, 2007. **33**(2): p. 135-170.
21. Bryers, R.W., *Fireside slagging, fouling, and high-temperature corrosion of heat-transfer surface due to impurities in steam-raising fuels*. Progress in Energy and Combustion Science, 1996. **22**(1): p. 29-120.

22. Bar-Ziv, E. and Kantorovich, II, *Mutual effects of porosity and reactivity in char oxidation*. Progress in Energy and Combustion Science, 2001. **27**(6): p. 667-697.
23. Feng, B. and S.K. Bhatia, *Percolative fragmentation of char particles during gasification*. Energy & Fuels, 2000. **14**(2): p. 297-307.
24. Jassim, E., et al., *The influence of fragmentation on the behavior of pyrite particles during pulverized coal combustion*. Fuel Processing Technology. **92**(5): p. 970-976.
25. Dacombe, P., et al., *Combustion-induced fragmentation behavior of isolated coal particles*. Fuel, 1999. **78**(15): p. 1847-1857.
26. Baxter, L.L., *Char fragmentation and fly-ash formation during pulverized-coal combustion*. Combustion and Flame, 1992. **90**(2): p. 174-184.
27. Yilmaz, S. and K.R. Cliffe, *Particle deposition simulation using the CFD code FLUENT*. Journal of the Institute of Energy, 2000. **73**(494): p. 65-68.
28. Khanna, R., et al., *Dissolution of carbon from coal-chars into liquid iron at 1550 degrees C*. Metallurgical and Materials Transactions B-Process Metallurgy and Materials Processing Science, 2005. **36**(6): p. 719-729.
29. Mehta, A.S. and V. Sahajwalla, *Influence of composition of slag and carbonaceous materials on the wettability at the slag/carbon interface during pulverised coal injection in a blast furnace*. Scandinavian Journal of Metallurgy, 2000. **29**(1): p. 17-29.
30. Mehta, A.S. and V. Sahajwalla, *Influence of temperature on the wettability at the slag/carbon interface during pulverised coal injection in a blast furnace*. Scandinavian Journal of Metallurgy, 2001. **30**(6): p. 370-378.
31. Mehta, A.S. and V. Sahajwalla, *Coal-char/slag interactions during pulverised coal injection in a blast furnace: Reaction kinetics and wetting investigations*. ISIJ International, 2003. **43**(10): p. 1512-1518.
32. Teasdale, S.L. and P.C. Hayes, *Observations of the reduction of FeO from slag by graphite, coke and coal char*. ISIJ International, 2005. **45**(5): p. 634-641.
33. Teasdale, S.L. and P.C. Hayes, *Kinetics of reduction of FeO from slag by graphite and coal chars*. ISIJ International, 2005. **45**(5): p. 642-650.
34. Hupa, M., B.J. Skrifvars, and A. Moilanen, *Measuring the sintering tendency of ash by a laboratory method*. Journal of the Institute of Energy, 1989. **62**(452): p. 131-137.
35. Nowok, J.W., et al., *The effect of surface-tension viscosity ratio of melts on the sintering propensity of amorphous coal ash slags*. Fuel, 1993. **72**(7): p. 1055-1061.
36. Jung, B.J. and H.H. Schobert, *Viscous sintering of coal ashes. I. Relationships of sinter point and sinter strength to particle-size and composition*. Energy & Fuels, 1991. **5**(4): p. 555-561.
37. Nowok, J.W., J.P. Hurley, and S.A. Benson, *The role of physical factors in mass transport during sintering of coal ashes and deposit deformation near the temperature of glass transformation*. Fuel Processing Technology, 1998. **56**(1-2): p. 89-101.
38. Nowok, J.W., et al., *Sintering behavior and strength development in various coal ashes*. Fuel, 1990. **69**(8): p. 1020-1028.
39. Takeda, M., et al., *Sintering behavior of various coal flying slag particles in the entrained-bed coal gasifiers - (Measurement of sintering temperatures of slag powder containing char and sintering temperatures of various coal slag)*. Jsme International Journal Series B-Fluids and Thermal Engineering, 2000. **43**(3): p. 497-502.
40. van Krevelen, D.W., ed. *Coal, Third Edition: Typology - Physics - Chemistry - Constitution (Coal Science & Technology)*. 3 ed. 1993 Elsevier Science.
41. Shackelford, J.F., *Introduction to Material Science for Engineers*. Seventh Edition ed. 2009: Pearson.
42. Marzec, A., *Macromolecular and molecular-model of coal structure*. Fuel Processing Technology, 1986. **14**: p. 39-46.
43. Ray, N.H., *Inorganic oxide glasses as ionic polymers*. British Polymer Journal, 1975. **7**(5): p. 307-317.

44. Suuberg, E.M., et al., *Coal macromolecular network structure-analysis - solvent swelling thermodynamics and its implications*. Energy & Fuels, 1994. **8**(6): p. 1247-1262.
45. Cody, G.D., A. Davis, and P.G. Hatcher, *Physical structural characterization of bituminous coals - stress-strain analysis in the pyridine-diluted state*. Energy & Fuels, 1993. **7**(4): p. 455-462.
46. Kobayashi, Y., H. Oda, and C. Yokokawa, *Temperature-dependence of propagation velocity of ultrasonic wave in coals*. Fuel, 1986. **65**(2): p. 177-181.
47. Fischer-Cripps, A.C., *A simple phenomenological approach to nanoindentation creep*. Materials Science and Engineering a-Structural Materials Properties Microstructure and Processing, 2004. **385**(1-2): p. 74-82.
48. Manias, E. *Voigt Model*. [cited; Available from: <http://www.plmsc.psu.edu/~manias/MatSE443/chapter11-5.pdf>.
49. Duffy, S. *Linear Viscoelasticity: Mechanical (Rheological) Models*. [cited; Available from: http://academic.csuohio.edu/duffy_s/Linear_Visco.pdf.
50. Yigit, A.S., A.P. Christoforou, and M.A. Majeed, *A nonlinear visco-elastoplastic impact model and the coefficient of restitution*. Nonlinear Dynamics, 2010. **66**(4): p. 509-521.
51. Hertz, H., *On the Contact of Elastic Solids*. Miscellaneous Papers, 1896: p. 146-152.
52. Johnson, K.L., K. Kendall, and A.D. Roberts, *Surface energy and contact of elastic solids*. Proceedings of the Royal Society of London Series a-Mathematical and Physical Sciences, 1971. **324**(1558): p. 301-&.
53. Maugis, D., *Contact, Adhesion and Rupture of Elastic Solids*. 2000, Verlag Berlin Heidelberg, Germany: Springer. 412.
54. Xu, D.W., K.M. Liechti, and K. Ravi-Chandar, *On the modified Tabor parameter for the JKR-DMT transition in the presence of a liquid meniscus*. Journal of Colloid and Interface Science, 2007. **315**: p. 772-785.
55. Kim, O.V. and P.F. Dunn, *A microsphere-surface impact model for implementation in computational fluid dynamics*. Journal of Aerosol Science, 2007. **38**(5): p. 532-549.
56. Li, X., P.F. Dunn, and R.M. Brach, *Experimental and numerical studies of microsphere oblique impact with planar surfaces*. Journal of Aerosol Science, 2000. **31**(5): p. 583-594.
57. Thornton, C. and Z.M. Ning, *A theoretical model for the stick/bounce behaviour of adhesive, elastic-plastic spheres*. Powder Technology, 1998. **99**(2): p. 154-162.
58. Wall, S., et al., *Measurements of kinetic-energy loss for particles impacting surfaces* Aerosol Science and Technology, 1990. **12**(4): p. 926-946.
59. Dunn, P.F., R.M. Brach, and M.J. Caylor, *Experiments on the low-velocity impact of microspheres with planar surfaces*. Aerosol Science and Technology, 1995. **23**(1): p. 80-95.
60. Dahneke, B., *Measurements of bouncing of small latex spheres*. Journal of Colloid and Interface Science, 1973. **45**(3): p. 584-590.
61. Gorham, D.A. and A.H. Kharaz, *The measurement of particle rebound characteristics*. Powder Technology, 2000. **112**(3): p. 193-202.
62. Cross, R., *Measurements of the horizontal coefficient of restitution for a superball and a tennis ball*. American Journal of Physics, 2002. **70**(5): p. 482-489.
63. Katta, R.R., et al., *High Velocity Oblique Impact and Coefficient of Restitution for Head Disk Interface Operational Shock*. Journal of Tribology-Transactions of the Asme, 2009. **131**(2).
64. Wu, C.Y., C. Thornton, and L.Y. Li, *A semi-analytical model for oblique impacts of elastoplastic spheres*. Proceedings of the Royal Society a-Mathematical Physical and Engineering Sciences, 2009. **465**(2103): p. 937-960.
65. Lorenz, A., C. Tuozzolo, and M.Y. Louge, *Measurements of impact properties of small, nearly spherical particles*. Experimental Mechanics, 1997. **37**(3): p. 292-298.
66. *Stress-strain curve*. [cited; Available from: http://en.wikipedia.org/wiki/Stress%E2%80%93strain_curve.
67. Ni, J., et al., *Submodel for Predicting Slag Deposition Formation in Slagging Gasification Systems*. Energy & Fuels, 2011. **25**(3): p. 1004-1009.

68. Inman, D.J., *Engineering Vibration*. Second ed. 2001, Upper Saddle River, NJ: Prentice Hall. 621.
69. Rushdi, A., et al., *Mechanistic prediction of ash deposition in a pilot-scale test facility*. Fuel, 2005. **84**(10): p. 1246-1258.
70. Li, S.H., Y.X. Wu, and K.J. Whitty, *Ash Deposition Behavior during Char-Slag Transition under Simulated Gasification Conditions*. Energy & Fuels, 2010. **24**: p. 1868-1876.
71. Ma, Z.H., et al., *A comprehensive slagging and fouling prediction tool for coal-fired boilers and its validation/application*. Fuel Processing Technology, 2007. **88**(11-12): p. 1035-1043.
72. Shimizu, T. and H. Tominaga, *A model of char capture by molten slag surface under high-temperature gasification conditions*. Fuel, 2006. **85**(2): p. 170-178.
73. McCarthy, F., et al., *Interfacial phenomena occurring during iron/char interactions in a blast furnace*. ISIJ International, 2005. **45**(9): p. 1261-1268.
74. Wu, C. and V. Sahajwalla, *Influence of melt carbon and sulfur on the wetting of solid graphite by Fe-C-S melts*. Metallurgical and Materials Transactions B-Process Metallurgy and Materials Processing Science, 1998. **29**(2): p. 471-477.
75. Li, S.H. and K.J. Whitty, *Investigation of Coal Char-Slag Transition during Oxidation: Effect of Temperature and Residual Carbon*. Energy & Fuels, 2009. **23**: p. 1998-2005.
76. Wang, X.H., et al., *Modeling of a coal-fired slagging combustor: Development of a slag submodel*. Combustion and Flame, 2007. **149**(3): p. 249-260.
77. Lee, B.E., et al., *Computational study of fouling deposit due to surface-coated particles in coal-fired power utility boilers*. Fuel, 2002. **81**(15): p. 2001-2008.
78. Tabakoff, W. and M.F. Malak, *Laser measurements of fly-ash rebound parameters for use in trajectory calculations*. Journal of Turbomachinery-Transactions of the Asme, 1987. **109**(4): p. 535-540.
79. Soundarrajan, N., N. Krishnamurthy, and S.V. Pisupati, *Physical and Chemical Characterization of Coal Particles Used as Entrained Flow Gasifier Feedstock: Heterogeneity in Mineral Matter Distribution*, in *2011 2nd International Conference on Advances in Energy Engineering*, D. Zeng, Editor. 2012, Elsevier Science Bv: Amsterdam. p. 1735-1740.
80. Soundarrajan, N., N. Krishnamurthy, and S.V. Pisupati, *Characterization of Size and Density Separated Fractions of a Bituminous Coal as a Feedstock for Entrained Slagging Gasification*. International Journal of Clean Coal and Energy, 2013. **2**(4): p. 58-67.
81. Feng, C., et al., *A Load-Based Multiple-Partial Unloading Micro-Indentation Technique for Mechanical Property Evaluation*. Experimental Mechanics, 2010. **50**(6): p. 737-743.
82. Machinist_Materials. *Machinist-Materials, Plastics Comparison Table*. [cited; Available from: http://www.machinistmaterials.com/comparison_table_for_plastics.htm].
83. Wu, T., E. Lester, and M. Cloke, *A burnout prediction model based around char morphology*. Energy & Fuels, 2006. **20**(3): p. 1175-1183.
84. Ni, J., et al., *Stochastic Modeling of the Particle Residence Time Distribution in an Opposed Multi-Burner Gasifier*. Chemical Engineering & Technology, 2008. **31**(10): p. 1487-1493.
85. Kantak, A.A. and R.H. Davis, *Oblique collisions and rebound of spheres from a wetted surface*. Journal of Fluid Mechanics, 2004. **509**: p. 63-81.
86. Slezak, A., et al., *CFD simulation of entrained-flow coal gasification: Coal particle density/size fraction effects*. Powder Technology, 2010. **203**(1): p. 98-108.
87. Hibbler, R.C., *Engineering Mechanics: Dynamics*. Eighth ed. 1997, Upper Saddle River, New Jersey: Prentice Hall.
88. NIH. *Research Services Branch*. [cited; Available from: <http://rsb.info.nih.gov/>].
89. Shaffer, F., *Method of Particle Trajectory Recognition in Particle Flows of High Particle Concentration using a Candidate Trajectory Tree Process with Variable Search Areas*. 2010: U.S.
90. Gopalan, B. and F. Shaffer, *A new method for decomposition of high speed particle image velocimetry data*. Powder Technology, 2012. **220**: p. 164-171.

91. Clayton, C.R.I., C.O.R. Abbireddy, and R. Schiebel, *A method of estimating the form of coarse particulates*. Geotechnique, 2009. **59**(6): p. 493-501.
92. Gibson, L.M., et al., *Image analysis measurements of particle coefficient of restitution for coal gasification applications*. Powder Technology, 2013. **247**: p. 30-43.
93. Li, H., W.G. Jiang, and X.Q. Feng, *Normal impact of adhesive microparticles with a film/substrate system: A numerical study*. Computational Materials Science, 2012. **60**: p. 130-136.
94. Kim, O.V. and P.F. Dunn, *Direct visualization and model validation of microsphere impact and surface capture*. Journal of Aerosol Science, 2008. **39**(4): p. 373-375.
95. Brach, R.M. and P.F. Dunn, *A mathematical-model of the impact and adhesion of microspheres*. Aerosol Science and Technology, 1992. **16**(1): p. 51-64.
96. Liu, G.Q., S.Q. Li, and Q. Yao, *A JKR-based dynamic model for the impact of micro-particle with a flat surface*. Powder Technology, 2011. **207**(1-3): p. 215-223.
97. Maw, N., J.R. Barber, and J.N. Fawcett, *The role of elastic tangential compliance in oblique impact*. Journal of Lubrication Technology-Transactions of the Asme, 1981. **103**(1): p. 74-80.
98. Ghiorso, M.S. and V.C. Kress, *An equation of state for silicate melts. II. Calibration of volumetric properties at 10(5) Pa*. American Journal of Science, 2004. **304**(8-9): p. 679-751.
99. Tomeczek, J. and H. Palugniok, *Kinetics of mineral matter transformation during coal combustion*. Fuel, 2002. **81**(10): p. 1251-1258.
100. Srinivasachar, S., et al., *Mineral behavior during coal combustion .2. illite transformations*. Progress in Energy and Combustion Science, 1990. **16**(4): p. 293-302.
101. Zhang, L.A., et al., *Experimental investigation of the combustion of bituminous coal in air and O(2)/CO(2) mixtures: 2. Variation of the transformation behaviour of mineral matter with bulk gas composition*. Fuel, 2011. **90**(4): p. 1361-1369.
102. Yuan, H.P., Q.F. Liang, and X. Gong, *Crystallization of Coal Ash Slags at High Temperatures and Effects on the Viscosity*. Energy & Fuels. **26**(6): p. 3717-3722.
103. Bool, L.E., T.W. Peterson, and J.O.L. Wendt, *The partitioning of iron during combustion of pulverized coal*. Combustion and Flame, 1995. **100**(1-2): p. 262-270.
104. Zeng, T.F., et al., *Iron transformations during combustion of Pittsburgh no. 8 coal*. Fuel, 2009. **88**(3): p. 566-572.
105. Srinivasachar, S., J.J. Helble, and A.A. Boni, *Mineral behavior during coal combustion .1. pyrite transformations*. Progress in Energy and Combustion Science, 1990. **16**(4): p. 281-292.
106. Qiu, J.R., F. Li, and C.G. Zheng, *Mineral transformation during combustion of coal blends*. International Journal of Energy Research, 1999. **23**(5): p. 453-463.
107. van Dyk, J.C., et al., *Viscosity predictions of the slag composition of gasified coal, utilizing FactSage equilibrium modelling*. Fuel, 2009. **88**(1): p. 67-74.
108. Gibson, L., et al., *Application of particle population model to determine the contribution to slag, flyash, syngas in entrained flow gasification from particle size distribution*. Energy & Fuels, 2013.
109. Hanao, M., et al., *Evaluation of surface tension of molten slag in multi-component systems*. ISIJ International, 2007. **47**(7): p. 935-939.
110. Massoudi, M. and P. Wang, *Slag Behavior in Gasifiers. Part II: Constitutive Modeling of Slag*. Energies. **6**(2): p. 807-838.
111. Ismail, K.A. and W.J. Stronge, *Viscoplastic analysis for direct impact of sports balls*. International Journal of Non-Linear Mechanics, 2012. **47**(4): p. 16-21.
112. Harb, J.N., C.J. Zygarlicke, and G.H. Richards, *The effect of particle composition and temperature on the deposition of 2 western united-states coals in a laminar drop-tube furnace*. Journal of the Institute of Energy, 1993. **66**(467): p. 91-98.
113. Chen, Y.-L., et al., *Experimental study on the influence of temperature on the mechanical properties of granite under uni-axial compression and fatigue loading*. International Journal of Rock Mechanics and Mining Sciences. **56**: p. 62-66.

**APPENDIX A CHARACTERIZATION OF PARTICLE SIZE DISTRIBUTION
OF BAILEY COAL**

Table A-1: Particle size analysis for particle size distribution of Bailey coal

Particle Size Classification							
PS1	PS2	PS3	PS4	PS5	PS6	PS7	
d>600µm	425-600µm	212-425µm	150-212µm	106-150µm	75-106µm	75-0µm	
Median Size	512.5	318.5	181	128	90.5	37.5	
Average Measurements taken in mm							
SG		Measurements in Chronological Order ---->				PSA	
		1	2	3	4	Average µm	Stand Dev
<1.3	sg1 ps1	854.3	838.7	896.2		863.1	29.7
	sg1 ps2	519.3	510.2	521.5		517.0	6.0
	sg1 ps3	313.8		313.8	315.5	314.4	1.0
	sg1 ps4	203.1	200.6	196.3		200.0	3.4
	sg1 ps5	137.9	136.6	134.9		136.5	1.5
	sg1 ps6	94.7	92.5	92.5		93.2	1.3
	sg1 ps7	26.1	25.5	26.6		26.1	0.6
1.3-1.9	sg2 ps1	751.1	750.0	705.1		735.4	26.3
	sg2 ps2	519.8	514.5	519.5		518.0	3.0
	sg2 ps3	320.7	322.0	326.4		323.0	3.0
	sg2 ps4		199.3	194.5	191.3	195.0	4.0
	sg2 ps5	137.2	133.6	130.6		133.8	3.3
	sg2 ps6	87.5	86.2	86.2		86.6	0.7
	sg2 ps7	0.3	0.7	0.6	0.5	0.5	0.1
1.9-2.6	sg3 ps1	832.8	814.5	728.3		791.9	55.8
	sg3 ps2	517.1	514.4	515.7		515.7	1.3
	sg3 ps3	339.4	345.4		330.6	338.5	7.4
	sg3 ps4		193.9	197.2	191.9	194.3	2.7
	sg3 ps5	124.2	126.2	120.5		123.6	2.9
	sg3 ps6	87.3	85.3	87.4	90.7	87.7	2.2
	sg3 ps7		0.5	0.9	0.5	0.6	0.2
>2.6	sg4 ps1		663.4	658.8	665.0	662.4	3.2
	sg4 ps2		492.7	485.3	501.3	493.1	8.0
	sg4 ps3	299.2	296.3	292.4		296.0	3.4
	sg4 ps4	206.9	197.4	201.5		201.9	4.8
	sg4 ps5	122.0	127.6	125.5		125.0	2.8
	sg4 ps6	92.0	94.2	91.9		92.7	1.3
	sg4 ps7	21.3	21.8	18.7		20.6	1.7

Table A-2: Mineral analysis for particle size distribution of Bailey coal

Specific Gravity	Particle Size	Weight Percent Minerals								
		Illite	Kaolinite	Pyrite	Quartz	Na	Ca	Mg	Fe	Sum
SG 1	PS 1	4.71	57.45	14.61	20.12	0.31	2.34	0.46	0.00	100
	PS 2	12.3	53.88	12.58	18.45	0.25	2.00	0.53	0.00	100
	PS 3	12.78	54.29	12.55	17.28	0.29	2.23	0.57	0.00	100
	PS 4	13.33	53.34	12.03	17.41	0.33	2.93	0.63	0.00	100
	PS 5	13.67	53.6	11.76	16.5	0.37	3.44	0.67	0.00	100
	PS 6	14.04	54.87	10.43	15.66	0.44	3.82	0.73	0.00	100
	PS 7	15.23	54.93	9.48	14.94	0.61	3.94	0.87	0.00	100
SG 2	PS 1	18.21	42.51	5.48	32.56	0.22	0.57	0.46	0.00	100
	PS 2	17.10	41.79	13.58	25.93	0.21	0.96	0.43	0.00	100
	PS 3	15.12	39.96	18.69	23.75	0.2	1.84	0.44	0.00	100
	PS 4	13.25	38.55	24.74	20.66	0.22	2.17	0.41	0.00	100
	PS 5	13.39	38.78	23.9	20.80	0.26	2.42	0.45	0.00	100
	PS 6	12.63	39.14	25.37	19.56	0.27	2.58	0.45	0.00	100
	PS 7	12.23	39.17	23.11	21.23	0.38	3.42	0.45	0.00	100
SG 3	PS 1	18.21	42.51	5.48	32.56	0.22	0.57	0.46	0.00	100
	PS 2	17.10	42.41	13.58	26.31	0.13	0.57	0.26	0.00	100
	PS 3	15.12	39.96	18.69	23.75	0.2	1.84	0.44	0.00	100
	PS 4	13.25	38.55	24.74	20.66	0.22	2.77	0.41	0.00	100
	PS 5	13.39	38.78	23.9	20.80	0.26	2.42	0.45	0.00	100
	PS 6	12.63	39.14	25.37	19.57	0.27	2.58	0.45	0.00	100
	PS 7	12.23	39.17	23.11	21.23	0.38	3.42	0.45	0.00	100
SG 4	PS 1	1.31	7.28	69.55	5.22	0.01	0.69	0.06	15.88	100
	PS 2	1.67	7.36	72.93	3.52	0	0.76	0.07	13.70	100
	PS 3	2.03	7.7	75.3	4.47	0.03	1.34	0.08	9.06	100
	PS 4	1.96	7.24	72.71	5.47	0.05	1.95	0.08	10.56	100
	PS 5	2.69	10.73	73.64	9.22	0.07	3.51	0.13	0.00	100
	PS 6	2.79	10.18	73.43	9.07	0.1	4.28	0.15	0.00	100
	PS 7	1.24	5.73	72.94	3.99	0.06	2.83	0.12	13.08	100

Table A-3: Ash composition for particle size distribution of Bailey coal

Specific Gravity	Particle Size	Weight Percent Ash								
		SiO ₂	Al ₂ O ₃	Fe ₂ O ₃	CaO	MgO	Na ₂ O	K ₂ O	SO ₃	Other
SG 1	PS 1	53.15	27.42	12.59	3.21	0.74	0.4	0.57	0.00	1.91
	PS 2	53.27	27.78	11.66	2.74	0.86	0.33	1.5	0.00	1.86
	PS 3	52.13	28.18	11.78	3.03	0.91	0.38	1.57	0.00	2.01
	PS 4	51.17	27.89	11.72	3.84	0.99	0.42	1.64	0.00	2.33
	PS 5	50.46	27.94	11.36	4.48	1.04	0.46	1.67	0.00	2.59
	PS 6	49.61	28.68	10.45	4.88	1.11	0.54	1.72	0.00	3.01
	PS 7	49.9	28.72	9.41	5.05	1.32	0.75	1.84	0.00	3.00
SG 2	PS 1	57.47	25.44	12.03	0.62	0.77	0.33	2.11	0.00	1.25
	PS 2	55.74	25.77	13.15	1.00	0.74	0.32	2.06	0.00	1.23
	PS 3	53.26	25.62	15.99	1.02	0.7	0.34	1.88	0.00	1.19
	PS 4	52.9	25.42	16.5	1.04	0.72	0.39	1.86	0.00	1.18
	PS 5	52.05	25.41	17.25	1.11	0.72	0.42	1.84	0.00	1.2
	PS 6	52.23	25.44	16.61	1.38	0.75	0.49	1.88	0.00	1.21
	PS 7	55.32	25.21	11.28	2.78	1.09	0.91	1.98	0.00	1.44
SG 3	PS 1	66.63	22.47	5.63	0.76	0.73	0.27	2.08	0.00	1.42
	PS 2	59.86	22.68	11.95	1.34	0.72	0.29	2.02	0.00	1.15
	PS 3	55.92	21.72	15.93	2.59	0.73	0.27	1.82	0.00	1.02
	PS 4	51.72	21.06	20.44	3.18	0.72	0.31	1.63	0.00	0.95
	PS 5	51.84	21.11	19.82	3.50	0.77	0.37	1.65	0.00	0.95
	PS 6	50.3	21.26	21.05	3.75	0.78	0.38	1.56	0.00	0.91
	PS 7	51.78	20.84	18.91	4.87	0.76	0.53	1.48	0.00	0.84
SG 4	PS 1	15.1	5.48	77.7	1.32	0.13	0.01	0.24	0.00	0.22
	PS 2	13.13	6.09	78.42	1.61	0.18	-0.01	0.33	0.00	0.24
	PS 3	16.41	6.89	72.5	3.20	0.23	0.06	0.42	0.00	0.29
	PS 4	16.93	6.05	71.86	4.19	0.21	0.1	0.38	0.00	0.28
	PS 5	18.01	5.97	69.91	5.12	0.23	0.1	0.35	0.00	0.31
	PS 6	17.85	5.78	68.82	6.29	0.26	0.14	0.37	0.00	0.5
	PS 7	12.52	4.67	76.03	5.79	0.29	0.13	0.24	0.00	0.33

APPENDIX B CALCULATION OF CRITICAL VELOCITIES

Table B-1: Calculated critical velocities for SG1 PS1

Temperature (K)	Surface Tension to Viscosity Ratio (σ/η) (cm/s)	Particle Young Modulus of Elasticity (GPa)	Particle Hertzian Stiffness (1/GPa)	Target Hertzian Stiffness (1/GPa)	Effective Stiffness (GPa)	Effective Contact Modulus (GPa)	K_h Hertzian Contact Stiffness (GPa)*m ⁵	Particle Yield Strength (Gpa)	Deformation of Yield Z (m)	Ky Linear Contact Stiffness (GPa)*m	A γ^2	B (Kh/Ky)	C $\{(3/2)(\gamma^2)(Kh/Ky)\}$	D C ⁴ *m	Critical Velocity V _{critical} E [Ky/B] ^(1/2)
1830	-3.32	12.000	0.02	2.63E-03	20.081	47.315	2.69E+12	0.0687	2.57E-02	6.47E+11	0.044	8529.67	558.88	20185.20	2.76
1818	-2.85	12.000	0.02	2.63E-03	20.081	47.315	2.69E+12	0.0666	2.42E-02	6.27E+11	0.044	8796.82	576.38	21475.88	2.63
1816	-2.86	12.000	0.02	2.63E-03	20.081	47.315	2.68E+12	0.0666	2.41E-02	6.24E+11	0.044	8796.31	576.35	22913.19	2.55
1807	-2.37	12.000	0.02	2.63E-03	20.081	47.315	2.69E+12	0.0645	2.27E-02	6.09E+11	0.044	9088.35	595.48	20383.10	2.66
1822	-3.10	12.000	0.02	2.63E-03	20.081	47.315	2.68E+12	0.0677	2.48E-02	6.32E+11	0.044	8653.06	566.96	22698.74	2.58
1800	-2.38	12.000	0.02	2.63E-03	20.081	47.315	2.67E+12	0.0645	2.24E-02	6.00E+11	0.044	9083.90	595.19	25788.23	2.37
1794	-2.19	12.000	0.02	2.63E-03	20.081	47.315	2.69E+12	0.0637	2.21E-02	6.01E+11	0.044	9199.17	602.74	26164.90	2.33
1819	-2.93	12.000	0.02	2.63E-03	20.081	47.315	2.68E+12	0.0670	2.42E-02	6.25E+11	0.044	8749.76	573.30	21680.92	2.63
1800	-2.33	12.000	0.02	2.63E-03	20.081	47.315	2.70E+12	0.0643	2.26E-02	6.08E+11	0.044	9112.53	597.07	24673.93	2.41
1825	-3.09	12.000	0.02	2.63E-03	20.081	47.315	2.69E+12	0.0677	2.50E-02	6.38E+11	0.044	8656.41	567.18	20023.52	2.75
1819	-2.84	12.000	0.02	2.63E-03	20.081	47.315	2.69E+12	0.0666	2.42E-02	6.27E+11	0.044	8803.91	576.85	20741.78	2.68
1818	-2.85	12.000	0.02	2.63E-03	20.081	47.315	2.69E+12	0.0666	2.41E-02	6.25E+11	0.044	8796.83	576.38	21168.89	2.65
1811	-2.72	12.000	0.02	2.63E-03	20.081	47.315	2.69E+12	0.0661	2.38E-02	6.22E+11	0.044	8874.34	581.46	23999.08	2.48
1816	-2.86	12.000	0.02	2.63E-03	20.081	47.315	2.69E+12	0.0667	2.41E-02	6.26E+11	0.044	8792.75	576.11	22703.95	2.56
1812	-2.55	12.000	0.02	2.63E-03	20.081	47.315	2.69E+12	0.0653	2.32E-02	6.14E+11	0.044	8980.71	588.43	20306.94	2.68
1815	-2.77	12.000	0.02	2.63E-03	20.081	47.315	2.69E+12	0.0663	2.39E-02	6.22E+11	0.044	8844.76	579.52	22208.32	2.58
1812	-2.70	12.000	0.02	2.63E-03	20.081	47.315	2.70E+12	0.0660	2.39E-02	6.25E+11	0.044	8886.67	582.27	23149.00	2.52
1830	-3.39	12.000	0.02	2.63E-03	20.081	47.315	2.72E+12	0.0691	2.66E-02	6.66E+11	0.044	8485.61	555.99	21296.10	2.69
1861	-4.56	12.000	0.02	2.63E-03	20.081	47.315	2.70E+12	0.0747	3.06E-02	7.08E+11	0.044	7849.41	514.31	13670.91	3.49
1830	-3.33	12.000	0.02	2.63E-03	20.081	47.315	2.69E+12	0.0688	2.58E-02	6.49E+11	0.044	8521.04	558.31	20444.63	2.74
1822	-3.02	12.000	0.02	2.63E-03	20.081	47.315	2.68E+12	0.0674	2.46E-02	6.31E+11	0.044	8698.31	569.93	21475.77	2.65
1807	-2.50	12.000	0.02	2.63E-03	20.081	47.315	2.69E+12	0.0651	2.30E-02	6.12E+11	0.044	9009.02	590.28	23023.41	2.51
1816	-2.76	12.000	0.02	2.63E-03	20.081	47.315	2.71E+12	0.0662	2.43E-02	6.34E+11	0.044	8855.84	580.25	21452.01	2.63
1847	-3.86	12.000	0.02	2.63E-03	20.081	47.315	2.69E+12	0.0713	2.77E-02	6.71E+11	0.044	8221.85	538.71	15576.16	3.20
1815	-2.82	12.000	0.02	2.63E-03	20.081	47.315	2.67E+12	0.0665	2.38E-02	6.19E+11	0.044	8818.74	577.82	22631.62	2.56
1797	-2.24	12.000	0.02	2.63E-03	20.081	47.315	2.68E+12	0.0639	2.21E-02	5.98E+11	0.044	9167.68	600.68	24824.00	2.40
1805	-2.43	12.000	0.02	2.63E-03	20.081	47.315	2.70E+12	0.0648	2.30E-02	6.13E+11	0.044	9049.71	592.95	23022.02	2.51
1827	-3.23	12.000	0.02	2.63E-03	20.081	47.315	2.71E+12	0.0683	2.58E-02	6.53E+11	0.044	8578.04	562.05	20688.30	2.72
1845	-3.92	12.000	0.02	2.63E-03	20.081	47.315	2.67E+12	0.0716	2.76E-02	6.66E+11	0.044	8190.70	536.67	17486.60	3.02
1796	-2.31	12.000	0.02	2.63E-03	20.081	47.315	2.69E+12	0.0642	2.25E-02	6.05E+11	0.044	9126.65	597.99	27247.36	2.30
1820	-2.94	12.000	0.02	2.63E-03	20.081	47.315	2.69E+12	0.0670	2.44E-02	6.30E+11	0.044	8747.27	573.13	21702.16	2.63
1815	-2.66	12.000	0.02	2.63E-03	20.081	47.315	2.72E+12	0.0658	2.41E-02	6.33E+11	0.044	8914.43	584.09	20064.92	2.71
1859	-4.35	12.000	0.02	2.63E-03	20.081	47.315	2.69E+12	0.0737	2.96E-02	6.94E+11	0.044	7957.88	521.41	13471.21	3.50
1819	-2.95	12.000	0.02	2.63E-03	20.081	47.315	2.70E+12	0.0670	2.47E-02	6.37E+11	0.044	8742.56	572.83	21973.81	2.61
1835	-3.39	12.000	0.02	2.63E-03	20.081	47.315	2.68E+12	0.0691	2.59E-02	6.48E+11	0.044	8488.69	556.19	18017.59	2.93
1811	-2.66	12.000	0.02	2.63E-03	20.081	47.315	2.69E+12	0.0658	2.37E-02	6.22E+11	0.044	8910.03	583.80	23188.80	2.52
1824	-3.06	12.000	0.02	2.63E-03	20.081	47.315	2.68E+12	0.0676	2.48E-02	6.33E+11	0.044	8676.82	568.52	20768.77	2.70
1809	-2.64	12.000	0.02	2.63E-03	20.081	47.315	2.68E+12	0.0657	2.33E-02	6.13E+11	0.044	8923.80	584.70	24086.72	2.47
1800	-2.40	12.000	0.02	2.63E-03	20.081	47.315	2.68E+12	0.0646	2.25E-02	6.03E+11	0.044	9071.62	594.39	25800.73	2.37
1802	-2.43	12.000	0.02	2.63E-03	20.081	47.315	2.72E+12	0.0647	2.34E-02	6.25E+11	0.044	9052.71	593.15	25583.98	2.38
1862	-4.46	12.000	0.02	2.63E-03	20.081	47.315	2.70E+12	0.0742	3.02E-02	7.03E+11	0.044	7901.49	517.72	12992.74	3.57
1829	-3.24	12.000	0.02	2.63E-03	20.081	47.315	2.72E+12	0.0684	2.60E-02	6.56E+11	0.044	8574.72	561.83	19586.12	2.79
1853	-4.20	12.000	0.02	2.63E-03	20.081	47.315	2.68E+12	0.0729	2.89E-02	6.84E+11	0.044	8038.96	526.72	15302.14	3.26
1811	-2.66	12.000	0.02	2.63E-03	20.081	47.315	2.70E+12	0.0658	2.38E-02	6.26E+11	0.044	8913.02	583.99	23252.56	2.51
1837	-3.63	12.000	0.02	2.63E-03	20.081	47.315	2.69E+12	0.0702	2.69E-02	6.63E+11	0.044	8351.71	547.22	19302.49	2.85
1824	-3.10	12.000	0.02	2.63E-03	20.081	47.315	2.72E+12	0.0677	2.55E-02	6.51E+11	0.044	8655.37	567.11	21330.97	2.66
1856	-4.35	12.000	0.02	2.63E-03	20.081	47.315	2.69E+12	0.0736	2.97E-02	6.96E+11	0.044	7959.75	521.53	14558.20	3.36
1825	-3.14	12.000	0.02	2.63E-03	20.081	47.315	2.69E+12	0.0679	2.52E-02	6.41E+11	0.044	8627.87	565.31	21295.47	2.67
1822	-3.01	12.000	0.02	2.63E-03	20.081	47.315	2.68E+12	0.0673	2.45E-02	6.29E+11	0.044	8708.05	570.56	20941.60	2.68
1805	-2.48	12.000	0.02	2.63E-03	20.081	47.315	2.67E+12	0.0650	2.27E-02	6.02E+11	0.044	9020.13	591.01	24127.62	2.45
1789	-2.11	12.000	0.02	2.63E-03	20.081	47.315	2.69E+12	0.0634	2.19E-02	5.97E+11	0.044	9246.33	605.83	27638.28	2.26

Table B-2: Calculated critical velocities for SG1 PS4

Temperature (K)	Surface Tension to Viscosity Ratio (σ/η) (cm/s)	Particle Young Modulus of Elasticity (GPa)	Particle Hertzian Stiffness (1/GPa)	Target Hertzian Stiffness (1/GPa)	Effective Stiffness (GPa)	Effective Contact Modulus (GPa)	K_h Hertzian Contact Stiffness (GPa)*m ⁵	Particle Yield Strength (Gpa)	Deformation of Yield Z (m)	K_y Linear Contact Stiffness (GPa)*m	A γ^2	B (Kh/Ky)	C $\{[3/2](\gamma^2)(Kh/Ky)\}$	D C^4*m	Critical Velocity $V_{critical}$ E [Ky/B] ^(1/2)
1851	-3.2	12.00	0.02	0.00	20.08	47.31	6.00E+08	0.07	0.00	3.20E+04	0.041	18754.59	1159.29	1223.75	5.11
1806	-3.0	12.00	0.02	0.00	20.08	47.31	6.00E+08	0.07	0.00	3.16E+04	0.041	18999.00	1174.39	3051.39	3.22
1853	-5.1	12.00	0.02	0.00	20.08	47.31	6.00E+08	0.08	0.00	3.62E+04	0.041	16564.62	1023.92	1845.02	4.43
1806	-2.9	12.00	0.02	0.00	20.08	47.31	6.00E+08	0.07	0.00	3.14E+04	0.041	19113.30	1181.46	2775.40	3.36
1848	-4.4	12.00	0.02	0.00	20.08	47.31	6.00E+08	0.07	0.00	3.48E+04	0.041	17266.10	1067.28	1678.57	4.55
1833	-3.6	12.00	0.02	0.00	20.08	47.31	6.00E+08	0.07	0.00	3.29E+04	0.041	18230.33	1126.88	1831.69	4.24
1872	-2.9	12.00	0.02	0.00	20.08	47.31	6.00E+08	0.07	0.00	3.12E+04	0.041	19211.78	1187.55	1037.76	5.49
1810	-3.2	12.00	0.02	0.00	20.08	47.31	6.00E+08	0.07	0.00	3.19E+04	0.041	18826.08	1163.71	2870.69	3.33
1839	-3.9	12.00	0.02	0.00	20.08	47.31	6.00E+08	0.07	0.00	3.35E+04	0.041	17921.97	1107.82	1738.14	4.39
1847	-4.6	12.00	0.02	0.00	20.08	47.31	6.00E+08	0.07	0.00	3.51E+04	0.041	17079.84	1055.76	1834.59	4.38
1815	-3.2	12.00	0.02	0.00	20.08	47.31	6.00E+08	0.07	0.00	3.20E+04	0.041	18782.46	1161.01	2408.86	3.64
1848	-4.2	12.00	0.02	0.00	20.08	47.31	6.00E+08	0.07	0.00	3.43E+04	0.041	17518.41	1082.87	1538.39	4.72
1840	-4.0	12.00	0.02	0.00	20.08	47.31	6.00E+08	0.07	0.00	3.37E+04	0.041	17792.42	1099.81	1744.82	4.40
1841	-4.4	12.00	0.02	0.00	20.08	47.31	6.00E+08	0.07	0.00	3.46E+04	0.041	17370.06	1073.70	2041.80	4.11
1821	-3.5	12.00	0.02	0.00	20.08	47.31	6.00E+08	0.07	0.00	3.27E+04	0.041	18357.42	1134.74	2589.93	3.55
1888	13.9	12.00	0.02	0.00	20.08	47.31	6.00E+08	0.02	0.00	1.02E+04	0.041	58837.25	3636.94	19751.54	0.72
1874	-4.9	12.00	0.02	0.00	20.08	47.31	6.00E+08	0.08	0.00	3.58E+04	0.041	16777.89	1037.10	1000.44	5.98
1822	-3.7	12.00	0.02	0.00	20.08	47.31	6.00E+08	0.07	0.00	3.30E+04	0.041	18197.99	1124.88	2788.17	3.44
1874	-5.5	12.00	0.02	0.00	20.08	47.31	6.00E+08	0.08	0.00	3.73E+04	0.041	16107.98	995.69	1080.85	5.87
1841	-4.3	12.00	0.02	0.00	20.08	47.31	6.00E+08	0.07	0.00	3.45E+04	0.041	17402.98	1075.74	2003.93	4.15
1806	-3.0	12.00	0.02	0.00	20.08	47.31	6.00E+08	0.07	0.00	3.15E+04	0.041	19032.74	1176.48	2909.72	3.29
1849	-4.5	12.00	0.02	0.00	20.08	47.31	6.00E+08	0.07	0.00	3.48E+04	0.041	17254.88	1066.58	1587.98	4.68
1877	-5.2	12.00	0.02	0.00	20.08	47.31	6.00E+08	0.08	0.00	3.67E+04	0.041	16371.14	1011.96	977.69	6.12
1847	-3.3	12.00	0.02	0.00	20.08	47.31	6.00E+08	0.07	0.00	3.22E+04	0.041	18636.18	1151.97	1292.44	4.99
1871	-5.0	12.00	0.02	0.00	20.08	47.31	6.00E+08	0.08	0.00	3.61E+04	0.041	16630.77	1028.01	1070.07	5.81
1844	-4.5	12.00	0.02	0.00	20.08	47.31	6.00E+08	0.07	0.00	3.48E+04	0.041	17246.14	1066.04	1899.75	4.28
1880	-4.3	12.00	0.02	0.00	20.08	47.31	6.00E+08	0.07	0.00	3.45E+04	0.041	17378.54	1074.23	909.64	6.16
1885	-6.5	12.00	0.02	0.00	20.08	47.31	6.00E+08	0.09	0.00	4.00E+04	0.041	14997.64	927.06	977.68	6.40
1859	-5.3	12.00	0.02	0.00	20.08	47.31	6.00E+08	0.08	0.00	3.68E+04	0.041	16327.45	1009.26	1649.61	4.72
1848	-4.2	12.00	0.02	0.00	20.08	47.31	6.00E+08	0.07	0.00	3.42E+04	0.041	17540.55	1084.24	1514.84	4.75
1848	-4.9	12.00	0.02	0.00	20.08	47.31	6.00E+08	0.08	0.00	3.59E+04	0.041	16728.44	1034.04	2140.41	4.09
1843	-4.5	12.00	0.02	0.00	20.08	47.31	6.00E+08	0.07	0.00	3.48E+04	0.041	17249.53	1066.25	1983.98	4.19
1838	-4.4	12.00	0.02	0.00	20.08	47.31	6.00E+08	0.07	0.00	3.46E+04	0.041	17366.50	1073.48	2355.70	3.83
1848	-4.4	12.00	0.02	0.00	20.08	47.31	6.00E+08	0.07	0.00	3.47E+04	0.041	17286.82	1068.56	1640.66	4.60
1824	-3.7	12.00	0.02	0.00	20.08	47.31	6.00E+08	0.07	0.00	3.30E+04	0.041	18162.35	1122.68	2527.55	3.62
1870	-5.7	12.00	0.02	0.00	20.08	47.31	6.00E+08	0.08	0.00	3.77E+04	0.041	15908.79	983.38	1242.63	5.51
1824	-3.7	12.00	0.02	0.00	20.08	47.31	6.00E+08	0.07	0.00	3.31E+04	0.041	18114.60	1119.73	2620.87	3.56
1844	-4.1	12.00	0.02	0.00	20.08	47.31	6.00E+08	0.07	0.00	3.40E+04	0.041	17661.34	1091.71	1633.39	4.56
1834	-4.0	12.00	0.02	0.00	20.08	47.31	6.00E+08	0.07	0.00	3.37E+04	0.041	17785.96	1099.41	2166.40	3.95
1835	-4.0	12.00	0.02	0.00	20.08	47.31	6.00E+08	0.07	0.00	3.37E+04	0.041	17793.31	1099.87	2059.59	4.05
1836	-4.0	12.00	0.02	0.00	20.08	47.31	6.00E+08	0.07	0.00	3.37E+04	0.041	17784.83	1099.34	2009.38	4.10
1842	-4.0	12.00	0.02	0.00	20.08	47.31	6.00E+08	0.07	0.00	3.37E+04	0.041	17828.62	1102.05	1622.70	4.55
1824	-3.7	12.00	0.02	0.00	20.08	47.31	6.00E+08	0.07	0.00	3.31E+04	0.041	18110.16	1119.45	2731.96	3.48

Table B-3: Calculated critical velocities for SG 1 PS7

Temperature (K)	Surface Tension to Viscosity Ratio (σ/η) (cm/s)	Particle Young Modulus of Elasticity (GPa)	Particle Hertzian Stiffness (1/GPa)	Target Hertzian Stiffness (1/GPa)	Effective Stiffness (GPa)	Effective Contact Modulus (GPa)	K_h Hertzian Contact Stiffness (GPa)*m ⁻⁵	Particle Yield Strength (Gpa)	Deformation of Yield Z (m)	K_y Linear Contact Stiffness (GPa)*m	A γ^2	B (Kh/Ky)	C {(3/2)(γ^2)(Kh/Ky)}	D C ⁴ *m	Critical Velocity V _{critical} E [Ky/B] ^{1/2}
1839	9	12.0	0.0	0.0	20.1	47.3	4.23E+08	0.0	0.0	7157.7	2.89	5.91E+04	2.56E+05	1.08E+10	8.12E-04
1835	8	12.0	0.0	0.0	20.1	47.3	4.23E+08	0.0	0.0	7316.2	2.89	5.78E+04	2.51E+05	9.94E+09	8.58E-04
1883	14	12.0	0.0	0.0	20.1	47.3	4.23E+08	0.0	0.0	5138.2	2.89	8.24E+04	3.57E+05	4.08E+10	3.55E-04
1885	14	12.0	0.0	0.0	20.1	47.3	4.23E+08	0.0	0.0	5060.5	2.89	8.36E+04	3.63E+05	4.34E+10	3.41E-04
1877	13	12.0	0.0	0.0	20.1	47.3	4.23E+08	0.0	0.0	5423.0	2.89	7.80E+04	3.38E+05	3.29E+10	4.06E-04
1847	9	12.0	0.0	0.0	20.1	47.3	4.23E+08	0.0	0.0	6812.9	2.89	6.21E+04	2.69E+05	1.32E+10	7.18E-04
1864	11	12.0	0.0	0.0	20.1	47.3	4.23E+08	0.0	0.0	6009.3	2.89	7.04E+04	3.05E+05	2.18E+10	5.25E-04
1856	10	12.0	0.0	0.0	20.1	47.3	4.23E+08	0.0	0.0	6382.1	2.89	6.63E+04	2.87E+05	1.72E+10	6.10E-04
1867	12	12.0	0.0	0.0	20.1	47.3	4.23E+08	0.0	0.0	5882.0	2.89	7.19E+04	3.12E+05	2.38E+10	4.97E-04
1863	11	12.0	0.0	0.0	20.1	47.3	4.23E+08	0.0	0.0	6061.0	2.89	6.98E+04	3.03E+05	2.11E+10	5.36E-04
1879	13	12.0	0.0	0.0	20.1	47.3	4.23E+08	0.0	0.0	5341.5	2.89	7.92E+04	3.43E+05	3.50E+10	3.91E-04
1877	13	12.0	0.0	0.0	20.1	47.3	4.23E+08	0.0	0.0	5399.6	2.89	7.84E+04	3.40E+05	3.35E+10	4.02E-04
1875	13	12.0	0.0	0.0	20.1	47.3	4.23E+08	0.0	0.0	5518.4	2.89	7.67E+04	3.32E+05	3.07E+10	4.24E-04
1882	14	12.0	0.0	0.0	20.1	47.3	4.23E+08	0.0	0.0	5163.6	2.89	8.20E+04	3.55E+05	4.00E+10	3.59E-04
1855	10	12.0	0.0	0.0	20.1	47.3	4.23E+08	0.0	0.0	6428.4	2.89	6.58E+04	2.85E+05	1.67E+10	6.21E-04
1886	14	12.0	0.0	0.0	20.1	47.3	4.23E+08	0.0	0.0	5012.2	2.89	8.44E+04	3.66E+05	4.51E+10	3.33E-04
1875	13	12.0	0.0	0.0	20.1	47.3	4.23E+08	0.0	0.0	5513.4	2.89	7.68E+04	3.33E+05	3.08E+10	4.23E-04
1878	13	12.0	0.0	0.0	20.1	47.3	4.23E+08	0.0	0.0	5353.2	2.89	7.91E+04	3.43E+05	3.47E+10	3.93E-04
1867	12	12.0	0.0	0.0	20.1	47.3	4.23E+08	0.0	0.0	5896.8	2.89	7.18E+04	3.11E+05	2.35E+10	5.00E-04
1874	12	12.0	0.0	0.0	20.1	47.3	4.23E+08	0.0	0.0	5554.2	2.89	7.62E+04	3.30E+05	2.99E+10	4.31E-04
1880	13	12.0	0.0	0.0	20.1	47.3	3.15E+08	0.0	0.0	2927.5	2.89	1.08E+05	4.67E+05	1.20E+11	1.56E-04
1859	11	12.0	0.0	0.0	20.1	47.3	3.15E+08	0.0	0.0	3468.9	2.89	9.09E+04	3.94E+05	6.07E+10	2.39E-04
1877	13	12.0	0.0	0.0	20.1	47.3	3.15E+08	0.0	0.0	3012.4	2.89	1.05E+05	4.54E+05	1.07E+11	1.68E-04
1853	10	12.0	0.0	0.0	20.1	47.3	3.15E+08	0.0	0.0	3642.4	2.89	8.66E+04	3.75E+05	4.99E+10	2.70E-04
1874	13	12.0	0.0	0.0	20.1	47.3	3.15E+08	0.0	0.0	3083.8	2.89	1.02E+05	4.43E+05	9.72E+10	1.78E-04
1877	13	12.0	0.0	0.0	20.1	47.3	3.15E+08	0.0	0.0	3006.5	2.89	1.05E+05	4.55E+05	1.08E+11	1.67E-04
1883	14	12.0	0.0	0.0	20.1	47.3	3.15E+08	0.0	0.0	2854.8	2.89	1.10E+05	4.79E+05	1.32E+11	1.47E-04
1868	12	12.0	0.0	0.0	20.1	47.3	3.15E+08	0.0	0.0	3247.1	2.89	9.71E+04	4.21E+05	7.90E+10	2.03E-04
1844	9	12.0	0.0	0.0	20.1	47.3	3.15E+08	0.0	0.0	3856.7	2.89	8.18E+04	3.55E+05	3.97E+10	3.12E-04
1887	14	12.0	0.0	0.0	20.1	47.3	3.15E+08	0.0	0.0	2734.4	2.89	1.15E+05	5.00E+05	1.57E+11	1.32E-04
1858	11	12.0	0.0	0.0	20.1	47.3	3.15E+08	0.0	0.0	3493.4	2.89	9.03E+04	3.91E+05	5.90E+10	2.43E-04
1860	11	12.0	0.0	0.0	20.1	47.3	3.15E+08	0.0	0.0	3440.9	2.89	9.17E+04	3.97E+05	6.27E+10	2.34E-04

Table B-4: Calculated critical velocities for SG2 PS1

Temperature (K)	Surface Tension to Viscosity Ratio (σ/η) (cm/s)	Particle Young Modulus of Elasticity (GPa)	Particle Hertzian Stiffness (1/GPa)	Target Hertzian Stiffness (1/GPa)	Effective Stiffness (GPa)	Effective Contact Modulus (GPa)	K_H Hertzian Contact Stiffness (GPa)*m ⁻⁵	Particle Yield Strength (Gpa)	Deformation of Yield Z (m)	Ky Linear Contact Stiffness (GPa)*m	A γ^2	B (Kh/Ky)	C (3/2)(γ^2)(Kh/Ky)}	D C^4 *m	Critical Velocity V _{critical} E [Ky/B] ^(1/2)
1880	-2.0	12.0	0.0185	2.63E-03	20.08	47.3	1.31E+09	0.063	5.15E-09	1.41E+05	0.0207	9.29E+03	288.97	2.15E+03	8.10
1873	-1.8	12.0	0.0185	2.63E-03	20.08	47.3	1.31E+09	0.062	5.02E-09	1.39E+05	0.0207	9.41E+03	292.76	2.24E+03	7.88
1838	-1.3	12.0	0.0185	2.63E-03	20.08	47.3	1.31E+09	0.060	4.69E-09	1.35E+05	0.0207	9.74E+03	302.86	2.61E+03	7.18
1854	-1.5	12.0	0.0185	2.63E-03	20.08	47.3	1.31E+09	0.061	4.78E-09	1.36E+05	0.0207	9.65E+03	300.08	2.45E+03	7.44
1868	-1.8	12.0	0.0185	2.63E-03	20.08	47.3	1.31E+09	0.062	5.02E-09	1.39E+05	0.0207	9.41E+03	292.69	2.28E+03	7.81
1878	-2.0	12.0	0.0185	2.63E-03	20.08	47.3	1.31E+09	0.063	5.12E-09	1.41E+05	0.0207	9.32E+03	289.77	2.17E+03	8.05
1888	-2.2	12.0	0.0185	2.63E-03	20.08	47.3	1.31E+09	0.064	5.25E-09	1.42E+05	0.0207	9.21E+03	286.31	2.06E+03	8.32
1864	-1.7	12.0	0.0185	2.63E-03	20.08	47.3	1.31E+09	0.062	4.92E-09	1.38E+05	0.0207	9.51E+03	295.68	2.34E+03	7.67
1889	-2.2	12.0	0.0185	2.63E-03	20.08	47.3	1.31E+09	0.064	5.26E-09	1.43E+05	0.0207	9.19E+03	285.87	2.05E+03	8.35
1874	-1.9	12.0	0.0185	2.63E-03	20.08	47.3	1.31E+09	0.062	5.05E-09	1.40E+05	0.0207	9.38E+03	291.91	2.22E+03	7.93
1857	-1.6	12.0	0.0185	2.63E-03	20.08	47.3	1.31E+09	0.061	4.86E-09	1.37E+05	0.0207	9.56E+03	297.44	2.41E+03	7.54
1851	-1.5	12.0	0.0185	2.63E-03	20.08	47.3	1.31E+09	0.061	4.81E-09	1.36E+05	0.0207	9.62E+03	299.14	2.48E+03	7.42
1825	-1.1	12.0	0.0185	2.63E-03	20.08	47.3	1.31E+09	0.059	4.57E-09	1.33E+05	0.0207	9.87E+03	306.88	2.73E+03	6.97
1884	-2.1	12.0	0.0185	2.63E-03	20.08	47.3	1.31E+09	0.063	5.19E-09	1.42E+05	0.0207	9.25E+03	287.83	2.11E+03	8.19
1833	-1.3	12.0	0.0185	2.63E-03	20.08	47.3	1.31E+09	0.060	4.64E-09	1.34E+05	0.0207	9.79E+03	304.37	2.66E+03	7.09
1872	-1.9	12.0	0.0185	2.63E-03	20.08	47.3	1.31E+09	0.062	5.04E-09	1.40E+05	0.0207	9.39E+03	292.10	2.24E+03	7.89
1832	-1.3	12.0	0.0185	2.63E-03	20.08	47.3	1.31E+09	0.060	4.64E-09	1.34E+05	0.0207	9.79E+03	304.47	2.66E+03	7.09
1870	-1.8	12.0	0.0185	2.63E-03	20.08	47.3	1.31E+09	0.062	4.98E-09	1.39E+05	0.0207	9.45E+03	293.92	2.46E+03	7.81
1883	-2.1	12.0	0.0185	2.63E-03	20.08	47.3	1.31E+09	0.063	5.21E-09	1.42E+05	0.0207	9.24E+03	287.38	2.11E+03	8.20
1887	-2.2	12.0	0.0185	2.63E-03	20.08	47.3	1.31E+09	0.064	5.27E-09	1.43E+05	0.0207	9.18E+03	285.65	2.06E+03	8.32
1857	-1.6	12.0	0.0185	2.63E-03	20.08	47.3	1.31E+09	0.061	4.84E-09	1.37E+05	0.0207	9.58E+03	298.03	2.41E+03	7.53
1864	-1.7	12.0	0.0185	2.63E-03	20.08	47.3	1.31E+09	0.062	4.94E-09	1.38E+05	0.0207	9.48E+03	294.92	2.33E+03	7.70
1844	-1.4	12.0	0.0185	2.63E-03	20.08	47.3	1.31E+09	0.061	4.74E-09	1.35E+05	0.0207	9.68E+03	301.08	2.55E+03	7.29
1872	-1.9	12.0	0.0185	2.63E-03	20.08	47.3	1.31E+09	0.062	5.05E-09	1.40E+05	0.0207	9.38E+03	291.75	2.24E+03	7.90
1852	-1.5	12.0	0.0185	2.63E-03	20.08	47.3	1.31E+09	0.061	4.82E-09	1.36E+05	0.0207	9.61E+03	298.78	2.46E+03	7.44
1871	-1.8	12.0	0.0185	2.63E-03	20.08	47.3	1.31E+09	0.062	4.97E-09	1.39E+05	0.0207	9.46E+03	294.27	2.27E+03	7.82
1870	-1.8	12.0	0.0185	2.63E-03	20.08	47.3	1.31E+09	0.062	5.01E-09	1.39E+05	0.0207	9.42E+03	292.89	2.26E+03	7.84
1864	-1.7	12.0	0.0185	2.63E-03	20.08	47.3	1.31E+09	0.062	4.91E-09	1.38E+05	0.0207	9.51E+03	295.93	2.34E+03	7.67
1868	-1.8	12.0	0.0185	2.63E-03	20.08	47.3	1.31E+09	0.062	5.01E-09	1.39E+05	0.0207	9.42E+03	292.85	2.28E+03	7.81
1857	-1.5	12.0	0.0185	2.63E-03	20.08	47.3	1.31E+09	0.061	4.81E-09	1.36E+05	0.0207	9.61E+03	299.06	2.42E+03	7.50
1829	-1.2	12.0	0.0185	2.63E-03	20.08	47.3	1.31E+09	0.060	4.61E-09	1.33E+05	0.0207	9.82E+03	305.49	2.69E+03	7.04
1865	-1.8	12.0	0.0185	2.63E-03	20.08	47.3	1.31E+09	0.062	4.98E-09	1.39E+05	0.0207	9.45E+03	293.82	2.31E+03	7.74
1854	-1.6	12.0	0.0185	2.63E-03	20.08	47.3	1.31E+09	0.061	4.85E-09	1.37E+05	0.0207	9.57E+03	297.76	2.44E+03	7.49
1883	-2.1	12.0	0.0185	2.63E-03	20.08	47.3	1.31E+09	0.063	5.19E-09	1.42E+05	0.0207	9.25E+03	287.78	2.12E+03	8.18
1858	-1.6	12.0	0.0185	2.63E-03	20.08	47.3	1.31E+09	0.061	4.86E-09	1.37E+05	0.0207	9.56E+03	297.36	2.40E+03	7.56
1855	-1.6	12.0	0.0185	2.63E-03	20.08	47.3	1.31E+09	0.061	4.84E-09	1.37E+05	0.0207	9.58E+03	298.05	2.43E+03	7.50
1872	-1.8	12.0	0.0185	2.63E-03	20.08	47.3	1.31E+09	0.062	5.01E-09	1.39E+05	0.0207	9.41E+03	292.82	2.25E+03	7.86
1870	-1.8	12.0	0.0185	2.63E-03	20.08	47.3	1.31E+09	0.062	4.96E-09	1.38E+05	0.0207	9.47E+03	294.57	2.28E+03	7.80
1858	-1.6	12.0	0.0185	2.63E-03	20.08	47.3	1.31E+09	0.061	4.85E-09	1.37E+05	0.0207	9.57E+03	297.73	2.40E+03	7.55
1880	-2.0	12.0	0.0185	2.63E-03	20.08	47.3	1.31E+09	0.063	5.15E-09	1.41E+05	0.0207	9.29E+03	289.00	2.15E+03	8.10
1856	-1.6	12.0	0.0185	2.63E-03	20.08	47.3	1.31E+09	0.061	4.83E-09	1.37E+05	0.0207	9.59E+03	298.31	2.42E+03	7.51
1855	-1.5	12.0	0.0185	2.63E-03	20.08	47.3	1.31E+09	0.061	4.81E-09	1.36E+05	0.0207	9.61E+03	299.03	2.44E+03	7.48
1853	-1.5	12.0	0.0185	2.63E-03	20.08	47.3	1.31E+09	0.061	4.78E-09	1.36E+05	0.0207	9.64E+03	299.92	2.46E+03	7.43
1853	-1.6	12.0	0.0185	2.63E-03	20.08	47.3	1.31E+09	0.061	4.84E-09	1.37E+05	0.0207	9.58E+03	298.11	2.45E+03	7.47
1844	-1.4	12.0	0.0185	2.63E-03	20.08	47.3	1.31E+09	0.060	4.71E-09	1.35E+05	0.0207	9.71E+03	302.05	2.55E+03	7.27
1860	-1.6	12.0	0.0185	2.63E-03	20.08	47.3	1.31E+09	0.061	4.89E-09	1.37E+05	0.0207	9.54E+03	296.67	2.38E+03	7.60
1883	-2.1	12.0	0.0185	2.63E-03	20.08	47.3	1.31E+09	0.063	5.21E-09	1.42E+05	0.0207	9.23E+03	287.19	2.11E+03	8.20
1849	-1.5	12.0	0.0185	2.63E-03	20.08	47.3	1.31E+09	0.061	4.77E-09	1.36E+05	0.0207	9.65E+03	300.28	2.50E+03	7.36
1856	-1.6	12.0	0.0185	2.63E-03	20.08	47.3	1.31E+09	0.061	4.83E-09	1.37E+05	0.0207	9.59E+03	298.42	2.42E+03	7.51
1855	-1.6	12.0	0.0185	2.63E-03	20.08	47.3	1.31E+09	0.061	4.85E-09	1.37E+05	0.0207	9.57E+03	297.61	2.43E+03	7.51
1836	-1.3	12.0	0.0185	2.63E-03	20.08	47.3	1.31E+09	0.060	4.67E-09	1.34E+05	0.0207	9.76E+03	303.47	2.63E+03	7.15
1865	-1.8	12.0	0.0185	2.63E-03	20.08	47.3	1.31E+09	0.062	4.96E-09	1.38E+05	0.0207	9.46E+03	294.40	2.32E+03	7.72
1865	-1.7	12.0	0.0185	2.63E-03	20.08	47.3	1.31E+09	0.062	4.92E-09	1.38E+05	0.0207	9.51E+03	295.72	2.33E+03	7.68
1848	-1.4	12.0	0.0185	2.63E-03	20.08	47.3	1.31E+09	0.061	4.74E-09	1.35E+05	0.0207	9.68E+03	301.14	2.51E+03	7.34
1872	-1.9	12.0	0.0185	2.63E-03	20.08	47.3	1.31E+09	0.062	5.04E-09	1.40E+05	0.0207	9.39E+03	292.19	2.25E+03	7.88
1869	-1.8	12.0	0.0185	2.63E-03	20.08	47.3	1.31E+09	0.062	5.01E-09	1.39E+05	0.0207	9.42E+03	293.00	2.28E+03	7.82

Table B-5: Calculated critical velocities for SG2 PS4

Temperature (K)	Surface Tension to Viscosity Ratio (σ/η) (cm/s)	Particle Young Modulus of Elasticity (GPa)	Particle Hertzian Stiffness (1/GPa)	Target Hertzian Stiffness (1/GPa)	Effective Stiffness (GPa)	Effective Contact Modulus (GPa)	K_h Hertzian Contact Stiffness (GPa)*m ⁻⁵	Particle Yield Strength (Gpa)	Deformation of Yield Z (m)	K_y Linear Contact Stiffness (GPa)*m	A γ^2	B (Kh/Ky)	C {(3/2)(γ^2)(Kh/Ky)}	D $C^4 \cdot m$	Critical Velocity $V_{critical}$ E [Ky/B] ^(1/2)
1840	-0.8	12.0	0.0185	2.63E-03	20.08	47.3	6.00E+08	0.058	9.17E-10	2.73E+04	0.0412	2.20E+04	1360.48	7.43E+03	1.92
1845	2.5	12.0	0.0185	2.63E-03	20.08	47.3	6.00E+08	0.046	5.87E-10	2.18E+04	0.0412	2.75E+04	1701.52	1.14E+04	1.38
1856	-0.4	12.0	0.0185	2.63E-03	20.08	47.3	6.00E+08	0.057	8.71E-10	2.66E+04	0.0412	2.26E+04	1396.13	7.62E+03	1.87
1805	-0.8	12.0	0.0185	2.63E-03	20.08	47.3	6.00E+08	0.058	9.11E-10	2.72E+04	0.0412	2.21E+04	1365.02	7.95E+03	1.85
1847	0.5	12.0	0.0185	2.63E-03	20.08	47.3	6.00E+08	0.053	7.66E-10	2.49E+04	0.0412	2.41E+04	1489.29	8.62E+03	1.70
1852	1.2	12.0	0.0185	2.63E-03	20.08	47.3	6.00E+08	0.051	7.02E-10	2.38E+04	0.0412	2.52E+04	1555.73	9.48E+03	1.59
1848	0.6	12.0	0.0185	2.63E-03	20.08	47.3	6.00E+08	0.053	7.61E-10	2.48E+04	0.0412	2.42E+04	1493.45	8.67E+03	1.69
1832	-1.6	12.0	0.0185	2.63E-03	20.08	47.3	6.00E+08	0.061	1.01E-09	2.87E+04	0.0412	2.09E+04	1294.14	7.26E+03	1.99
1803	-0.8	12.0	0.0185	2.63E-03	20.08	47.3	6.00E+08	0.058	9.13E-10	2.72E+04	0.0412	2.21E+04	1363.57	7.98E+03	1.85
1851	1.1	12.0	0.0185	2.63E-03	20.08	47.3	6.00E+08	0.051	7.08E-10	2.39E+04	0.0412	2.51E+04	1549.03	9.38E+03	1.60
1824	-1.0	12.0	0.0185	2.63E-03	20.08	47.3	6.00E+08	0.059	9.40E-10	2.76E+04	0.0412	2.17E+04	1344.13	7.58E+03	1.91
1884	0.1	12.0	0.0185	2.63E-03	20.08	47.3	6.00E+08	0.055	8.06E-10	2.56E+04	0.0412	2.35E+04	1451.28	8.26E+03	1.76
1832	0.4	12.0	0.0185	2.63E-03	20.08	47.3	6.00E+08	0.054	7.78E-10	2.51E+04	0.0412	2.39E+04	1477.88	8.41E+03	1.73
1847	-0.9	12.0	0.0185	2.63E-03	20.08	47.3	6.00E+08	0.059	9.33E-10	2.75E+04	0.0412	2.18E+04	1349.41	7.28E+03	1.94
1844	0.1	12.0	0.0185	2.63E-03	20.08	47.3	6.00E+08	0.055	8.13E-10	2.57E+04	0.0412	2.34E+04	1444.82	8.14E+03	1.78
1831	0.3	12.0	0.0185	2.63E-03	20.08	47.3	6.00E+08	0.054	7.94E-10	2.54E+04	0.0412	2.37E+04	1462.89	8.27E+03	1.75
1841	-0.5	12.0	0.0185	2.63E-03	20.08	47.3	6.00E+08	0.057	8.80E-10	2.67E+04	0.0412	2.25E+04	1389.38	7.65E+03	1.87
1824	-1.3	12.0	0.0185	2.63E-03	20.08	47.3	6.00E+08	0.060	9.82E-10	2.82E+04	0.0412	2.13E+04	1314.81	7.52E+03	1.94
1884	7.4	12.0	0.0185	2.63E-03	20.08	47.3	6.00E+08	0.033	3.04E-10	1.57E+04	0.0412	3.82E+04	2362.42	3.26E+04	0.69
1847	1.9	12.0	0.0185	2.63E-03	20.08	47.3	6.00E+08	0.049	6.39E-10	2.28E+04	0.0412	2.64E+04	1630.12	1.04E+04	1.48
1849	-0.7	12.0	0.0185	2.63E-03	20.08	47.3	6.00E+08	0.058	9.00E-10	2.70E+04	0.0412	2.22E+04	1373.31	7.46E+03	1.90
1828	-0.9	12.0	0.0185	2.63E-03	20.08	47.3	6.00E+08	0.058	9.27E-10	2.74E+04	0.0412	2.19E+04	1353.68	7.55E+03	1.91
1874	-0.2	12.0	0.0185	2.63E-03	20.08	47.3	6.00E+08	0.056	8.38E-10	2.61E+04	0.0412	2.30E+04	1423.24	7.88E+03	1.82
1847	-0.9	12.0	0.0185	2.63E-03	20.08	47.3	6.00E+08	0.059	9.30E-10	2.75E+04	0.0412	2.19E+04	1351.38	7.29E+03	1.94
1855	-1.4	12.0	0.0185	2.63E-03	20.08	47.3	6.00E+08	0.060	9.91E-10	2.83E+04	0.0412	2.12E+04	1309.26	6.86E+03	2.03
1848	1.4	12.0	0.0185	2.63E-03	20.08	47.3	6.00E+08	0.050	6.79E-10	2.35E+04	0.0412	2.56E+04	1581.37	9.78E+03	1.55
1834	-1.3	12.0	0.0185	2.63E-03	20.08	47.3	6.00E+08	0.060	9.81E-10	2.82E+04	0.0412	2.13E+04	1315.86	7.29E+03	1.97
1841	-0.6	12.0	0.0185	2.63E-03	20.08	47.3	6.00E+08	0.057	8.85E-10	2.68E+04	0.0412	2.24E+04	1385.07	7.61E+03	1.88
1847	-0.8	12.0	0.0185	2.63E-03	20.08	47.3	6.00E+08	0.058	9.10E-10	2.72E+04	0.0412	2.21E+04	1365.92	7.41E+03	1.91
1841	-0.6	12.0	0.0185	2.63E-03	20.08	47.3	6.00E+08	0.057	8.85E-10	2.68E+04	0.0412	2.24E+04	1385.23	7.61E+03	1.88
1852	0.3	12.0	0.0185	2.63E-03	20.08	47.3	6.00E+08	0.054	7.88E-10	2.53E+04	0.0412	2.37E+04	1467.92	8.40E+03	1.73
1830	-0.2	12.0	0.0185	2.63E-03	20.08	47.3	6.00E+08	0.056	8.39E-10	2.61E+04	0.0412	2.30E+04	1422.30	7.95E+03	1.81
1848	1.1	12.0	0.0185	2.63E-03	20.08	47.3	6.00E+08	0.051	7.12E-10	2.40E+04	0.0412	2.50E+04	1544.76	9.29E+03	1.61
1874	13.0	12.0	0.0185	2.63E-03	20.08	47.3	6.00E+08	0.023	1.45E-10	1.08E+04	0.0412	5.54E+04	3423.60	8.76E+04	0.35
1806	-0.8	12.0	0.0185	2.63E-03	20.08	47.3	6.00E+08	0.058	9.19E-10	2.73E+04	0.0412	2.20E+04	1359.13	7.94E+03	1.85
1826	-0.7	12.0	0.0185	2.63E-03	20.08	47.3	6.00E+08	0.058	9.02E-10	2.70E+04	0.0412	2.22E+04	1371.75	7.67E+03	1.88
1872	0.5	12.0	0.0185	2.63E-03	20.08	47.3	6.00E+08	0.053	7.71E-10	2.50E+04	0.0412	2.40E+04	1484.46	8.69E+03	1.70
1823	-0.7	12.0	0.0185	2.63E-03	20.08	47.3	6.00E+08	0.058	9.00E-10	2.70E+04	0.0412	2.22E+04	1373.95	7.71E+03	1.87
1838	-0.2	12.0	0.0185	2.63E-03	20.08	47.3	6.00E+08	0.056	8.43E-10	2.61E+04	0.0412	2.30E+04	1419.73	7.91E+03	1.82
1821	-1.0	12.0	0.0185	2.63E-03	20.08	47.3	6.00E+08	0.059	9.40E-10	2.76E+04	0.0412	2.17E+04	1344.26	7.64E+03	1.90
1883	0.4	12.0	0.0185	2.63E-03	20.08	47.3	6.00E+08	0.054	7.78E-10	2.51E+04	0.0412	2.39E+04	1477.15	8.63E+03	1.71
1839	2.2	12.0	0.0185	2.63E-03	20.08	47.3	6.00E+08	0.048	6.13E-10	2.23E+04	0.0412	2.69E+04	1664.98	1.07E+04	1.44
1871	2.5	12.0	0.0185	2.63E-03	20.08	47.3	6.00E+08	0.047	5.91E-10	2.19E+04	0.0412	2.74E+04	1694.40	1.21E+04	1.35
1846	-0.3	12.0	0.0185	2.63E-03	20.08	47.3	6.00E+08	0.056	8.54E-10	2.63E+04	0.0412	2.28E+04	1410.00	7.80E+03	1.84
1803	-0.8	12.0	0.0185	2.63E-03	20.08	47.3	6.00E+08	0.058	9.20E-10	2.73E+04	0.0412	2.20E+04	1358.37	7.98E+03	1.85
1885	1.2	12.0	0.0185	2.63E-03	20.08	47.3	6.00E+08	0.051	6.98E-10	2.38E+04	0.0412	2.52E+04	1559.45	9.94E+03	1.55
1855	0.2	12.0	0.0185	2.63E-03	20.08	47.3	6.00E+08	0.054	7.98E-10	2.54E+04	0.0412	2.36E+04	1458.87	8.30E+03	1.75
1848	-0.9	12.0	0.0185	2.63E-03	20.08	47.3	6.00E+08	0.058	9.23E-10	2.73E+04	0.0412	2.19E+04	1356.57	7.32E+03	1.93
1818	-0.9	12.0	0.0185	2.63E-03	20.08	47.3	6.00E+08	0.059	9.32E-10	2.75E+04	0.0412	2.18E+04	1349.93	7.71E+03	1.89

Table B-6: Calculated critical velocities for SG2 PS7

Temperature (K)	Surface Tension to Viscosity Ratio (σ/η) (cm/s)	Particle Young Modulus of Elasticity (GPa)	Particle Hertzian Stiffness (1/GPa)	Target Hertzian Stiffness (1/GPa)	Effective Stiffness (GPa)	Effective Contact Modulus (GPa)	K_h Hertzian Contact Stiffness (GPa)*m ⁵	Particle Yield Strength (GPa)	Deformation of Yield Z (m)	K_y Linear Contact Stiffness (GPa)*m	A γ^2	B (Kh/Ky)	C $\{(3/2)(\gamma^2)(Kh/Ky)\}$	D $C^4 \cdot m$	Critical Velocity $V_{critical}$ E [Ky/B] ^(1/2)
1868	9.6	12.0	0.0185	2.63E-03	20.08	47.3	3.15E+08	0.0289	6.24E-11	3.74E+03	0.00436	8.44E+04	551.37	9.00E-01	64.45
1841	7.2	12.0	0.0185	2.63E-03	20.08	47.3	3.15E+08	0.0340	8.68E-11	4.41E+03	0.00436	7.16E+04	467.57	4.65E-01	97.32
1874	10.3	12.0	0.0185	2.63E-03	20.08	47.3	3.15E+08	0.0276	5.71E-11	3.58E+03	0.00436	8.82E+04	576.39	1.07E+00	57.68
1876	10.5	12.0	0.0185	2.63E-03	20.08	47.3	3.15E+08	0.0273	5.59E-11	3.54E+03	0.00436	8.91E+04	582.39	1.12E+00	56.21
1876	10.4	12.0	0.0185	2.63E-03	20.08	47.3	3.15E+08	0.0274	5.62E-11	3.55E+03	0.00436	8.89E+04	581.01	1.11E+00	56.54
1855	8.4	12.0	0.0185	2.63E-03	20.08	47.3	3.15E+08	0.0314	7.38E-11	4.06E+03	0.00436	7.76E+04	507.18	6.44E-01	79.42
1878	10.7	12.0	0.0185	2.63E-03	20.08	47.3	3.15E+08	0.0268	5.38E-11	3.47E+03	0.00436	9.09E+04	593.63	1.21E+00	53.59
1853	8.2	12.0	0.0185	2.63E-03	20.08	47.3	3.15E+08	0.0319	7.61E-11	4.13E+03	0.00436	7.64E+04	499.39	6.06E-01	82.55
1845	7.5	12.0	0.0185	2.63E-03	20.08	47.3	3.15E+08	0.0333	8.29E-11	4.31E+03	0.00436	7.32E+04	478.33	5.10E-01	91.94
1878	10.7	12.0	0.0185	2.63E-03	20.08	47.3	3.15E+08	0.0269	5.43E-11	3.48E+03	0.00436	9.05E+04	591.40	1.19E+00	54.09
1837	6.9	12.0	0.0185	2.63E-03	20.08	47.3	3.15E+08	0.0347	9.02E-11	4.49E+03	0.00436	7.02E+04	458.63	4.31E-01	102.14
1866	9.4	12.0	0.0185	2.63E-03	20.08	47.3	3.15E+08	0.0293	6.42E-11	3.79E+03	0.00436	8.32E+04	543.74	8.51E-01	66.73
1888	11.9	12.0	0.0185	2.63E-03	20.08	47.3	3.15E+08	0.0248	4.61E-11	3.21E+03	0.00436	9.82E+04	641.35	1.65E+00	44.17
1870	9.8	12.0	0.0185	2.63E-03	20.08	47.3	3.15E+08	0.0285	6.10E-11	3.69E+03	0.00436	8.54E+04	557.95	9.44E-01	62.57
1872	10.0	12.0	0.0185	2.63E-03	20.08	47.3	3.15E+08	0.0281	5.93E-11	3.64E+03	0.00436	8.66E+04	565.81	9.98E-01	60.42
1879	10.8	12.0	0.0185	2.63E-03	20.08	47.3	3.15E+08	0.0267	5.34E-11	3.46E+03	0.00436	9.12E+04	595.96	1.23E+00	53.06
1863	9.1	12.0	0.0185	2.63E-03	20.08	47.3	3.15E+08	0.0298	6.67E-11	3.86E+03	0.00436	8.17E+04	533.57	7.89E-01	69.96
1845	7.5	12.0	0.0185	2.63E-03	20.08	47.3	3.15E+08	0.0332	8.27E-11	4.30E+03	0.00436	7.33E+04	478.95	5.12E-01	91.64
1861	8.9	12.0	0.0185	2.63E-03	20.08	47.3	3.15E+08	0.0303	6.88E-11	3.92E+03	0.00436	8.04E+04	525.12	7.40E-01	72.81
1863	9.1	12.0	0.0185	2.63E-03	20.08	47.3	3.15E+08	0.0298	6.67E-11	3.86E+03	0.00436	8.16E+04	533.40	7.88E-01	70.02
1875	10.4	12.0	0.0185	2.63E-03	20.08	47.3	3.15E+08	0.0274	5.64E-11	3.55E+03	0.00436	8.87E+04	579.87	1.10E+00	56.82
1875	10.3	12.0	0.0185	2.63E-03	20.08	47.3	3.15E+08	0.0276	5.69E-11	3.57E+03	0.00436	8.84E+04	577.49	1.08E+00	57.41
1887	11.7	12.0	0.0185	2.63E-03	20.08	47.3	3.15E+08	0.0251	4.71E-11	3.25E+03	0.00436	9.71E+04	634.49	1.58E+00	45.37
1875	10.3	12.0	0.0185	2.63E-03	20.08	47.3	3.15E+08	0.0276	5.69E-11	3.57E+03	0.00436	8.84E+04	577.40	1.08E+00	57.43
1877	10.5	12.0	0.0185	2.63E-03	20.08	47.3	3.15E+08	0.0272	5.53E-11	3.52E+03	0.00436	8.96E+04	585.57	1.14E+00	55.45
1870	9.8	12.0	0.0185	2.63E-03	20.08	47.3	3.15E+08	0.0285	6.10E-11	3.69E+03	0.00436	8.54E+04	557.85	9.43E-01	62.59
1847	7.7	12.0	0.0185	2.63E-03	20.08	47.3	3.15E+08	0.0328	8.08E-11	4.25E+03	0.00436	7.41E+04	484.46	5.36E-01	89.06
1836	6.8	12.0	0.0185	2.63E-03	20.08	47.3	3.15E+08	0.0348	9.09E-11	4.51E+03	0.00436	6.99E+04	456.78	4.24E-01	103.17
1890	12.2	12.0	0.0185	2.63E-03	20.08	47.3	3.15E+08	0.0244	4.45E-11	3.16E+03	0.00436	1.00E+05	653.22	1.77E+00	42.19
1872	10.0	12.0	0.0185	2.63E-03	20.08	47.3	3.15E+08	0.0281	5.93E-11	3.64E+03	0.00436	8.66E+04	565.53	9.96E-01	60.49
1864	9.2	12.0	0.0185	2.63E-03	20.08	47.3	3.15E+08	0.0296	6.57E-11	3.84E+03	0.00436	8.22E+04	537.30	8.11E-01	68.75
1890	12.1	12.0	0.0185	2.63E-03	20.08	47.3	3.15E+08	0.0244	4.46E-11	3.16E+03	0.00436	9.99E+04	652.50	1.76E+00	42.30
1859	8.8	12.0	0.0185	2.63E-03	20.08	47.3	3.15E+08	0.0306	7.00E-11	3.96E+03	0.00436	7.97E+04	520.81	7.16E-01	74.32
1863	9.1	12.0	0.0185	2.63E-03	20.08	47.3	3.15E+08	0.0299	6.69E-11	3.87E+03	0.00436	8.15E+04	532.54	7.83E-01	70.30
1841	7.2	12.0	0.0185	2.63E-03	20.08	47.3	3.15E+08	0.0340	8.66E-11	4.40E+03	0.00436	7.16E+04	467.99	4.67E-01	97.10
1851	8.0	12.0	0.0185	2.63E-03	20.08	47.3	3.15E+08	0.0322	7.79E-11	4.17E+03	0.00436	7.56E+04	493.67	5.78E-01	84.96
1878	10.7	12.0	0.0185	2.63E-03	20.08	47.3	3.15E+08	0.0268	5.40E-11	3.48E+03	0.00436	9.07E+04	592.87	1.20E+00	53.76
1858	8.7	12.0	0.0185	2.63E-03	20.08	47.3	3.15E+08	0.0308	7.12E-11	3.99E+03	0.00436	7.90E+04	516.17	6.91E-01	76.00
1877	10.6	12.0	0.0185	2.63E-03	20.08	47.3	3.15E+08	0.0271	5.52E-11	3.51E+03	0.00436	8.98E+04	586.45	1.15E+00	55.24
1856	8.5	12.0	0.0185	2.63E-03	20.08	47.3	3.15E+08	0.0312	7.29E-11	4.04E+03	0.00436	7.81E+04	510.26	6.60E-01	78.23
1871	9.9	12.0	0.0185	2.63E-03	20.08	47.3	3.15E+08	0.0283	5.99E-11	3.66E+03	0.00436	8.61E+04	562.78	9.77E-01	61.23
1867	9.5	12.0	0.0185	2.63E-03	20.08	47.3	3.15E+08	0.0291	6.36E-11	3.77E+03	0.00436	8.36E+04	546.31	8.67E-01	65.95
1877	10.6	12.0	0.0185	2.63E-03	20.08	47.3	3.15E+08	0.0270	5.47E-11	3.50E+03	0.00436	9.01E+04	588.71	1.17E+00	54.71
1877	10.6	12.0	0.0185	2.63E-03	20.08	47.3	3.15E+08	0.0270	5.48E-11	3.50E+03	0.00436	9.01E+04	588.40	1.17E+00	54.78
1865	9.3	12.0	0.0185	2.63E-03	20.08	47.3	3.15E+08	0.0294	6.49E-11	3.81E+03	0.00436	8.27E+04	540.51	8.31E-01	67.73
1888	11.9	12.0	0.0185	2.63E-03	20.08	47.3	3.15E+08	0.0249	4.63E-11	3.22E+03	0.00436	9.79E+04	639.95	1.63E+00	44.41
1862	9.0	12.0	0.0185	2.63E-03	20.08	47.3	3.15E+08	0.0301	6.77E-11	3.89E+03	0.00436	8.10E+04	529.33	7.64E-01	71.37
1877	10.6	12.0	0.0185	2.63E-03	20.08	47.3	3.15E+08	0.0270	5.48E-11	3.50E+03	0.00436	9.00E+04	588.33	1.17E+00	54.80
1874	10.3	12.0	0.0185	2.63E-03	20.08	47.3	3.15E+08	0.0277	5.73E-11	3.58E+03	0.00436	8.81E+04	575.45	1.07E+00	57.92
1841	7.2	12.0	0.0185	2.63E-03	20.08	47.3	3.15E+08	0.0340	8.67E-11	4.41E+03	0.00436	7.16E+04	467.69	4.66E-01	97.26
1880	10.9	12.0	0.0185	2.63E-03	20.08	47.3	3.15E+08	0.0264	5.24E-11	3.43E+03	0.00436	9.21E+04	601.66	1.28E+00	51.81
1854	8.3	12.0	0.0185	2.63E-03	20.08	47.3	3.15E+08	0.0315	7.45E-11	4.08E+03	0.00436	7.73E+04	504.79	6.32E-01	80.36
1847	7.6	12.0	0.0185	2.63E-03	20.08	47.3	3.15E+08	0.0330	8.14E-11	4.27E+03	0.00436	7.39E+04	482.66	5.28E-01	89.89
1879	10.8	12.0	0.0185	2.63E-03	20.08	47.3	3.15E+08	0.0267	5.34E-11	3.46E+03	0.00436	9.13E+04	596.28	1.23E+00	52.99
1856	8.5	12.0	0.0185	2.63E-03	20.08	47.3	3.15E+08	0.0312	7.28E-11	4.04E+03	0.00436	7.81E+04	510.55	6.62E-01	78.11
1884	11.3	12.0	0.0185	2.63E-03	20.08	47.3	3.15E+08	0.0257	4.96E-11	3.33E+03	0.00436	9.46E+04	618.21	1.42E+00	48.42
1837	6.9	12.0	0.0185	2.63E-03	20.08	47.3	3.15E+08	0.0347	9.02E-11	4.49E+03	0.00436	7.02E+04	458.63	4.31E-01	102.14

Table B-7: Calculated critical velocities for SG3 PS1

Temperature (K)	Surface Tension to Viscosity Ratio (σ/η) (cm/s)	Particle Young Modulus of Elasticity (GPa)	Particle Hertzian Stiffness (1/GPa)	Target Hertzian Stiffness (1/GPa)	Effective Stiffness (GPa)	Effective Contact Modulus (GPa)	K_h Hertzian Contact Stiffness (GPa)*m ³	Particle Yield Strength (GPa)	Deformation of Yield Z (m)	Ky Linear Contact Stiffness (GPa)*m	A γ^2	B (Kh/Ky)	C $\{(\beta/2)(\gamma^2)\}(Kh/Ky)\}$	D C^2*m	Critical Velocity $V_{critical}$ E [Ky/B] ^(1/2)
1896	7.5	12.0	0.0185	2.63E-03	20.08	47.3	1.31E+09	0.0333	1.43E-09	7.44E+04	9.80E-03	1.76E+04	259.01	2.50E+03	5.45
1872	5.7	12.0	0.0185	2.63E-03	20.08	47.3	1.31E+09	0.0375	1.82E-09	8.38E+04	9.80E-03	1.56E+04	229.89	1.55E+03	7.35
1873	5.8	12.0	0.0185	2.63E-03	20.08	47.3	1.31E+09	0.0372	1.79E-09	8.32E+04	9.80E-03	1.58E+04	231.61	1.59E+03	7.22
1858	5.0	12.0	0.0185	2.63E-03	20.08	47.3	1.31E+09	0.0395	2.01E-09	8.82E+04	9.80E-03	1.49E+04	218.42	1.25E+03	8.40
1881	6.5	12.0	0.0185	2.63E-03	20.08	47.3	1.31E+09	0.0357	1.65E-09	7.99E+04	9.80E-03	1.64E+04	241.25	1.86E+03	6.55
1844	4.2	12.0	0.0185	2.63E-03	20.08	47.3	1.31E+09	0.0416	2.24E-09	9.30E+04	9.80E-03	1.41E+04	207.20	1.02E+03	9.52
1877	6.1	12.0	0.0185	2.63E-03	20.08	47.3	1.31E+09	0.0365	1.72E-09	8.15E+04	9.80E-03	1.61E+04	236.26	1.72E+03	6.89
1869	5.6	12.0	0.0185	2.63E-03	20.08	47.3	1.31E+09	0.0379	1.85E-09	8.47E+04	9.80E-03	1.55E+04	227.57	1.48E+03	7.56
1853	4.7	12.0	0.0185	2.63E-03	20.08	47.3	1.31E+09	0.0403	2.10E-09	9.00E+04	9.80E-03	1.46E+04	214.08	1.16E+03	8.82
1859	4.9	12.0	0.0185	2.63E-03	20.08	47.3	1.31E+09	0.0395	2.02E-09	8.84E+04	9.80E-03	1.48E+04	217.96	1.26E+03	8.39
1866	5.4	12.0	0.0185	2.63E-03	20.08	47.3	1.31E+09	0.0383	1.90E-09	8.56E+04	9.80E-03	1.53E+04	225.00	1.42E+03	7.77
1878	6.2	12.0	0.0185	2.63E-03	20.08	47.3	1.31E+09	0.0363	1.70E-09	8.11E+04	9.80E-03	1.62E+04	237.65	1.76E+03	6.78
1864	5.2	12.0	0.0185	2.63E-03	20.08	47.3	1.31E+09	0.0387	1.94E-09	8.66E+04	9.80E-03	1.51E+04	222.43	1.36E+03	7.98
1873	5.9	12.0	0.0185	2.63E-03	20.08	47.3	1.31E+09	0.0371	1.78E-09	8.30E+04	9.80E-03	1.58E+04	232.23	1.61E+03	7.19
1860	5.0	12.0	0.0185	2.63E-03	20.08	47.3	1.31E+09	0.0393	2.00E-09	8.79E+04	9.80E-03	1.49E+04	219.27	1.28E+03	8.29
1883	6.5	12.0	0.0185	2.63E-03	20.08	47.3	1.31E+09	0.0356	1.64E-09	7.97E+04	9.80E-03	1.65E+04	241.87	1.90E+03	6.47
1873	5.8	12.0	0.0185	2.63E-03	20.08	47.3	1.31E+09	0.0372	1.79E-09	8.32E+04	9.80E-03	1.58E+04	231.58	1.59E+03	7.24
1869	5.6	12.0	0.0185	2.63E-03	20.08	47.3	1.31E+09	0.0379	1.86E-09	8.48E+04	9.80E-03	1.55E+04	227.17	1.48E+03	7.58
1865	5.3	12.0	0.0185	2.63E-03	20.08	47.3	1.31E+09	0.0385	1.92E-09	8.61E+04	9.80E-03	1.52E+04	223.83	1.40E+03	7.85
1880	6.3	12.0	0.0185	2.63E-03	20.08	47.3	1.31E+09	0.0362	1.69E-09	8.08E+04	9.80E-03	1.62E+04	238.33	1.79E+03	6.72
1883	6.6	12.0	0.0185	2.63E-03	20.08	47.3	1.31E+09	0.0355	1.63E-09	7.93E+04	9.80E-03	1.65E+04	243.02	1.93E+03	6.41
1867	5.5	12.0	0.0185	2.63E-03	20.08	47.3	1.31E+09	0.0382	1.88E-09	8.53E+04	9.80E-03	1.54E+04	225.86	1.44E+03	7.69
1861	5.1	12.0	0.0185	2.63E-03	20.08	47.3	1.31E+09	0.0392	1.99E-09	8.76E+04	9.80E-03	1.50E+04	219.82	1.30E+03	8.22
1838	3.9	12.0	0.0185	2.63E-03	20.08	47.3	1.31E+09	0.0423	2.32E-09	9.47E+04	9.80E-03	1.38E+04	203.55	9.53E+02	9.97
1868	5.6	12.0	0.0185	2.63E-03	20.08	47.3	1.31E+09	0.0378	1.85E-09	8.45E+04	9.80E-03	1.55E+04	228.11	1.48E+03	7.55
1855	4.8	12.0	0.0185	2.63E-03	20.08	47.3	1.31E+09	0.0399	2.06E-09	8.92E+04	9.80E-03	1.47E+04	216.04	1.20E+03	8.62
1841	4.0	12.0	0.0185	2.63E-03	20.08	47.3	1.31E+09	0.0421	2.29E-09	9.40E+04	9.80E-03	1.39E+04	204.93	9.79E+02	9.80
1871	5.8	12.0	0.0185	2.63E-03	20.08	47.3	1.31E+09	0.0374	1.81E-09	8.36E+04	9.80E-03	1.57E+04	230.40	1.56E+03	7.33
1875	5.9	12.0	0.0185	2.63E-03	20.08	47.3	1.31E+09	0.0370	1.77E-09	8.27E+04	9.80E-03	1.58E+04	232.88	1.63E+03	7.11
1867	5.5	12.0	0.0185	2.63E-03	20.08	47.3	1.31E+09	0.0381	1.87E-09	8.51E+04	9.80E-03	1.54E+04	226.41	1.45E+03	7.66
1875	6.0	12.0	0.0185	2.63E-03	20.08	47.3	1.31E+09	0.0368	1.75E-09	8.22E+04	9.80E-03	1.59E+04	234.26	1.66E+03	7.03
1849	4.4	12.0	0.0185	2.63E-03	20.08	47.3	1.31E+09	0.0409	2.16E-09	9.14E+04	9.80E-03	1.43E+04	210.80	1.10E+03	9.13
1874	5.9	12.0	0.0185	2.63E-03	20.08	47.3	1.31E+09	0.0370	1.77E-09	8.27E+04	9.80E-03	1.58E+04	232.99	1.63E+03	7.11
1863	5.2	12.0	0.0185	2.63E-03	20.08	47.3	1.31E+09	0.0389	1.95E-09	8.69E+04	9.80E-03	1.51E+04	221.79	1.34E+03	8.05
1882	6.4	12.0	0.0185	2.63E-03	20.08	47.3	1.31E+09	0.0358	1.66E-09	8.00E+04	9.80E-03	1.64E+04	240.84	1.87E+03	6.54
1878	6.2	12.0	0.0185	2.63E-03	20.08	47.3	1.31E+09	0.0363	1.71E-09	8.12E+04	9.80E-03	1.61E+04	237.15	1.75E+03	6.81
1875	5.9	12.0	0.0185	2.63E-03	20.08	47.3	1.31E+09	0.0370	1.77E-09	8.28E+04	9.80E-03	1.58E+04	232.76	1.63E+03	7.12
1871	5.8	12.0	0.0185	2.63E-03	20.08	47.3	1.31E+09	0.0374	1.81E-09	8.37E+04	9.80E-03	1.57E+04	230.21	1.55E+03	7.35
1865	5.3	12.0	0.0185	2.63E-03	20.08	47.3	1.31E+09	0.0385	1.91E-09	8.60E+04	9.80E-03	1.52E+04	223.99	1.39E+03	7.86
1868	5.5	12.0	0.0185	2.63E-03	20.08	47.3	1.31E+09	0.0381	1.88E-09	8.52E+04	9.80E-03	1.54E+04	226.25	1.45E+03	7.66
1864	5.3	12.0	0.0185	2.63E-03	20.08	47.3	1.31E+09	0.0387	1.93E-09	8.64E+04	9.80E-03	1.52E+04	222.91	1.37E+03	7.96
1866	5.5	12.0	0.0185	2.63E-03	20.08	47.3	1.31E+09	0.0382	1.88E-09	8.53E+04	9.80E-03	1.54E+04	225.78	1.43E+03	7.72
1868	5.6	12.0	0.0185	2.63E-03	20.08	47.3	1.31E+09	0.0379	1.86E-09	8.48E+04	9.80E-03	1.55E+04	227.24	1.47E+03	7.59
1861	5.1	12.0	0.0185	2.63E-03	20.08	47.3	1.31E+09	0.0392	1.99E-09	8.77E+04	9.80E-03	1.49E+04	219.65	1.30E+03	8.23
1855	4.7	12.0	0.0185	2.63E-03	20.08	47.3	1.31E+09	0.0401	2.08E-09	8.96E+04	9.80E-03	1.46E+04	215.04	1.19E+03	8.69
1864	5.3	12.0	0.0185	2.63E-03	20.08	47.3	1.31E+09	0.0386	1.93E-09	8.63E+04	9.80E-03	1.52E+04	223.30	1.38E+03	7.91
1849	4.4	12.0	0.0185	2.63E-03	20.08	47.3	1.31E+09	0.0409	2.17E-09	9.15E+04	9.80E-03	1.43E+04	210.45	1.09E+03	9.16
1880	6.3	12.0	0.0185	2.63E-03	20.08	47.3	1.31E+09	0.0361	1.69E-09	8.08E+04	9.80E-03	1.62E+04	238.51	1.79E+03	6.71
1886	6.7	12.0	0.0185	2.63E-03	20.08	47.3	1.31E+09	0.0350	1.59E-09	7.84E+04	9.80E-03	1.67E+04	245.88	2.03E+03	6.22
1867	5.5	12.0	0.0185	2.63E-03	20.08	47.3	1.31E+09	0.0381	1.88E-09	8.52E+04	9.80E-03	1.54E+04	226.06	1.44E+03	7.69
1869	5.6	12.0	0.0185	2.63E-03	20.08	47.3	1.31E+09	0.0379	1.85E-09	8.47E+04	9.80E-03	1.55E+04	227.57	1.49E+03	7.54
1849	4.5	12.0	0.0185	2.63E-03	20.08	47.3	1.31E+09	0.0408	2.16E-09	9.13E+04	9.80E-03	1.44E+04	210.98	1.10E+03	9.12
1860	5.1	12.0	0.0185	2.63E-03	20.08	47.3	1.31E+09	0.0391	1.98E-09	8.75E+04	9.80E-03	1.50E+04	220.27	1.29E+03	8.22
1846	4.3	12.0	0.0185	2.63E-03	20.08	47.3	1.31E+09	0.0414	2.21E-09	9.25E+04	9.80E-03	1.42E+04	208.27	1.05E+03	9.40
1882	6.4	12.0	0.0185	2.63E-03	20.08	47.3	1.31E+09	0.0358	1.66E-09	8.00E+04	9.80E-03	1.64E+04	240.70	1.86E+03	6.56

Table B-8: Calculated critical velocities for SG3 PS4

Temperature (K)	Surface Tension to Viscosity Ratio (σ/η) (cm/s)	Particle Young Modulus of Elasticity (GPa)	Particle Hertzian Stiffness (1/GPa)	Target Hertzian Stiffness (1/GPa)	Effective Stiffness (GPa)	Effective Contact Modulus (GPa)	K_h Hertzian Contact Stiffness (GPa)*m ⁵	Particle Yield Strength (GPa)	Deformation of Yield Z (m)	K_y Linear Contact Stiffness (GPa)*m	A γ^2	B (Kh/Ky)	C {(3/2)(γ^2)(Kh/Ky)}	D $C^4 \cdot m$	Critical Velocity V _{critical} E [Ky/B] ^{1/2}
1821	6.3	12.0	0.0185	2.63E-03	20.08	47.3	6.00E+08	0.0360	3.51E-10	1.69E+04	6.60E-02	3.56E+04	3522.23	7.13E+05	0.15
1838	7.8	12.0	0.0185	2.63E-03	20.08	47.3	6.00E+08	0.0327	2.89E-10	1.53E+04	6.60E-02	3.92E+04	3879.21	1.02E+06	0.12
1828	7.5	12.0	0.0185	2.63E-03	20.08	47.3	6.00E+08	0.0333	3.01E-10	1.56E+04	6.60E-02	3.84E+04	3804.85	8.91E+05	0.13
1821	6.2	12.0	0.0185	2.63E-03	20.08	47.3	6.00E+08	0.0363	3.57E-10	1.70E+04	6.60E-02	3.53E+04	3491.70	7.02E+05	0.16
1831	8.1	12.0	0.0185	2.63E-03	20.08	47.3	6.00E+08	0.0321	2.79E-10	1.50E+04	6.60E-02	3.99E+04	3950.49	9.86E+05	0.12
1840	8.5	12.0	0.0185	2.63E-03	20.08	47.3	6.00E+08	0.0311	2.63E-10	1.46E+04	6.60E-02	4.11E+04	4071.70	1.16E+06	0.11
1885	13.2	12.0	0.0185	2.63E-03	20.08	47.3	6.00E+08	0.0228	1.41E-10	1.07E+04	6.60E-02	5.62E+04	5564.13	4.05E+06	0.05
1848	9.0	12.0	0.0185	2.63E-03	20.08	47.3	6.00E+08	0.0301	2.46E-10	1.41E+04	6.60E-02	4.25E+04	4206.63	1.35E+06	0.10
1878	13.0	12.0	0.0185	2.63E-03	20.08	47.3	6.00E+08	0.0230	1.44E-10	1.08E+04	6.60E-02	5.56E+04	5504.50	3.64E+06	0.05
1843	8.3	12.0	0.0185	2.63E-03	20.08	47.3	6.00E+08	0.0316	2.70E-10	1.48E+04	6.60E-02	4.06E+04	4015.94	1.15E+06	0.11
1849	8.4	12.0	0.0185	2.63E-03	20.08	47.3	6.00E+08	0.0313	2.65E-10	1.47E+04	6.60E-02	4.09E+04	4052.07	1.25E+06	0.11
1867	11.9	12.0	0.0185	2.63E-03	20.08	47.3	6.00E+08	0.0248	1.67E-10	1.16E+04	6.60E-02	5.15E+04	5100.18	2.63E+06	0.07
1865	9.5	12.0	0.0185	2.63E-03	20.08	47.3	6.00E+08	0.0291	2.30E-10	1.37E+04	6.60E-02	4.40E+04	4352.01	1.71E+06	0.09
1876	12.5	12.0	0.0185	2.63E-03	20.08	47.3	6.00E+08	0.0238	1.53E-10	1.12E+04	6.60E-02	5.38E+04	5327.14	3.26E+06	0.06
1870	12.4	12.0	0.0185	2.63E-03	20.08	47.3	6.00E+08	0.0240	1.56E-10	1.12E+04	6.60E-02	5.34E+04	5283.82	2.94E+06	0.06
1884	14.2	12.0	0.0185	2.63E-03	20.08	47.3	6.00E+08	0.0213	1.23E-10	9.97E+03	6.60E-02	6.02E+04	5961.50	4.76E+06	0.05
1836	7.3	12.0	0.0185	2.63E-03	20.08	47.3	6.00E+08	0.0337	3.08E-10	1.58E+04	6.60E-02	3.80E+04	3760.28	9.32E+05	0.13
1848	9.0	12.0	0.0185	2.63E-03	20.08	47.3	6.00E+08	0.0301	2.45E-10	1.41E+04	6.60E-02	4.26E+04	4216.41	1.36E+06	0.10
1849	8.0	12.0	0.0185	2.63E-03	20.08	47.3	6.00E+08	0.0322	2.81E-10	1.51E+04	6.60E-02	3.97E+04	3934.87	1.16E+06	0.11
1848	9.3	12.0	0.0185	2.63E-03	20.08	47.3	6.00E+08	0.0295	2.37E-10	1.39E+04	6.60E-02	4.33E+04	4288.57	1.41E+06	0.10
1854	9.8	12.0	0.0185	2.63E-03	20.08	47.3	6.00E+08	0.0286	2.22E-10	1.34E+04	6.60E-02	4.48E+04	4433.57	1.63E+06	0.09
1843	8.3	12.0	0.0185	2.63E-03	20.08	47.3	6.00E+08	0.0316	2.71E-10	1.48E+04	6.60E-02	4.05E+04	4011.53	1.15E+06	0.11
1822	6.4	12.0	0.0185	2.63E-03	20.08	47.3	6.00E+08	0.0358	3.48E-10	1.68E+04	6.60E-02	3.57E+04	3536.70	7.27E+05	0.15
1878	13.4	12.0	0.0185	2.63E-03	20.08	47.3	6.00E+08	0.0224	1.36E-10	1.05E+04	6.60E-02	5.72E+04	5658.01	3.86E+06	0.05
1827	7.2	12.0	0.0185	2.63E-03	20.08	47.3	6.00E+08	0.0339	3.11E-10	1.59E+04	6.60E-02	3.78E+04	3741.52	8.51E+05	0.14
1876	12.6	12.0	0.0185	2.63E-03	20.08	47.3	6.00E+08	0.0236	1.51E-10	1.11E+04	6.60E-02	5.42E+04	5369.77	3.32E+06	0.06
1826	7.3	12.0	0.0185	2.63E-03	20.08	47.3	6.00E+08	0.0337	3.09E-10	1.58E+04	6.60E-02	3.79E+04	3756.37	8.46E+05	0.14
1827	7.1	12.0	0.0185	2.63E-03	20.08	47.3	6.00E+08	0.0342	3.17E-10	1.60E+04	6.60E-02	3.74E+04	3704.41	8.33E+05	0.14
1848	8.3	12.0	0.0185	2.63E-03	20.08	47.3	6.00E+08	0.0316	2.70E-10	1.48E+04	6.60E-02	4.05E+04	4013.88	1.21E+06	0.11
1834	7.9	12.0	0.0185	2.63E-03	20.08	47.3	6.00E+08	0.0323	2.84E-10	1.52E+04	6.60E-02	3.96E+04	3918.38	1.00E+06	0.12
1810	6.6	12.0	0.0185	2.63E-03	20.08	47.3	6.00E+08	0.0354	3.40E-10	1.66E+04	6.60E-02	3.61E+04	3577.92	6.56E+05	0.16
1858	8.6	12.0	0.0185	2.63E-03	20.08	47.3	6.00E+08	0.0309	2.60E-10	1.45E+04	6.60E-02	4.14E+04	4095.84	1.37E+06	0.10
1856	8.4	12.0	0.0185	2.63E-03	20.08	47.3	6.00E+08	0.0313	2.66E-10	1.47E+04	6.60E-02	4.09E+04	4049.31	1.32E+06	0.11
1847	8.8	12.0	0.0185	2.63E-03	20.08	47.3	6.00E+08	0.0304	2.51E-10	1.43E+04	6.60E-02	4.21E+04	4163.82	1.31E+06	0.10
1848	8.9	12.0	0.0185	2.63E-03	20.08	47.3	6.00E+08	0.0303	2.50E-10	1.42E+04	6.60E-02	4.22E+04	4177.15	1.33E+06	0.10
1840	9.0	12.0	0.0185	2.63E-03	20.08	47.3	6.00E+08	0.0302	2.47E-10	1.42E+04	6.60E-02	4.24E+04	4195.89	1.23E+06	0.11
1877	12.8	12.0	0.0185	2.63E-03	20.08	47.3	6.00E+08	0.0234	1.49E-10	1.10E+04	6.60E-02	5.47E+04	5415.77	3.43E+06	0.06
1887	13.8	12.0	0.0185	2.63E-03	20.08	47.3	6.00E+08	0.0219	1.30E-10	1.03E+04	6.60E-02	5.85E+04	5792.47	4.59E+06	0.05
1855	10.3	12.0	0.0185	2.63E-03	20.08	47.3	6.00E+08	0.0275	2.06E-10	1.29E+04	6.60E-02	4.65E+04	4602.42	1.78E+06	0.09
1805	5.5	12.0	0.0185	2.63E-03	20.08	47.3	6.00E+08	0.0382	3.96E-10	1.79E+04	6.60E-02	3.35E+04	3318.21	5.55E+05	0.18
1872	12.7	12.0	0.0185	2.63E-03	20.08	47.3	6.00E+08	0.0236	1.51E-10	1.11E+04	6.60E-02	5.43E+04	5374.21	3.14E+06	0.06
1856	9.6	12.0	0.0185	2.63E-03	20.08	47.3	6.00E+08	0.0290	2.28E-10	1.36E+04	6.60E-02	4.42E+04	4370.92	1.60E+06	0.09
1843	9.0	12.0	0.0185	2.63E-03	20.08	47.3	6.00E+08	0.0302	2.47E-10	1.41E+04	6.60E-02	4.24E+04	4199.41	1.27E+06	0.11
1844	8.9	12.0	0.0185	2.63E-03	20.08	47.3	6.00E+08	0.0303	2.48E-10	1.42E+04	6.60E-02	4.23E+04	4187.33	1.29E+06	0.10
1871	12.5	12.0	0.0185	2.63E-03	20.08	47.3	6.00E+08	0.0238	1.53E-10	1.11E+04	6.60E-02	5.39E+04	5331.52	3.04E+06	0.06
1859	10.4	12.0	0.0185	2.63E-03	20.08	47.3	6.00E+08	0.0274	2.04E-10	1.29E+04	6.60E-02	4.67E+04	4621.95	1.88E+06	0.08
1843	8.4	12.0	0.0185	2.63E-03	20.08	47.3	6.00E+08	0.0313	2.65E-10	1.47E+04	6.60E-02	4.09E+04	4053.64	1.18E+06	0.11
1887	14.5	12.0	0.0185	2.63E-03	20.08	47.3	6.00E+08	0.0208	1.17E-10	9.75E+03	6.60E-02	6.16E+04	6095.89	5.20E+06	0.04
1877	13.1	12.0	0.0185	2.63E-03	20.08	47.3	6.00E+08	0.0229	1.43E-10	1.08E+04	6.60E-02	5.58E+04	5525.93	3.62E+06	0.05

Table B-9: Calculated critical velocities for SG3 PS7

Temperature (K)	Surface Tension to Viscosity Ratio (σ/η) (cm/s)	Particle Young Modulus of Elasticity (GPa)	Particle Hertzian Stiffness (1/GPa)	Target Hertzian Stiffness (1/GPa)	Effective Stiffness (GPa)	Effective Contact Modulus (GPa)	K_h Hertzian Contact Stiffness (GPa)*m ⁻⁵	Particle Yield Strength (Gpa)	Deformation of Yield Z (m)	K_y Linear Contact Stiffness (GPa)*m	A γ^2	B (Kh/Ky)	C {(3/2)}(γ^2)(Kh/Ky)}	D C^4m	Critical Velocity $V_{critical}$ E [Ky/B] ^(1/2)
1886	11.6	12.0	0.0185	2.63E-03	20.08	47.3	3.15E+08	0.0253	4.79E-11	3.27E+03	2.82E-02	9.63E+04	4078.59	2.51E+04	0.36
1870	9.8	12.0	0.0185	2.63E-03	20.08	47.3	3.15E+08	0.0285	6.10E-11	3.69E+03	2.82E-02	8.54E+04	3614.50	1.55E+04	0.49
1877	10.6	12.0	0.0185	2.63E-03	20.08	47.3	3.15E+08	0.0271	5.51E-11	3.51E+03	2.82E-02	8.98E+04	3802.56	1.90E+04	0.43
1858	8.7	12.0	0.0185	2.63E-03	20.08	47.3	3.15E+08	0.0308	7.11E-11	3.99E+03	2.82E-02	7.90E+04	3346.27	1.14E+04	0.59
1891	12.2	12.0	0.0185	2.63E-03	20.08	47.3	3.15E+08	0.0242	4.40E-11	3.14E+03	2.82E-02	1.00E+05	4253.76	2.97E+04	0.33
1874	10.2	12.0	0.0185	2.63E-03	20.08	47.3	3.15E+08	0.0277	5.77E-11	3.59E+03	2.82E-02	8.78E+04	3716.54	1.73E+04	0.46
1835	6.8	12.0	0.0185	2.63E-03	20.08	47.3	3.15E+08	0.0350	9.18E-11	4.53E+03	2.82E-02	6.96E+04	2945.18	6.83E+03	0.81
1877	10.6	12.0	0.0185	2.63E-03	20.08	47.3	3.15E+08	0.0270	5.47E-11	3.50E+03	2.82E-02	9.02E+04	3817.73	1.93E+04	0.43
1868	9.7	12.0	0.0185	2.63E-03	20.08	47.3	3.15E+08	0.0288	6.22E-11	3.73E+03	2.82E-02	8.45E+04	3577.78	1.49E+04	0.50
1863	9.2	12.0	0.0185	2.63E-03	20.08	47.3	3.15E+08	0.0298	6.66E-11	3.86E+03	2.82E-02	8.17E+04	3458.39	1.30E+04	0.55
1876	10.5	12.0	0.0185	2.63E-03	20.08	47.3	3.15E+08	0.0273	5.59E-11	3.54E+03	2.82E-02	8.91E+04	3773.35	1.84E+04	0.44
1853	8.2	12.0	0.0185	2.63E-03	20.08	47.3	3.15E+08	0.0318	7.56E-11	4.11E+03	2.82E-02	7.67E+04	3245.24	1.01E+04	0.64
1845	7.5	12.0	0.0185	2.63E-03	20.08	47.3	3.15E+08	0.0332	8.27E-11	4.30E+03	2.82E-02	7.33E+04	3103.57	8.42E+03	0.71
1835	6.8	12.0	0.0185	2.63E-03	20.08	47.3	3.15E+08	0.0350	9.17E-11	4.53E+03	2.82E-02	6.96E+04	2947.69	6.85E+03	0.81
1877	10.6	12.0	0.0185	2.63E-03	20.08	47.3	3.15E+08	0.0270	5.47E-11	3.50E+03	2.82E-02	9.01E+04	3815.33	1.92E+04	0.43
1849	7.8	12.0	0.0185	2.63E-03	20.08	47.3	3.15E+08	0.0326	7.97E-11	4.22E+03	2.82E-02	7.47E+04	3160.76	9.06E+03	0.68
1870	9.8	12.0	0.0185	2.63E-03	20.08	47.3	3.15E+08	0.0285	6.10E-11	3.69E+03	2.82E-02	8.54E+04	3614.42	1.55E+04	0.49
1877	10.6	12.0	0.0185	2.63E-03	20.08	47.3	3.15E+08	0.0271	5.49E-11	3.50E+03	2.82E-02	9.00E+04	3810.58	1.91E+04	0.43
1891	12.2	12.0	0.0185	2.63E-03	20.08	47.3	3.15E+08	0.0243	4.42E-11	3.14E+03	2.82E-02	1.00E+05	4246.39	2.95E+04	0.33
1867	9.5	12.0	0.0185	2.63E-03	20.08	47.3	3.15E+08	0.0291	6.34E-11	3.77E+03	2.82E-02	8.37E+04	3543.79	1.43E+04	0.51
1885	11.5	12.0	0.0185	2.63E-03	20.08	47.3	3.15E+08	0.0255	4.86E-11	3.30E+03	2.82E-02	9.56E+04	4048.33	2.44E+04	0.37
1835	6.8	12.0	0.0185	2.63E-03	20.08	47.3	3.15E+08	0.0350	9.17E-11	4.53E+03	2.82E-02	6.96E+04	2947.93	6.85E+03	0.81
1886	11.6	12.0	0.0185	2.63E-03	20.08	47.3	3.15E+08	0.0253	4.81E-11	3.28E+03	2.82E-02	9.61E+04	4068.51	2.49E+04	0.36
1839	7.0	12.0	0.0185	2.63E-03	20.08	47.3	3.15E+08	0.0344	8.88E-11	4.46E+03	2.82E-02	7.07E+04	2994.82	7.30E+03	0.78
1851	8.0	12.0	0.0185	2.63E-03	20.08	47.3	3.15E+08	0.0322	7.79E-11	4.18E+03	2.82E-02	7.55E+04	3198.00	9.49E+03	0.66
1843	7.4	12.0	0.0185	2.63E-03	20.08	47.3	3.15E+08	0.0336	8.47E-11	4.35E+03	2.82E-02	7.25E+04	3067.36	8.04E+03	0.74
1865	9.3	12.0	0.0185	2.63E-03	20.08	47.3	3.15E+08	0.0294	6.49E-11	3.81E+03	2.82E-02	8.27E+04	3503.08	1.37E+04	0.53
1877	10.6	12.0	0.0185	2.63E-03	20.08	47.3	3.15E+08	0.0271	5.49E-11	3.51E+03	2.82E-02	9.00E+04	3809.51	1.91E+04	0.43
1868	9.6	12.0	0.0185	2.63E-03	20.08	47.3	3.15E+08	0.0290	6.29E-11	3.75E+03	2.82E-02	8.41E+04	3559.11	1.46E+04	0.51
1861	8.9	12.0	0.0185	2.63E-03	20.08	47.3	3.15E+08	0.0303	6.87E-11	3.92E+03	2.82E-02	8.04E+04	3404.95	1.22E+04	0.57
1837	6.9	12.0	0.0185	2.63E-03	20.08	47.3	3.15E+08	0.0347	9.03E-11	4.50E+03	2.82E-02	7.02E+04	2970.83	7.07E+03	0.80
1861	8.9	12.0	0.0185	2.63E-03	20.08	47.3	3.15E+08	0.0303	6.87E-11	3.92E+03	2.82E-02	8.05E+04	3406.09	1.22E+04	0.57
1849	7.8	12.0	0.0185	2.63E-03	20.08	47.3	3.15E+08	0.0325	7.94E-11	4.22E+03	2.82E-02	7.48E+04	3167.48	9.14E+03	0.68
1864	9.2	12.0	0.0185	2.63E-03	20.08	47.3	3.15E+08	0.0296	6.58E-11	3.84E+03	2.82E-02	8.22E+04	3479.81	1.33E+04	0.54
1886	11.6	12.0	0.0185	2.63E-03	20.08	47.3	3.15E+08	0.0253	4.80E-11	3.28E+03	2.82E-02	9.62E+04	4073.04	2.50E+04	0.36
1884	11.4	12.0	0.0185	2.63E-03	20.08	47.3	3.15E+08	0.0256	4.92E-11	3.32E+03	2.82E-02	9.51E+04	4024.56	2.38E+04	0.37
1842	7.2	12.0	0.0185	2.63E-03	20.08	47.3	3.15E+08	0.0339	8.61E-11	4.39E+03	2.82E-02	7.19E+04	3042.45	7.78E+03	0.75
1874	10.3	12.0	0.0185	2.63E-03	20.08	47.3	3.15E+08	0.0277	5.73E-11	3.58E+03	2.82E-02	8.80E+04	3727.38	1.75E+04	0.45
1869	9.7	12.0	0.0185	2.63E-03	20.08	47.3	3.15E+08	0.0288	6.20E-11	3.73E+03	2.82E-02	8.47E+04	3584.54	1.50E+04	0.50
1839	7.0	12.0	0.0185	2.63E-03	20.08	47.3	3.15E+08	0.0344	8.89E-11	4.46E+03	2.82E-02	7.07E+04	2993.56	7.29E+03	0.78
1878	10.7	12.0	0.0185	2.63E-03	20.08	47.3	3.15E+08	0.0268	5.38E-11	3.47E+03	2.82E-02	9.09E+04	3849.60	1.99E+04	0.42
1869	9.7	12.0	0.0185	2.63E-03	20.08	47.3	3.15E+08	0.0288	6.19E-11	3.72E+03	2.82E-02	8.47E+04	3585.92	1.50E+04	0.50
1864	9.3	12.0	0.0185	2.63E-03	20.08	47.3	3.15E+08	0.0296	6.56E-11	3.83E+03	2.82E-02	8.23E+04	3484.04	1.34E+04	0.54
1870	9.8	12.0	0.0185	2.63E-03	20.08	47.3	3.15E+08	0.0285	6.11E-11	3.70E+03	2.82E-02	8.53E+04	3611.77	1.54E+04	0.49
1885	11.5	12.0	0.0185	2.63E-03	20.08	47.3	3.15E+08	0.0255	4.87E-11	3.30E+03	2.82E-02	9.55E+04	4042.61	2.42E+04	0.37
1882	11.2	12.0	0.0185	2.63E-03	20.08	47.3	3.15E+08	0.0260	5.06E-11	3.37E+03	2.82E-02	9.37E+04	3967.95	2.25E+04	0.39
1878	10.7	12.0	0.0185	2.63E-03	20.08	47.3	3.15E+08	0.0269	5.43E-11	3.49E+03	2.82E-02	9.05E+04	3830.87	1.95E+04	0.42

Table B-10: Calculated critical velocities for SG4 PS1

Temperature (K)	Surface Tension to Viscosity Ratio (σ/η) (cm/s)	Particle Young Modulus of Elasticity (GPa)	Particle Hertzian Stiffness (1/GPa)	Target Hertzian Stiffness (1/GPa)	Effective Stiffness (GPa)	Effective Contact Modulus (GPa)	K_h Hertzian Contact Stiffness (GPa)*m ⁻⁵	Particle Yield Strength (Gpa)	Deformation of Yield Z (m)	Ky Linear Contact Stiffness (GPa)*m	A Y ²	B (Kh/Ky)	C {(3/2)}(Y ²)(Kh/Ky)}	D C ⁴ *m	Critical Velocity V _{critical} E [Ky/B] ^(1/2)
897	1.31E-05	55.0	4.04E-03	2.63E-03	63.63	149.9	4.15E+09	0.0550	3.90E-10	1.23E+05	4.36E-03	3.37E+04	220.52	2.55E+03	6.94
901	1.48E-05	55.0	4.04E-03	2.63E-03	63.63	149.9	4.15E+09	0.0550	3.90E-10	1.23E+05	4.36E-03	3.37E+04	220.52	2.56E+03	6.93
1364	1.72E-01	55.0	4.04E-03	2.63E-03	63.63	149.9	4.15E+09	0.0544	3.81E-10	1.22E+05	4.36E-03	3.41E+04	223.08	2.65E+03	6.78
1847	1.90E+01	55.0	4.04E-03	2.63E-03	63.63	149.9	4.15E+09	0.0154	3.07E-11	3.45E+04	4.36E-03	1.20E+05	786.29	4.08E+05	0.29
1840	1.80E+01	55.0	4.04E-03	2.63E-03	63.63	149.9	4.15E+09	0.0164	3.48E-11	3.68E+04	4.36E-03	1.13E+05	738.25	3.17E+05	0.34
1394	2.54E-01	55.0	4.04E-03	2.63E-03	63.63	149.9	4.15E+09	0.0541	3.77E-10	1.21E+05	4.36E-03	3.43E+04	224.31	2.71E+03	6.68
908	1.83E-05	55.0	4.04E-03	2.63E-03	63.63	149.9	4.15E+09	0.0550	3.90E-10	1.23E+05	4.36E-03	3.37E+04	220.52	2.56E+03	6.93
1545	1.43E+00	55.0	4.04E-03	2.63E-03	63.63	149.9	4.15E+09	0.0500	3.22E-10	1.12E+05	4.36E-03	3.71E+04	242.64	3.71E+03	5.49
887	9.41E-06	55.0	4.04E-03	2.63E-03	63.63	149.9	4.15E+09	0.0550	3.90E-10	1.23E+05	4.36E-03	3.37E+04	220.52	2.53E+03	6.97
889	9.97E-06	55.0	4.04E-03	2.63E-03	63.63	149.9	4.15E+09	0.0550	3.90E-10	1.23E+05	4.36E-03	3.37E+04	220.52	2.54E+03	6.97
1341	1.27E-01	55.0	4.04E-03	2.63E-03	63.63	149.9	4.15E+09	0.0546	3.84E-10	1.22E+05	4.36E-03	3.40E+04	222.40	2.62E+03	6.83
918	2.48E-05	55.0	4.04E-03	2.63E-03	63.63	149.9	4.15E+09	0.0550	3.90E-10	1.23E+05	4.36E-03	3.37E+04	220.52	2.56E+03	6.93
909	1.90E-05	55.0	4.04E-03	2.63E-03	63.63	149.9	4.15E+09	0.0550	3.90E-10	1.23E+05	4.36E-03	3.37E+04	220.52	2.56E+03	6.93
898	1.34E-05	55.0	4.04E-03	2.63E-03	63.63	149.9	4.15E+09	0.0550	3.90E-10	1.23E+05	4.36E-03	3.37E+04	220.52	2.56E+03	6.94
903	1.54E-05	55.0	4.04E-03	2.63E-03	63.63	149.9	4.15E+09	0.0550	3.90E-10	1.23E+05	4.36E-03	3.37E+04	220.52	2.53E+03	6.97
893	1.13E-05	55.0	4.04E-03	2.63E-03	63.63	149.9	4.15E+09	0.0550	3.90E-10	1.23E+05	4.36E-03	3.37E+04	220.52	2.54E+03	6.95
1826	1.63E+01	55.0	4.04E-03	2.63E-03	63.63	149.9	4.15E+09	0.0185	4.40E-11	4.13E+04	4.36E-03	1.01E+05	656.82	1.99E+05	0.46
912	2.07E-05	55.0	4.04E-03	2.63E-03	63.63	149.9	4.15E+09	0.0550	3.90E-10	1.23E+05	4.36E-03	3.37E+04	220.52	2.55E+03	6.94
912	2.07E-05	55.0	4.04E-03	2.63E-03	63.63	149.9	4.15E+09	0.0550	3.90E-10	1.23E+05	4.36E-03	3.37E+04	220.52	2.56E+03	6.93
911	1.99E-05	55.0	4.04E-03	2.63E-03	63.63	149.9	4.15E+09	0.0550	3.90E-10	1.23E+05	4.36E-03	3.37E+04	220.52	2.55E+03	6.95
894	1.17E-05	55.0	4.04E-03	2.63E-03	63.63	149.9	4.15E+09	0.0550	3.90E-10	1.23E+05	4.36E-03	3.37E+04	220.52	2.55E+03	6.94
903	1.55E-05	55.0	4.04E-03	2.63E-03	63.63	149.9	4.15E+09	0.0550	3.90E-10	1.23E+05	4.36E-03	3.37E+04	220.52	2.54E+03	6.96
902	1.51E-05	55.0	4.04E-03	2.63E-03	63.63	149.9	4.15E+09	0.0550	3.90E-10	1.23E+05	4.36E-03	3.37E+04	220.52	2.55E+03	6.95
904	1.63E-05	55.0	4.04E-03	2.63E-03	63.63	149.9	4.15E+09	0.0550	3.90E-10	1.23E+05	4.36E-03	3.37E+04	220.52	2.55E+03	6.94
909	1.87E-05	55.0	4.04E-03	2.63E-03	63.63	149.9	4.15E+09	0.0550	3.90E-10	1.23E+05	4.36E-03	3.37E+04	220.52	2.55E+03	6.94
905	1.67E-05	55.0	4.04E-03	2.63E-03	63.63	149.9	4.15E+09	0.0550	3.90E-10	1.23E+05	4.36E-03	3.37E+04	220.52	2.56E+03	6.94
914	2.16E-05	55.0	4.04E-03	2.63E-03	63.63	149.9	4.15E+09	0.0550	3.90E-10	1.23E+05	4.36E-03	3.37E+04	220.52	2.55E+03	6.94
902	1.50E-05	55.0	4.04E-03	2.63E-03	63.63	149.9	4.15E+09	0.0550	3.90E-10	1.23E+05	4.36E-03	3.37E+04	220.52	2.54E+03	6.96
1641	3.61E+00	55.0	4.04E-03	2.63E-03	63.63	149.9	4.15E+09	0.0432	2.41E-10	9.66E+04	4.36E-03	4.30E+04	280.88	6.66E+03	3.81
904	1.60E-05	55.0	4.04E-03	2.63E-03	63.63	149.9	4.15E+09	0.0550	3.90E-10	1.23E+05	4.36E-03	3.37E+04	220.52	2.54E+03	6.96
1813	1.48E+01	55.0	4.04E-03	2.63E-03	63.63	149.9	4.15E+09	0.0204	5.37E-11	4.56E+04	4.36E-03	9.10E+04	594.60	1.34E+05	0.58
907	1.77E-05	55.0	4.04E-03	2.63E-03	63.63	149.9	4.15E+09	0.0550	3.90E-10	1.23E+05	4.36E-03	3.37E+04	220.52	2.56E+03	6.93
904	1.60E-05	55.0	4.04E-03	2.63E-03	63.63	149.9	4.15E+09	0.0550	3.90E-10	1.23E+05	4.36E-03	3.37E+04	220.52	2.55E+03	6.95
1314	8.73E-02	55.0	4.04E-03	2.63E-03	63.63	149.9	4.15E+09	0.0547	3.86E-10	1.22E+05	4.36E-03	3.39E+04	221.81	2.59E+03	6.87
1816	1.51E+01	55.0	4.04E-03	2.63E-03	63.63	149.9	4.15E+09	0.0201	5.18E-11	4.48E+04	4.36E-03	9.26E+04	605.22	1.43E+05	0.56
1765	1.02E+01	55.0	4.04E-03	2.63E-03	63.63	149.9	4.15E+09	0.0277	9.89E-11	6.19E+04	4.36E-03	6.70E+04	438.08	3.94E+04	1.25
915	2.27E-05	55.0	4.04E-03	2.63E-03	63.63	149.9	4.15E+09	0.0550	3.90E-10	1.23E+05	4.36E-03	3.37E+04	220.52	2.56E+03	6.93
914	2.19E-05	55.0	4.04E-03	2.63E-03	63.63	149.9	4.15E+09	0.0550	3.90E-10	1.23E+05	4.36E-03	3.37E+04	220.52	2.56E+03	6.93
900	1.40E-05	55.0	4.04E-03	2.63E-03	63.63	149.9	4.15E+09	0.0550	3.90E-10	1.23E+05	4.36E-03	3.37E+04	220.52	2.54E+03	6.96

Table B-11: Calculated critical velocities for SG4 PS4

Temperature (K)	Surface Tension to Viscosity Ratio (σ/η) (cm/s)	Particle Young Modulus of Elasticity (GPa)	Particle Hertzian Stiffness (1/GPa)	Target Hertzian Stiffness (1/GPa)	Effective Stiffness (GPa)	Effective Contact Modulus (GPa)	K_h Hertzian Contact Stiffness (GPa)*m ⁻⁵	Particle Yield Strength (Gpa)	Deformation of Yield Z (m)	K_y Linear Contact Stiffness (GPa)*m	A γ^2	B (Kh/Ky)	C $\{(3/2)(\gamma^2)(Kh/Ky)\}$	D C ⁴ *m	Critical Velocity $V_{critical}$ E [Ky/B] ^[1/2]
897	1.31E-05	55.0	4.04E-03	2.63E-03	63.63	149.9	4.15E+09	0.0550	3.90E-10	1.23E+05	4.36E-03	3.37E+04	220.52	2.55E+03	6.94
901	1.48E-05	55.0	4.04E-03	2.63E-03	63.63	149.9	4.15E+09	0.0550	3.90E-10	1.23E+05	4.36E-03	3.37E+04	220.52	2.56E+03	6.93
1364	1.72E-01	55.0	4.04E-03	2.63E-03	63.63	149.9	4.15E+09	0.0544	3.81E-10	1.22E+05	4.36E-03	3.41E+04	223.08	2.65E+03	6.78
1847	1.90E+01	55.0	4.04E-03	2.63E-03	63.63	149.9	4.15E+09	0.0154	3.07E-11	3.45E+04	4.36E-03	1.20E+05	786.29	4.08E+05	0.29
1840	1.80E+01	55.0	4.04E-03	2.63E-03	63.63	149.9	4.15E+09	0.0164	3.48E-11	3.68E+04	4.36E-03	1.13E+05	738.25	3.17E+05	0.34
1394	2.54E-01	55.0	4.04E-03	2.63E-03	63.63	149.9	4.15E+09	0.0541	3.77E-10	1.21E+05	4.36E-03	3.43E+04	224.31	2.71E+03	6.68
908	1.83E-05	55.0	4.04E-03	2.63E-03	63.63	149.9	4.15E+09	0.0550	3.90E-10	1.23E+05	4.36E-03	3.37E+04	220.52	2.56E+03	6.93
1545	1.43E+00	55.0	4.04E-03	2.63E-03	63.63	149.9	4.15E+09	0.0500	3.22E-10	1.12E+05	4.36E-03	3.71E+04	242.64	3.71E+03	5.49
887	9.41E-06	55.0	4.04E-03	2.63E-03	63.63	149.9	4.15E+09	0.0550	3.90E-10	1.23E+05	4.36E-03	3.37E+04	220.52	2.53E+03	6.97
889	9.97E-06	55.0	4.04E-03	2.63E-03	63.63	149.9	4.15E+09	0.0550	3.90E-10	1.23E+05	4.36E-03	3.37E+04	220.52	2.54E+03	6.92
1341	1.27E-01	55.0	4.04E-03	2.63E-03	63.63	149.9	4.15E+09	0.0546	3.84E-10	1.22E+05	4.36E-03	3.40E+04	222.40	2.62E+03	6.83
918	2.48E-05	55.0	4.04E-03	2.63E-03	63.63	149.9	4.15E+09	0.0550	3.90E-10	1.23E+05	4.36E-03	3.37E+04	220.52	2.56E+03	6.93
909	1.90E-05	55.0	4.04E-03	2.63E-03	63.63	149.9	4.15E+09	0.0550	3.90E-10	1.23E+05	4.36E-03	3.37E+04	220.52	2.56E+03	6.93
898	1.34E-05	55.0	4.04E-03	2.63E-03	63.63	149.9	4.15E+09	0.0550	3.90E-10	1.23E+05	4.36E-03	3.37E+04	220.52	2.56E+03	6.94
903	1.54E-05	55.0	4.04E-03	2.63E-03	63.63	149.9	4.15E+09	0.0550	3.90E-10	1.23E+05	4.36E-03	3.37E+04	220.52	2.53E+03	6.97
893	1.13E-05	55.0	4.04E-03	2.63E-03	63.63	149.9	4.15E+09	0.0550	3.90E-10	1.23E+05	4.36E-03	3.37E+04	220.52	2.54E+03	6.95
1826	1.63E+01	55.0	4.04E-03	2.63E-03	63.63	149.9	4.15E+09	0.0185	4.40E-11	4.13E+04	4.36E-03	1.01E+05	656.82	1.99E+05	0.46
912	2.07E-05	55.0	4.04E-03	2.63E-03	63.63	149.9	4.15E+09	0.0550	3.90E-10	1.23E+05	4.36E-03	3.37E+04	220.52	2.55E+03	6.94
912	2.07E-05	55.0	4.04E-03	2.63E-03	63.63	149.9	4.15E+09	0.0550	3.90E-10	1.23E+05	4.36E-03	3.37E+04	220.52	2.56E+03	6.93
911	1.99E-05	55.0	4.04E-03	2.63E-03	63.63	149.9	4.15E+09	0.0550	3.90E-10	1.23E+05	4.36E-03	3.37E+04	220.52	2.55E+03	6.95
894	1.17E-05	55.0	4.04E-03	2.63E-03	63.63	149.9	4.15E+09	0.0550	3.90E-10	1.23E+05	4.36E-03	3.37E+04	220.52	2.55E+03	6.94
903	1.55E-05	55.0	4.04E-03	2.63E-03	63.63	149.9	4.15E+09	0.0550	3.90E-10	1.23E+05	4.36E-03	3.37E+04	220.52	2.54E+03	6.96
902	1.51E-05	55.0	4.04E-03	2.63E-03	63.63	149.9	4.15E+09	0.0550	3.90E-10	1.23E+05	4.36E-03	3.37E+04	220.52	2.55E+03	6.95
904	1.63E-05	55.0	4.04E-03	2.63E-03	63.63	149.9	4.15E+09	0.0550	3.90E-10	1.23E+05	4.36E-03	3.37E+04	220.52	2.55E+03	6.94
909	1.87E-05	55.0	4.04E-03	2.63E-03	63.63	149.9	4.15E+09	0.0550	3.90E-10	1.23E+05	4.36E-03	3.37E+04	220.52	2.55E+03	6.94
905	1.67E-05	55.0	4.04E-03	2.63E-03	63.63	149.9	4.15E+09	0.0550	3.90E-10	1.23E+05	4.36E-03	3.37E+04	220.52	2.56E+03	6.94
914	2.16E-05	55.0	4.04E-03	2.63E-03	63.63	149.9	4.15E+09	0.0550	3.90E-10	1.23E+05	4.36E-03	3.37E+04	220.52	2.55E+03	6.94
902	1.50E-05	55.0	4.04E-03	2.63E-03	63.63	149.9	4.15E+09	0.0550	3.90E-10	1.23E+05	4.36E-03	3.37E+04	220.52	2.54E+03	6.96
1641	3.61E+00	55.0	4.04E-03	2.63E-03	63.63	149.9	4.15E+09	0.0432	2.41E-10	9.66E+04	4.36E-03	4.30E+04	280.88	6.66E+03	3.81
904	1.60E-05	55.0	4.04E-03	2.63E-03	63.63	149.9	4.15E+09	0.0550	3.90E-10	1.23E+05	4.36E-03	3.37E+04	220.52	2.54E+03	6.96
1813	1.48E+01	55.0	4.04E-03	2.63E-03	63.63	149.9	4.15E+09	0.0204	5.37E-11	4.56E+04	4.36E-03	9.10E+04	594.60	1.34E+05	0.58
907	1.77E-05	55.0	4.04E-03	2.63E-03	63.63	149.9	4.15E+09	0.0550	3.90E-10	1.23E+05	4.36E-03	3.37E+04	220.52	2.56E+03	6.93
904	1.60E-05	55.0	4.04E-03	2.63E-03	63.63	149.9	4.15E+09	0.0550	3.90E-10	1.23E+05	4.36E-03	3.37E+04	220.52	2.55E+03	6.95
1314	8.73E-02	55.0	4.04E-03	2.63E-03	63.63	149.9	4.15E+09	0.0547	3.86E-10	1.22E+05	4.36E-03	3.39E+04	221.81	2.59E+03	6.87
1816	1.51E+01	55.0	4.04E-03	2.63E-03	63.63	149.9	4.15E+09	0.0201	5.18E-11	4.48E+04	4.36E-03	9.26E+04	605.22	1.43E+05	0.56
1765	1.02E+01	55.0	4.04E-03	2.63E-03	63.63	149.9	4.15E+09	0.0277	9.89E-11	6.19E+04	4.36E-03	6.70E+04	438.08	3.94E+04	1.25
915	2.27E-05	55.0	4.04E-03	2.63E-03	63.63	149.9	4.15E+09	0.0550	3.90E-10	1.23E+05	4.36E-03	3.37E+04	220.52	2.56E+03	6.93
914	2.19E-05	55.0	4.04E-03	2.63E-03	63.63	149.9	4.15E+09	0.0550	3.90E-10	1.23E+05	4.36E-03	3.37E+04	220.52	2.56E+03	6.93
900	1.40E-05	55.0	4.04E-03	2.63E-03	63.63	149.9	4.15E+09	0.0550	3.90E-10	1.23E+05	4.36E-03	3.37E+04	220.52	2.54E+03	6.96
903	1.57E-05	55.0	4.04E-03	2.63E-03	63.63	149.9	4.15E+09	0.0550	3.90E-10	1.23E+05	4.36E-03	3.37E+04	220.52	2.55E+03	6.94
893	1.14E-05	55.0	4.04E-03	2.63E-03	63.63	149.9	4.15E+09	0.0550	3.90E-10	1.23E+05	4.36E-03	3.37E+04	220.52	2.55E+03	6.95
1652	3.97E+00	55.0	4.04E-03	2.63E-03	63.63	149.9	4.15E+09	0.0422	2.29E-10	9.43E+04	4.36E-03	4.40E+04	287.78	7.34E+03	3.58
910	1.96E-05	55.0	4.04E-03	2.63E-03	63.63	149.9	4.15E+09	0.0550	3.90E-10	1.23E+05	4.36E-03	3.37E+04	220.52	2.56E+03	6.93
921	2.71E-05	55.0	4.04E-03	2.63E-03	63.63	149.9	4.15E+09	0.0550	3.90E-10	1.23E+05	4.36E-03	3.37E+04	220.52	2.56E+03	6.94
910	1.95E-05	55.0	4.04E-03	2.63E-03	63.63	149.9	4.15E+09	0.0550	3.90E-10	1.23E+05	4.36E-03	3.37E+04	220.52	2.56E+03	6.93
920	2.59E-05	55.0	4.04E-03	2.63E-03	63.63	149.9	4.15E+09	0.0550	3.90E-10	1.23E+05	4.36E-03	3.37E+04	220.52	2.55E+03	6.95
1780	1.15E+01	55.0	4.04E-03	2.63E-03	63.63	149.9	4.15E+09	0.0255	8.35E-11	5.69E+04	4.36E-03	7.29E+04	476.57	5.52E+04	1.02
907	1.79E-05	55.0	4.04E-03	2.63E-03	63.63	149.9	4.15E+09	0.0550	3.90E-10	1.23E+05	4.36E-03	3.37E+04	220.52	2.54E+03	6.96
898	1.34E-05	55.0	4.04E-03	2.63E-03	63.63	149.9	4.15E+09	0.0550	3.90E-10	1.23E+05	4.36E-03	3.37E+04	220.52	2.55E+03	6.95
900	1.42E-05	55.0	4.04E-03	2.63E-03	63.63	149.9	4.15E+09	0.0550	3.90E-10	1.23E+05	4.36E-03	3.37E+04	220.52	2.55E+03	6.94
902	1.50E-05	55.0	4.04E-03	2.63E-03	63.63	149.9	4.15E+09	0.0550	3.90E-10	1.23E+05	4.36E-03	3.37E+04	220.52	2.56E+03	6.94
906	1.70E-05	55.0	4.04E-03	2.63E-03	63.63	149.9	4.15E+09	0.0550	3.90E-10	1.23E+05	4.36E-03	3.37E+04	220.52	2.55E+03	6.94
904	1.62E-05	55.0	4.04E-03	2.63E-03	63.63	149.9	4.15E+09	0.0550	3.90E-10	1.23E+05	4.36E-03	3.37E+04	220.52	2.56E+03	6.94
907	1.76E-05	55.0	4.04E-03	2.63E-03	63.63	149.9	4.15E+09	0.0550	3.90E-10	1.23E+05	4.36E-03	3.37E+04	220.52	2.55E+03	6.95
1554	1.56E+00	55.0	4.04E-03	2.63E-03	63.63	149.9	4.15E+09	0.0496	3.17E-10	1.11E+05	4.36E-03	3.75E+04	244.77	3.84E+03	5.37
1861	2.10E+01	55.0	4.04E-03	2.63E-03	63.63	149.9	4.15E+09	0.0135	2.34E-11	3.01E+04	4.36E-03	1.38E+05	900.75	7.00E+05	0.21

Table B-12: Calculated critical velocities for SG

Temperature (K)	Surface Tension to Viscosity Ratio (σ/η) (cm/s)	Particle Young Modulus of Elasticity (GPa)	Particle Hertzian Stiffness (1/GPa)	Target Hertzian Stiffness (1/GPa)	Effective Stiffness (GPa)	Effective Contact Modulus (GPa)	K_h Hertzian Contact Stiffness (GPa)*m ⁻⁵	Particle Yield Strength (Gpa)	Deformation of Yield Z (m)	K_y Linear Contact Stiffness (GPa)*m	A γ^2	B (Kh/Ky)	C $\{[3/2](\gamma^2)(Kh/Ky)\}$	D $C^4 \cdot m$	Critical Velocity $V_{critical}$ E [Ky/B] ^(1/2)
1860	38.35	12.0	1.85E-02	2.63E-03	20.08	47.31	5.05E+08	0.0076	1.12E-11	2.53E+03	3.96E-02	1.99E+05	1.18E+04	6.34E+07	0.01
1873	38.29	12.0	1.85E-02	2.63E-03	20.08	47.31	5.05E+08	0.0074	1.04E-11	2.44E+03	3.96E-02	2.07E+05	1.23E+04	7.32E+07	0.01
1875	40.00	12.0	1.85E-02	2.63E-03	20.08	47.31	5.05E+08	0.0089	1.53E-11	2.96E+03	3.96E-02	1.70E+05	1.01E+04	3.37E+07	0.01
1867	39.62	12.0	1.85E-02	2.63E-03	20.08	47.31	5.05E+08	0.0069	9.20E-12	2.30E+03	3.96E-02	2.20E+05	1.31E+04	9.36E+07	0.00
1877	41.79	12.0	1.85E-02	2.63E-03	20.08	47.31	5.05E+08	0.0065	8.06E-12	2.15E+03	3.96E-02	2.35E+05	1.39E+04	1.22E+08	0.00
1864	37.77	12.0	1.85E-02	2.63E-03	20.08	47.31	5.05E+08	0.0078	1.17E-11	2.59E+03	3.96E-02	1.95E+05	1.16E+04	5.82E+07	0.01
1889	41.49	12.0	1.85E-02	2.63E-03	20.08	47.31	5.05E+08	0.0079	1.18E-11	2.61E+03	3.96E-02	1.94E+05	1.15E+04	5.65E+07	0.01
1844	34.44	12.0	1.85E-02	2.63E-03	20.08	47.31	5.05E+08	0.0087	1.46E-11	2.89E+03	3.96E-02	1.75E+05	1.04E+04	3.74E+07	0.01
1845	32.99	12.0	1.85E-02	2.63E-03	20.08	47.31	5.05E+08	0.0079	1.18E-11	2.60E+03	3.96E-02	1.94E+05	1.15E+04	5.66E+07	0.01
1875	38.62	12.0	1.85E-02	2.63E-03	20.08	47.31	5.05E+08	0.0083	1.33E-11	2.77E+03	3.96E-02	1.83E+05	1.08E+04	4.45E+07	0.01
1873	39.51	12.0	1.85E-02	2.63E-03	20.08	47.31	5.05E+08	0.0097	1.79E-11	3.20E+03	3.96E-02	1.58E+05	9.36E+03	2.48E+07	0.01
1868	37.30	12.0	1.85E-02	2.63E-03	20.08	47.31	5.05E+08	0.0080	1.23E-11	2.65E+03	3.96E-02	1.90E+05	1.13E+04	5.24E+07	0.01
1870	37.57	12.0	1.85E-02	2.63E-03	20.08	47.31	5.05E+08	0.0087	1.45E-11	2.88E+03	3.96E-02	1.75E+05	1.04E+04	3.78E+07	0.01
1854	34.72	12.0	1.85E-02	2.63E-03	20.08	47.31	5.05E+08	0.0103	2.02E-11	3.40E+03	3.96E-02	1.48E+05	8.81E+03	1.94E+07	0.01
1887	40.98	12.0	1.85E-02	2.63E-03	20.08	47.31	5.05E+08	0.0079	1.18E-11	2.61E+03	3.96E-02	1.94E+05	1.15E+04	5.64E+07	0.01
1873	38.24	12.0	1.85E-02	2.63E-03	20.08	47.31	5.05E+08	0.0069	9.20E-12	2.30E+03	3.96E-02	2.20E+05	1.31E+04	9.36E+07	0.00
1859	38.05	12.0	1.85E-02	2.63E-03	20.08	47.31	5.05E+08	0.0068	8.83E-12	2.25E+03	3.96E-02	2.24E+05	1.33E+04	1.02E+08	0.00
1875	38.56	12.0	1.85E-02	2.63E-03	20.08	47.31	5.05E+08	0.0081	1.27E-11	2.69E+03	3.96E-02	1.87E+05	1.11E+04	4.95E+07	0.01
1875	38.63	12.0	1.85E-02	2.63E-03	20.08	47.31	5.05E+08	0.0078	1.18E-11	2.60E+03	3.96E-02	1.94E+05	1.15E+04	5.72E+07	0.01
1869	37.41	12.0	1.85E-02	2.63E-03	20.08	47.31	5.05E+08	0.0079	1.19E-11	2.61E+03	3.96E-02	1.93E+05	1.15E+04	5.60E+07	0.01
1877	39.04	12.0	1.85E-02	2.63E-03	20.08	47.31	5.05E+08	0.0077	1.14E-11	2.56E+03	3.96E-02	1.97E+05	1.17E+04	6.06E+07	0.01
1865	36.77	12.0	1.85E-02	2.63E-03	20.08	47.31	5.05E+08	0.0079	1.20E-11	2.62E+03	3.96E-02	1.92E+05	1.14E+04	5.48E+07	0.01
1874	38.48	12.0	1.85E-02	2.63E-03	20.08	47.31	5.05E+08	0.0103	2.05E-11	3.43E+03	3.96E-02	1.47E+05	8.74E+03	1.88E+07	0.01
1864	36.54	12.0	1.85E-02	2.63E-03	20.08	47.31	5.05E+08	0.0100	1.92E-11	3.32E+03	3.96E-02	1.52E+05	9.03E+03	2.15E+07	0.01
1853	34.57	12.0	1.85E-02	2.63E-03	20.08	47.31	5.05E+08	0.0097	1.82E-11	3.23E+03	3.96E-02	1.56E+05	9.29E+03	2.40E+07	0.01
1872	37.97	12.0	1.85E-02	2.63E-03	20.08	47.31	5.05E+08	0.0066	8.27E-12	2.18E+03	3.96E-02	2.32E+05	1.38E+04	1.16E+08	0.00
1872	38.00	12.0	1.85E-02	2.63E-03	20.08	47.31	5.05E+08	0.0098	1.84E-11	3.24E+03	3.96E-02	1.56E+05	9.24E+03	2.35E+07	0.01
1869	37.43	12.0	1.85E-02	2.63E-03	20.08	47.31	5.05E+08	0.0092	1.63E-11	3.05E+03	3.96E-02	1.65E+05	9.82E+03	3.00E+07	0.01
1811	29.10	12.0	1.85E-02	2.63E-03	20.08	47.31	5.05E+08	0.0072	9.81E-12	2.37E+03	3.96E-02	2.13E+05	1.26E+04	8.23E+07	0.01
1856	35.07	12.0	1.85E-02	2.63E-03	20.08	47.31	5.05E+08	0.0089	1.51E-11	2.95E+03	3.96E-02	1.71E+05	1.02E+04	3.46E+07	0.01
1841	34.70	12.0	1.85E-02	2.63E-03	20.08	47.31	5.05E+08	0.0082	1.29E-11	2.72E+03	3.96E-02	1.86E+05	1.10E+04	4.78E+07	0.01
1877	39.04	12.0	1.85E-02	2.63E-03	20.08	47.31	5.05E+08	0.0073	1.02E-11	2.42E+03	3.96E-02	2.08E+05	1.24E+04	7.58E+07	0.01
1878	39.09	12.0	1.85E-02	2.63E-03	20.08	47.31	5.05E+08	0.0125	3.01E-11	4.15E+03	3.96E-02	1.22E+05	7.22E+03	8.75E+06	0.02
1867	37.96	12.0	1.85E-02	2.63E-03	20.08	47.31	5.05E+08	0.0095	1.74E-11	3.15E+03	3.96E-02	1.60E+05	9.51E+03	2.66E+07	0.01
1876	41.46	12.0	1.85E-02	2.63E-03	20.08	47.31	5.05E+08	0.0078	1.17E-11	2.59E+03	3.96E-02	1.95E+05	1.16E+04	5.79E+07	0.01
1875	40.91	12.0	1.85E-02	2.63E-03	20.08	47.31	5.05E+08	0.0097	1.81E-11	3.22E+03	3.96E-02	1.57E+05	9.30E+03	2.43E+07	0.01
1872	38.03	12.0	1.85E-02	2.63E-03	20.08	47.31	5.05E+08	0.0121	2.79E-11	4.00E+03	3.96E-02	1.26E+05	7.50E+03	1.02E+07	0.02
1869	37.55	12.0	1.85E-02	2.63E-03	20.08	47.31	5.05E+08	0.0080	1.22E-11	2.65E+03	3.96E-02	1.91E+05	1.13E+04	5.31E+07	0.01
1868	37.24	12.0	1.85E-02	2.63E-03	20.08	47.31	5.05E+08	0.0095	1.73E-11	3.15E+03	3.96E-02	1.60E+05	9.51E+03	2.64E+07	0.01
1879	39.39	12.0	1.85E-02	2.63E-03	20.08	47.31	5.05E+08	0.0088	1.50E-11	2.93E+03	3.96E-02	1.72E+05	1.02E+04	3.53E+07	0.01
1880	39.58	12.0	1.85E-02	2.63E-03	20.08	47.31	5.05E+08	0.0080	1.23E-11	2.66E+03	3.96E-02	1.90E+05	1.13E+04	5.22E+07	0.01
1856	37.07	12.0	1.85E-02	2.63E-03	20.08	47.31	5.05E+08	0.0089	1.52E-11	2.95E+03	3.96E-02	1.71E+05	1.02E+04	3.43E+07	0.01
1874	38.38	12.0	1.85E-02	2.63E-03	20.08	47.31	5.05E+08	0.0101	1.94E-11	3.33E+03	3.96E-02	1.51E+05	9.00E+03	2.11E+07	0.01
1820	29.02	12.0	1.85E-02	2.63E-03	20.08	47.31	5.05E+08	0.0094	1.70E-11	3.12E+03	3.96E-02	1.62E+05	9.61E+03	2.75E+07	0.01
1883	40.11	12.0	1.85E-02	2.63E-03	20.08	47.31	5.05E+08	0.0081	1.26E-11	2.69E+03	3.96E-02	1.88E+05	1.12E+04	5.00E+07	0.01
1877	39.01	12.0	1.85E-02	2.63E-03	20.08	47.31	5.05E+08	0.0125	3.01E-11	4.15E+03	3.96E-02	1.22E+05	7.22E+03	8.78E+06	0.02
1863	38.71	12.0	1.85E-02	2.63E-03	20.08	47.31	5.05E+08	0.0093	1.64E-11	3.07E+03	3.96E-02	1.64E+05	9.77E+03	3.04E+07	0.01

VITA

LaTosha Gibson attended North Carolina Agricultural and Technical State University located at Greensboro, NC where she attained her B.S. degree in Mechanical Engineering in 2000. She also obtained her M.S. degree in Aerospace Engineering at North Carolina State University in 2006. She has worked for the Pacific National Northwest Laboratory and Office of Fossil Energy under the Department of Energy through the Mickey Leland Program prior to attending Penn State University. She has also been selected for the Alfred Sloan Fellowship and has worked at the National Energy Technology Laboratory at the Morgantown, WV site. She looks forward to a career in the energy and power industry.